



UNIVERSIDAD NACIONAL AUTÓNOMA DE MÉXICO
POSGRADO EN CIENCIAS FÍSICAS
INSTITUTO DE CIENCIAS NUCLEARES

**INTENSE MAGNETIC FIELDS, HIGH TEMPERATURE AND DENSITY
EFFECTS ON QCD-RELATED PHENOMENA**

TESIS

QUE PARA OPTAR POR EL GRADO DE:
DOCTOR EN CIENCIAS (FÍSICA)

PRESENTA:
JORGE DAVID CASTAÑO YEPES, M. Sc.

TUTOR PRINCIPAL
DR. JOSÉ ALEJANDRO AYALA MERCADO (ICN-UNAM)

MIEMBROS DEL COMITÉ TUTOR
DR. SARIRA SAHU (ICN-UNAM)
DR. GENARO TOLEDO SÁNCHEZ (IF-UNAM)

CIUDAD DE MÉXICO, ENERO DE 2021



Universidad Nacional
Autónoma de México

Dirección General de Bibliotecas de la UNAM

Biblioteca Central

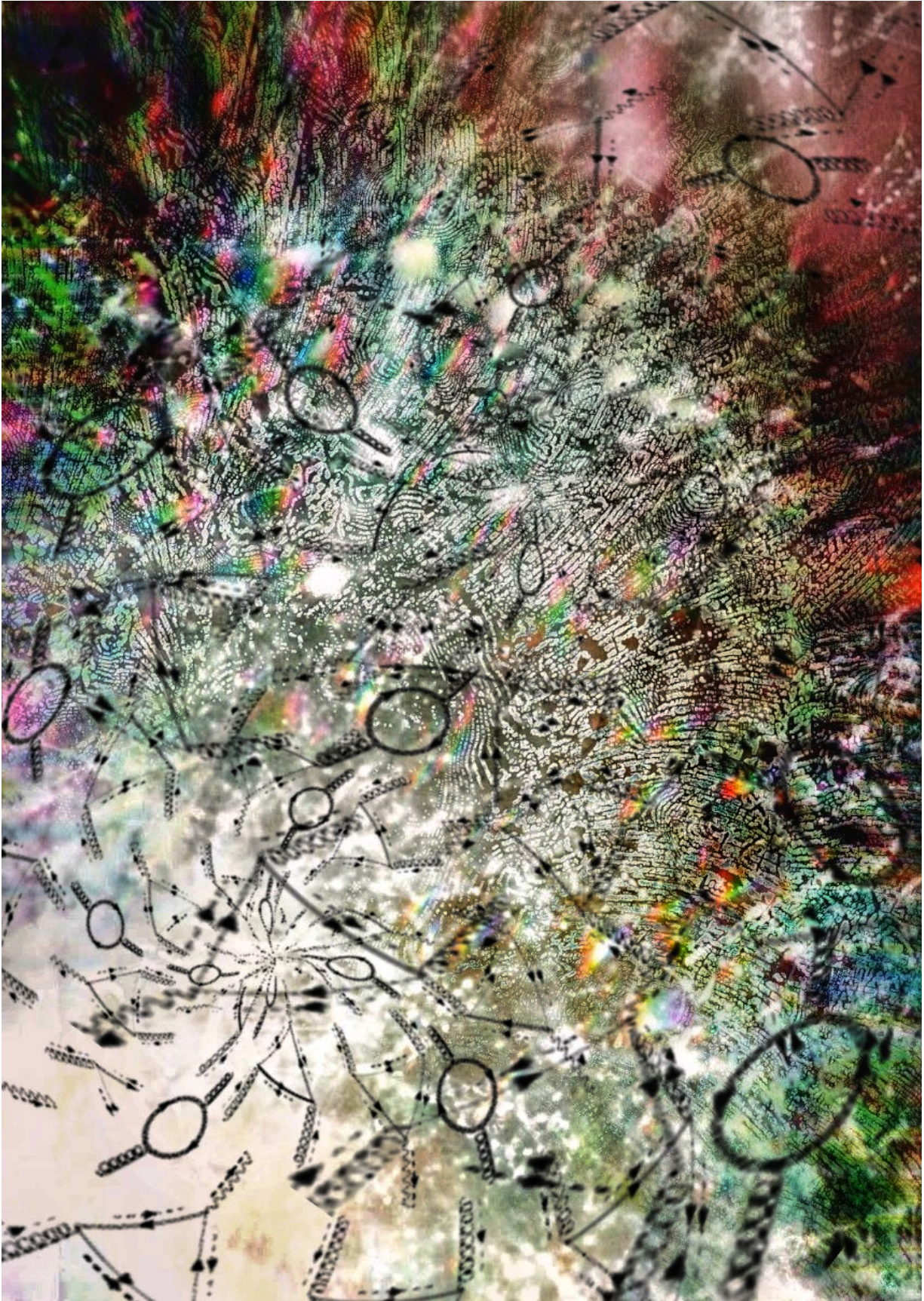


UNAM – Dirección General de Bibliotecas
Tesis Digitales
Restricciones de uso

DERECHOS RESERVADOS ©
PROHIBIDA SU REPRODUCCIÓN TOTAL O PARCIAL

Todo el material contenido en esta tesis esta protegido por la Ley Federal del Derecho de Autor (LFDA) de los Estados Unidos Mexicanos (México).

El uso de imágenes, fragmentos de videos, y demás material que sea objeto de protección de los derechos de autor, será exclusivamente para fines educativos e informativos y deberá citar la fuente donde la obtuvo mencionando el autor o autores. Cualquier uso distinto como el lucro, reproducción, edición o modificación, será perseguido y sancionado por el respectivo titular de los Derechos de Autor.



*A mis padres y a mi hermana.
A Cristian y a Paps.*

*“Study hard what interests you the most
in the most undisciplined, irreverent
and original manner possible.”
—Richard Feynman.*

Contents

Abstract	x
Resumen	xii
Acknowledgments	xiv
Statement of Originality	xv
List of Publications	xvi
Introduction	1
1 The QCD Phase Diagram and the Critical End Point from the Linear Sigma Model	10
1.1 Quantum Chromodynamics	11
1.1.1 QCD Flavor Symmetry	12
1.1.2 QCD Chiral Symmetry	14
1.1.3 Asymptotic Freedom	17
1.2 Generalities of the QCD Phase Diagram	17
1.3 The QCD Phase Diagram from the Linear Sigma Model Point of View	20
1.3.1 Symmetries of the Linear Sigma Model	21
1.3.2 Spontaneous Symmetry Breaking of the Linear Sigma Model	23
1.3.3 Effective Potential for the $L\sigma M$	25
1.3.4 Effective Potential in the High Temperature Approximation	27
1.3.5 Effective Potential in the Low Temperature Approximation	29

1.3.6	Locating the CEP and Computing the Pressure	32
1.4	Conclusion	37
2	The Direct Photon Excess	39
2.1	Relativistic Hydrodynamics and Elliptic Flow	40
2.2	The Direct Photon Puzzle	44
2.3	The Color Glass Condensate (CGC)	49
2.4	Magnetic Fields in a Relativistic Heavy-Ion Collision	57
2.5	Prompt Photon Production by Gluon Fusion in a Magnetized Medium	61
2.5.1	Photon invariant momentum distribution and elliptic flow	66
2.6	Centrality Dependence of the Photon Production by Gluon Fusion and Gluon Splitting in a Magnetized Medium	70
2.6.1	Photon invariant momentum distribution and elliptic flow from gluon fusion and gluon splitting channels	71
2.6.2	Magnetic Field Strength and Space Time Volume from UrQMD	72
2.6.3	Photon Invariant Distribution and Harmonic Coefficient with UrQMD simulations	78
2.6.4	Comparison with PHENIX data	80
2.7	Conclusion	82
3	Gluon Polarization Tensor in Magnetized and Thermomagnetic Media	85
3.1	Magnetized Gluon Polarization Tensor from the Sum of All Landau Levels	87
3.1.1	Tensor Basis	89
3.1.2	Elimination of spurious tensors	92
3.1.3	Obtaining the Vacuum Polarization Tensor	94
3.1.4	Strong Field Limit	95
3.1.5	Weak Field Limit	97
3.1.6	Thresholds for an arbitrary magnetic field	98
3.2	Gluon Polarization Tensor in a Hot and Strongly Magnetized Medium	102
3.2.1	Gluon Polarization Tensor in the High Temperature and Strong Magnetic Field Limits	102

3.2.2	Correction to the gluon Debye mass	104
3.3	Gluon Polarization Tensor in a Weakly Magnetized Medium	106
3.3.1	Weak Field Approximation of the Fermion Propagator Revisited	106
3.3.2	One-Loop Gluon Polarization Tensor	111
3.3.3	Gluon Dispersion Relation and Polarizations	114
3.4	Conclusion	118
A	High-Temperature Approximation for the One-Loop Boson and Fermion Effective Potentials	119
B	Schwinger's Phase Factor	126
C	Matrix element for the process $gg \rightarrow \gamma$ with all the quarks in the LLL	128
D	Calculation of \widetilde{M} for the process $gg \rightarrow \gamma$	130
E	Invariant Momentum Distribution and Flow Coefficient Calculation for the Process $gg \rightarrow \gamma$	136
F	Proof of Eq. (2.70)	141
G	Derivation of tensor structures of Eqs. (3.7)	143
H	Tensor manipulation of Eqs. (3.7)	154
I	Vacuum contribution in the HTL and LLL approximations	156
J	Calculation of \widetilde{P}^L and \widetilde{P}^T when $q^2 \ll m_f^2 \ll T^2$	159
K	Calculation of \widetilde{P}^L and \widetilde{P}^T when $m_f^2 \ll p^2 \ll T^2$	161
L	Calculation of $i\Pi_{(1,1)}^{\mu\nu}$, $i\Pi_{(2,0)}^{\mu\nu}$ and $i\Pi_{(0,2)}^{\mu\nu}$	163
	Bibliography	168

List of Figures

1	Lorentz diagram which schematizes the stages in a relativistic heavy-ion collision. The z -coordinate represents the collision axis, and the proper time τ characterizes the duration of each phase.	2
2	Critical points conjectured for the QCD phase diagram beyond the $\mu_B \sim T$ region: The Critical End Point (CEP), the critical point induced by the Quark-Hadron Continuity (QHC), the Liquid-Gas Transition of nuclear matter (LGT) and an approximate Triple Point (TP) [41].	5
1.1	Schematic representation of the state-of-the-art for the QCD phase diagram on the T and μ_B plane.	18
1.2	Order parameter for (a) a first-order phase transition and (b) a second-order phase transition. The transition occurs at the critical temperature T_c	25
1.3	Self-energy Feynman diagrams for each boson species. From top to bottom, each line of diagrams contributes to Π_σ , Π_{π^0} , and Π_{π^\pm} , respectively.	27
1.4	Thermodynamic potential $V(v)$ as a function of the order parameter v for temperatures lower, equal, and great than the critical temperature T_c . The phase transition is classified as (a) first-order and (b) second-order.	32
1.5	Phase diagram computed from the high-temperature approximation. The orange band is crossover transition region found by the LQCD Taylor expansion method [149].	34
1.6	Phase diagram computed from the low-temperature approximation. The orange band is crossover transition region found by the LQCD Taylor expansion method [149].	35

-
- 1.7 CEP location from different approaches. The points with error bars come from LQCD extensions and they are taken from Refs. [120] (red), [158] (blue), [159] (black), [121] (magenta), and [160] (green). The black filled symbols correspond to the low-temperature approach of Eq. (1.87) when the coupling constants (λ, g) are: $(2.2, 1.7)$ for \blacksquare , $(2.4, 1.65)$ for \blacktriangle , $(2.1, 1.725)$ for \bullet , $(2.5, 1.7)$ for \blacktriangledown , and $(2.7, 1.6)$ for \blacktriangleright . The empty symbols are the effective models predictions: \square from Ref. [161], \otimes from Ref. [153], ∇ from Ref. [156], \odot from Ref. [154], \triangleleft from Ref. [162], \triangleright from Ref. [155], \triangle from Ref. [157], \circ from Ref. [163], and \diamond from Ref. [152]. 36
- 1.8 Pressure in units of T^4 . (a) Comparison between the results obtained from the low and high temperature-approximations and the LQCD data for two light flavors. (b) Pressure from LQCD simulations for 2 and 3 light flavors and 2 light + 1 heavy quark, compared with the named approaches. The arrows indicate the Stefan-Boltzmann gas or the ideal gas limit. The data were taken from Ref. [164]. 37
- 2.1 Transverse momentum spectra for pions, kaons and protons, as a function of the transverse momentum p_\perp for two centralities: 0 – 5% and 30 – 40%. The red (pions), green (kaons), and blue (protons) lines correspond to the predictions of the hydrodynamical calculations by Ryu *et al.* [182]. The continuous and dashed lines are referred to the maxima and minimal centralities, respectively. The experimental data are taken from Ref. [183] (ALICE Collaboration) and Refs. [184, 185] (CMS Collaboration). 42
- 2.2 Charged particle flows v_2 , v_3 and v_4 as a function of the transverse momentum p_\perp for the centralities 0 – 5%. The red, green, and blue correspond to the predictions of the hydrodynamical calculations of Ryu *et al.* [182]. The experimental data are taken from Ref. [183] (ALICE Collaboration) and Refs. [184, 185] (CMS Collaboration). 43
- 2.3 Experimental direct p_\perp photon spectra reported from different PHENIX measurements and compared with the $p + p$ fit (dashed line) and with the $p + p$ scaled by the corresponding average number of binary collisions N_{coll} (continuous line). Only the central value is shown. For details see Refs. [62, 64, 193–195]. 44
- 2.4 Experimental direct p_\perp photon spectra reported by the ALICE collaboration in Pb+Pb collisions at different centralities. The data is compared to NLO pQCD predictions for the direct photon yield in $p + p$ collisions, which are scaled by the number of binary nucleon collisions N_{coll} for each centrality class. Only the central value is shown. For details see Ref. [60]. 45
- 2.5 Scheme of some relevant processes for photon production in the Paquet’s hydrodynamical model: (a) prompt photons, (b) thermal photons from QGP [68, 69], (c) thermal photons for mesonic reactions [57, 70], and (d) non-cocktail decays. 46

2.6	Hydrodynamical calculation of the direct photon spectra for Au+Au collisions by Paquet <i>et al.</i> from Ref. [71] in two centrality ranges: (a) 0–20% and (b) 20–40%. The calculations are compared with the experimental data from PHENIX [64].	47
2.7	Hydrodynamical calculation of the direct photon spectra for Pb+Pb collisions by Paquet <i>et al.</i> from Ref. [71] for the centrality 0–40%. The calculations are compared with the experimental data from ALICE [66].	48
2.8	Hydrodynamical calculation of the flow coefficient v_2 for the direct and thermal photons by Paquet <i>et al.</i> [71], compared with (a) PHENIX data with centrality 20–40% [202, 203] and (b) ALICE data with centrality 0–40% [66].	48
2.9	Deep Inelastic Scattering: an electron with 4-momentum l_μ is scattered by a proton with 4-momentum p_μ exchanging a virtual photon γ^* with 4-momentum q_μ . If the proton is broken the final hadronic states are represented by the set X	50
2.10	Gluon bremsstrahlung from a quark in perturbative QCD at lowest order.	52
2.11	Parton production described by pQCD in a DIS configuration: (a) Evolution for high Q^2 at fixed x (<i>diluted system</i>) (b) Evolution for high Q^2 and small x (<i>dense system</i>).	53
2.12	Parton distribution functions for the proton in the LHC for computed at LO as a function of the momentum fraction x at the scales (a) $Q^2 = 10 \text{ GeV}^2$ and (b) $Q^2 = 10^4 \text{ GeV}^2$. In each plot, the PDFs are shown for gluons (g), valence quarks (u_v, d_v), sea-quarks (\bar{u}, \bar{d}), strange quarks (s) and charm quarks (c). The error bands correspond to a confidence-level uncertainty of 68%. Note that the gluon PDF is scaled by a factor of 10.	54
2.13	Parton distribution functions for the proton in the LHC for computed at NLO as a function of the momentum fraction x at the scales (a) $Q^2 = 10 \text{ GeV}^2$ and (b) $Q^2 = 10^4 \text{ GeV}^2$. In each plot, the PDFs are shown for gluons (g), valence quarks (u_v, d_v), sea-quarks (\bar{u}, \bar{d}), strange quarks (s) and charm quarks (c). The error bands correspond to a confidence-level uncertainty of 68%. Note that the gluon PDF is scaled by a factor of 10.	55
2.14	Parton distribution functions for the proton in the LHC for computed at NNLO as a function of the momentum fraction x at the scales (a) $Q^2 = 10 \text{ GeV}^2$ and (b) $Q^2 = 10^4 \text{ GeV}^2$. In each plot, the PDFs are shown for gluons (g), valence quarks (u_v, d_v), sea-quarks (\bar{u}, \bar{d}), strange quarks (s) and charm quarks (c). The error bands correspond to a confidence-level uncertainty of 68%. Note that the gluon PDF is scaled by a factor of 10.	56
2.15	(a) Magnetic field space-time evolution at the center of the collision computed in Refs. [72, 74] when the impact parameter b is changed. (b) Magnetic field in units of the squared pion mass m_π^2 in z -direction for several points (x, z) in the plane perpendicular to the charge's motion with $b = 10 \text{ fm}$ [74]. The inset represents the geometry in the transverse plane ($y = 0$) of a noncentral heavy-ion collision.	60

2.16	Feynman diagrams contributing to the production of a photon with four-momentum q^μ from the fusion of gluons with four-momentum p^μ and k^μ . Note the charge flow in each diagram, which differentiates the quark from the antiquark. The fermion lines represent the magnetized propagator of Eq. (2.42).	62
2.17	Feynman diagrams contributing to the process $gg \rightarrow \gamma$ in the presence of a magnetic field. The double lines represent that quark propagator in the 1LL, whereas the single lines represent the propagator in the LLL. The arrows in the propagators are the charge flow and the arrows on the sides represent the momentum direction.	64
2.18	Geometry of the heavy-ion collision: The magnetic field lies on the transverse plane and the photon momentum q_\perp lies in the reaction plane.	67
2.19	(a) Photon invariant momentum distribution obtained from Eq. (2.60) compared with the difference between the PHENIX data [64] and direct photons from Ref. [71]. (b) Harmonic coefficient v_2 computed from Eq. (2.65) compared with PHENIX data [65] and the elliptic flow of the direct photons from Ref. [71]. The green (black) points and errors are experimental measurements with the conversion (calorimeter) method. In both figures, the band shows variations of the parameter $ eB $ within the indicated ranges.	68
2.20	Impact of the flow velocity with $\beta = 0.25$ for (a) Photon invariant momentum distribution obtained from Eq. (2.60) compared with the difference between the PHENIX data [64] and direct photons from Ref. [71]. (b) Harmonic coefficient v_2 computed from Eq. (2.65) compared with PHENIX data [65] and the elliptic flow of the direct photons from Ref. [71]. The green (black) points and errors are measures with the conversion (calorimeter) method. In both figures, the band shows variations of the parameter $ eB $ within the indicated ranges.	70
2.21	Feynman diagrams contributing to the process $g \rightarrow g\gamma$ in the presence of a magnetic field. The double lines represent that quark propagator in the 1LL, whereas the single lines represent the propagator in the LLL. The arrows in the propagators are the charge flow and the arrows on the sides represent the momentum direction.	71
2.22	Stages of a UrQMD simulation for a Pb+Pb collision at CERN/SPS energies.	74
2.23	Magnetic field strength for directions parallel (\hat{x}) and perpendicular (\hat{y}, \hat{z}) to the collision axis for three centrality classes in an Au-Au reaction. The magnetic field is produced by spectators [(a), (c), (e)] and participants + spectators [(b), (d), (f)].	75
2.24	Magnetic field intensity in units of pion mass squared (m_π^2) at the center of the interaction region ($\mathbf{x} = 0$) for several centrality classes and two colliding species with $\sqrt{s_{\text{NN}}} = 200$ GeV. The magnetic field is assumed to be produced by (a) spectators and (b) spectators + participants.	76

2.25	Cross-sections (dashed lines) for two colliding nuclei of radii r_1 and r_2 in (a) a maximal peripheral collision (<i>geometrical cross-section</i>), and (b) a peripheral collision with impact parameter b	77
2.26	(a) Number of participants as function of the time for Au-Au and Cu-Cu collisions in different centrality classes. (b) Interaction volume eAu-Au and Cu-Cu collisions in different centrality classes. Both results are obtained by considering $\sqrt{s_{NN}} = 200$ GeV.	78
2.27	Invariant momentum distribution Au+Au collisions in the 0-20%, 20-40% and 40-60% centrality classes and Cu+Cu collisions in the 0-40% centrality class at $\sqrt{s_{NN}} = 200$ GeV considering the magnetic field generated by (a) participants and (b) participants and spectators.	79
2.28	Harmonic coefficient v_2^{mag} for Au+Au collisions in the 0-20%, 20-40% and 40-60% centrality classes and Cu+Cu collisions in the 0-40% centrality class at $\sqrt{s_{NN}} = 200$ GeV considering the magnetic field generated by (a) participants and (b) participants and spectators.	80
2.29	Difference between PHENIX data [64,265] and the hydrodynamical calculation of Ref. [71] for Au-Au collisions at $\sqrt{s_{NN}} = 200$ GeV compared to the calculation of the invariant yield considering contribution to the magnetic field strength produced by the spectators, and spectators + participants for (a) the 0-20% and (b) 20-40% centrality classes.	81
2.30	Harmonic coefficient v_2 computed from Eq. (2.81) compared with PHENIX data [65] and the elliptic flow of the direct photons from Ref. [71]. The green (black) points and errors are experimental measurements with the conversion (calorimeter) method corresponding to Au+Au collisions at $\sqrt{s_{NN}} = 200$ GeV in the 20-40% centrality class. The red (blue) curve takes into account the magnetic elliptic flow when the field is generated by the spectators (spectators+participants). . .	82
3.1	One-loop diagram representing the gluon polarization tensor.	87
3.2	Real and imaginary parts of the function $I(\rho_{\parallel}^2)$ defined in Eq. (3.47) compared with the result including the spurious contribution of $I_1(\rho_{\parallel}^2)$ from Eq. (3.49). . .	97
3.3	Real and imaginary parts of the coefficients $\hat{\Pi}_{\parallel}$, $\hat{\Pi}_{\perp}$ and $\hat{\Pi}_0$ from Eqs. (3.53)-(3.55) as functions of ρ^2 for fixed values of ρ_{\parallel}^2 and ρ_{\perp}^2 . For comparison, these coefficients are also plotted including the spurious contributions from A_1 and A_2 , given by Eqs. (3.29a)-(3.29c).	99
3.4	Real and imaginary parts of the function $J(\rho_{\parallel}^2)$ defined in Eq. (3.61) for $\mathcal{B} = 1.5$ and added up to $n_{\text{max}} = 100$. Notice the emergence of different resonant thresholds when the quark magnetic mass includes consecutive Landau levels. .	101

3.5	Feynman diagrams contributing to the one-loop gluon polarization tensor in the weak field limit up to $\mathcal{O}(q_f B ^2)$. From the left to the right: $i\Pi_{(1,1)}^{\mu\nu}$, $i\Pi_{(2,0)}^{\mu\nu}$ and $i\Pi_{(0,2)}^{\mu\nu}$	111
3.6	Gluon magnetic mass for the coefficients P_0 and P_\perp found by the intersection of the functions at the left and right-side of Eq. (3.105) for a fixed value of the magnetic field and for $\alpha_s = g^2/4\pi = 0.3$. The triangle represents the physical expected mass whereas the circle is a spurious mass.	115
3.7	Dispersion relation for the mode P_0 obtained with the weak field expansion up to order $\mathcal{O}(B^2)$ and compared with the general expression at all orders (massless regime). The figure is constructed with the condition $p_3^2 = ap_\perp^2$ for two values of a and a fixed value of $ q_f B $. The inset shows a complete agreement with the motion along the light cone.	115
3.8	Dispersion relation for the modes P_\parallel and P_\perp obtained with the weak field expansion up to order $\mathcal{O}(B^2)$ and compared with the general expression at all orders (massless regime). The figure is constructed with the condition $p_3^2 = ap_\perp^2$ for two values of a and a fixed value of $ q_f B $. The inset shows deviations with respect to the motion along the light cone.	116
3.9	Solutions of Eq. (3.105) for the mode P_0 as a function of p_0/m_f for several values of p_\perp with the constriction $p_3^2 = ap_\perp^2$. The plot compares the coefficient obtained from the approximation up to $\mathcal{O}(B^2)$ with the result obtained to all orders in B . As can be noticed the former gives a spurious solution for $p_\perp \leq p_\perp^* \simeq 0.1209m_f$, which disappears when the latter is considered. The same behavior is present in the coefficient P_\perp	116
3.10	Normalized tensor coefficients \hat{P}_\parallel and \hat{P}_\perp with the on-shell condition $p^2 = 0$ as a function of p_\perp^2/m_f^2 computed from the weak field expansion given by Eqs. (3.104b)-(3.104c) (full symbols) and compared with the general expressions found in Eq. (3.44) (open symbols) for three values of $ q_f B $	117
C.1	Feynman diagrams contributing to the process $gg \rightarrow \gamma$ with all the fermions in the loop are in the LLL.	128
D.1	Feynman diagrams contributing to the process when the fermion with momentum r is in the 1LL and the fermions with momentum s and t are in the LLL.	131

Abstract

In this thesis, the effects of high-temperature, dense systems, and strong magnetic fields on Quantum Chromodynamics related phenomena are studied in different perspectives. The primary motivation is provided by experimental setups in heavy-ion collisions at the RHIC and LHC laboratories, where the strongly interacting matter reaches thermal, dense, and magnetized phases.

The first problem to handle out is the QCD chiral symmetry restoration, which gives information about the phase transition between the hadronic matter to the Quark-Gluon plasma state. In order to make quantitative predictions, the Linear Sigma Model, coupled to quarks, is used as an effective model of low-energy QCD. In the framework of the thermal field theory, particularly, the imaginary-time formalism, the fermion, and boson effective potentials, up to the ring diagrams' contribution, were computed as a function of the temperature quark-chemical potential and the chiral condensate. Constrictions on the coupling constants and physical masses are imposed, leading to a sketch of the QCD-phase diagram and a plausible location of the so-called Critical End Point. The pressure is also computed, and the results show that the model reproduces, on average, the number of degrees of freedom.

The second analysis is made at the intense magnetic field and high gluon density regimes. To improve the hydrodynamical calculations which fail to describe the photon invariant momentum distribution and the elliptic flow coefficient at low photon's momentum, two new channels for photon production are proposed: the gluon fusion and the gluon splitting. Those processes are demonstrated to be allowed by the presence of an intense magnetic field. The electromagnetic radiation produced by the named mechanism may be found at the pre-equilibrium stage called the Color Glass Condensate, given its coexistence with the intense magnetic fields in a heavy-ion collision. To consider a realistic space-temporal evolution of the magnetic background, the centrality, and the reaction volume, the proposal is complemented with simulations with the UrQMD formalism, showing a good agreement with the experimental data for photon's momentum below 1.5 GeV.

Finally, the screening properties of a thermomagnetic gluon medium are computed from the one-loop gluon polarization tensor. Starting from the fermion propagator written as a sum over Landau levels, the polarization tensor is computed for the magnetic field's arbitrary strength. It is shown that there are several thresholds associated with quark/antiquark pair-productions when the gluon's momentum resonates with a particular Landau level. Moreover, the birefringence phenomenon is found. On the other hand, the limits of Hard Thermal Loops and weak

magnetic field show that the generated Debye mass changes according to the energy scales' hierarchy and the order of expansion for the magnetized fermion propagator.

Resumen

En esta tesis, desde diversas perspectivas, se estudian los efectos de las temperaturas y densidades altas, así como los campos magnéticos intensos en fenómenos relacionados con la Cromodinámica Cuántica (QCD). La motivación principal se fundamenta en las condiciones experimentales en colisiones de iones pesados de los laboratorios RHIC y LHC, en donde la materia que interactúa fuertemente alcanza fases térmicas, densas y magnetizadas.

El primer problema a tratar es la restauración de la simetría quiral de la QCD, la cual da información acerca de la transición de fase de la materia hadrónica al estado de Plasma de Quarks y Gluones. Para hacer predicciones cuantitativas, el Modelo Sigma Lineal acoplado con quarks es usado como modelo efectivo para QCD a baja energía. Mediante el formalismo de la teoría térmica de campos, en particular, el desarrollo en el tiempo imaginario, los potenciales efectivos para fermiones y bosones son calculados con correcciones de diagramas de anillo. Dichos potenciales resultan en funciones de la temperatura, el potencial químico de quarks y el condensado quiral. Se imponen restricciones a las constantes de acoplamiento, que en conjunto con los valores de las masas físicas, permiten hacer un esbozo del diagrama de fases para la QCD y dar una posible ubicación del Punto Crítico. La presión también es calculada, mostrando que el modelo utilizado sólo reproduce en promedio los grados de libertad del sistema.

El segundo análisis se centra en el régimen de campo magnético intenso y alta densidad de gluones. Con el fin de mejorar los cálculos hidrodinámicos, los cuales fallan a la hora de describir la distribución invariante de fotones y el coeficiente de flujo elíptico, se proponen dos nuevos canales para la producción de fotones: la fusión y la división de gluones. El formalismo muestra que dichos procesos están permitidos siempre y cuando exista un campo magnético de fondo, lo cual implica que este tipo de radiación proviene de una etapa de pre-equilibrio denominada *Color Glass Condensate*, que coexiste con campos magnéticos intensos generados por la colisión. Para considerar una evolución espacio-temporal realista del campo magnético, de la centralidad y del volumen de interacción, la propuesta es complementada con simulaciones en el marco del formalismo UrQMD, mostrando que los resultados tienen un buen acuerdo con los datos experimentales cuando el momento del fotón está por debajo de 1.5 GeV.

Finalmente, las propiedades de apantallamiento para el gluón en un medio termomagnético son calculadas a partir del tensor de polarización a un bucle. Empezando por el propagador de fermión escrito como una suma de niveles de Landau, el tensor de polarización se obtiene para una intensidad arbitraria del campo magnético. Se muestra que existen diferentes umbrales, los cuales se asocian a producción de pares quark/antiquark cuando el momento del gluón resuena

con alguno de los niveles de Landau. Además, se encuentra que el fenómeno de birrefringencia existe para este sistema. Por otro lado, en los límites de alta temperatura (*Hard Thermal Loop*) y campo magnético débil, se muestra que la masa de Debye cambia de acuerdo a la gerarquía entre las escalas de energía y el orden de la expansión del propagador de fermión magnetizado.

“If each of my words were a drop of water, you would see through them and glimpse what I feel: gratitude, acknowledgment.”

— Octavio Paz.

Acknowledgments

I am indebted to Mexico: all my present (and future) career is thanks to this beautiful country, its people, and the support that they gave me. Words are not enough to express my gratitude.

To the Universidad Nacional Autónoma de México for opening its doors and allowing me to be part of the highest house of studies in Latin America: it is an honor and a dream come true to call it my *alma mater*.

Of course, this process would not have been possible without the guidance of my supervisor Alejandro Ayala. Since my master’s studies, he has become a unique mentor in academia and life. His patience, motivation, and friendship are inspirational, and he has become an example to follow.

Many thanks to the Matter Under Extreme Conditions group members. In particular, to Malena, Alfredo Raya, Saúl, Luis, Jordi, and Isabel. Their close collaboration over all these years was fundamental to the results presented in this thesis.

I also want to thank professor Marcelo Loewe and Enrique Muñoz for allowing me to do two research stays at the Pontificia Universidad Católica de Chile. Their academic support and hospitality made these visits one of the most enriching experiences I ever had.

To all my officemates, Turri, Omar, Edgar Rosas, Louis, Edgar Guzmán, Juan Carlos, Juan José, Tonatiuh, Hugo, and Eduardo: physics, laughs, coffee and friends always will be an excellent combination.

Thanks to Esaú Ortiz for the back cover art. *Now, the boutonniere may say “Castaño”, but the hat says “Evú”.*

And finally, to my life mates, Cristian and Paps: all the things are better with their company.

Statement of Originality

The calculations and results presented in this thesis are original and collaborative work.

Chapter 1 and Appendix A cover my contributions to calculating the linear sigma model's thermodynamic potentials, as well as the discussion, guidance, and corrections made by the authors of the corresponding article in Ref. [1].

Chapter 2 and Appendices B, C, D, and E have my calculations for the matrix elements, photon's momentum invariant distribution, and elliptic flow corresponding to the gluon fusion mechanism. All the procedures were discussed, revised, and corrected by the authors of Ref. [2]. The computational details of Sec. 2.6 were addressed by Jordi Salinas, Dr. Maria Elena Tejada-Yeomans, and Dr. Isabel Dominguez Jimenez. My contribution consisted of the calculation of the gluon splitting channel and discussion of the results. All the authors of Ref. [3] agreed to consing such information in the present thesis.

Chapter 3 and Appendices G and H present my work at the academic stay in the Pontificia Universidad Católica de Chile. Those calculations were revised and discussed by all the authors of Ref. [4]. Section 3.2 is included because of discussions coming from the findings of Sec. 3.1, which leads to expand and correct the results of previous work and is published in Ref. [5]. Section 3.3 is the result of collaborative work and is currently undergoing peer-review [6].

The other sections constitute the state-of-the-art around the topics presented. The figures were reproduced with their respective citations.

List of Publications

This thesis is based on the following published articles:

1. *Chiral symmetry transition in the linear sigma model with quarks: Counting effective QCD degrees of freedom from low to high temperature.*
Alejandro Ayala, Jorge David Castaño-Yepes, J. J. Cobos-Martinez, Saul Hernandez-Ortiz, Ana Julia Mizher, Alfredo Raya.
Int. J. Mod. Phys. A **31**, 1650199 (2016).
2. *Prompt photon yield and elliptic flow from gluon fusion induced by magnetic fields in relativistic heavy-ion collisions.*
Alejandro Ayala, Jorge David Castaño-Yepes, C. A. Dominguez, L. A. Hernandez, Saúl Hernandez-Ortiz, María Elena Tejeda-Yeomans.
Phys. Rev. D **96**, 014023 (2017).
3. *Centrality dependence of photon yield and elliptic flow from gluon fusion and splitting induced by magnetic fields in relativistic heavy-ion collisions.*
Alejandro Ayala, Jorge David Castaño-Yepes, Isabel Domínguez, Jordi Salinas San Martín, María Elena Tejeda-Yeomans.
Eur. Phys. J. A **56**, 53 (2020).
4. *Gluon polarization tensor in a magnetized medium: Analytic approach starting from the sum over Landau levels.*
Alejandro Ayala, Jorge David Castaño-Yepes, Enrique Muñoz, Marcelo Loewe.
Phys. Rev. D **101**, 036016 (2020).
5. *Thermal corrections to the gluon magnetic Debye mass*
Alejandro Ayala, Jorge David Castaño-Yepes, C. A. Dominguez, S. Hernandez-Ortiz, L. A. Hernandez, M. Loewe, D. Manreza Paret, R. Zamora.
Rev. Mex. Fis. **66** (4) 446-461, (2020).

and the manuscript under peer-review:

1. *Gluon polarization tensor and dispersion relation in a weakly magnetized medium.*
Alejandro Ayala, Jorge David Castaño-Yepes, L. A. Hernández, Jordi Salinas, R. Zamora.
preprint arXiv:2009.00830.

Also, participation in several meetings produced the following proceedings:

1. *Thermal photons from gluon fusion with magnetic fields.*
Alejandro Ayala, Jorge David Castaño-Yepes, C. A. Dominguez, L. A. Hernandez.
EPJ Web of Conferences **141**, 02007 (2017).
2. *Using the Linear Sigma Model with quarks to describe the QCD phase diagram and to locate the critical end point.*
Alejandro Ayala, Jorge David Castaño-Yepes, Jos Antonio Flores, Saúl Hernández-Ortíz, L. A. Hernández.
EPJ Web of Conferences **172**, 08002 (2018).
3. *Prompt photon yield and v_2 coefficient from gluon fusion induced by magnetic field in heavy-ion collision.*
Alejandro Ayala, Jorge David Castaño-Yepes, C. A. Dominguez, L. A. Hernández, Saúl Hernández-Ortíz, María Elena Tejada-Yeomans.
EPJ Web of Conferences **172**, 08004 (2018).
4. *New channels of prompt-photon production by magnetic fields in heavy-ion collisions.*
Alejandro Ayala, Jorge David Castaño-Yepes, Isabel Domínguez, Jordi Salinas San Martín, María Elena Tejada-Yeomans.
J. Phys. Conf. Ser. **1602**, 012014 (2020).

And as product of collaborations in different topics, the following articles were published:

1. *In situ photoacoustic characterization for porous silicon growing: detection principles.*
C. F. Ramirez-Gutierrez, Jorge David Castaño-Yepes, M. E. Rodriguez-Garcia.
J. Appl. Phys. **119**, 185103 (2016).
2. *Modeling the photoacoustic signal during the porous silicon formation.*
C. F. Ramirez-Gutierrez, Jorge David Castaño-Yepes, M. E. Rodriguez-Garcia.
J. Appl. Phys. **121**, 025103 (2017).
3. *A comparative study on heat capacity, magnetization and magnetic susceptibility for a GaAs quantum dot with asymmetric confinement.*
J. D. Castaño-Yepes, C. F. Ramirez-Gutierrez, H. Correa-Gallego, Edgar A. Gómez.
Phys. E. **103**, 464-470 (2018).
4. *Perturbation theory for open quantum systems at the steady state.*
Edgar A. Gómez, Jorge David Castaño-Yepes, Saravana Prakash Thirumuruganandham
Results in Physics **10**, 353-355, (2018).
5. *Porosity and roughness determination of porous silicon thin films by genetic algorithms.*
C. F. Ramirez-Gutierrez, Jorge David Castaño-Yepes, M. E. Rodriguez-Garcia.
Optik **173**, 271-278 (2018).

-
6. *Optical interferometry and photoacoustics as in-situ techniques to characterize the porous silicon formation: a review.*
C. F. Ramirez-Gutierrez, Jorge David Castaño-Yepes, M. E. Rodriguez-Garcia.
Open Mater. Sci. **4**, 23fi??32 (2018).
 7. *Effects of the interface roughness in the optical response of one-dimensional photonic crystals of porous silicon.*
I. A. Lujan-Cabrera, C. F. Ramirez-Gutierrez, Jorge David Castaño-Yepes, M. E. Rodriguez-Garcia.
Phys. B. **560**, 133-139, (2019).
 8. *Impact of a topological defect and Rashba spin-orbit interaction on the thermo-magnetic and optical properties of a 2D semiconductor quantum dot with Gaussian confinement.*
Jorge David Castaño-Yepes, D. A. Amor-Quiroz, C. F. Ramirez-Gutierrez, and Edgar A. Gómez.
Phys. E. **109**, 59-66, (2019).
 9. *Super-statistical description of thermo-magnetic properties of a system of 2DGaAs quantum dots with gaussian confinement and Rashba spinforbit interaction.*
Jorge David Castaño-Yepes and D. A. Amor-Quiroz.
Phys. A **548**, 123871 (2020).
 10. *Optical intersubband properties of a core-shell semiconductor-topological insulator quantum dot described by θ -Electrodynamics.*
Jorge David Castaño-Yepes, O. J. Franca, C. F. Ramirez-Gutierrez, J. C. del Valle.
Phys. E. **123**, 114202 (2020).
 11. *Comments on “Superstatistical properties of the one-dimensional Dirac oscillator” by Abdelmalek Boumali et al.*
Jorge David Castaño-Yepes, I. A. Lujan-Cabrera, C. F. Ramirez-Gutierrez.
Phys. A., 125206 (2020)– In Press.

Introduction

In the study of nuclear and subnuclear matter, Quantum Chromodynamics (QCD) is the fundamental theory that describes the degrees of freedom related to the strong interaction, i.e., the quarks and gluons [7, 8]. From the beginning of the QCD formulation, two remarkable characteristics of that theory make it difficult to study from the theoretical and experimental perspectives: the *Asymptotic Freedom*, which difficult the calculations from a perturbative scheme for arbitrary energy scales [9, 10], and the *Color Confinement*, that forbid quarks and gluons to be isolated and independent entities [11, 12]. Even so, QCD has become an extremely successful theory, and all its predictions have been tested in particle accelerators over more than 50 years.

The QCD's theoretical vacuum properties are extensively studied, from the processes involving only quarks and gluons to the hadron's spectrum description. Experimental findings complement these studies, giving a global understanding of the strong interaction in normal conditions [13]. However, relativistic heavy-ion experiments carried out at the BNL Relativistic Heavy-Ion Collider (RHIC) and CERN Large Hadron Collider (LHC) had found relevant information which proves the existence of a state of matter in where quarks and gluons are not confined to individual nucleons in the so-called *Quark-Gluon Plasma* (QGP) [14–19]. In such experiments, there are several and remarkable differences between the results obtained when one considers proton-proton ($p+p$) and nucleus-nucleus ($A+A$) collisions [20–24]. In principle, the differences between both kinds of reactions can be attributed to the amount of matter which is involved in the collision: at first approximation, the proton can be considered as a point-like particle, and therefore, a $p+p$ -collision does not create a strongly interacting medium which screens or interacts with the reaction products¹. Thus, the in-medium QCD's characterization is expected to be realized by analyzing the data obtained from AA -experiments whose participants have a large number of nucleons (Au or Pb) which can interact total or partially in a region of a few Fermis long.

The energy deposited in the region created during heavy-ion collision is finally released into particle production so that one can expect collective dynamics and the possibility to study the theory in extreme conditions as high-temperature, large densities, and intense external magnetic fields. That situation becomes of great interest because, in principle, ultra-relativistic limits that give high temperatures and densities can reach the proper energy scales of QCD breaking the confinement of quarks and gluons, which brings insights into the evolution of the early universe.

¹There are signatures of the QGP formation in pp -collisions. See Refs. [25–28]

Nevertheless, because its features and the uncontrolled situation after the nuclear collision, the evolution of the strongly interacting matter passes through several phases, each characterized by energy scales, bulk parameters, and strength of its interactions. Three main phases are of particular interest: the pre-equilibrium state denominated color glass condensate or *Glasma*, the thermalized quark-gluon plasma, and the final stage of hadronization. The QCD asymptotic freedom and the color confinements play a crucial role in the theoretical description of such stages, particularly the very early one admits and perturbative approach. On the other hand, for example, the high-density phases characterized by collective, nonfi?? linear phenomena need computational tools beyond the ordinary perturbation theory.

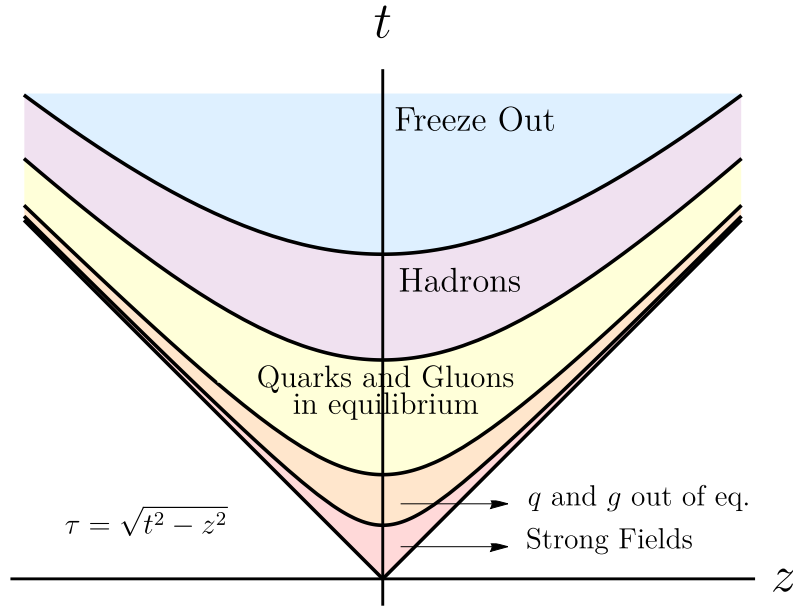


Figure 1: Lorentz diagram which schematizes the stages in a relativistic heavy-ion collision. The z -coordinate represents the collision axis, and the proper time τ characterizes the duration of each phase.

The space-time evolution of a heavy-ion collision is schematized in Fig. 1, giving a general description of the main QCD phases as follows [29]:

Before the collision ($t < 0$), in the center-of-mass frame, which corresponds to experiments carried out at LHC and RHIC, both nuclei are contracted longitudinally by a Lorentz factor $\gamma \sim 100$, so that the colliding objects resemble two thin disks. In the described situation, disks have an abundant number of gluons with a small fraction $x \ll 1$ of the longitudinal momentum, and therefore, by the Heisenberg's dispersion relations, the gluon density is increased by $1/x$ implying relatively sizeable transverse momentum. For example, in a typical Au-Au or Pb-Pb collisions $k_{\perp} \sim 2$ GeV for $x = 10^{-4}$; thus, given the QCD asymptotic freedom, the coupling between such gluons is weak. This stage is known as the *color glass condensate* (CGC).

At the moment of the collision ($\tau = 0$) the processes involving considerable momentum transference ($Q \gtrsim 10$ GeV) evolve fastly ($\tau \sim 1/Q$), producing *hard particles* which have high energy and transverse momenta, such as jets, direct photons, dilepton pairs, heavy quarks, and vector bosons, which are easily identified at the final stage of the reaction. After the collision, at $\tau \simeq 0.2$

fm/c corresponding to a momentum scales $Q \sim 1$ GeV, the gluon content of each nucleus breaks into partonic constituents. The dynamics at this point is fundamental for final observables because most of the particles detected come from the hadronization of such partons. A gluonic high-density medium precedes the partonic production, which has an energy density estimated around $\epsilon \gtrsim 15$ GeV/fm³ for Pb-Pb collision at the LHC, corresponding to 3 times greater than in RHIC Au-Au experiments and three times larger than the nuclear matter. Such a stage is not in equilibrium; i.e., the temperature cannot be defined yet; nevertheless, it forms a boson condensate with particular features, which is the so-called *glasma*.

The next step concerns the QGP identification directly: in a proton-proton collision, the produced particles have a weak interaction between them, leading to a rapid separation and independent dynamics until the hadronization stage. That means that in such collision, there is not an interacting medium for the liberated partons. Nevertheless, for heavy-ion reactions, the situation becomes more complicated, given that partons liberated by the collision do interact with a stronger coupling and exhibit collective phenomena. The experimental data shows that the named partonic matter reaches thermal equilibrium in a short thermalization time $\tau \sim 1$ fm/c, which is a characteristic of strong interactions between constituents making the perturbative methods inapplicable. The rapid thermalization regime is followed by the QGP phase, where quarks and gluons are practically free. From the fact that the overall system keeps expanding and cooling down, it is necessary to assume only local thermal equilibrium in a way that the temperature is space-dependent.

The transit from quarks and gluons to hadrons, i.e., the hadronization stage, occurs when the local temperature reaches the confinement temperature $T_c = 150 - 180$ MeV (see Chapter 1) after a time of $\tau \sim 10$ fm/c. There exist a time window where the hadrons become a system relatively dense so that it is still possible to define a notion of temperature. Its duration is about $10 \lesssim \tau \lesssim 20$ fm/c, and it is identified as a *hadron gas* that continues expanding and cooling down. Finally, when $\tau \sim 20$ fm/c, the hadron gas density decreases to a point where its constituents do not interact anymore so that the interaction rate is lower than the expansion rate. Such a scenario is known as the *freeze-out* regime. It is assumed that detected hadrons come from this stage, and the momentum distribution has a thermal signature of the last fluid-like phase just before the freeze-out. The data analysis shows that indeed the particle spectra are well described by Maxwell-Boltzmann thermal distributions, obtaining a freeze-out temperature $T_f \simeq 170$ MeV.

From the fact that the coupling strength of the several stages in the heavy-ion-collision varies considerably, it is logical to work with QCD effective models in each regime. Also, note that not only a coupling constant based description has to be made, but the active degrees of freedom have also be taken into account. The linear sigma model presented in Chapter 1 is an excellent example of such effective degrees of freedom. In general terms, the theoretical framework currently adopted in the calculations is outlined in the following structure:

- At the very early stages, the dynamic is governed by gluons in a high density and not thermalized states: the CGC and the glasma state. Both are characterized by a semi-hard energy scale with $\alpha_s \sim 0.3$, and although the perturbation theory is formally valid, an expansion in powers of α_s is not straightforwardly obtained given by it is necessary

to sum an infinite class of Feynman graphs enhanced by the high energy and partonic occupation. The latter gives rise to the so-called *CGC effective theory*, which takes into account fundamental aspects as the nuclei wave functions before the collision and the relevant phenomenology at the early stages of the reaction. Such formalism offers quasi-classical color fields as the relevant degrees of freedom. A field point of view instead of a particle description obeys to the dense medium since the phase space occupation numbers are large so that the particle overlap resembles coherent states which are well treated by classical fields.

- At the next stage, the system expands and becomes less dense; hence, the particle treatment is relevant. This point is understood as a breaking of the classical fields into quarks and gluons. Moreover, given that the coupling evolution is continuous, it is expected that such degrees of freedom are weakly coupled and admit a kinetic theory model. That formalism suggests that the free path between two successive collisions is much longer than any other microscopic scale (because the small α_s). Still, it cannot explain the rapid thermalization before the QGP formation.
- The locally thermalized QGP phase lies in a regime between the strong and weak coupling: the temperature estimation for such stage is around $T \sim 500 - 600$ MeV so that $\alpha_s \sim 0.3 - 0.4$. Nonetheless, several effective models can be performed at this point, as well as lattice QCD simulations, which serve as a comparative guide. Of particular interest, thermodynamic quantities as the QGP pressure or energy density are well known from several calculation methods. In particular, if the coupling is weak, techniques such as the *Hard Thermal Loop (HTL)* effective theory have a good agreement with the lattice simulations. The latter is a version of the kinetic theory which assumes long-range interactions of thermalized quasi-particles in a picture where their masses and couplings are temperature-dependent. In that sense, the QGP is identified as a soft-interacting gas of thermal quarks and gluons.
- Once the collision has reached the QGP phase, the system is assumed to be in local thermal equilibrium, given its continuous expansion. At this stage, the *Relativistic Hydrodynamics* is the adequate effective theory to describe the space-time evolution.

This thesis is devoted to studying QCD phenomena related to heavy-ion collisions' early and thermal stages, where the temperature, density, and magnetic fields are extreme.

In the high temperature-baryonic density regimes, it is established that a phase transition achieves the transit from the hadronic matter to the QGP. Moreover, besides the confinement, the chiral symmetry breaking is present in the QCD formalism, leading to light Goldstone particles' description, identified as pions and a non-zero quark condensate. The phase transition from the QGP to hadronic degrees of freedom is then associated with the spontaneous symmetry breaking of the chiral symmetry allowing chiral condensates' formation. On the other hand, since the fundamental QCD's scale is $\Lambda_{\text{QCD}} \sim 200$ MeV, it is expected that quarks and gluons would be liberated for temperatures around $T \sim \Lambda_{\text{QCD}} \sim \mathcal{O}(10^{12})$ K and/or baryonic densities $n_B \sim \Lambda_{\text{QCD}}^3 \sim 1 \text{ fm}^{-3}$. The named critical values may be present in the deep interior of compact stellar objects like neutron stars, where the temperature is low, but the density is increased.

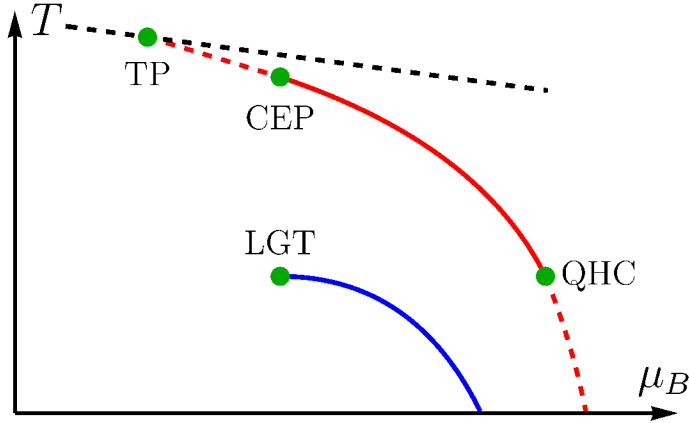


Figure 2: Critical points conjectured for the QCD phase diagram beyond the $\mu_B \sim T$ region: The Critical End Point (CEP), the critical point induced by the Quark-Hadron Continuity (QHC), the Liquid-Gas Transition of nuclear matter (LGT) and an approximate Triple Point (TP) [41].

Several efforts to observe and know the equation of state for those objects have been conducted to test the deconfinement predictions [30]. Clearly, the heavy-ion collisions provide the desired dense and hot mediums.

The nature and structure of the phase transition can be described from theoretical grounds. In the T - n_B plane, the critical temperature T_c is associated with the Hagedorn's limiting temperature T_H using the Statistical Bootstrap Model (SBM), and the phase transition is identified as second-order [31, 32]. In a primitive approximation, the hadron resonance gas at finite temperature is a good starting point so that the density of states $\rho(m)$ (predominantly mesons) is proportional to $\exp(m/T_H)$, where m is the resonance mass and $T_H \simeq 0.19$ GeV is the Regge slope parameter [33]. At the partition function level, the exponential growth is balanced by the Boltzmann factor; thus, the integration over m is singular for $T > T_H$, yielding T_H 's identification as the Hagedorn temperature. A similar argument is applied to know the critical baryonic chemical potential n_B^c : the density of states and the Boltzmann factor are $\exp(m_B/T_H)$ and $\exp[-(m_B - \mu_B)/T]$, respectively. Hence, the limiting temperature is given by $T = (1 - \mu_B/m_B) T_H$, which gives an estimate for the critical density at the low-temperature region: $T = 0 \rightarrow n_B^c \gtrsim 1$ GeV. Now, given that the hadron picture breaks down above the limiting temperature is reasonable to argue a hadronic overlapping and percolating at T_H , resembling the physics behind the quark deconfinement [34, 35].

The phase transition associated with chiral symmetry restoration is identified as an evolution from a system with heavy constituent quarks to a state with light current quarks. [36]. The order parameter is identified with the chiral condensate $\langle \bar{\psi}\psi \rangle$, which in the vacuum is $\langle \bar{\psi}\psi \rangle_0 \simeq (0.24\text{GeV})^3$. That value imposes a natural scale to conjecture the critical temperature and densities. It can be demonstrated that $\langle \bar{\psi}\psi \rangle$ decreases with the temperature and with the baryonic density, indicating a hadron melting in extreme environments [37–40].

The phase diagram is not well established, and its main characteristics are conjectured from the theoretical and phenomenological guides. Nevertheless, there are arguments to make statements around some limit cases, mostly in the region of high temperature and small baryonic

chemical potential $\mu_B \ll T$ and for asymptotically high density $\mu_B \gg \Lambda_{\text{QCD}}$. The several phases of the strongly interacting matter allow sketching the phase diagram passing from the *hadronic matter* to the QGP, and possible configurations that lead to *quarkyonic matter* and *color superconductivity* scenarios. In section 1.2, more details about such phases are discussed.

If there are several phases for the QCD matter, are there different critical points associated with each one? Figure 2 shows the proposed critical points in regions inaccessible for the current experiments and computational tools. Those points are characterized by $\mu_B \sim T$ and postulated from effective models. Chiral models predict the so-called QCD-*Critical End Point* (CEP) defined as the point where the phase transition associated with chiral symmetry restoration passes to be second-order ($\mu_B < \mu_{\text{CEP}}$) to be first-order ($\mu_B > \mu_{\text{CEP}}$) [42–46]. Another first-order phase line, which ends in a critical point for $T \ll \mu_B$, corresponds to cold systems where their degenerate flavors do not have a defined separation between the superfluid nuclear matter and the superconducting quark matter. That point is known as the *Quark–Hadron Continuity* critical point (QHC) [47–51].

The *Liquid-Gas Transition* (LGT) critical point is located when the liquid-gas first-order phase transition for low T turns into second-order. The phases are described in terms of the nucleon properties: the nucleon mass is $m_N \simeq 939$ MeV, and the isospin-symmetric systems have binding energy close to 16 MeV; thus, the baryon chemical potential of nuclear matter arises from $\mu_B = \mu_{NM} \simeq 924$ MeV at $T = 0$. In this value, the density n_B varies from $n_B = 0$ to the nuclear density $n_B = n_0 = 0.17 \text{ fm}^{-3}$. The fragmentation into droplets with densities n_0 is allowed for $n_B < n_0$. Experimentally, heavy-ion collisions show that $\mu_{\text{LGT}} \sim \mu_{NM}$ and $T_{\text{LGT}} = 15 \sim 20$ MeV [52]. Finally, particle detections in collider experiments happens after the freeze-out, a thermally equilibrated gas of non-interacting mesons, baryons, and resonances, with associated μ_B running as a function of the collision energy. Fitting the particle ratios allows to extract the (μ_B, T) data for the freeze-out. Although such data do not correspond to a phase transition boundary, there are arguments to localize the sudden fix of chemical species near a phase transition [53]. Hence, the mesons dominate the freeze-out line for $\mu_B \ll m_N$, whereas for increasing μ_B , baryonic states are excited, indicating a transition point where the latter surpasses the former. Analysis from the QCD-large N_c limit suggests that finite baryon density accompanied by a growing pressure is found when μ_B is greater than the lowest baryon mass, giving rise to a cold, dense state called *quarkyonic matter* [54]. Figure 2 indicates that the phase diagram is separated into three regions: confined, deconfined and quarkyonic phases, where each line corresponds to a first-order boundary. The junction point of such lines is known as the *Triple Point* (TP) [55]. To find the transition lines, and the critical points are of great interest to the QCD-community. For that reason, the first part of this thesis is devoted to elucidating one of the named phase transitions: Chapter 1 presents the QCD phase diagram obtained from the chiral symmetry restoration using the *Linear Sigma Model* coupled to quarks in the framework of the *Thermal Field Theory*. In particular, the analysis is focused on the CEP location as a function of the effective model coupling constants.

The second part of the thesis focuses on the extreme magnetic fields and high-gluon density reached in the early stages of a heavy-ion collision and their consequences in the direct photon detection at the later stages. As stated above, all the information on the collision evolution comes from the analysis of the final hadronic states, so that the theoretical, as well as the experimental

studies. To do this, it is necessary to take into account the multiple interactions (decays, early hadronizations, radiation, thermalization, among others), and final configurations. Hence, the system to study is very complex, making it necessary to find a clean probe containing factual information about the several configurations.

Photons are excellent candidates for testing the QCD properties: given that they don't have color charge, they cannot be scattered by the process in which the strong interaction dominates. Of course, photons would react with electromagnetic charges (quarks), but it is well established that at the first stages of the collision, the pre-equilibrium state is dominated by the presence of gluons (see Sec. 2.3). On the other hand, at the equilibrium phases (thermalized QGP) and the hadronization stages, photons interact with all charged particles, and from Compton scattering or decays, more photons are produced. Fortunately, the current hydrodynamical and perturbative calculations, as well as the experimental efforts, can take into account these mechanisms and differentiate them from each other [56–61]. Therefore, in order to understand the main properties of strongly interacting matter under extreme conditions at a heavy-ion collision, the description of the photon production mechanisms is a major area of study. Currently, direct photon measurements have been carried out at RHIC and LHC [60, 62–67], from where it is possible to identify several photon sources: prompt photons (from partonic Compton interactions), thermal (produced at the QGP and thermalized phases), and Hadronic decays (when the freeze-out is established) [57, 68–70]. Moreover, hydrodynamical calculations describe the photon invariant momentum distribution accurately for ranges of $p_{\perp}^{\gamma} \gtrsim 2$ GeV [71]. Nevertheless, when the photon production is decomposed in its angular distribution through the *flow coefficients*, the theoretical description fails: such incompatibility summarizes the so-called *direct photon puzzle*.

The deviations of the predicted number of photons from the experimental data may be due to novel photon production mechanisms that were not yet considered. In search of those channels, the prompt radiation can be increased by an extra ingredient: the existence of large strength magnetic fields in peripheral heavy-ion collisions, with a magnitude of order of the hadronic scale ($|B| \sim m_{\pi}^2 \sim 10^{18}$ Gauss) [72–76]. Since a magnetic field induces the breaking of rotational invariance, this field is not only a source of an excess photon yield but also of an increase of the second harmonic coefficient of the Fourier expansion in the azimuthal photon distribution. These magnetic fields have a short duration (~ 0.5 fm), and they are well localized in space, mostly in the participant's region (colliding hadrons) and in the transverse direction of the collision. On the other hand, the magnetic field peak intensity is found before the thermal phase (QGP) is created. During these early stages, its presence coincides with that CGC phase: a dense medium dominated by gluons with small longitudinal momentum fraction [77–83]. With this in mind, the present manuscript studies the photon production in stages where the magnetic field makes it possible the creation of photons from processes otherwise not allowed. In particular, attention is centered on channels which include gluons as initial states where the magnetic effects are encoded in the electromagnetic interaction of virtual quarks. Chapter 2 describes the *photon puzzle* together with the *gluon fusion* and *gluon splitting* magnetic-induced photon production. Both channels are computed at the lowest order in α_s by assuming a static and constant magnetic field. The invariant momentum distribution and the elliptic flow coefficient are computed analytically, and their contribution is understood as a yield over the hydrodynamical calculations. Moreover, to account for the centrality dependence of the parameters, the UrQMD

formalism is used. The results are compared with experimental data from RHIC and ALICE, indicating an improvement at low photon transverse momentum.

As was stated, CGC phase coincides with the intense magnetic field generation, which is mostly present in the collision region; therefore, the dense gluonic medium is strongly magnetized. Besides the photon production channels opened by the field, the question about the magnetic effects on the CGC excitation spectrum naturally appears. That information is encoded in the *Polarization Tensor* from which the dynamic masses, dispersion relation, and medium's screening are analyzed. In fact, the one-loop gluon polarization tensor has been computed at zero temperature in standard perturbation theory, relating the vacuum QCD screening properties [84]. Furthermore, that calculation is also made for finite temperature and magnetic field in the *Hard Thermal Loop* (the temperature is the hard scale) and *Lowest Landau Level* (the magnetic field is the dominant energy scale) approximations [85–87]. Breaking of both Lorentz and rotational symmetries shows that the gluon self-interaction becomes important for collective excitations with momenta $p \sim gT$, and for very intense magnetic fields, the Debye screening disappears, whereas the dynamical screening remains. Moreover, the magnetic field opens a threshold for pair production of masses m_f when the gluon momentum component parallel to the magnetic field reaches the value $p_{\parallel}^2 = 4m_f^2$ [88]. In Chapter 3 the gluon polarization tensor is computed by taking into account all the possible energy scales combinations: zero temperature and arbitrary magnetic field, the mass or gluon momentum the lowest energy scale, and the weak field approximation. Such calculations show the role of temperature and magnetic field into the polarization orientation and the Debye's induced mass.

The above discussion leads to the present thesis motivation, which can be summarized in the following research questions:

1. Is it possible to approximate the QCD-phase diagram and give a plausible location of the Critical End Point from the chiral symmetry restoration described by the *Linear Sigma Model*?
2. Can the magnetic field in a dense gluon system open new channels for prompt photon production in order to improve the experimental data description?
3. What is the impact of the temperature, the magnetic field, and the energy scales hierarchy on the gluon polarization tensor and the CGC screening properties?

To answer these questions, the manuscript is organized as follows:

Chapter 1, in Sec. 1.1, introduces the QCD main aspects with a particular interest in its flavor and chiral symmetries, and asymptotic freedom. Section 1.2 gives a general panorama of the state-of-art of the QCD-phase diagram, both from the theoretical and experimental perspectives. Section 1.3 is about the Linear Sigma Model coupled to quarks and its symmetries, together with the spontaneous symmetry breaking and restoration from thermal and density effects. The results show that the transition lines and the CEP location are sensitive to the value of the effective coupling constants, and the pressure is only approximated as an average description of the degrees of freedom.

Chapter 2 is about the *direct photon excess* or *photon puzzle*. In Sec. 2.1, an overall description of the hydrodynamical calculations and its accurate description of the elliptic flow for several experimental data is presented. Section 2.2 explains the *photon puzzle's* origin. Sections 2.3 and 2.4 are centered on the physics of the early stages in a heavy-ion collision, giving a review for the CGC phase and the magnetic field creation, respectively. Section 2.5 presents the photon production proposal from gluon fusion and the comparison with RHIC and ALICE data. Finally, in Sec. 2.6, the gluon splitting channel is computed and added to the gluon fusion one. In this section, the invariant momentum distribution and elliptic flow for the produced photons are improved using simulations in the UrQMD formalism, which consider the space-time evolution of the magnetic field, reaction volume, and the collision centrality.

Chapter 3 is dedicated to studying the magnetic field and the temperature effects on the gluon polarization tensor. The energy scale hierarchy also plays a fundamental role in such a description. In Sec. 3.1, the gluon polarization tensor is computed for an arbitrary magnetic field at zero temperature by resumming all the Landau Levels contribution to the fermion propagator. Section 3.2 computes the same object but in the lowest Landau Level approximation at finite temperature. Here, the comparison between the gluon mass and momentum with the temperature has significant consequences in the polarization tensor coefficients. Section 3.3 studies the Debye mass and gluons dispersion relation in a weakly magnetized medium without temperature.

Each chapter has its conclusions and the detailed calculations are presented at the Appendices.

*“In every branch of knowledge,
the progress is proportional to the
amount of facts on which to build,
and therefore to the facility of ob-
taining data.”*

– James Clerk Maxwell

Chapter 1

The QCD Phase Diagram and the Critical End Point from the Linear Sigma Model

This chapter is devoted to the phenomenological search of the QCD phase diagram and the so-called Critical End Point, which constitutes the point where the deconfinement and chiral phase transition pass from being second-order (at high temperatures and low densities) to be first order (at low temperatures and high densities). The analysis is based on the Linear Sigma Model ($L\sigma M$) coupled with quarks in the thermal field theory framework that effectively models the QCD degrees of freedom and can be promoted to take into account the chiral symmetry restoration.

The chapter starts with a general description of the QCD formalism, particularly the fundamental aspects of its field theory formalism, which covers Section 1.1. The symmetries of the QCD Lagrangian are presented in subsections 1.1.1 and 1.1.2, corresponding to the flavor and chiral symmetry. The latter is of great importance in this work, given that the QCD phase diagram will be built in terms of the chiral symmetry restoration. Moreover, subsection 1.1.3 briefly exposes the QCD Asymptotic Freedom.

Section 1.2 is about the generalities of the QCD phase diagram. Here, the description of the several phases that the strongly interacting matter pass through is accomplished from a theoretical and experimental perspective.

In Section 1.3, the Linear Sigma Model is presented as an attempt to describe the low-energy Hadronic physics. Subsection 1.2 demonstrates that at symmetry level, the $L\sigma M$ Lagrangian has the same invariances as the QCD one; thus, the physical description of the QCD phase diagram can be achieved by such effective treatment. In subsection 1.3, the concept of hidden symmetry and Nambu-Goldstone theorem is discussed, leading to the implementation of the so-called Spontaneous Symmetry Breaking for the $L\sigma M$. Such treatment makes possible the identification of an order parameter as the chiral quark condensate.

From subsections 1.3.3 to 1.3.5, the effective thermodynamic potential is computed by the implementation of the thermal field theory formalism. In such treatment, the potential energy for bosons and fermions is calculated at tree-level and one-loop corrections. Moreover, ring contributions are also taken into account. The thermodynamic description is made by separating the high-temperature approximation, where the expressions become more manageable and analytically solvable, and the low-temperature regime, where the results are found numerically.

Finally, in subsection 1.3.6, the phase diagram is computed, and the CEP location is achieved by imposing constrictions to the coupling parameters λ and g . The critical line at high-temperature and low quark-chemical potential follow the predictions computed in the Lattice QCD framework, whereas the CEP lies in a region compatible with other theoretical studies. The CEP identification depends on the coupling choice, which encodes the information about the degrees of freedom in the model. The results of the pressure support that asseveration: although the $L\sigma M$ does not give the exact functional behavior of that quantity, the high and low-temperature approximations together with the value of the coupling constants reproduces in average the findings reported by Lattice QCD.

The results showed in this chapter are based in the following published manuscripts:

- Article
Chiral symmetry transition in the linear sigma model with quarks: Counting effective QCD degrees of freedom from low to high temperature.
Alejandro Ayala, Jorge David Castaño-Yepes, J. J. Cobos-Martinez, Saul Hernandez-Ortiz, Ana Julia Mizher, Alfredo Raya.
Int. J. Mod. Phys. A **31**, 1650199 (2016).
- Proceeding
Using the Linear Sigma Model with quarks to describe the QCD phase diagram and to locate the critical end point
Alejandro Ayala, Jorge David Castaño-Yepes, Jose Antonio Flores, Saul Hernandez-Ortiz, L. A. Hernandez.
EPJ Web of Conferences **172**, 08002 (2018).

1.1 Quantum Chromodynamics

In order to describe the physics at the nuclear scale and related phenomena, the *Quantum Chromodynamics* (QCD) has been developed as the fundamental theory which describes the strongly interacting matter [7, 8]. It is well established that QCD fundamental degrees of freedom are the *quarks* and *gluons*, which are the basic blocks of the so-called hadronic matter. The very nature of QCD does not allow that quarks and gluons to exist as isolated entities: the well known *QCD Asymptotic Freedom* [9, 10] demands that all the states in nature need to be colorless, i.e., strongly interacting matter can only exist as *baryons* or *mesons* or bound states of quarks, which are named *hadrons* [89, 90]. Thus, a full understanding of the QCD dynamics can be constructed

from two scenarios: one, concerning the (theoretical) study of free quarks and gluons and the other pointing at the hadronic (theoretical and experimental) physics.

Formally, QCD is the $SU(3)$ non-Abelian gauge theory of the color charge, both quarks (fermions) and gluons (bosons) carry color charge. The fundamental representation of $SU(3)$ describes the former with a quark field $\psi_j^{(\alpha)}(x)$ with mass $m^{(\alpha)}$ where $\alpha = u, s, d, \dots$ labels the flavor (the type of quark) and $j = 1, 2, 3, \dots, N_c$ is the color index. The gauge bosons are defined by the field A_μ^a , wherein the adjoint representation of the color (gauge group) degrees of freedom $a = 1, \dots, N_c^2 - 1$, resulting in 8 color indices for gluons. Classical QCD is defined by the Lagrangian:

$$\mathcal{L} = \sum_{\alpha} \bar{\psi}_j^{\alpha} (i\not{D}_{jk} - m^{\alpha}\delta_{jk}) \psi_k^{\alpha} - \frac{1}{4} G_a^{\mu\nu} G_{\mu\nu}^a, \quad (1.1)$$

where the repeated color indices are summed over, and the gauge field tensor $G_{\mu\nu}^a$ is given by

$$G_{\mu\nu}^a = \partial_{\mu} A_{\nu}^a - \partial_{\nu} A_{\mu}^a - g_3 f^{abc} A_{\mu}^b A_{\nu}^c, \quad (1.2)$$

with g_3 the $SU(3)$ coupling parameter. The covariant derivative is given in terms of the group generators $\boldsymbol{\lambda}$, the Gell-Mann matrices, as follows:

$$\mathbf{D}_{\mu}\psi = \left(\partial_{\mu} + ig_3 A_{\mu}^a \frac{\boldsymbol{\lambda}_a}{2} \right) \psi, \quad (1.3)$$

and the structure constants f^{abc} can be found from the commutation relations obeyed by the generators and the trace in group space:

$$[\boldsymbol{\lambda}_a, \boldsymbol{\lambda}_b] = 2if_{abc}\boldsymbol{\lambda}_c \quad (1.4a)$$

and

$$\text{Tr} \{ \boldsymbol{\lambda}_a \boldsymbol{\lambda}_b \} = 2\delta_{ab}. \quad (1.4b)$$

1.1.1 QCD Flavor Symmetry

The symmetry of a Lagrangian is a fundamental piece for the analysis of a field theory, given that the information about the conserved quantities, as well as its breaking, have significant consequences in the physical predictions [91–93]. Symmetry arguments can introduce restrictions over the system constituents interactions or fix the form of the Lagrangian structure. Moreover, if the symmetry is related to the local dynamics (space-time dependent), the gauge theories are a natural result. On the other hand, if the symmetry is space-time independent (global symmetry), it can classify particles according to quantum numbers or predict the existence of massless particles.

The flavor sector of quarks in Eq. (1.1) have a *flavor symmetry* which can be analyzed as follows [94]: suppose that the number of all N_f flavors have the same mass m , so that the quark Lagrangian becomes:

$$\mathcal{L}_q = \sum_{\alpha} \bar{\psi}^{\alpha} (i\not{D} - m) \psi_{\alpha}, \quad (1.5)$$

where the color index are omitted. Equation (1.5) is invariant under infinitesimal global transformations η^a given by:

$$\delta\psi^\alpha = -\frac{i}{2}\delta\eta^a (\boldsymbol{\lambda}^a)_\beta^\alpha \psi^\beta, \quad (1.6a)$$

$$\delta\bar{\psi}^\alpha = \frac{i}{2}\delta\eta^a \bar{\psi}^\beta (\boldsymbol{\lambda}^a)_\beta^\alpha, \quad (1.6b)$$

and

$$\delta A_\mu = 0. \quad (1.6c)$$

From the Noether's theorem, the $N_f^2 - 1$ conserved currents are

$$j_\mu^a(x) = -\frac{i}{2} \frac{\partial \mathcal{L}_q}{\partial (\partial^\mu \psi^\alpha)} (\boldsymbol{\lambda}^a)_\beta^\alpha \psi^\beta = \frac{1}{2} \bar{\psi}_\alpha \gamma_\mu (\boldsymbol{\lambda}^a)_\beta^\alpha \psi^\beta, \quad (1.7)$$

so that

$$\partial^\mu j_\mu^a(x) = 0. \quad (1.8)$$

The conserved charges will be

$$Q^a = \int d^3x j_0^a(x), \quad (1.9)$$

and they satisfy

$$[H, Q^a] = 0, \quad (1.10)$$

is such a way that the corresponding operators satisfy the group algebra:

$$[Q^a, Q^b] = i f_{abc} Q^c. \quad (1.11)$$

Thus, QCD is characterized by the existence of N_f quark fields with equal masses, which are preserved after renormalization, given that the coupling constant is invariant under the group transformations.

Hadronic Approximate Flavor Symmetry

A real description of the flavor symmetry comes about by considering not equal masses for the quarks. The Lagrangian of Eq. (1.5) in that situation reads:

$$\mathcal{L}_q = \sum_\alpha \bar{\psi}^\alpha (i\not{D} - m_\alpha) \psi_\alpha, \quad (1.12)$$

where the mass term is not invariant under de transformations of Eq. (1.6), i.e., the Noether's currents are not conserved:

$$\partial^\mu j_\mu^a = -\frac{i}{2} \sum_{\alpha,\beta} (m_\alpha - m_\beta) \bar{\psi}_\alpha (\boldsymbol{\lambda}^a)_\beta^\alpha \psi^\beta \neq 0. \quad (1.13)$$

Now, if the mass difference is smaller than the QCD energy scale $\Lambda_{\text{QCD}} \sim 300 \text{ MeV}$, the term corresponding to the mass difference can be regarded as a perturbation of the Lagrangian with equal masses \mathcal{L}_0 :

$$\mathcal{L} = \mathcal{L}_0 + \Delta\mathcal{L}. \quad (1.14)$$

In the current state of the art, QCD has $N_f = 6$, so that the mass difference between the light quarks (u, d, s) and the heavy quarks (c, b, t) is large ($> 1 \text{ GeV}$); therefore, the approximate flavor symmetry can be expected only within the space of the three light quarks. Hence the flavor symmetry is connected with the $SU(2)$ symmetry for u and d , and with $SU(3)$ symmetry for u, d, s .

Concerning the isospin symmetry, nucleons and kaons could be organized as doublets in $SU(2)$, and the pions in the triplet (adjoint) of $SU(3)$. Moreover, the mass difference in each multiplet is small which implies that $|m_u - m_d| \sim \text{few MeV}$.

On the other hand, for the $SU(3)$ symmetry, the baryons, and mesons can be grouped in several multiplets, so that in each one, the mass difference reads:

$$m_s - \frac{m_u + m_d}{2} \sim 100 \text{ MeV} \gg |m_u - m_d| \sim \text{few MeV}. \quad (1.15)$$

Finally, the heavy quark sector admits an approximate flavor symmetry when baryons are made of $q_h q_l q_l$ and mesons are made of $\bar{q}_h q_l$, where $q_h = c, b, t$ and $q_l = u, d, s$.

1.1.2 QCD Chiral Symmetry

The fermion sector of QCD admits other kinds of unitary transformations. In particular, the transformation mediated by the matrix γ_5 is of interest because it gives information about the parity of the field theory. To explore such symmetry in the quark sector, the axial flavor transformations in its infinitesimal form are:

$$\delta\psi^\alpha = -\frac{i}{2} \delta\eta^a (\boldsymbol{\lambda}^a)_\beta^\alpha \gamma_5 \psi^\beta, \quad (1.16a)$$

$$\delta\bar{\psi}^\alpha = -\frac{i}{2} \delta\eta^a \bar{\psi}^\beta \gamma_5 (\boldsymbol{\lambda}^a)_\beta^\alpha, \quad (1.16b)$$

and

$$\delta A_\mu = 0. \quad (1.16c)$$

By assuming equal mass for the quarks, the Lagrangian of Eq. (1.1) is not invariant under the above transformations:

$$\delta\mathcal{L}_q = im \delta\eta^a (\boldsymbol{\lambda}^a)^\alpha_\beta \gamma_5 \psi^\beta, \quad (1.17)$$

thus, QCD is invariant under axial transformations only if the quarks are massless. For the unequal quark masses, the above equation is:

$$\delta\mathcal{L}_q = \frac{i}{2} \delta\eta^a (\{\mathbb{M}, \boldsymbol{\lambda}^a\})^\alpha_\beta \gamma_5 \psi^\beta, \quad (1.18)$$

where $\mathbb{M} = \text{diag}(m_1, m_2, \dots, m_{N_f})$ and $\{\cdot, \cdot\}$ is the anticommutator.

To understand the meaning of the chiral symmetry, consider the massless case where the Lagrangian is invariant under the flavor and axial transformations, with conserved currents and charges given by:

$$j_\mu^a(x) = \frac{1}{2} \bar{\psi}_\alpha \gamma_\mu (\boldsymbol{\lambda}^a)^\alpha_\beta \psi^\beta \rightarrow Q^a = \int d^3x j_0^a(x), \quad (1.19a)$$

and

$$j_{5\mu}^a(x) = \frac{1}{2} \bar{\psi}_\alpha \gamma_\mu \gamma_5 (\boldsymbol{\lambda}^a)^\alpha_\beta \psi^\beta \rightarrow Q_5^a = \int d^3x j_{5,0}^a(x), \quad (1.19b)$$

which satisfies the following algebra:

$$\begin{aligned} [Q^a, Q^b] &= if_{abc} Q^c \\ [Q_5^a, Q_5^b] &= if_{abc} Q^c \\ [Q^a, Q_5^b] &= if_{abc} Q_5^c. \end{aligned} \quad (1.20)$$

From the above, it is clear that the axial charges do not form a closed algebra, but if the right and left charges are defined as:

$$\begin{aligned} Q_R^a &\equiv \frac{1}{2} (Q^a + Q_5^a) \\ Q_L^a &\equiv \frac{1}{2} (Q^a - Q_5^a), \end{aligned} \quad (1.21)$$

the algebra is closed in both charges:

$$\begin{aligned} [Q_R^a, Q_R^b] &= if_{abc} Q_R^c \\ [Q_L^a, Q_L^b] &= if_{abc} Q_L^c \\ [Q_R^a, Q_L^b] &= 0. \end{aligned} \quad (1.22)$$

Therefore, the right and left-handed charges define a subgroup of transformations, namely,

$$\text{Chiral Group} = SU(N_f)_R \otimes SU(N_f)_L. \quad (1.23)$$

At Lagrangian level, the chiral symmetry is realized by separating the fermions with definite chirality (i.e., handedness):

$$\mathcal{L}_q = \mathcal{L}_R + \mathcal{L}_L, \quad (1.24)$$

where

$$\mathcal{L}_{R,L} = i\bar{\psi}_{R,L}\not{D}\psi_{R,L}. \quad (1.25)$$

The Lagrangians $\mathcal{L}_{R,L}$ are invariant under the global chiral phase transformations:

$$\psi_{R,L}(x) \rightarrow \exp(-i\alpha_{R,L})\psi_{R,L}(x), \quad (1.26)$$

with $\alpha_{R,L}$ real and constant phases. The total vector and axial charges

$$\begin{aligned} Q &= Q_R + Q_L \\ Q_5 &= Q_L - Q_R, \end{aligned} \quad (1.27)$$

accounts for the number of left-handed and right-handed particles.

Clearly, given the quark masses, the Lagrangian of Eq. (1.1) is not chiral symmetric. That Lagrangian can be written by separating explicitly the term which breaks the symmetry, and for $N_f = 2$ reads:

$$\begin{aligned} \mathcal{L} &= \mathcal{L}_{\text{symmetric}} + \mathcal{L}_{\text{break}} \\ &= \mathcal{L}_{\text{symmetric}} + m_u\bar{\psi}_u\psi_u + m_d\bar{\psi}_d\psi_d \\ &= \mathcal{L}_{\text{symmetric}} + m_q\bar{\psi}\psi + \delta m_q \frac{\bar{\psi}_u\psi_u - \bar{\psi}_d\psi_d}{2}, \end{aligned} \quad (1.28)$$

where

$$m_q = m_u + m_d, \quad (1.29a)$$

$$\delta m_q = m_u - m_d \quad (1.29b)$$

and

$$\bar{\psi}\psi = \frac{\bar{\psi}_u\psi_u + \bar{\psi}_d\psi_d}{2}. \quad (1.29c)$$

The operator $\bar{\psi}\psi$ and its vacuum expectation value $\langle\bar{\psi}\psi\rangle$ (the so-called *chiral condensate*) characterize the magnitude of the symmetry breaking: if $\langle\bar{\psi}\psi\rangle = 0$ the chiral symmetry is restored. In the following section, the generalities of the QCD phase diagram are described in terms of such condensate.

1.1.3 Asymptotic Freedom

Compared with the other fundamental forces described by the Standard Model, Asymptotic Freedom is a feature belonging only to QCD, which establishes that the coupling constant of color g decreases as the scale of renormalization μ_R is increased. Such behavior implies that the perturbative methods are not applicable in all the QCD scales.

The running of the QCD coupling is understood from the analysis of the beta-function obtained from 1-loop diagrams [9, 10, 13]:

$$\beta(g) = \mu_R \frac{dg(\mu_R)}{d\mu_R} = - \left(11 - \frac{3}{2} N_f \right) \frac{g^3}{(4\pi)^2} - \left(102 - \frac{38}{3} N_f \right) \frac{g^5}{(4\pi)^4} + \mathcal{O}(g^7), \quad (1.30)$$

so that, by defining $\alpha_s(t) \equiv \bar{g}^2(t)/4\pi$, where $\bar{g}(t)$ is the running coupling constant with the constriction $\bar{g}(0) = g$, the asymptotic freedom is encoded in the following relation:

$$\alpha_s(\mu_R^2) = \frac{12\pi}{(33 - 2N_f) \ln(\mu_R^2/\Lambda^2)} \left[1 - \frac{6(153 - 19N_f) \ln(\ln(\mu_R^2/\Lambda^2))}{(33 - 2N_f)^2 \ln(\mu_R^2/\Lambda^2)} \right] + \dots, \quad (1.31)$$

where N_f is the number of flavors with mass less than $\sqrt{\mu_R^2}$, and Λ is the scale at which \bar{g} diverges around $\Lambda \equiv \Lambda_{QCD} \simeq 200$ MeV.

The above results give essential properties of the vacuum and scales of QCD [95]. First, the beta function comes from the divergent term of the one-loop corrections to the quark-gluon vertex. The sign on the leading-order in Eq. (1.30) is negative for $N_f = 6$ and positive if $N_f > 16$ (it has severe implications in the quark family numbers). Thus, the screening resulting from virtual quark-antiquark pairs' spontaneous creation is overwhelmed by contributions from virtual gluons, which implies that the QCD vacuum is a paramagnetic medium and antiscreens the color charge. Second, although it is not a proven result, there is a considerable amount of works that indicates that the QCD coupling continues growing when the energy is reduced, leading to the quark confinement phenomenon. Moreover, in comparison with Quantum Electrodynamics (QED), where the perturbative approaches are given in terms of the free parameter $\alpha_{em}(\mu_R^2 = 0) \simeq 1/137$, in QCD the result of Eq. (1.31) implies that α_s is not free at all. Indeed, the running coupling is closely related to the mass scale Λ ; thus, the strong interaction description requires not only a Lagrangian but also a value of Λ . In particular, QCD perturbation approaches can be applied for large mass scales M^2 with $\Lambda^2/M^2 \ll 1$, leaving other energy regimes for purely numerical treatment.

1.2 Generalities of the QCD Phase Diagram

Understanding the matter properties requires a full description of its components in terms of its thermodynamic quantities, such as temperature, density, and the number of particles. It is well known that modifications of the named parameters give rise to the so-called phase transitions: an abrupt and discontinuous change in the system's properties. Such phase transitions can be accompanied by a change of the aggregation state of the matter, i.e., from solid to liquid,

gas, or plasma. A way to visualize the different phases of a system is by constructing a Phase Diagram, a graphical representation of the physical properties when the thermodynamic variables are modified, and the whole system reaches the equilibrium. In general, crossing a line in the diagram means a phase transition, and each line represents the coexistence of two or more phases.

It is well established that the strongly interacting matter can pass through different states (plasma, gas) and phases (chiral, hadronic, superconducting). Its description can give valuable information about the stages after the Big Bang and the general formation of the universe. Therefore, an experimental and theoretical construction of the QCD phase diagram (QCD-PD) is of great interest to the scientific community. Because of the asymptotic freedom of QCD, it is difficult to collect data from cosmological observations, since the quarks and gluons are confined within hadrons. As was commented in previous sections, the relativistic heavy-ion collisions can break the confinement of such degrees of freedom, and therefore, those experiments are fundamental to build up the QCD-PD.

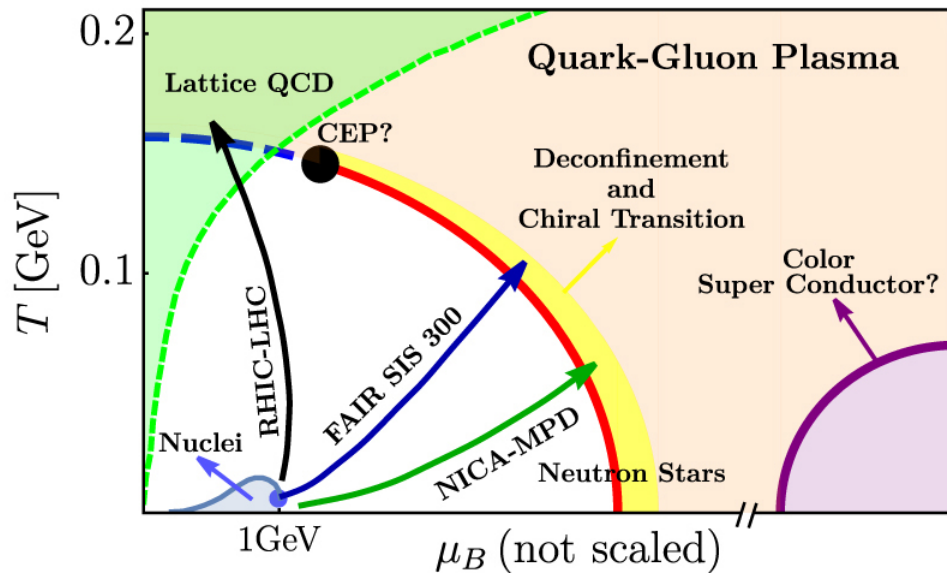


Figure 1.1: Schematic representation of the state-of-the-art for the QCD phase diagram on the T and μ_B plane.

Figure 1.1 shows a sketch which summarizes the current experimental, theoretical, and phenomenological knowledge about the main phases of the QCD sector when the temperature (T) and the net baryonic chemical potential (μ_B) are considered. For low temperatures and low μ_B , the quarks and gluons cannot exist as free; thus, the region on such a diagram represents the hadronic phase. Given that the light-quark chemical potential μ is related to the net baryonic chemical potential by $\mu_B = 3\mu$, nuclear matter corresponds to in $\mu_B \sim 3\mu$. In general terms, that low energetic region has been well described. There is a phase transition for $\mu_B = 0$ and finite temperature, which has been extensively studied in numerical lattice simulations and depends on the number of colors and flavors [96, 97]. A first-order phase transition is found for

$N_c = 3$ and $N_f = 0$ with a critical temperature $T_c \simeq 270$ MeV [98]. For $N_f > 0$ light flavors, there is more than one phase transition.

For the high temperature and low baryonic chemical potential region, the information is provided by the experiments carried out at the BNL Relativistic Heavy Ion Collider (RHIC) [14–18] and the CERN Large Hadron Collider (LHC) [19, 99]. For high temperatures, the QGP is formed, which corresponds to a phase where the quarks and gluons can be considered as free. For almost vanishing μ_B , Lattice QCD calculations have shown that this change of phase is an analytical crossover and therefore, it is not a real phase transition [100–102]. In that sense, a pseudo-critical temperature T_c for $\mu_B = 0$ is defined. Several values of T_c have been reported by lattice calculations with 2+1 quark flavors: the MILC collaboration reported $T_c = 169(12)(4)$ MeV [103], BNLRBC-Bielefeld collaboration obtained $T_c = 193(7)(4)$ MeV [104], the Wuppertal-Budapest collaboration found the smaller number with $T_c = 147(2)(3)$ MeV [105–107], the HotQCD collaboration calculated $T_c = 154(9)$ MeV [108, 109] and $T_c = 155(1)(8)$ MeV [110].

The named lattice QCD calculations cannot be extrapolated to $\mu \neq 0$ because of the *sing problem* [111]. This problem comes from the properties of the fermion determinant, which appears in the averages on QFT. If $M = (\not{D} + m + \mu\gamma_0)$ is the fermion matrix, it can be shown that

$$\det(\not{D} + m + \mu\gamma_0) = [\det(\not{D} + m - \mu^*\gamma_0)]^*, \quad (1.32)$$

which implies that the determinant is not real unless $\mu = 0$ or purely imaginary, and therefore, the Monte Carlo sampling fails, given the oscillating nature of the averages. The green region in Fig. 1.1 schematizes the window of parameters in which lattice QCD can be applied in the present context.

The other extreme of the QCD phase diagram is the case $T \sim 0$ and $\mu_B > 0$. In this case, different model approaches indicate that the transition along the horizontal axis is strongly first order [42–45, 112–116]. Such approaches are made of effective models, assumption of the quarks masses, random matrix models or general thermodynamic considerations. Although the calculation methods are different, the general conclusion is that a deconfined phase is not only reached, but a chiral restoration transition is performed. The chiral phase transition is commonly described by the quark condensate $\langle \bar{\psi}\psi \rangle$ which can be written as [117]:

$$\langle \bar{\psi}\psi \rangle = \frac{\partial \Omega}{\partial m}, \quad (1.33)$$

where Ω is free energy, and m is the quark mass. The last object identifies the order parameter, because in the Nambu-Goldstone phase $\langle \bar{\psi}\psi \rangle \neq 0$, whereas for the Wigner-Weyl phase $\langle \bar{\psi}\psi \rangle = 0$, with the identification $m = 0$ as the chiral limit. To distinguish the chiral and deconfinement transitions is a matter of intense study. It has been suggested that magnetic fields can break the similarities between both phases [118], but recent lattice QCD calculations showed that magnetic fields up to 3.25 GeV^2 do not give significant differences [119].

From the above, a line of first-order phase transitions at low temperatures, and high μ_B has to finish somewhere to give rise to a crossover line. The starting point of the pseudo phase transition begins called the Critical End Point (CEP). To find it, from the theoretical point of view, lattice calculations have been extended to finite chemical potential by Taylor expansions

or Fourier expansion of the grand canonical partition function, locating the CEP in the region $(\mu^{\text{CEP}}/T_c, T^{\text{CEP}}/T_c) \sim (1-1.4, 0.9-0.95)$ [120–123]. The experimental search is led by the RHIC beam energy scan program. In the PHENIX and STAR experiments, the Bose-Einstein correlations (BEC) as a signature for the possible formation of QGP has been reported for Au+Au collisions for $\sqrt{S_{NN}} = 7.7, 11.5, 19.6, 27, 39,$ and 62.4 GeV [124, 125]. The low energy ensures that the stopping power is enough to increase μ_B , and therefore, the exploration of a region far from the vertical axis in the phase diagram is achieved. Although the motivation of conserve non-vanishing baryon chemical potential is well established, the signals of QGP formation become weak [126, 127]. Other observables such as event-by-event fluctuations of conserved charges, kurtosis or cumulants at the CERN, and future experiments as the Facility for Antiprotons and Ion Research (FAIR) in GSI and the Nuclotron-based Heavy-Ion Collider Facility NICA at JINR can give information about other unexplored regions in the QCD phase diagram. Nonetheless, the current knowledge is not conclusive about the existence and location of the CEP [128–132].

Finally, for asymptotically large $\mu_B \gg \Lambda_{\text{QCD}}$, the ground state is analyzed in terms of a weak-coupled system. Here, an analogy with condensed matter physics can be made: the quark matter behaves as electrons in a metal at low temperatures, so that the QCD-ground state should form Cooper pairs in the denominated Color Superconductivity (CSC) phase. Given that there is no single color and flavor, many Cooper pairing patterns may appear and give rise to several CSC kinds [47, 48, 133, 134].

1.3 The QCD Phase Diagram from the Linear Sigma Model Point of View

As it was commented on, the description of the strongly interacting matter when the temperature and density (chemical potential) varies, is of great interest for the QCD phase diagram construction. There are two QCD phase transitions whose understanding represents a challenge: the restoration of chiral symmetry (chiral phase transition), and the deconfinement of quarks and gluons to form the so-called quark-gluon plasma. Currently, there is no agreement on what kind of relationship such phase transitions have and the order of each one. The experiments and theoretical calculations cannot answer if both phase transitions occur at the same temperature or if they manifest at independent T_c . Also, the order of transition varies if with the number of quarks and its masses: if the quarks are considered as massless, lattice calculations predict a second-order phase transition [135–137], whereas the effective models suggest the transition becomes first-order [138, 139].

To understand the dynamics of the chiral restoration, the quark condensate plays the role of the order parameter: it passes from a certain value at the hadronic phase to approximately zero at the QGP phase. Such chiral symmetry breaking is essential to describe the hadronic sector, given that baryons have mass, and there is not parity doubled partners. In that sense, the breaking of that global symmetry implies the existence of massless Goldstone bosons which can be identified as pions (at a first approximation) so that in some region of parameters the symmetry is restored, i.e., the quark condensate disappears [140–142]. A mechanism to describe the latter is the so-

called Spontaneous Symmetry Breaking (SSB), originally proposed by Nambu and Goldstone to describe the superconductivity in metals [143–145]. In general terms, in the SSB, although the Lagrangian remains with global symmetry, the vacuum-solutions are not symmetric, and therefore, if the system transits to one of these low-energy states, the named symmetry is broken around them. That formalism, together with the $SU(3) \times SU(3)$ algebra, can explain the SSB in the low energy sector of QCD.

A Lagrangian which exhibits SSB is the Linear Sigma Model (L σ M). This model was constructed to study the chiral symmetry in the pion–nucleon system, and given that it has the same symmetries of QCD, it can be regarded as a low energy version of such theory [146]. The Lagrangian of the L σ M coupled to quarks is given by:

$$\begin{aligned} \mathcal{L} = & \frac{1}{2} (\partial_\mu \sigma)^2 + \frac{1}{2} (\partial_\mu \boldsymbol{\pi})^2 + \frac{a^2}{2} (\sigma^2 + \boldsymbol{\pi}^2) - \frac{\lambda}{4} (\sigma^2 + \boldsymbol{\pi}^2)^2 \\ & + i\bar{\psi} \gamma^\mu \partial_\mu \psi - g\bar{\psi} (\sigma + i\boldsymbol{\gamma}_5 \boldsymbol{\tau} \cdot \boldsymbol{\pi}) \psi, \end{aligned} \quad (1.34)$$

where ψ is an $SU(2)$ isospin doublet, $\boldsymbol{\pi}$ is an isospin triplet, and σ is an isospin singlet. The neutral pion π^0 is taken as the third component of $\boldsymbol{\pi}$, and the charged pions are defined as $\pi^\pm = (\pi_1 \mp i\pi_2)/2$. The mass squared a^2 , as well as the coupling constants λ and g , are chosen as positive.

1.3.1 Symmetries of the Linear Sigma Model

As studied in Sec. 1.1, the symmetries play a crucial role in the physical description of the QCD phenomena. In that sense, if one desires to get close to the latter, the effective model necessarily has to inherit such symmetries. For that purpose, it is useful to rewrite the Lagrangian of Eq. (1.34) in terms of the matrix field

$$\Sigma \equiv \sigma + i\boldsymbol{\tau} \cdot \boldsymbol{\pi}, \quad (1.35)$$

so that

$$\sigma^2 + \boldsymbol{\pi}^2 = \frac{1}{2} \text{Tr} (\Sigma^\dagger \Sigma). \quad (1.36)$$

Therefore, in terms of the chiral fields $\psi_{R,L}$ the Lagrangian becomes

$$\begin{aligned} \mathcal{L} = & \frac{1}{4} \text{Tr} (\partial_\mu \Sigma \partial^\mu \Sigma^\dagger) + \frac{a^2}{4} \text{Tr} (\Sigma^\dagger \Sigma) - \frac{\lambda}{16} \text{Tr}^2 (\Sigma^\dagger \Sigma) + i\bar{\psi}_L \gamma^\mu \partial_\mu \psi_L + i\bar{\psi}_R \gamma^\mu \partial_\mu \psi_R \\ & - g (\bar{\psi}_L \Sigma \psi_R + \bar{\psi}_R \Sigma^\dagger \psi_L). \end{aligned} \quad (1.37)$$

The above expression implies that the meson sector is invariant under rotations among the σ and $\boldsymbol{\pi}$ fields. On the other hand, the right and left-handed fermions couples together only through interaction with the Σ field. The total symmetry of the Lagrangian is then separated into a left and right invariances, namely:

$$\psi_{R,L} \rightarrow \psi'_{R,L} = U_{R,L} \psi_{R,L}, \quad (1.38a)$$

and

$$\Sigma \rightarrow \Sigma' = U_L \Sigma U_R^\dagger, \quad (1.38b)$$

which is regarded to an $SU(2)_L \times SU(2)_R$ symmetry with $U_{R,L}$ arbitrary $SU(2)$ matrices:

$$U_{R,L} = \exp(-i\alpha_{R,L} \cdot \boldsymbol{\tau}/2). \quad (1.39)$$

Besides a $SU(2)$ isospin rotations on the left and right-handed fermions, the meson sector of the Lagrangian involve isospin rotations among the π fields plus transformations between the σ and π fields given by

$$\sigma \rightarrow \sigma' = \frac{1}{2} \text{Tr} \left(U_L U_R^\dagger \right) \sigma + \frac{i}{2} \text{Tr} \left(U_L \boldsymbol{\tau}^k U_R^\dagger \right) \pi^k, \quad (1.40a)$$

and

$$\pi^k \rightarrow \pi'^k = -\frac{i}{2} \text{Tr} \left(\boldsymbol{\tau}^k U_L U_R^\dagger \right) \sigma + \frac{1}{2} \text{Tr} \left(\boldsymbol{\tau}^k U_L \boldsymbol{\tau}^l U_R^\dagger \right) \pi^l, \quad (1.40b)$$

which in infinitesimal form reads:

$$\sigma \rightarrow \sigma' \simeq \sigma + \frac{1}{2} (\boldsymbol{\alpha}_L - \boldsymbol{\alpha}_R) \cdot \boldsymbol{\pi}, \quad (1.41a)$$

and

$$\pi^k \rightarrow \pi'^k \simeq \pi^k - \frac{1}{2} (\alpha_L^k - \alpha_R^k) \sigma - \frac{1}{2} \epsilon^{klm} \pi^l (\alpha_L^m + \alpha_R^m). \quad (1.41b)$$

The conserved currents associated at the named invariances are:

$$J_{L\mu}^k = \bar{\psi}_L \gamma_\mu \frac{\boldsymbol{\tau}^k}{2} \psi_L - \frac{1}{2} (\sigma \partial_\mu \pi^k - \pi^k \partial_\mu \sigma) + \frac{1}{2} \epsilon^{klm} \pi^l \partial_\mu \pi^m, \quad (1.42a)$$

and

$$J_{R\mu}^k = \bar{\psi}_R \gamma_\mu \frac{\boldsymbol{\tau}^k}{2} \psi_R + \frac{1}{2} (\sigma \partial_\mu \pi^k - \pi^k \partial_\mu \sigma) + \frac{1}{2} \epsilon^{klm} \pi^l \partial_\mu \pi^m, \quad (1.42b)$$

such that by combine them give the conserved vector current:

$$V_\mu^k = J_{L\mu}^k + J_{R\mu}^k = \bar{\psi} \gamma_\mu \frac{\boldsymbol{\tau}^k}{2} \psi + \epsilon^{klm} \pi^l \partial_\mu \pi^m, \quad (1.43)$$

and the conserved axial-vector current:

$$A_\mu^k = J_{L\mu}^k - J_{R\mu}^k = \bar{\psi} \gamma_\mu \gamma_5 \frac{\boldsymbol{\tau}^k}{2} \psi + \pi^k \partial_\mu \sigma - \sigma \partial_\mu \pi^k. \quad (1.44)$$

The presented results confirm that the L σ M has the same symmetries of the QCD Lagrangian; therefore, the former is regarded as an effective model of low-energy hadron dynamics. The next sections will show that chiral spontaneous symmetry breaking present in Eq. (1.34) is a good approximation to describe the QCD phase diagram in terms of the restoration of the chiral symmetry.

1.3.2 Spontaneous Symmetry Breaking of the Linear Sigma Model

It is well established that certain Lagrangians contain *hidden* symmetries that occur when the ground state of the theory does not fulfill the invariance requirements. Such realization appears when the Noether's conserved charge Q acts as a global symmetry transformation into the vacuum state:

$$|0\rangle \rightarrow e^{i\alpha Q} |0\rangle, \quad (1.45)$$

where α is a continuous parameter. The vacuum invariance implies that for all α

$$e^{i\alpha Q} |0\rangle = |0\rangle, \quad (1.46)$$

which is provided by

$$Q |0\rangle = 0. \quad (1.47)$$

The above results show that the vacuum is unique so that if new states $|\alpha\rangle \neq |0\rangle$ appears from the action of Q , they are degenerate. The latter is easily proved from the Noether's theorem for the (time) conserved charge:

$$\dot{Q} = i[H, Q] = 0, \quad (1.48)$$

but given that $H |0\rangle = E_0 |0\rangle$, then

$$H |\alpha\rangle = H e^{i\alpha Q} |0\rangle = e^{i\alpha Q} H |0\rangle = E_0 |\alpha\rangle. \quad (1.49)$$

Also, note that such degeneration is continuous because α is a continuous parameter.

A family of continuous states which share the vacuum energy is interpreted as particles, given that they are excitations around the ground state. Moreover, the lowest energy in the spectrum is identified as the particle's mass; hence, the zero-energy excitations obtained from symmetry transformations must correspond to massless particles which their quantum numbers are associated with the conserved charge Q . That is known as the *Nambu-Goldstone theorem* [84].

For the particular case of the $L\sigma M$, note that the potential energy of Eq. (1.34) given by

$$V(\sigma, \pi) = -\frac{a^2}{2} (\sigma^2 + \pi^2) + \frac{\lambda}{4} (\sigma^2 + \pi^2)^2, \quad (1.50)$$

has a minimum located at the unique configuration $\sigma = \pi = 0$ for $a^2 > 0$, whereas if $a^2 < 0$ implies that the minimum is located at

$$v^2 \equiv \sigma^2 + \pi^2 = \frac{a^2}{\lambda}, \quad (1.51)$$

which defines a 3-sphere in the 4-dimensional space of the fields. Thus, the fields can acquire a configuration around one of those classical minima, independent of which direction it points, implying that the ground state is degenerated, yielding into a hidden symmetry.

To simplify the calculations, the following ground state is selected:

$$\langle \sigma \rangle = v, \quad \langle \boldsymbol{\pi} \rangle = 0, \quad (1.52)$$

which implies that the $\boldsymbol{\pi}$ direction do not require any energy, so that the pions become massless or the so-called *Goldstone bosons*. The particular ground state configuration of Eq. (1.52) has the same physics of the other vacuum states in such a way that one can perform a σ -field redefinition, i.e.,

$$\sigma \rightarrow \sigma + v, \quad (1.53)$$

and replacing into Eq. (1.34), the Lagrangian density becomes:

$$\begin{aligned} \mathcal{L} &= \frac{1}{2} (\partial_\mu \sigma)^2 + \frac{1}{2} (\partial_\mu \boldsymbol{\pi})^2 + i\bar{\psi} \gamma^\mu \partial_\mu \psi - \frac{\lambda}{4} v^4 + \frac{a^2}{2} v^2 \\ &- \frac{1}{2} (3\lambda v^2 - a^2) \sigma^2 - \frac{1}{2} (\lambda v^2 - a^2) \boldsymbol{\pi}^2 - gv\bar{\psi}\psi \\ &- \frac{\lambda}{4} (\sigma^2 + \boldsymbol{\pi}^2)^2 - g\bar{\psi} (\sigma + i\gamma_5 \boldsymbol{\tau} \cdot \boldsymbol{\pi}) \psi. \end{aligned} \quad (1.54)$$

The Lagrangians of Eqs. (1.34) and (1.54) have the same physical information because no additional field sources or interaction were added. However, the above Lagrangian possesses new features:

- (i) The boson fields σ and $\boldsymbol{\pi}$, and the fermion isospin doublet generate dynamic masses in terms of v , namely

$$m_\sigma^2 = 3\lambda v^2 - a^2, \quad (1.55a)$$

$$m_\pi^2 = \lambda v^2 - a^2, \quad (1.55b)$$

and

$$m_f^2 = gv. \quad (1.55c)$$

If the v value is given by Eq. (1.51), the pions are massless, the mass degeneracy $m_\sigma = m_\pi$ is not longer present and the normal isospin invariance associated to axial current of Eq. (1.44) remains.

- (ii) The original SU(2) chiral symmetry is *spontaneously* broken by the term $m_f^2 \bar{\psi}\psi$.

Clearly, the theory returns to be chiral symmetric if $m_f = 0$ which implies $v = 0$. That scenario can be accomplished if v is promoted as an order parameter, i.e., for some thermal configuration, there exists a transition from massive fermions ($v \neq 0$) to a chiral phase of massless fermions ($v = 0$). The order of the named phase transition is given by how v goes to zero: if in the critical temperature T_c the order parameter is discontinuous, the transition is first-order, but if v tends continuously to zero, the transition is second-order or a crossover. Fig. 1.2 shows the order parameter's behavior in a first-order and second-order phase transition.

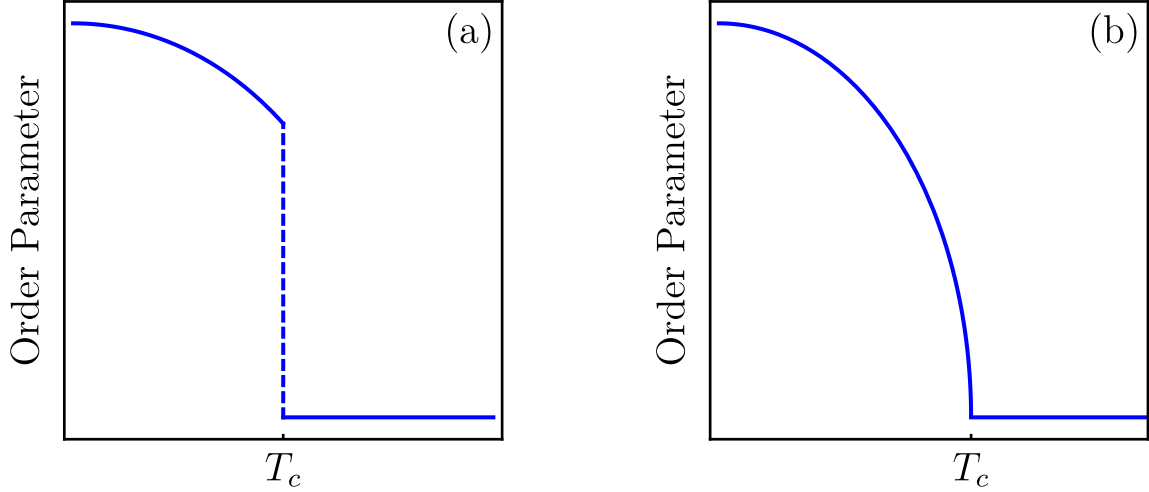


Figure 1.2: Order parameter for (a) a first-order phase transition and (b) a second-order phase transition. The transition occurs at the critical temperature T_c .

1.3.3 Effective Potential for the L σ M

The chiral phase transition can be modeled by the Lagrangian of Eq. (1.54) from the imaginary-time formalism of the thermal field theory. To implement a phase diagram in the $T - \mu$ plane, the quark chemical potential is included by assuming the conservation of the baryon number Q , and therefore, the equilibrium system is described by the grand canonical partition function

$$\mathcal{Z} = \text{Tr} [e^{-\beta(\mathcal{H} - \mu Q)}], \text{ with } \beta = 1/T, \quad (1.56)$$

from which the thermodynamic potential is calculated.

It can be shown that such potential corresponds to the interacting part of the Lagrangian in Eq. (1.54):

$$V_{\text{int}} = \frac{\lambda}{4} v^4 - \frac{a^2}{2} v^2 + \frac{\lambda}{4} (\sigma^2 + \boldsymbol{\pi}^2)^2 + g \bar{\psi} (\sigma + i\gamma_5 \boldsymbol{\tau} \cdot \boldsymbol{\pi}) \psi, \quad (1.57)$$

so that the classical or *tree* level contribution is

$$V_{\text{cl}} = \frac{\lambda}{4} v^4 - \frac{a^2}{2} v^2, \quad (1.58)$$

and the quantum corrections are determined by

$$\mathcal{L}_{\text{int}} = \frac{\lambda}{4} (\sigma^2 + \boldsymbol{\pi}^2)^2 + g \bar{\psi} (\sigma + i\gamma_5 \boldsymbol{\tau} \cdot \boldsymbol{\pi}) \psi. \quad (1.59)$$

In general terms, the thermal potential is a power series in λ . For this work, only the tree-level, the one-loop, and the ring contributions (plasma screening effects) will be taken into account for bosons and fermions. In the following, the expressions for the effective potentials, self-energy, and ring contributions are well-known results found in Ref. [147].

First, the one-loop boson potential can be written as

$$V_b^{(1)} = T \sum_n \int \frac{d^3k}{(2\pi)^3} \ln D(\omega_n, \mathbf{k})^{-1/2}, \quad (1.60)$$

where

$$D(\omega_n, \mathbf{k}) = \frac{1}{\omega_n^2 + \mathbf{k}^2 + m_b^2}, \quad (1.61)$$

is the free propagator, m_b is the boson's mass and $\omega_n = 2n\pi T$ are the Matsubara's frequencies.

On the other hand, the one-loop correction for fermions at finite temperature and chemical potential μ is

$$V_f^{(1)} = -T \sum_n \int \frac{d^3k}{(2\pi)^3} \text{Tr} [\ln S(\tilde{\omega}_n - i\mu, \mathbf{k})^{-1}], \quad (1.62)$$

where

$$S(\tilde{\omega}_n, \mathbf{k}) = \frac{1}{\gamma_0 \tilde{\omega}_n + \not{k} + m_f}, \quad (1.63)$$

is the propagator of a fermion with mass m_f and Matsubara frequencies $\tilde{\omega}_n = (2n + 1)\pi T$.

Finally, the ring contribution is given by

$$V^{\text{(ring)}} = \frac{T}{2} \sum_n \int \frac{d^3k}{(2\pi)^3} \ln [1 + \Pi(m_b, T, \mu) D(\omega_n, \mathbf{k})], \quad (1.64)$$

where $\Pi(m_b, T, \mu)$ is the boson's self-energy.

Figure. 1.3 shows the diagrammatic representation of the terms contributing to $\Pi(m_b, T, \mu)$, such that each boson has a self-energy corresponding to a boson-boson and boson-fermion loops, and the total self-energy is given by

$$\Pi_l(T, \mu) = \Pi_l^b(T) + \sum_{j=u,d} \Pi_j^f(T, \mu), \quad (1.65)$$

where l runs for the boson fields (σ, π^0, π^\pm) and j for the two light quark flavors (u, d). The explicit form of the pure bosonic part of $\Pi_l^b(T)$ is

$$\Pi_\sigma^b = \lambda \left[3I \left(\sqrt{m_\sigma^2 + \Pi_\sigma^b} \right) + 2I \left(\sqrt{m_{\pi^\pm}^2 + \Pi_{\pi^\pm}^b} \right) + I \left(\sqrt{m_{\pi^0}^2 + \Pi_{\pi^0}^b} \right) \right], \quad (1.66a)$$

$$\Pi_{\pi^0}^b = \lambda \left[I \left(\sqrt{m_\sigma^2 + \Pi_\sigma^b} \right) + 2I \left(\sqrt{m_{\pi^\pm}^2 + \Pi_{\pi^\pm}^b} \right) + 3I \left(\sqrt{m_{\pi^0}^2 + \Pi_{\pi^0}^b} \right) \right], \quad (1.66b)$$

$$\Pi_{\pi^\pm}^b = \lambda \left[I \left(\sqrt{m_\sigma^2 + \Pi_\sigma^b} \right) + 4I \left(\sqrt{m_{\pi^\pm}^2 + \Pi_{\pi^\pm}^b} \right) + I \left(\sqrt{m_{\pi^0}^2 + \Pi_{\pi^0}^b} \right) \right]. \quad (1.66c)$$

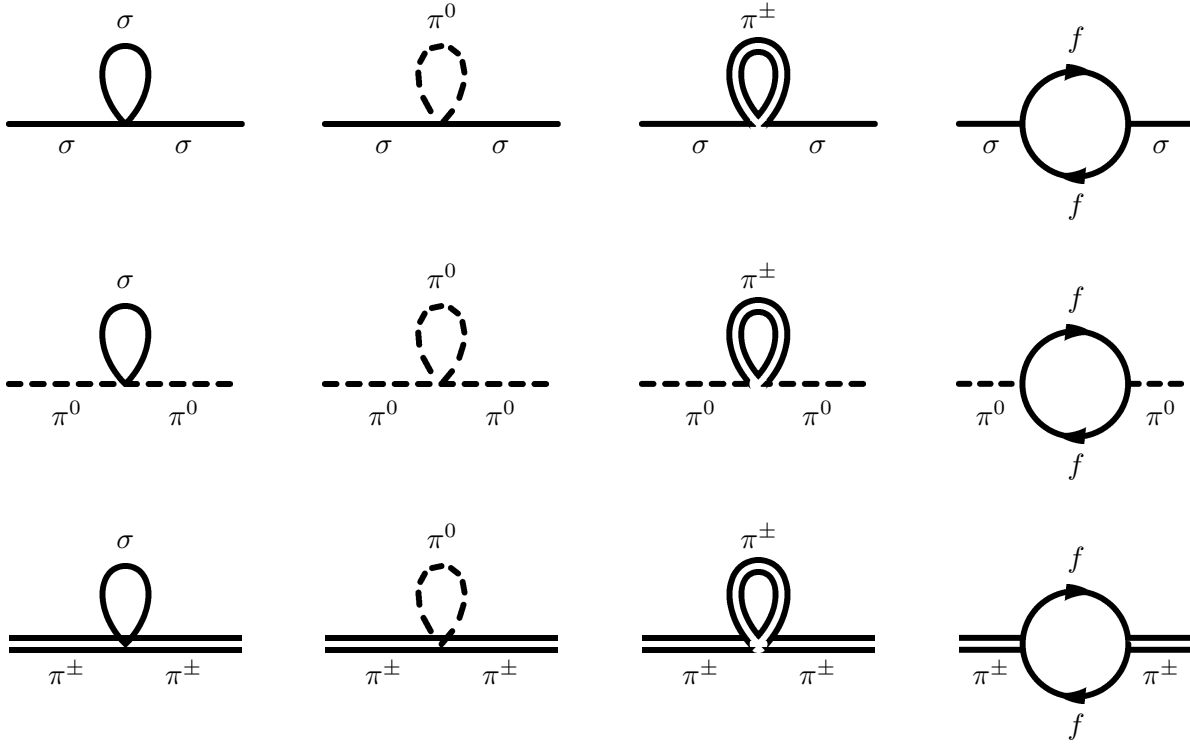


Figure 1.3: Self-energy Feynman diagrams for each boson species. From top to bottom, each line of diagrams contributes to Π_σ , Π_{π^0} , and Π_{π^\pm} , respectively.

where

$$I(x) = \frac{1}{2\pi^2} \int dk \frac{k^2}{\sqrt{k^2 + x}} n(\sqrt{k^2 + x}), \quad (1.67)$$

and $n(x)$ is the Bose-Einstein distribution. Moreover, the self-energy for the fermionic loop has the form

$$\Pi^f = -gT^2 \sum_n \int \frac{d^3k}{(2\pi)^3} \text{Tr} [S(\tilde{\omega}_n - i\mu, \mathbf{k}) S(\tilde{\omega}_n - \omega - i\mu, \mathbf{k} - \mathbf{p})]. \quad (1.68)$$

Equations (1.58), (1.60), (1.62), (1.64) and (1.66) define exactly at $\mathcal{O}(\lambda)$ the full thermodynamic information of the model. Still, as can be noticed, they have a non-trivial solution: for example, the expressions for the bosons self-energies are given by a self-consistent form, which implies a numeric treatment or the implementation of some approximations. In the following sections, high and low-temperature approaches will be treated.

1.3.4 Effective Potential in the High Temperature Approximation

From the phenomenology described at the beginning of this section, the current knowledge of the QCD phase diagram comes from experiments and lattice calculations in the high temperature-

low chemical potential region. Therefore, by choosing an appropriate hierarchy of scales, the analysis can be simplified. To implement such a regime, for the first approximation, the temperature is taken as the dominant energy scale, i.e., $T \gg \mu \gg m_q$. The corresponding calculations to this scheme are shown in Appendix A.

To simplify the expressions of the boson's self-energy, note that near the phase transition the quarks and boson masses can be neglected, and therefore, in Eq. (1.66) this can be implemented by setting $m_i^2 + \Pi_i = 0$, which yields:

$$\Pi_\sigma^b = \Pi_{\pi^0}^b = \Pi_{\pi^\pm}^b = \frac{6\lambda}{2\pi^2} \int dk \frac{k}{e^{k/T} - 1} = \frac{\lambda T^2}{2}. \quad (1.69)$$

The fermionic self-energy can be computed without the scale hierarchy $T \gg \mu$ by assuming that near the critical temperature, the chiral symmetry is restored; namely, $m_f = 0$, so that:

$$\Pi_j^f = -N_c g^2 \frac{T^2}{\pi^2} [\text{Li}_2(-e^{\mu/T}) + \text{Li}_2(-e^{-\mu/T})], \quad (1.70)$$

where N_c accounts for the number of colors for each quark, and $\text{Li}_2(x)$ is the second-order polylogarithm function. Thus, the total self-energy for N_f quark-flavors becomes

$$\Pi_l(T, \mu) = \frac{\lambda T^2}{2} - N_f N_c g^2 \frac{T^2}{\pi^2} [\text{Li}_2(-e^{\mu/T}) + \text{Li}_2(-e^{-\mu/T})]. \quad (1.71)$$

For the bosonic effective potential of Eq. (1.60), the sum over Matsubara frequencies gives

$$V_b^{(1)} = \frac{1}{2\pi} \int dk k^2 \left[\frac{\sqrt{k^2 + m_b^2}}{2} + T \ln \left(1 - e^{-\sqrt{k^2 + m_b^2}/T} \right) \right], \quad (1.72)$$

which is composed of two pieces: one corresponding to the vacuum contribution and another one corresponding to the matter or T -dependent correction. The former can be regularized in the MS-scheme with renormalization scale $\tilde{\mu} = a e^{-1/2}$, whereas the latter is computed from the approximation $m_b/T \ll 1$. By taking only the dominant terms, the one-loop effective potential at high temperature is

$$V_{b,\text{HT}}^{(1)} = \sum_{i=\sigma,\pi} \left\{ -\frac{m_i^4}{64\pi^2} \left[\ln \left(\frac{a^2}{4\pi T^2} \right) - \gamma_e + \frac{1}{2} \right] - \frac{\pi T^4}{90} + \frac{m_i^2 T^2}{24} - \frac{m_i^3 T}{12\pi} \right\}, \quad (1.73)$$

where γ_e is the Euler–Mascheroni constant.

The effective potential for fermions also have a piece of vacuum and a piece of matter, i.e., after summing the Matsubara frequencies the result is

$$V_f^{(1)} = -\frac{1}{\pi^2} \int dk k^2 \sqrt{k^2 + m_f^2} + \frac{T}{\pi^2} \int dk k^2 \left\{ \ln \left[1 + e^{-(\sqrt{k^2 + m_f^2} - \mu)/T} \right] + \ln \left[1 + e^{-(\sqrt{k^2 + m_f^2} + \mu)/T} \right] \right\}, \quad (1.74)$$

so that by applying the MS-regularization scheme, and the approximations $m_f/T \ll 1$ and $\mu/T \ll 1$, the leading terms of this potential are

$$V_{f,\text{HT}}^{(1)} = \sum_{f=u,d} \left\{ \frac{m_f^4}{16\pi^2} \left[\ln \left(\frac{a^2}{4\pi T^2} \right) - \gamma_e + \frac{1}{2} - \psi^0 \left(\frac{1}{2} + \frac{i\mu}{2\pi T} \right) - \psi^0 \left(\frac{i\mu}{2\pi T} \right) \right] \right. \\ \left. - 8m_f^2 T^2 [\text{Li}_2(-e^{\mu/T}) + \text{Li}_2(-e^{-\mu/T})] + 32T^4 [\text{Li}_4(-e^{\mu/T}) + \text{Li}_4(-e^{-\mu/T})] \right\}. \quad (1.75)$$

The plasma screening effects are computed from the lowest Matsubara frequency which is the dominant term [147], so that Eq. (1.64) is simplified to

$$V_{\text{HT}}^{(\text{ring})} = \frac{T^2}{4\pi^2} \int dk k^2 \left\{ \ln [k^2 + m_b^2 + \Pi] - \ln [k^2 + m_b^2] \right\} \\ = \frac{T}{12\pi} \left[m_b^3 - (m_b^2 + \Pi)^{3/2} \right]. \quad (1.76)$$

By joining all the pieces, the first-order effective potential up to the ring diagrams for the $L\sigma M$ with N_c quark colours at high temperature is

$$V_{\text{HT}}^{\text{eff}} = -\frac{a^2}{2}v^2 + \frac{\lambda}{4}v^4 \\ - \sum_{i=\sigma,\pi} \left\{ \frac{m_i^4}{64\pi^2} \left[\ln \left(\frac{a^2}{4\pi T^2} \right) - \gamma_e + \frac{1}{2} \right] + \frac{\pi T^4}{90} - \frac{m_i^2 T^2}{24} + \frac{T}{12\pi} (m_i^2 + \Pi)^{3/2} \right\} \\ + N_c \sum_{f=u,d} \left\{ \frac{m_f^4}{16\pi^2} \left[\ln \left(\frac{a^2}{4\pi T^2} \right) - \gamma_e + \frac{1}{2} - \psi^0 \left(\frac{1}{2} + \frac{i\mu}{2\pi T} \right) - \psi^0 \left(\frac{i\mu}{2\pi T} \right) \right] \right. \\ \left. - 8m_f^2 T^2 [\text{Li}_2(-e^{\mu/T}) + \text{Li}_2(-e^{-\mu/T})] + 32T^4 [\text{Li}_4(-e^{\mu/T}) + \text{Li}_4(-e^{-\mu/T})] \right\}, \quad (1.77)$$

where the boson and fermion masses are given by Eq. (1.55), consequently, the effective potential is an explicit function of the order parameter v .

1.3.5 Effective Potential in the Low Temperature Approximation

The high-temperature approximation results is a useful simplification to perform the momentum integration in the effective potentials, resulting in analytical expressions. If one desires to get information about the chiral symmetry restoration when $T \sim \mu$ or $T < \mu$, numerical integration must be performed. Nevertheless, the integrals can be manipulated to obtain simpler integrals.

The first convenient manipulation is for the ring contribution of Eq. (1.64), by taking into account the sum over the bosonic fields:

$$V^{(\text{ring})} = \frac{T}{2} \sum_{i=\sigma,\pi} \sum_{n=-\infty}^{\infty} \int \frac{d^3k}{(2\pi)^3} \ln [1 + \Pi_i(m_i, T, \mu) D(\omega_n, \mathbf{k})]. \quad (1.78)$$

Replacing the expression for $D(\omega_n, \mathbf{k})$ from Eq. (1.61) it is easy to show that

$$\begin{aligned} V^{(\text{ring})} &= \frac{T}{2} \sum_{i=\sigma,\pi} \sum_{n=-\infty}^{\infty} \int \frac{d^3k}{(2\pi)^3} \ln \left[\frac{k^2 + m_i^2 + \omega_n^2 + \Pi_i}{k^2 + m_i^2 + \omega_n^2} \right] \\ &= \frac{T}{2} \sum_{i=\sigma,\pi} \sum_{n=-\infty}^{\infty} \int \frac{d^3k}{(2\pi)^3} \left[\ln(k^2 + m_i^2 + \omega_n^2 + \Pi_i) - \ln(k^2 + m_i^2 + \omega_n^2) \right]. \end{aligned} \quad (1.79)$$

Now, the one-loop of Eq. (1.60) can be written as

$$\begin{aligned} V_b^{(1)} &= T \sum_{i=\sigma,\pi} \sum_{n=-\infty}^{\infty} \int \frac{d^3k}{(2\pi)^3} \ln D(\omega_n, \mathbf{k})^{-1/2} \\ &= \frac{T}{2} \sum_{i=\sigma,\pi} \sum_{n=-\infty}^{\infty} \int \frac{d^3k}{(2\pi)^3} \ln(k^2 + m_i^2 + \omega_n^2), \end{aligned} \quad (1.80)$$

therefore,

$$\begin{aligned} V_b^{(1)} + V^{(\text{ring})} &= \frac{T}{2} \sum_{i=\sigma,\pi} \sum_{n=-\infty}^{\infty} \int \frac{d^3k}{(2\pi)^3} \ln(k^2 + m_i^2 + \omega_n^2 + \Pi_i) \\ &= T \sum_{i=\sigma,\pi} \sum_{n=-\infty}^{\infty} \int \frac{d^3k}{(2\pi)^3} \ln [D^{(\text{ring})}]^{-1/2}. \end{aligned} \quad (1.81)$$

The above equation implies that the calculation of $V_b^{(1)} + V^{(\text{ring})}$ can be performed as if the integral contains a simple boson propagator with the replacement $m_i^2 \rightarrow m_i^2 + \Pi_i$.

Note that Eq. (1.81) can be manipulated in the form

$$\begin{aligned} V_b^{(1)} + V^{(\text{ring})} &= T \sum_{i=\sigma,\pi} \sum_{n=-\infty}^{\infty} \int \frac{d^3k}{(2\pi)^3} \int dm^2 \frac{\partial}{\partial m^2} \ln [D^{(\text{ring})}]^{-1/2} \\ &= -\frac{T}{2} \sum_{i=\sigma,\pi} \sum_{n=-\infty}^{\infty} \int \frac{d^3k}{(2\pi)^3} \int dm^2 [D^{(\text{ring})}]^{-1} \frac{\partial}{\partial m^2} [D^{(\text{ring})}] \\ &= \frac{1}{2} \sum_{i=\sigma,\pi} \int \frac{d^3k}{(2\pi)^3} \int dm^2 T \sum_{n=-\infty}^{\infty} \frac{1}{\omega_n^2 + k^2 + m_i^2 + \Pi_i}, \end{aligned} \quad (1.82)$$

and from the identity [147]

$$T \sum_{n=-\infty}^{\infty} \frac{1}{\omega_n^2 + \omega^2} = \frac{1}{2\omega} \left(1 + \frac{2}{e^{\omega/T} - 1} \right), \quad (1.83)$$

it follows that

$$\begin{aligned}
V_b^{(1)} + V^{(\text{ring})} &= \frac{1}{2} \sum_{i=\sigma,\pi} \int \frac{d^3k}{(2\pi)^3} \int dm^2 \frac{1}{2\sqrt{k^2 + m_i^2 + \Pi_i}} \left[1 + \frac{1}{\exp\left(\frac{\sqrt{k^2 + m_i^2 + \Pi_i}}{T}\right) - 1} \right] \\
&= \sum_{i=\sigma,\pi} \int \frac{d^3k}{(2\pi)^3} \left[\frac{\omega_i}{2} + T \ln(1 - e^{-\omega_i/T}) \right], \tag{1.84}
\end{aligned}$$

where $\omega_i^2 = k^2 + m_i^2 + \Pi_i$.

For the self-energies, the fermionic contribution is taken to be the same as Eq. (1.70). This choice is adequate for the temperatures of interest, namely, close to the phase transition, given that T can still be considered large compared to the fermion mass. The same argument applies to the effective fermionic potential at low temperatures.

At the bosonic sector, the temperature cannot be taken small compared to the mass parameter a . Therefore, none expansion can be performed. Nevertheless, from the fact that the neutral and charged pions have the same mass as a consequence of isospin symmetry, the set of Eqs. (1.66) is reduced to the more straightforward system:

$$\Pi_\sigma^b = \lambda \left[3I \left(\sqrt{m_\sigma^2 + \Pi_\sigma^b} \right) + 3I \left(\sqrt{m_\pi^2 + \Pi_\pi^b} \right) \right], \tag{1.85a}$$

$$\Pi_\pi^b = \lambda \left[I \left(\sqrt{m_\sigma^2 + \Pi_\sigma^b} \right) + 5I \left(\sqrt{m_\pi^2 + \Pi_\pi^b} \right) \right], \tag{1.85b}$$

which leads to the low-temperature self-energy interaction

$$\Pi_l = \Pi_l^b - N_c N_f g^2 \frac{T^2}{\pi^2} \left[\text{Li}_2(-e^{\mu/T}) + \text{Li}_2(-e^{-\mu/T}) \right]. \tag{1.86}$$

By collecting Eqs. (1.75), (1.81), and (1.86), and after mass renormalization at the scale $\tilde{\mu} = a e^{-1/2}$, the effective potential in the low temperature approximation is

$$\begin{aligned}
V_{\text{LT}}^{\text{eff}} &= -\frac{a^2}{2} v^2 + \frac{\lambda}{4} v^4 - \sum_{i=\sigma,\pi} \left\{ \frac{(m_i^2 + \Pi_i)^2}{64\pi^2} \left[\ln \left(\frac{4\pi a^2}{m_i^2 + \Pi_i} \right) - \gamma_e + \frac{1}{2} \right] \right. \\
&+ \left. \frac{T}{2\pi^2} \int dk k^2 \ln \left[1 - \exp \left(-\frac{\sqrt{k^2 + m_i^2 + \Pi_i}}{T} \right) \right] \right\} \\
&+ N_c \sum_{f=u,d} \left\{ \frac{m_f^4}{16\pi^2} \left[\ln \left(\frac{a^2}{4\pi T^2} \right) - \gamma_e + \frac{1}{2} - \psi^0 \left(\frac{1}{2} + \frac{i\mu}{2\pi T} \right) - \psi^0 \left(\frac{i\mu}{2\pi T} \right) \right] \right. \\
&- \left. 8m_f^2 T^2 \left[\text{Li}_2(-e^{\mu/T}) + \text{Li}_2(-e^{-\mu/T}) \right] + 32T^4 \left[\text{Li}_4(-e^{\mu/T}) + \text{Li}_4(-e^{-\mu/T}) \right] \right\}. \tag{1.87}
\end{aligned}$$

Equations (1.77) and (1.87) help to describe a wide range of the $T - \mu$ plane. The parameters a , λ , and g are chosen by comparison with other works and by lattice inspired calculations. That will be explained in the next subsection.

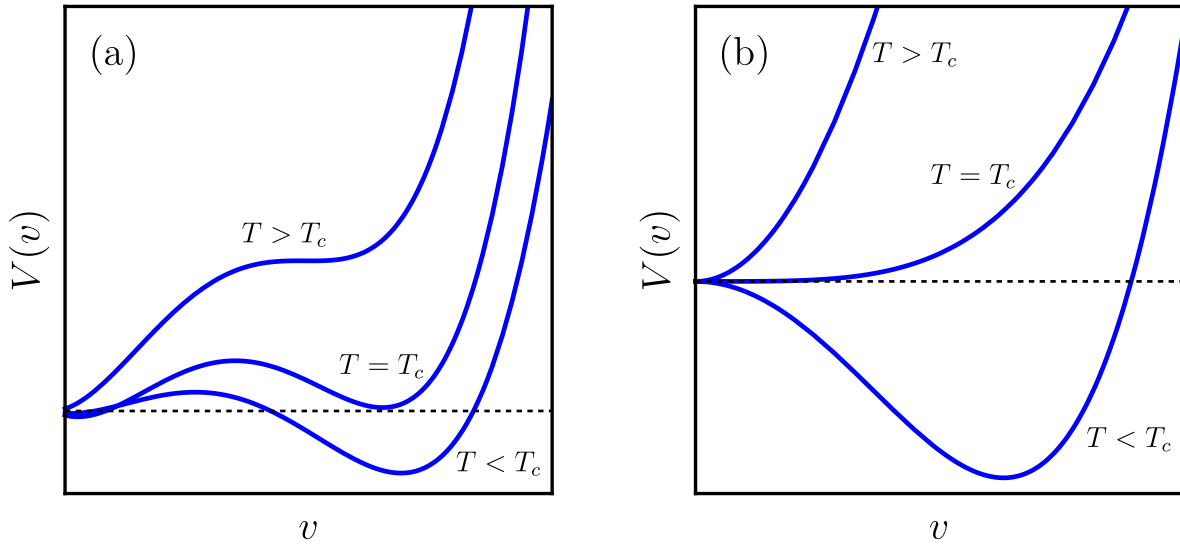


Figure 1.4: Thermodynamic potential $V(v)$ as a function of the order parameter v for temperatures lower, equal, and greater than the critical temperature T_c . The phase transition is classified as (a) first-order and (b) second-order.

1.3.6 Locating the CEP and Computing the Pressure

The discussed framework enables the study of the chiral phase transition when the temperature and the quark-chemical potential vary independently. It is worthy of mentioning that the present formalism only reproduces effective or average values of the thermodynamic observables along the transition curve, which will be appreciated at the pressure's behavior. Thus, the results given by the Linear Sigma Model have to be improved for a theory that takes into account the fundamental QCD degrees of freedom, i.e., quarks and gluons. In the following, the results presented need to be understood as a rough approximation to the real CEP location.

Classification of the phase transition order is given in terms of the value of the order parameter, as discussed in Fig. 1.2. This is achieved by following the behavior of the effective potential V^{eff} when the critical parameters T_c and μ_c are reached. From a pure thermodynamic description, the system prefers to be in the lowest energy state, which is translated as the minimum of the potential. In that sense, there are three possible cases as a function of the thermal parameters, as is shown in Fig. 1.4:

- (i) The system has a temperature $T < T_c$, and the symmetry is broken.
- (ii) The system has a temperature $T = T_c$, and the symmetry is restored.
- (iii) The system has a temperature $T > T_c$, and the symmetry remains.

Of particular interest is when the thermal parameters coincide with the critical ones, i.e., when $T = T_c$. It is well established that there are two configurations for the free energy (effective

potential) at the critical line when it is analyzed as a function of the order parameter ¹. Figure 1.4(a) shows two stable minima located at $v = 0$ and $v \neq 0$, which implies that although the symmetry is restored, the order parameter can have two possible values. By following the thermal evolution of those minima, one can notice that the stable minimum evolves continuously from $v \neq 0$ at $T < T_c$ to $v = 0$ and $v \neq 0$ for $T = T_c$, and remains to be $v = 0$ for $T > T_c$. That evolution corresponds to Fig. 1.2(a), and therefore, it describes a first-order phase transition. On the other hand, the evolution of the stable minimum in Fig 1.4(b) implies a single value of v which goes continuously from $v \neq 0$ for $T < T_c$ to $v = 0$ for $T = T_c$ and continues in $v = 0$ for $T > T_c$, thus, by comparing with Fig. 1.2(b) such behaviour correspond to a second-order phase transition. Hence, the critical parameters on the chiral phase transition and its order will be reported by following the shape of V^{eff} given by Eqs. (1.77) and (1.87), in terms of the vacuum expectation value v .

The $L\sigma M$ has three free parameters, namely, a , λ and g , which need to be fixed to the current phenomenology to give an appropriate description of the phase transition. The parameter a is fixed by the bosons vacuum masses, which is implemented by solving for a the Eqs. (1.55a) and (1.55b), that is:

$$a = \sqrt{\frac{m_\sigma^2 - 3m_\pi^2}{2}}. \quad (1.88)$$

Furthermore, to connect with the lattice data at $\mu = 0$, notice that the thermal boson masses are given by

$$m_b^2(T) = m_{b,\text{vac}}^2 + \Pi_b(T, \mu = 0), \quad (1.89)$$

where $m_{b,\text{vac}}^2$ corresponds to Eqs. (1.55a) and (1.55b) and $\Pi_b(T, \mu = 0)$ is the high temperature approximation for the self-energy of Eq. (1.71). Explicitly, they have the form

$$m_\sigma^2(T) = 3\lambda v^2 - a^2 + \frac{\lambda T}{2} + \frac{N_f N_c g^2 T^2}{6}, \quad (1.90a)$$

$$m_\pi^2(T) = \lambda v^2 - a^2 + \frac{\lambda T}{2} + \frac{N_f N_c g^2 T^2}{6}. \quad (1.90b)$$

At the phase transition ($T = T_c$), the curvature of the effective potential vanishes for $v = 0$. Since the boson thermal masses are proportional to this curvature, they also vanish at $v = 0$. Therefore, from Eqs. (1.90) a relation of the model parameters and the critical temperature T_c is obtained

$$a = T_c \sqrt{\frac{\lambda}{2} + \frac{N_f N_c g^2}{6}}. \quad (1.91)$$

¹It can be argued the existence of phase transitions of a superior order in terms of the Ehrenfest classification, which takes into account the n -th derivative of a thermodynamic potential. As an example, the 2D Chern-insulators present a third-order topological phase transition. However, there is neither broken symmetry nor local order parameters involved in this transition. Therefore, its discussion is beyond the scope of this thesis.

The present work takes into account only two quark flavors in the chiral limit, so it is adequate to compare with lattice simulations for $N_f = 2 + 1$. Then, the value of the critical temperature at $\mu = 0$ is taken to be $T_c \simeq 170$ MeV [148]. The Eqs. (1.88) and (1.91) provide constrictions to the coupling λ and g through experimental/computational constants.

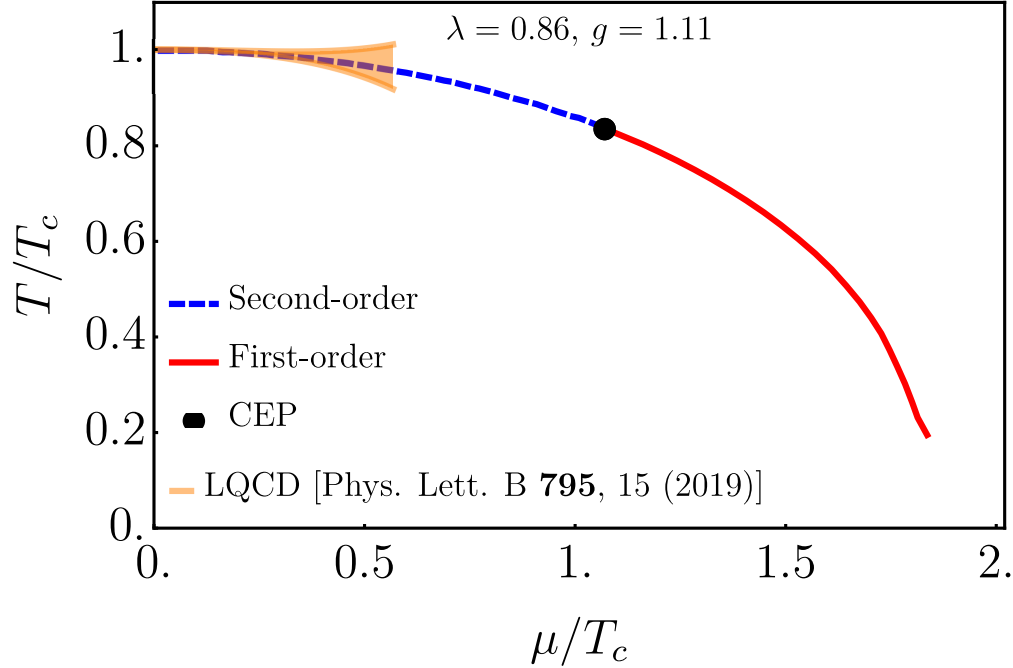


Figure 1.5: Phase diagram computed from the high-temperature approximation. The orange band is crossover transition region found by the LQCD Taylor expansion method [149].

Figure 1.5 shows the phase diagram obtained from the high-temperature approximation. To obtain it, λ and g were chosen in such a way they satisfy Eqs. (1.88) and (1.91) and have a value $\sim \mathcal{O}(1)$. It is worth mentioning that in order to obtain a second-order phase transition at $\mu = 0$, it is necessary that $g^2 > \lambda$, which implies that the fermionic sector is more important at high densities. As can be noticed, the model reproduces a crossover at low chemical potentials in agreement with the results found by the LQCD Taylor expansion method [149]. The second-order phase transition line continues to $\mu/T_c \sim 1$ and gives rise to first-order phase transitions. The CEP is between those two regimes, and the effective potential predicts a continuous transit between them. Nonetheless, given that the analysis is made step by step in the values of μ and T , its exact location lies in a tiny band around the black dot showed in the phase diagram. Moreover, the knee-shape at low temperatures and high densities is a consequence of the non-applicability of the approximation $T \gg \mu$; however, the critical line follows the desired behavior.

The Critical End Point is found to be located at $(\mu_{\text{CEP}}/T_c, T_{\text{CEP}}/T_c) \sim (1.07016, 0.834889)$ or $(\mu_{\text{CEP}}, T_{\text{CEP}}) \sim (181.927 \text{ MeV}, 141.931 \text{ MeV})$. This value is close around the extensions of lattice QCD, which reports the CEP location in the range $(\mu^{\text{CEP}}/T_c, T^{\text{CEP}}/T_c) \sim (1.0 - 1.4, 0.9 - 0.95)$ [120–123] and at the upper limit of calculations with effective models where $(\mu^{\text{CEP}}/T_c, T^{\text{CEP}}/T_c) \sim (1.0 - 2.0, 0.4 - 0.8)$ [150–157].

To fix the coupling constant values at the low-temperature approximation, the restriction $T_c/a =$

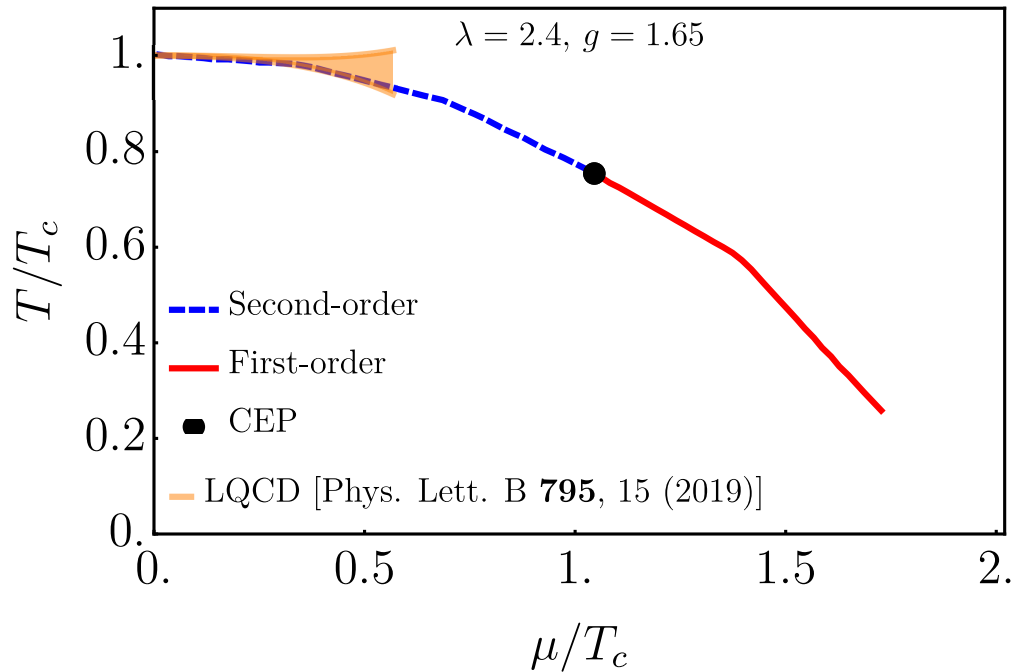


Figure 1.6: Phase diagram computed from the low-temperature approximation. The orange band is crossover transition region found by the LQCD Taylor expansion method [149].

$1/2$ was imposed, which means to set with $m_\sigma \simeq 540$ MeV. Also, the condition that the CEP is near the values obtained at the high-temperature approximation constrains the parameters λ and g . That gives $\lambda = 2.4$ and $g = 1.65$. Its difference compared with the high-temperature sets of couplings is a measure of the change in the effective degrees of freedom in each phase. Figure 1.6 shows the phase diagram resulting from those considerations. As well as in the high-temperature regime, the crossover and the first-order lines were obtained. The former has a good correspondence with the lattice predictions and the latter starts inside the region where other effective models suggest the CEP position. The transition line smoothness is lost because of the numerical integration to solve the self-consistent system of Eqs. (1.85) and (1.87), but in essence, the phase diagram obtained from both temperature criteria are the same.

The effective model admits a window of values for λ and g in such a way that they respect the Eqs. (1.88) and (1.91) and reproduces the CEP location close to the other works predictions. Figure 1.7 shows the CEP locations computed from the low-temperature result of Eq. (1.87) when the coupling constants are changed (black filled symbols), compared with LQCD extensions (points with error bars), and results taken from other models (empty white symbols). It can be noticed that the change of λ and g moves considerably the CEP in such a way that if the boson interaction is stronger than the fermionic one, the first-order phase transition begins at lower temperatures and large quark densities. Moreover, this coupling scenario lies in a region of critical points reported by calculations made from effective estimates based on Nambu-Jona-Lasinio type models with Polyakov loop for 2+1 quarks [153–157], the linear sigma model with $N_f = 3$ [162], and perturbation theory [152]. Remarkably, the CEP obtained from lower values of the couplings is closer to the LQCD extensions. Thus, the correct choice of degrees of freedom for bosons and fermions moves the phase line, which provides at the model with versatility in

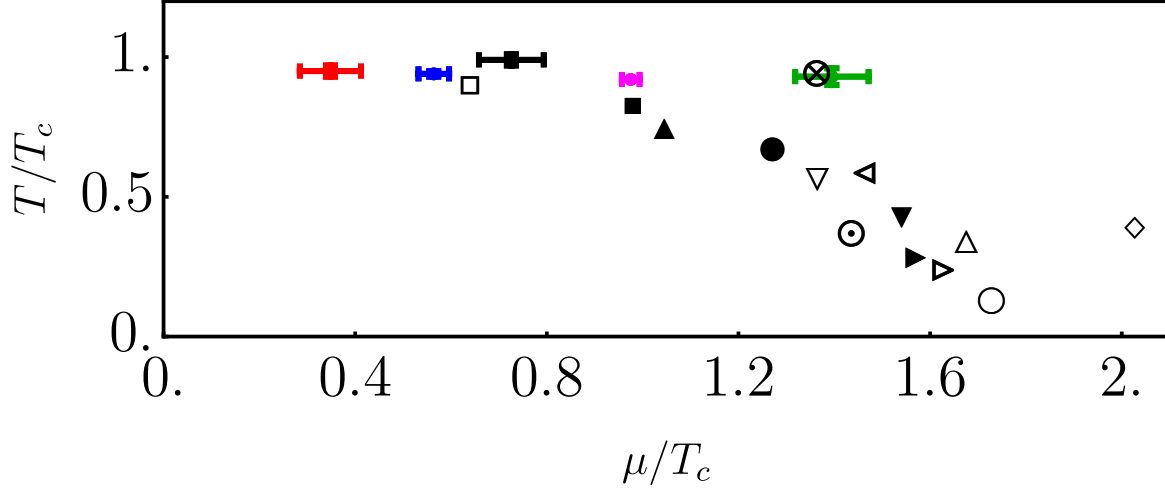


Figure 1.7: CEP location from different approaches. The points with error bars come from LQCD extensions and they are taken from Refs. [120] (red), [158] (blue), [159] (black), [121] (magenta), and [160] (green). The black filled symbols correspond to the low-temperature approach of Eq. (1.87) when the coupling constants (λ, g) are: $(2.2, 1.7)$ for \blacksquare , $(2.4, 1.65)$ for \blacktriangle , $(2.1, 1.725)$ for \bullet , $(2.5, 1.7)$ for \blacktriangledown , and $(2.7, 1.6)$ for \blacktriangleright . The empty symbols are the effective models predictions: \square from Ref. [161], \otimes from Ref. [153], ∇ from Ref. [156], \odot from Ref. [154], \triangleleft from Ref. [162], \triangleright from Ref. [155], \triangle from Ref. [157], \circ from Ref. [163], and \diamond from Ref. [152].

terms of the change of few parameters in order to reproduce current or future physical results.

To test the accuracy of the model in contrast with well-defined observables, the pressure is computed for the low and high-temperature results. Such variable is related to the effective potential as:

$$P = -V^{\text{eff}}(v = 0). \quad (1.92)$$

Figure 1.8(a) shows the pressure for $\mu = 0$ in units of T^4 from the results of the present effective model, compared with LQCD data of 2 light flavors [164]. The coupling constants were chosen for the low-temperature (LT) potential as $\lambda_{\text{LT}} = 2.4$ and $g_{\text{LT}} = 1.65$, and for the high-temperature (HT) approximation as $\lambda_{\text{HT}} = 0.86$ and $g_{\text{HT}} = 1.11$. As can be noticed, the prediction is a constant value for such a thermodynamic variable, with a sudden jump from the LT regime to the HT description.

That behavior can be understood in terms of QCD degrees of freedom (DOF): it is expected that bulk thermodynamic observables like pressure or energy density change abruptly from the hadronic matter at LT to the deconfined phase at HT. Both limits are usually modeled by

$$\frac{P}{T^4} = \begin{cases} \frac{3\pi^2}{90}, & T \rightarrow 0 \\ (16 + \frac{21}{2}N_f) \frac{\pi^2}{90}, & T \rightarrow \infty, \end{cases} \quad (1.93)$$

where N_f is the number of flavors [164, 165]. The HT limit is the pressure in the so-called Stephan-Boltzman (P_{SB}) or ideal gas limit.

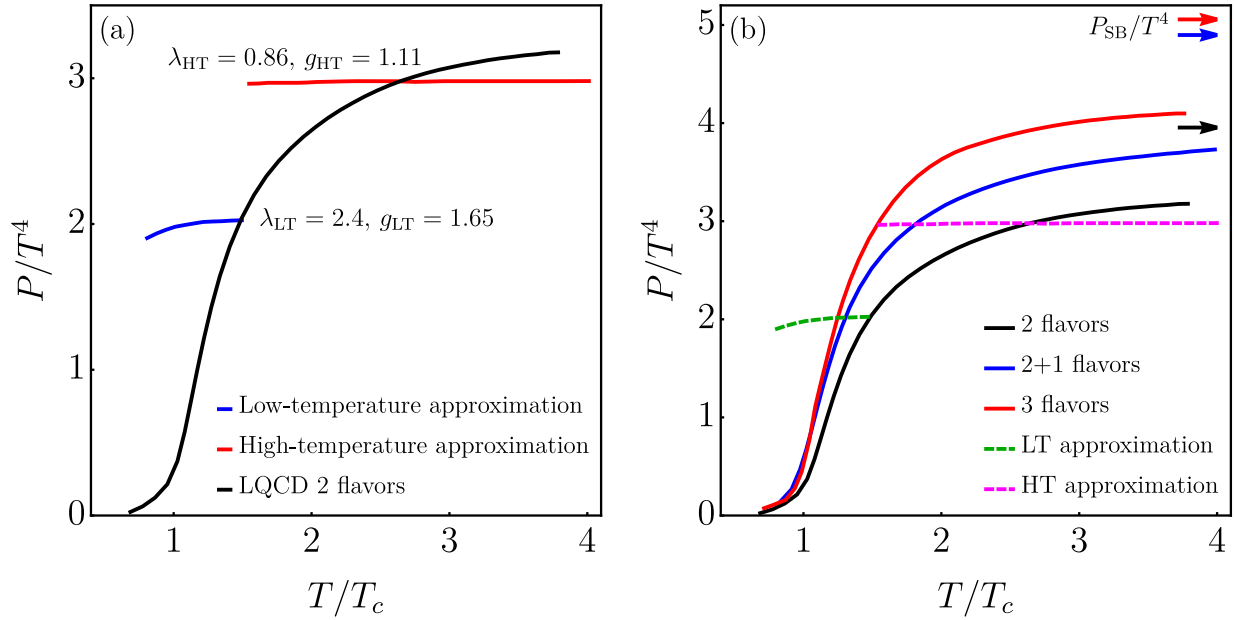


Figure 1.8: Pressure in units of T^4 . (a) Comparison between the results obtained from the low and high temperature-approximations and the LQCD data for two light flavors. (b) Pressure from LQCD simulations for 2 and 3 light flavors and 2 light + 1 heavy quark, compared with the named approaches. The arrows indicate the Stefan-Boltzmann gas or the ideal gas limit. The data were taken from Ref. [164].

Figure 1.8(b) shows the pressure normalized to T^4 when the number of degrees of freedom (DOF) corresponding to the number of quarks is changed, together with the effective pressure of the present formalism. The number of DOF has a considerable impact on P , indicating that the QCD phase transition at high temperature is deconfined. However, the transition takes place at rather small values of the pressure, and for temperatures $T \geq 2T_c$, it is close to the ideal gas limit where the light DOF can be identified. Thus, the quasi-constant nature of P computed from the L σ M is interpreted as an average description of the sudden change in the number of DOF. Moreover, the values of the coupling constants have a similar interpretation: the discontinuity in P around T_c is due to the depth of the potential of Eq. (1.77), i.e., for smaller couplings the effective potential becomes predominantly negative and therefore the pressure rises. Hence, the L σ M couplings reflect how the model can effectively incorporate the change in the DOF from the hadronic to the partonic description.

1.4 Conclusion

The QCD chiral symmetry restoration was studied from the L σ M as an effective hadronic model. Using the thermal field theory formalism, the boson and fermion potential energies were computed, as well as the self-energy corrections and ring diagrams up to the one-loop approximation. As was discussed, given the hierarchy between the energy scales, namely, the temperature, chemical potential, and fermion mass, the formalism was separated into two regimes: one when

the temperature is the dominant scale and other when the chemical potential grows. In the former, the expression has an analytical description, whereas, in the latter, a numeral treatment is implemented.

From the fact that the Linear Sigma Model presents the Spontaneous Symmetry Breaking, the σ - expectation value v is chosen as the order parameter of the theory. Thus, the phase transition and its order were identified whit condition $v = 0$ is reached from some configuration of T and μ . Moreover, the free coupling constant g and λ are set by phenomenological constraints at $\mu = 0$, where Lattice QCD simulations define the critical temperature T_c with two-light quarks flavors.

The results showed in Figs. 1.5 and 1.6, constructed from the high and low-temperature approximations, respectively, suggest that the formalism gives a QCD phase diagram with the desired properties, and the location of the Critical End Point depending on the coupling constants values. Moreover, as Fig. 1.7 indicates, the CEP's location yields in a T - μ region comparable with other models, and Lattice QCD extensions. Therefore, the implemented scenario gives a general description of the chiral symmetry restoration without an involved mathematical formalism.

Finally, the low-energy and effective nature of the Linear Sigma Model cannot give accurate results obtained from a pure QCD treatment. Such a limitation is well depicted in Fig. 1.8 when the pressure computed from LsM is compared with lattice QCD simulations, which have a high level of confidence given that they are computed when $\mu = 0$. Nonetheless, the sudden change of degrees of freedom is described as an average of the values of the coupling constants g and λ .

*“It is more important to have beauty
in one’s equations than to have them
fit experiment.”*

– Paul Dirac

Chapter 2

The Direct Photon Excess

In this chapter, the effects of intense magnetic field on the photon production of a heavy-ion collision are studied, in particular, the photon sources coming from gluon fusion and gluon splitting channels are proposed to improve the explanation of the experimental data for the invariant momentum distribution and the elliptic flow coefficient v_2 reported by ALICE and PHENIX experiments. To take into account the high gluon abundance and the peak of the magnetic field produced in peripheral collisions, the proposed processes are assumed to take place in the early stages of the reaction in the so-called *shattered glasma* state. With the purpose of giving a general description of the problem, the theoretical framework, and of explain the assumptions of the calculations, this chapter is organized as follows:

Section 2.1 is devoted to giving a general discussion about the relativistic hydrodynamical calculations applied to the understanding of the particle production and elliptic flow after a heavy-ion collision experiment. In Sec. 2.2 the problem statement is presented: the deviations of the hydrodynamical calculations of the photon production and elliptic flow from the experimental data reported for ALICE and PHENIX in the region of photon’s low momentum. Such a problem is known as the *photon puzzle*. The physics of the early stages on a heavy-ion collision is explained in Sec. 2.3 from which the named photon production channels are inspired. In particular, the high gluon occupation number and its implications on the parton distribution functions are discussed. Section 2.4 presents the main aspects of the magnetic fields in heavy-ion collisions.

The photon production by gluon fusion is proposed and computed in Sec. 2.5. whereas the gluon splitting mechanism is discussed in Sec. 2.6. The comparison with the experimental data is performed with phenomenological parameters for the former but computed with the ultra-relativistic quantum molecular dynamics (UrQMD) for the later. In both cases, the analytic calculation is carried out by considering the magnetic field as the dominant energy scale and a gluon occupation modeled by a Bose-Einstein-like distribution function.

The calculations and results presented in this chapter are based on the following manuscripts:

- Alejandro Ayala, Jorge David Castaño-Yepes, C. A. Dominguez, L. A. Hernandez, Saul Hernandez-Ortiz, and Maria Elena Tejada-Yeomans, *Prompt photon yield and elliptic flow from gluon fusion induced by magnetic fields in relativistic heavy-ion collisions*, Phys. Rev. D **96**, 014023 (2017); Erratum Phys. Rev. D **96**, 119901 (2017).
- Alejandro Ayala, Jorge David Castaño-Yepes, Isabel Dominguez Jimenez, Jordi Salinas San Martin, Maria Elena Tejada-Yeomans, *Centrality dependence of photon yield and elliptic flow from gluon fusion and splitting induced by magnetic fields in relativistic heavy-ion collisions*, Eur. Phys. J. A **56**, 53 (2020).
- Alejandro Ayala, Jorge David Castaño-Yepes, C. A. Dominguez, L. A. Hernandez, *Thermal photons from gluon fusion with magnetic fields*, EPJ Web of Conferences **141**, 02007 (2017).
- Alejandro Ayala, Jorge David Castaño-Yepes, C. A. Dominguez, L. A. Hernandez, Saul Hernandez-Ortiz, and Maria Elena Tejada-Yeomans, *Prompt photon yield and v_2 coefficient from gluon fusion induced by magnetic field in heavy-ion collision*, EPJ Web of Conferences **172**, 08004 (2018).
- Alejandro Ayala, Jorge David Castaño-Yepes, Isabel Dominguez Jimenez, Jordi Salinas San Martin, Maria Elena Tejada-Yeomans, *New channels of prompt-photon production by magnetic fields in heavy-ion collisions*, J. Phys. Conf. Ser. **1602**, 012014 (2020).

2.1 Relativistic Hydrodynamics and Elliptic Flow

The characterization of the QGP is of great interest for the understanding of the matter which participates in the strong interaction. As it was mentioned, in the technologies of the current experiments based on heavy-ion collisions, there is not a direct control on the dynamics of the participants in each measurement. Hence, the collected signals may have information from stages before and after of the QGP formation. That is why the photons become an excellent (and necessary) probe to test such a state of matter: they do not interact strongly and that feature enables them to escape from the system freely; thus, the photon measurements contain relevant information about the space-temporal evolution of the colliding system.

For each kind of particle produced at the collision, the final momentum distribution is related to the average number of particles N and its Fourier decomposition in the azimuthal angle ϕ

$$E \frac{d^3 N}{d^3 p} = \frac{1}{2\pi} \frac{dN}{p_T dp_T dy} \left[1 + 2 \sum_{n=1}^{\infty} v_n \cos n(\phi - \Psi_n) \right], \quad (2.1)$$

where p_{\perp} is the transverse moment, y is the rapidity with respect to the reaction plane and Ψ_n is an angle that defines the reaction plane which is related to spatial orientation [166]. The

flow coefficients v_n can include information about the pseudorapidity η as well as momentum dependence [167, 168]. The hydrodynamical models allow making interpretations of the flow coefficients obtained from the experimental measurements [167, 169].

The relativistic hydrodynamical calculations analyze the flow of conserved quantities, such as energy, momentum, or other charges. Mathematically, the main equations of the formalism are

$$\begin{aligned}\partial_\mu T^{\mu\nu} &= 0, \\ \partial_\mu J_i^\mu &= 0,\end{aligned}\tag{2.2}$$

where $T^{\mu\nu}$ is the stress-energy tensor and J_i^μ denotes other conserved charges (net baryon number, electric charge, etc). In a differential form, these equations read

$$\begin{aligned}\frac{d}{dt} \int_V d^3x T^{0\nu} &= - \int_{\partial V} dS_i T^{i\nu}, \\ \frac{d}{dt} \int_V d^3x J_B^0 &= - \int_{\partial V} dS_i J_B^i,\end{aligned}\tag{2.3}$$

where the direct volume dependence is established. The form of Eqs. (2.3) accepts a direct interpretation in terms of the time variation of conserved quantities from incident currents in a finite volume. Therefore, the hydrodynamical framework is centered on the study of the dynamics of the currents [170].

The application of the Relativistic Hydrodynamics (RH) to the study of the QGP arises from the fact that RH is a bulk theory, where the system is assumed to be made of a large number of particles in equilibrium. Their characterization can be reached by a few variables, such as the temperature, collective velocity, and chemical potential. These quantities control energy density, momentum density, and charge density, respectively. Although the heavy-ion reaction is not static or in equilibrium, it is possible to argue local equilibrium by assuming the expansion rate is much slower than the microscopic interaction rate. In those conditions, the local temperature $T(t, \mathbf{x})$, chemical potential $\mu(t, \mathbf{x})$, and collective velocity $u^\mu(t, \mathbf{x})$ are close to describing Lagrange multipliers to fix the average energy, momentum and net charge, giving rise to a theory of conserved laws.

The conversion from fluid-viscous dynamics to a particle description of the collision requires *particlization* approaches which are hybrids of ideal or dissipative hydrodynamics (for the early partonic stages) and transport/dilute gas models for the hadronization time scales [171–180]. The matching is made on a constant energy-density or constant temperature hypersurface and the invariant momentum distribution of Eq. (2.1) is usually found by the Cooper-Frye formula [181]

$$E \frac{d^3 N_i}{d^3 p} = p^\mu d\sigma_\mu(x) f_i(x, \mathbf{p}),\tag{2.4}$$

where $d\sigma_\mu(x)$ is the local surface element vector that is normal to the hypersurface, x is the spacetime, \mathbf{p} is the momentum and f_i is the phase space density for particle species i , which is related to Eqs. (2.2) through

$$T^{\mu\nu}(x) = \int \frac{d^3 p}{E} p^\mu p^\nu f(x, \mathbf{p}).\tag{2.5}$$

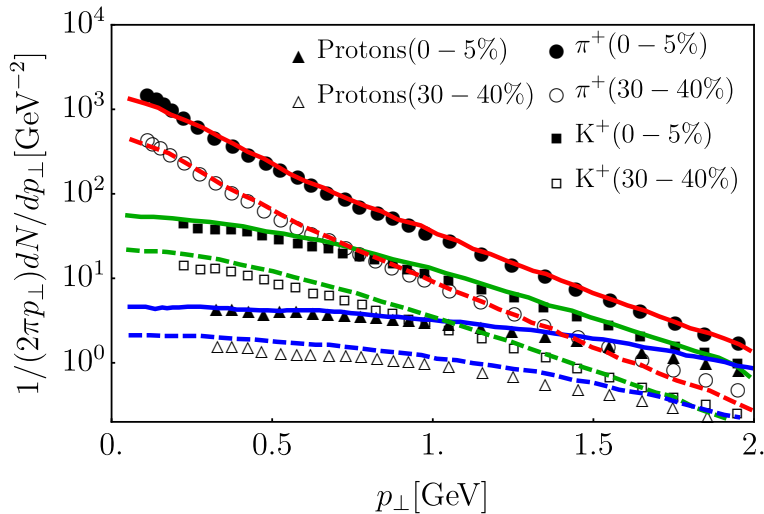


Figure 2.1: Transverse momentum spectra for pions, kaons and protons, as a function of the transverse momentum p_{\perp} for two centralities: 0 – 5% and 30 – 40%. The red (pions), green (kaons), and blue (protons) lines correspond to the predictions of the hydrodynamical calculations by Ryu *et al.* [182]. The continuous and dashed lines are referred to the maxima and minimal centralities, respectively. The experimental data are taken from Ref. [183] (ALICE Collaboration) and Refs. [184, 185] (CMS Collaboration).

The stress-energy tensor, as well as the phase-space distribution, varies according to the model requirements, and once the such models for $T^{\mu\nu}$ and f_i are chosen, the hydrodynamical calculations work as follows:

1. **Initial Condition:** The QGP needs to be presented in some initial configuration. Generally, the Glauber model as a Monte-Carlo approximation for the geometrical distribution of the energy density deposited in the transverse plane is used [186]. Also, the Color Glass Condensate is useful. The last one will be discussed in Sec. 2.3. The system size and centrality are defined in this step.
2. **Pre-Equilibrium:** A hydrodynamical calculation cannot be accomplished unless the medium reaches some degree of local momentum isotropization. In its inputs, the relaxation time and the strength of the interaction after the collision are crucial [187–189].
3. **Hydrodynamical Evolution** The fluid expansion starts with constrains as shear and bulk viscosities, and with the definition of local temperature. The system can interact with external fields (electric, magnetic). Finally, by solving the relations (2.2), the equation of state of QGP is achieved, which gives relevant information about the medium (phase transitions, momentum anisotropies).
4. **Particlization and final states:** The particlization in the Cooper-Frye formalism of Eq. (2.4) allows describing the final states as hadrons, and therefore, the usual techniques of particle and field theory physics can be used. These final states carry on the relevant information of the QGP.

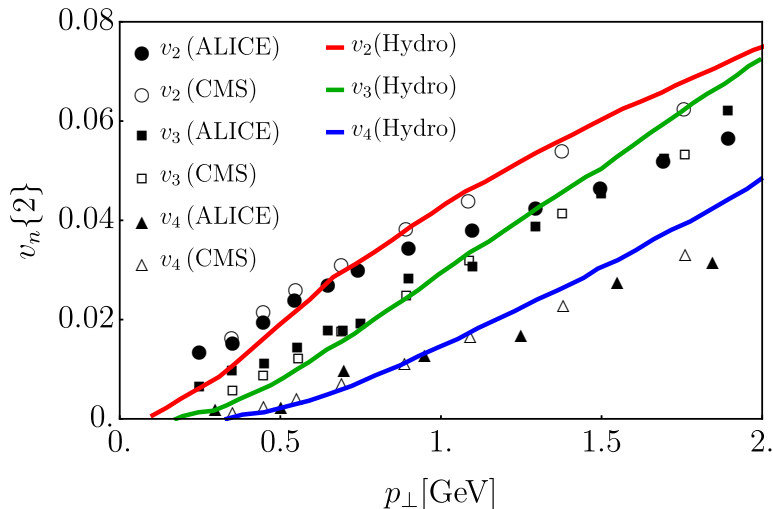


Figure 2.2: Charged particle flows v_2 , v_3 and v_4 as a function of the transverse momentum p_\perp for the centralities 0 – 5%. The red, green, and blue correspond to the predictions of the hydrodynamical calculations of Ryu *et al.* [182]. The experimental data are taken from Ref. [183] (ALICE Collaboration) and Refs. [184, 185] (CMS Collaboration).

As an example of HD-calculations for heavy-ion collisions, the work of Ryu *et al.* is a good starting point [182]. Their initial conditions are determined by using the IP-Glasma model [190, 191], i.e., an impact-parameter-dependent saturation model for gluons (Glasma), combined with the classical Yang-Mills description of initial Glasma fields. The thermalization time is set to $\tau_0 = 0.4$ fm. The stress-energy tensor is chosen as a composition of a free-ideal part and a dissipative contribution:

$$T^{\mu\nu} = \underbrace{\epsilon u^\mu u^\nu - \Delta^{\mu\nu} P_0(\epsilon)}_{\text{ideal}} + \underbrace{\pi^{\mu\nu} - \Delta^{\mu\nu} \Pi}_{\text{dissipative}}, \quad (2.6)$$

where ϵ is the local energy-density, $P_0(\epsilon)$ is the thermodynamics pressure, u^μ is the four-velocity, Π is the bulk viscous pressure, $\pi^{\mu\nu}$ is the shear-stress tensor, and the projector operator is $\Delta^{\mu\nu} = g^{\mu\nu} - u^\mu u^\nu$. The named parameters were selected as follows: P_0 was fixed according to the equation of state taken from lattice QCD calculations in the chemical equilibrium of a hadronic gas at low temperatures [192], whereas Π and $\pi^{\mu\nu}$ were found by solving relaxation-type equations of the kinetic theory which include non-linear terms such that couple them. Finally, the momentum distribution of hadrons is calculated via the Cooper-Frye formalism.

Figure 2.1 shows the results obtained from the above calculations for the p_T spectra of pions, kaons, and protons in two centrality classes. Moreover, Fig. 2.2 shows the charged particle's flow coefficients extracted from the transverse momentum spectra. Both hydrodynamical predictions are compared with the ALICE and CMS experimental data [183–185]. As it can be noticed, the viscosity, the thermalization assumptions, and the pre-equilibrium saturated state are fundamental to have a good description of the observables. Therefore, it can be concluded that RH is a useful phenomenological framework to analyze the findings in a heavy-ion reaction.

2.2 The Direct Photon Puzzle

As it was commented on the last section, the HD calculations give excellent results when its predictions are compared with the experimental data of the hadronic final states. In terms of the heavy-ion reaction characterization, the hadron spectra can carry on the information of several stages in the collision. Additionally, such information is encoded in a considerable kind of asymptotic states (protons, kaons, pions, etc.). Therefore, the measured signal is plagued with noise, and this makes data analysis difficult. Photons are a clean and abundant source of information within the above described scenario: given that they do not participate in the strong interaction, a photon produced in the QGP phase scapes from the medium without significant scattering processes. In such a way, photons constitute excellent probes to test the strongly interacting matter.

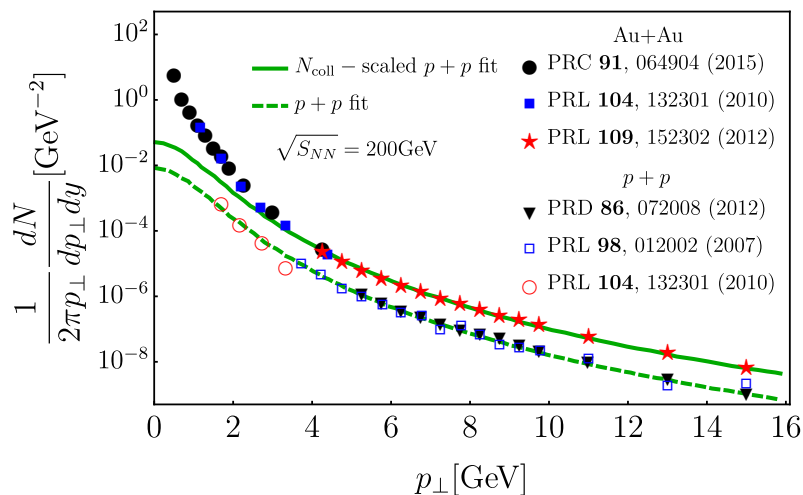


Figure 2.3: Experimental direct p_{\perp} photon spectra reported from different PHENIX measurements and compared with the $p + p$ fit (dashed line) and with the $p + p$ scaled by the corresponding average number of binary collisions N_{coll} (continuous line). Only the central value is shown. For details see Refs. [62, 64, 193–195].

The photon invariant distribution measurements have been reported by the PHENIX [62–65] and ALICE [60, 66, 67] experiments, for low and intermediate transverse momentum in Au-Au, Cu-Cu and Pb-Pb collisions for different centralities. Figures 2.3 and 2.4 shows the invariant p_{\perp} photon spectra for the so-called *direct photons*, i.e., the measurements without photons that come from hadronic decays or final stages. Each collaboration compares the experimental results with theoretical calculations using perturbative-QCD (pQCD) by considering a scaling of the binary collisions for protons. As can be noticed, the PHENIX results in Fig. 2.3 show an enhancement above the direct photon production in comparison to the $p + p$ results. This enhancement is found at low transverse momenta ($p_{\perp} = 3\text{GeV}$), where the named calculations do not reproduce the overall data behavior. For the ALICE results show in Fig. 2.4, the increase in direct photon production at low p_{\perp} is also observed. Moreover, the yield over the pQCD calculations is present for different centralities, which makes it evident that other radiation sources have to be taken into account. In that way, the invariant momentum distribution has a

slope which suggests a foot print of a thermal phase, and therefore, photons must be created in an equilibrated medium.

To give a phenomenological explanation of the low pt deviations, Paquet *et al.* have developed a hydrodynamical approach to study several photon sources in a thermalized medium, namely the QGP [71]. Their work is based on phenomenology which describes the stress-energy tensor of Eq. (2.6), namely, an initial state made of a color glass condensate, where the gluonic fields evolve according to the Yang-Mills equations. Here, the thermalization initial time is set to $\tau_0 = 0.4$ fm, and the viscous properties of the QGP are taken into account.

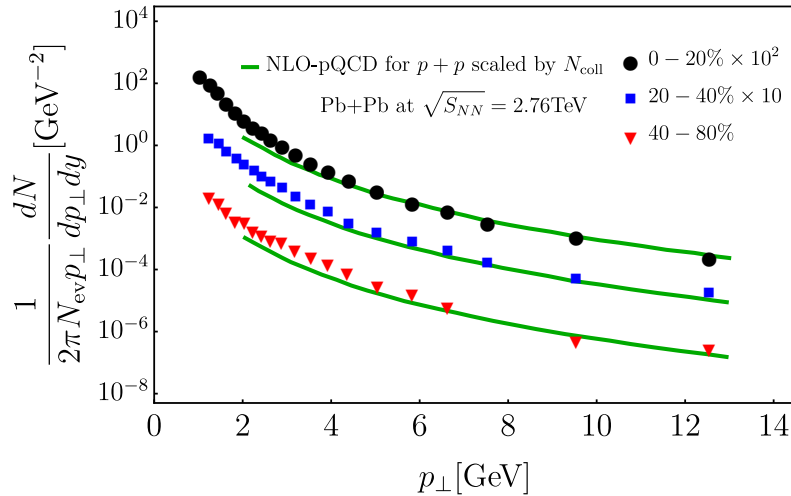


Figure 2.4: Experimental direct p_{\perp} photon spectra reported by the ALICE collaboration in Pb+Pb collisions at different centralities. The data is compared to NLO pQCD predictions for the direct photon yield in $p + p$ collisions, which are scaled by the number of binary nucleon collisions N_{coll} for each centrality class. Only the central value is shown. For details see Ref. [60].

The photon sources coming from the named calculations are classified in each stage of the heavy-ion collision:

- **Prompt Photons:** This refers to photons produced in the early stages of the ion collision through partonic Compton interactions, quark-antiquark annihilations, and bremsstrahlung radiation. Figure 2.5a schematizes the origin of a prompt photon. All prompt photon's sources from hadronic interactions can be known by pQCD-techniques and basically the number of photons can be scaled by the binary proton-proton collisions through proton-parton distribution and parton-to-photon fragmentation functions at next-to-leading order (NLO) [193, 196–200].
- **Thermal Photons:** This refers to photons produced in the QGP phase which in the partonic sector are calculated by thermal field theory techniques at LO and NLO [68, 69]. Those calculations includes near-collinear bremsstrahlung and inelastic pair annihilation contributions. For hadrons with temperatures lower or comparable with the crossover temperature, the photons are calculated by mesonic reactions [57, 70]. Also, the barionic contributions in the form $NN \rightarrow NN\gamma$ and $\pi N \rightarrow \pi N\gamma$, with N a nucleon, are taken

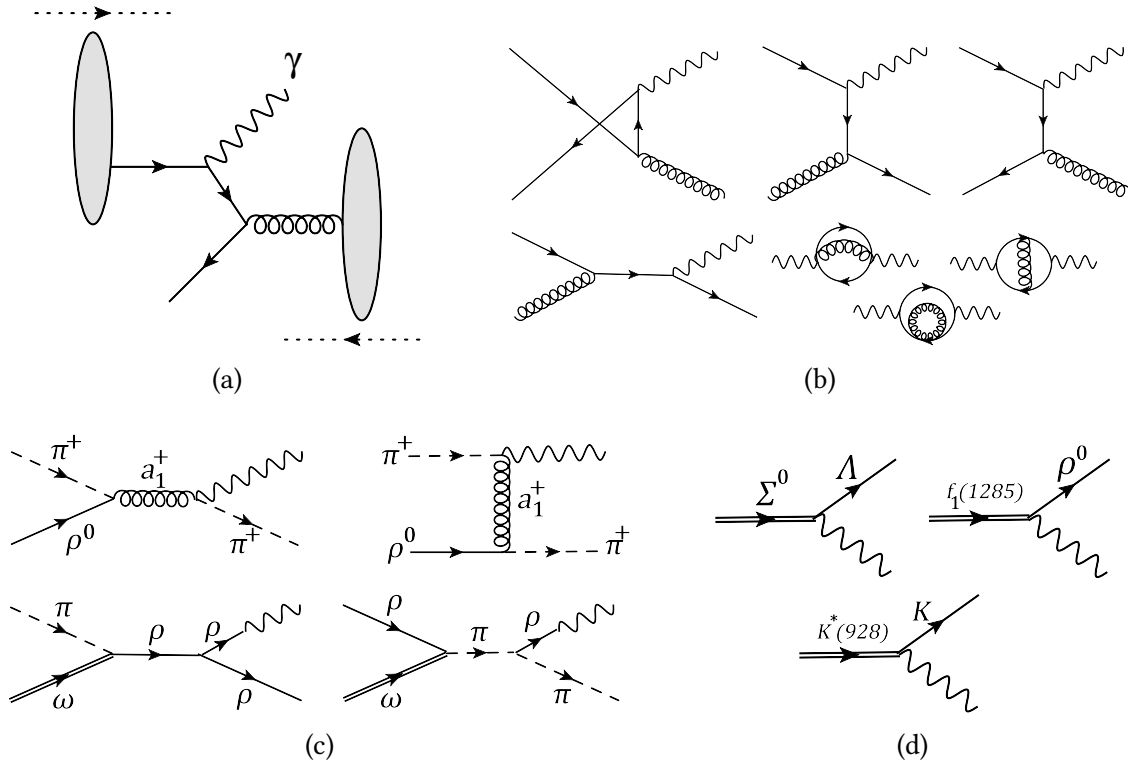


Figure 2.5: Scheme of some relevant processes for photon production in the Paquet’s hydrodynamical model: (a) prompt photons, (b) thermal photons from QGP [68, 69], (c) thermal photons for mesonic reactions [57, 70], and (d) non-cocktail decays.

into account. Figures 2.5b and 2.5c schematizes some of the processes which contributes to the named calculations.

- **Noncocktail Hadronic Decay Photons:** These are photons coming from the early hadronization stages and which have not been subtracted from the photon production of the final hadronic interactions. Such a subtraction is known as the *cocktail*, which is made of $(\pi^0, \eta, \rho, \omega, \eta', \phi)$ for LHC and (π^0, η, η') for RHIC [201, 202]. For both LHC and RHIC, the noncocktail sources are dominated by the channels $\Sigma^0 \rightarrow \Lambda \gamma$, $f_1(1285) \rightarrow \rho^0 \gamma$ and $K^*(928) \rightarrow K \gamma$. Also, the channel $\pi^0 \rightarrow e^+ e^- \gamma$ is considered as a noncocktail contribution at RHIC given that in comparison with ALICE it is not subtracted. Fig. 2.5d illustrates the channels which contributes to the NC radiation.

Figure 2.6 shows the photon invariant momentum distribution of the Paquet’s hydrodynamical calculations compared with the RHIC’s data for Au-Au collisions at $\sqrt{S_{NN}} = 200\text{GeV}$. The direct photons are obtained by adding the contributions of the prompt, thermal, and *non-cocktail* photons. As can be noticed from the two centrality cases, the calculation for $p_{\perp} \sim 1.5\text{ GeV}$ underestimates the PHENIX data central points roughly by a factor of 3. The same behavior is found when the model is compared against the ALICE data for Pb-Pb collisions at $\sqrt{S_{NN}} = 2.76\text{TeV}$ in Fig. 2.7. It is clear that the theoretical predictions cannot reproduce the experimental data unless the error bars of statistical and systematic uncertainties are taken into account.

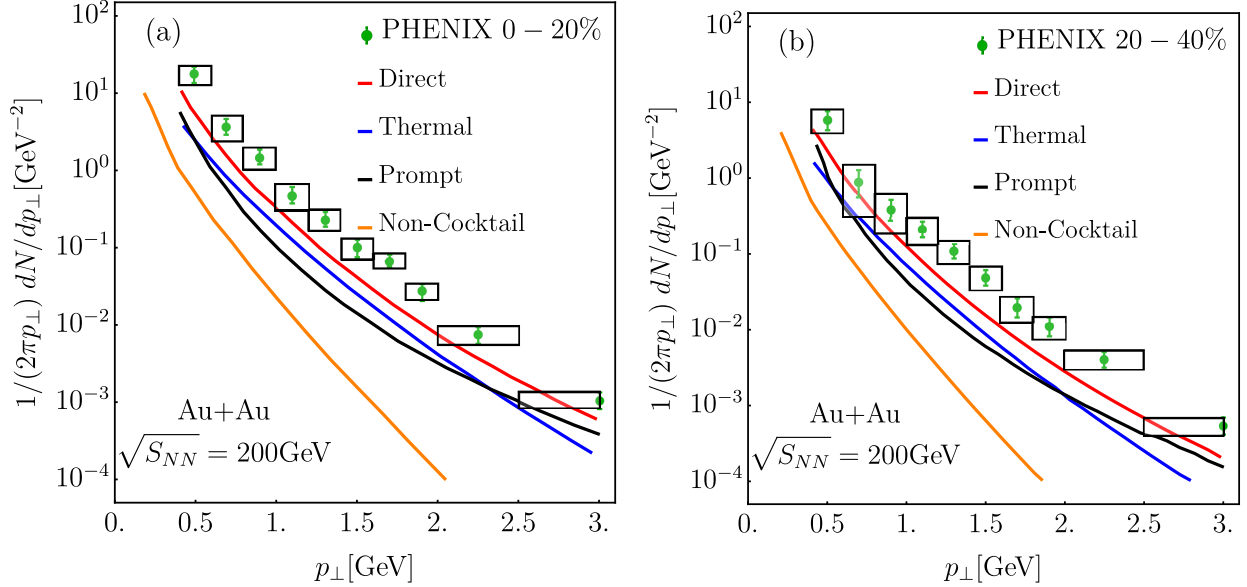


Figure 2.6: Hydrodynamical calculation of the direct photon spectra for Au+Au collisions by Paquet *et al.* from Ref. [71] in two centrality ranges: (a) 0–20% and (b) 20–40%. The calculations are compared with the experimental data from PHENIX [64].

On the other hand, when the flow coefficient v_2 is calculated from Eq. (2.1) and compared with the experimental data by PHENIX and ALICE for different centralities, the theoretical predictions cannot describe the overall behavior of this observable. As is shown in Fig. 2.8 the predicted direct photons anisotropy underestimates the measured spectrum even by taking into account the large error bars. This problem is known as *The Direct Photon Puzzle*: a challenge to describe the direct photon spectra from which the elliptic flow coefficient v_2 can be obtained in such a manner that both approximations fit the experimental measurements.

It is worth to mention that for both experiments, the hydrodynamical curve for the thermal photons gives a good description of the elliptic flow. Nevertheless, the harmonic coefficient v_2 need to be constructed from a weighted average, namely:

$$v_2(p_\perp) = \frac{\sum_i \frac{dN^{(i)}}{dp_\perp}(p_\perp) v_2^{(i)}(p_\perp)}{\sum_i \frac{dN^{(i)}}{dp_\perp}(p_\perp)}, \quad (2.7)$$

where the sum runs for the i -th mechanism of photon production. In that sense, although the thermal photons have an intrinsic flow close to the data, the corresponding weight reduces their contribution to the total flow. In this chapter, I discuss the prompt photon production at the early stages of a relativistic heavy-ion collision, therefore, it is necessary to give several relevant aspects of those initial times.

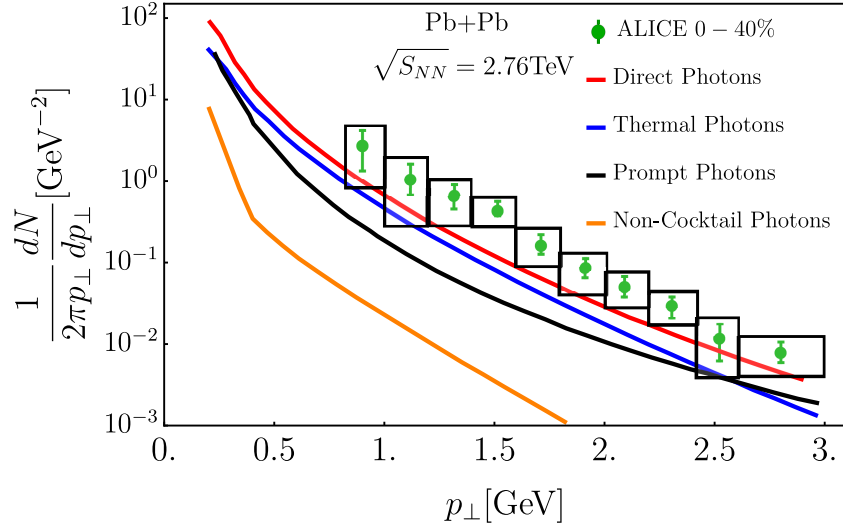


Figure 2.7: Hydrodynamical calculation of the direct photon spectra for Pb+Pb collisions by Paquet *et al.* from Ref. [71] for the centrality 0 – 40%. The calculations are compared with the experimental data from ALICE [66].

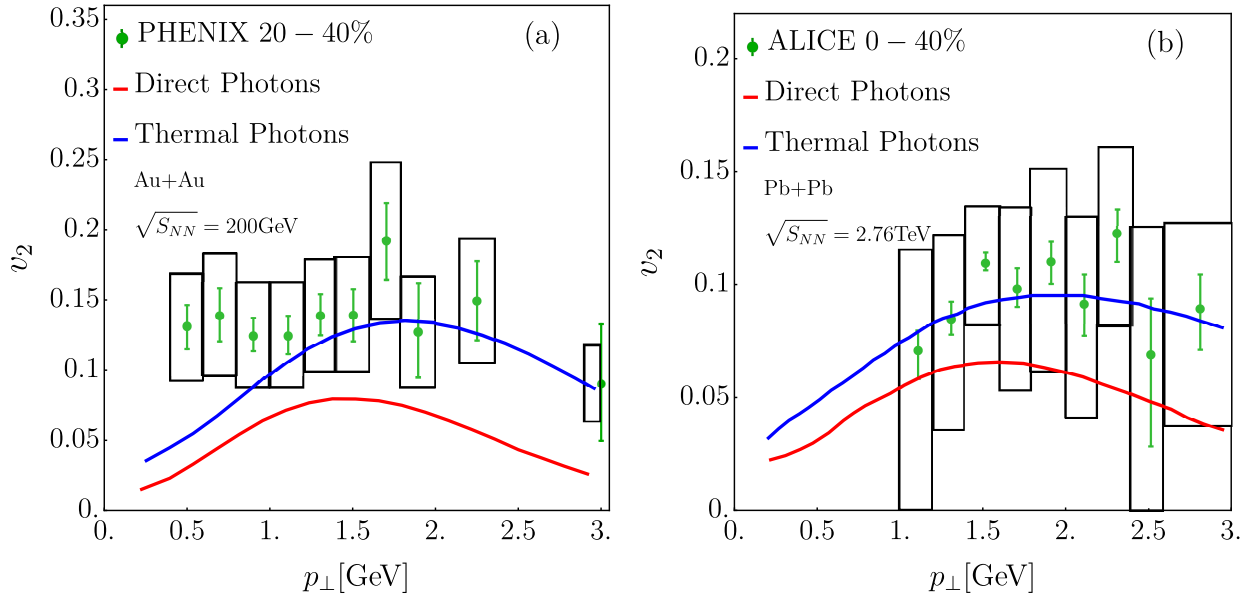


Figure 2.8: Hydrodynamical calculation of the flow coefficient v_2 for the direct and thermal photons by Paquet *et al.* [71], compared with (a) PHENIX data with centrality 20 – 40% [202, 203] and (b) ALICE data with centrality 0 – 40% [66].

2.3 The Color Glass Condensate (CGC)

Deep Inelastic Scattering and Parton Distribution Functions

As it was commented on the Introduction, at the early stages of a heavy-ion collision, the hadronic and partonic wave functions behave in a particular way, due the Lorentz contraction. Collision times are characterized by a high- density, state of QCD, with its principal characteristic being a large number of gluons.

The hadronic structure depends on the scale used to be tested, encoded in the scattering process' kinematics, that is, although the cross-section is a boost-invariant object, its interpretation in terms of partons depends on the energy scale at which this is computed. The valence quarks bounded by gluons in a colorless state is a good description of a hadron in the rest frame, so that there is a probability to generate quark-antiquark pairs as virtual particles. Such fluctuations coming from the gluon exchange are non-perturbative because they occur at energy and momentum scales of order Λ_{QCD} where the coupling constant is $\mathcal{O}(1)$, and the binding is strong. On the other hand, the typical scale for vacuum fluctuations (namely quark-antiquarks pumped from the vacuum) is also Λ_{QCD} ; therefore, in the rest frame is not possible to speak of a *hadron structure*, given that vacuum fluctuations are not distinguishable from hadronic (partonic) fluctuations.

If the hadron is viewed in a boosted reference frame along $p = p_z$ with Lorentz factor $\gamma \gg 1$, the 4-momentum passes from being $p^\mu = (M, 0, 0, 0)$ to $p^\mu = (M, 0, 0, p)$, so that in the so-called Infinite Momentum Frame (IMF), $E = \sqrt{M^2 + p^2} \simeq p$, the life-time of the hadronic fluctuations is:

$$\Delta t_{\text{boost}} = \gamma \Delta t_{\text{rest}} \sim \frac{\gamma}{\Lambda_{\text{QCD}}}, \quad (2.8)$$

which implies that the boost-invariant vacuum fluctuations with life-time $\Delta t_{\text{vacuum}} \sim \Lambda_{\text{QCD}}^{-1}$ can be well differentiated from the hadronic fluctuations. The time given in Eq. (2.8) is larger compared to a typical collision time, hence, the fluctuations are recognized as individual free particles called *partons*. That situation allows factorizing the cross-section for hadron-hadron collisions into the product of *parton-distribution functions* and *partonic cross-sections*. The former is the probability to find a parton with particular kinematical characteristics in the hadron wave-function, and the latter describes the collision between partons of projectile and target.

For a large range of energy scales, the partonic cross-section may be computed analytically. Still, by its definition, the parton distribution function cannot be calculated in a perturbative framework. Nonetheless, depending on the resolution of Deep Inelastic Scattering (DIS) experiments, some features of such processes are approximated by perturbation theory.

Figure 2.9 shows the DIS of an electron with 4-momentum l_μ is scattered by a proton with 4-momentum p_μ exchanging a virtual photon γ^* with 4-momentum q_μ . The final electron has a 4-momentum $l'_\mu = l_\mu - q_\mu$ and the photon is considered space-like so that

$$q^2 = -2l \cdot l' = -2E_l E_{l'} (1 - \cos \theta_{ll'}) \equiv -Q^2, \quad (2.9)$$

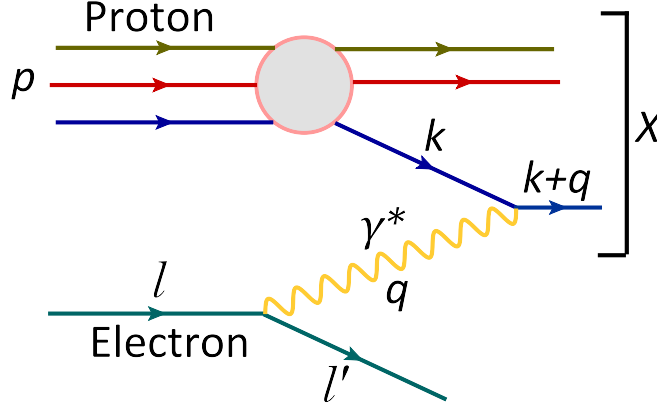


Figure 2.9: Deep Inelastic Scattering: an electron with 4-momentum l_μ is scattered by a proton with 4-momentum p_μ exchanging a virtual photon γ^* with 4-momentum q_μ . If the proton is broken the final hadronic states are represented by the set X .

where the quantity $Q^2 > 0$ is called the *virtuality*. The space-like photon exchanged for a proton in the IMF measures partons localized in the transverse plane in the area $\Sigma \sim 1/Q^2$. Such partons carry a longitudinal momentum $k_z = xp$ with x the Bjorken variable given by [204]:

$$x \equiv \frac{Q^2}{2(p \cdot q)} = \frac{Q^2}{s^2 + Q^2 - M^2}, \quad (2.10)$$

where $s \equiv (p + q)^2$ is the invariant energy squared. The invariant variables x and Q totally determine the partons transverse length $1/Q$ which participates into the scattering. Note that that parton needs to be a quark or antiquark, given that the photon does not couple to gluons.

The energy difference at the emission photon vertex gives the *transverse resolution* of the virtual photon, i.e.,

$$\Delta E = |\mathbf{k} + \mathbf{q}| - |\mathbf{k}| = \sqrt{(xp)^2 + q_\perp^2} - xp \simeq \frac{q_\perp^2}{2xp}, \quad (2.11)$$

where the 4-momentum of the space-like photon is chosen as $q_\mu = (0, \mathbf{q}_\perp, 0)$ and $Q^2 = q_\perp^2$. Therefore, the collision time is

$$\Delta t_{\text{coll}} \simeq \frac{2xp}{q_\perp^2}. \quad (2.12)$$

To be tested by the virtual photon, the quark (antiquark) excitation must have a lifetime $\Delta t_{\text{fluc}} > \Delta t_{\text{coll}}$. The former is estimated in the IMF by its longitudinal momentum $k_z = xp$ for quarks near of the mass-shell condition ($k_\mu \simeq xp_\mu$, $k^2 \simeq 0$) boosted by a Lorentz factor $\gamma = k_z/k_\perp$, so that

$$\Delta t_{\text{fluc}} = \gamma \Delta t_{\text{rest}} \simeq \frac{2k_z}{k_\perp^2} = \frac{2xp}{k_\perp^2}, \quad (2.13)$$

hence, to satisfy $\Delta t_{\text{fluc}} > \Delta t_{\text{coll}}$ it follows that $k_\perp^2 < Q^2$ which means the DIS resolution measures partons with transverse momentum smaller than virtuality Q .

The above analysis admits an expression for the DIS cross-section given by:

$$\sigma_{\gamma^*p} = \frac{4\pi^2\alpha_{\text{em}}}{Q^2} F_2(x, Q^2), \quad (2.14)$$

which is built from the elementary cross-section in the photon absorption by a quark weighted by the structure-function:

$$F_2(x, Q^2) = \sum_f e_f^2 x [q_f(x, Q^2) + \bar{q}_f(x, Q^2)], \quad (2.15)$$

with

$$q_f(x, Q^2) \equiv \frac{dN_f(Q^2)}{dx} = \int^Q d^2\mathbf{k}_\perp \frac{dN_f}{dx d^2\mathbf{k}_\perp}, \quad (2.16)$$

so that $q_f(x, Q^2)dx$ is the number of quarks (\bar{q}_f for antiquarks) with flavor f with longitudinal momentum fraction between x and $x + dx$. Note that even the condition $k_\perp^2 < Q^2$ is always satisfied by partons with $k_\perp \sim \Lambda_{\text{QCD}}$ if $Q^2 \gg \Lambda_{\text{QCD}}^2$, which implies the structure function $F_2(x, Q^2)$ must be independent of Q^2 satisfying the *Bjorken scaling*. Nevertheless, the experimental data shows that the Bjorken scaling is valid for $x \gtrsim 0.1$ [205–207]. The radiative processes give the phenomenology behind that result: although the transverse momenta for valence quarks are around Λ_{QCD} , virtual excitations with large k_\perp can be generated by bremsstrahlung. Moreover, even when they have short lifetimes, there is a window of values for k_\perp that contribute to DIS [208].

The current experiments can lead to collisions with small x understood as a high-energy regimen where $s \gg Q^2$. Consider a parton-parton collision inside a hadronic scattering: in the Center of Mass (COM) frame, each parton has the 4-momentum $k_i^\mu = x_i p_i^\mu + k_{i\perp}^\mu$, where $p_1^\mu = (p, 0, 0, p)$ and $p_2^\mu = (p, 0, 0, -p)$ so that $p = \sqrt{s}/2$. If two particles are produced by the partonic collision, with transverse momenta $\mathbf{p}_{a\perp}$ and $\mathbf{p}_{b\perp}$ the energy-momentum conservation implies:

$$\mathbf{p}_{a\perp} + \mathbf{p}_{b\perp} = \mathbf{k}_{1\perp} + \mathbf{k}_{2\perp}, \quad (2.17)$$

and

$$\begin{aligned} x_1 &= \frac{p_{a\perp}}{\sqrt{s}} e^{y_a} + \frac{p_{b\perp}}{\sqrt{s}} e^{y_b}, \\ x_2 &= \frac{p_{a\perp}}{\sqrt{s}} e^{-y_a} + \frac{p_{b\perp}}{\sqrt{s}} e^{-y_b}, \end{aligned} \quad (2.18)$$

where y_i is the rapidity.

For RHIC and LHC, the average hadronic momentum at the latter stages is around 1 GeV, so that the total number of produced hadrons (multiplicity) has $p_\perp \leq 2$ GeV; therefore, by considering $p_{a,b\perp} \sim 1$ GeV and for central rapidities $y_{a,b} \sim 0$, the longitudinal momentum fraction is [209–211]:

$$\begin{aligned} x_i &\simeq 10^{-2} \quad \text{for } \sqrt{s} = 200 \text{ GeV (RHIC)}, \\ x_i &\simeq 4 \times 10^{-4} \quad \text{for } \sqrt{s} = 2.76 \text{ TeV (LHC)}. \end{aligned} \quad (2.19)$$

Gluon Distribution Functions

As was mentioned, gluons do not interact with photons, which implies that gluonic excitations must come from radiative processes. In perturbative QCD, gluons are produced via bremsstrahlung, so that they are collinear and have $x \ll 1$ and relatively small transverse momentum [29, 212].

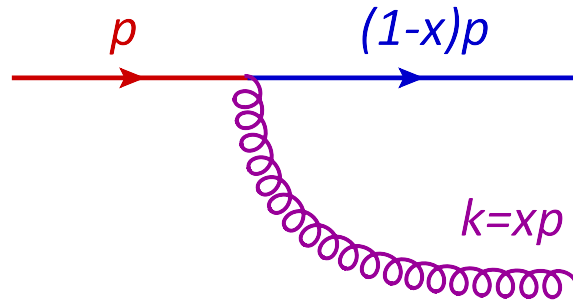


Figure 2.10: Gluon bremsstrahlung from a quark in perturbative QCD at lowest order.

Figure 2.10 shows the elemental diagram for gluon bremsstrahlung from a quark in perturbative QCD at lowest order. The parent quark with momentum p emits a gluon with longitudinal momentum $k = xp$ and transverse momentum k_{\perp} , so that at the end of the process, there is a quark with longitudinal momentum $(1 - x)p$ and transverse momentum $-k_{\perp}$. By considering $x \ll 1$ and a LO in α_s that gluon production channel has a differential probability given by [213]:

$$dP_{\text{Brem}} \simeq C_R \frac{\alpha_s(k_{\perp}^2)}{\pi^2} \frac{d^2 k_{\perp}}{k_{\perp}^2} \frac{dx}{x}, \quad (2.20)$$

where C_R is the Casimir in the $SU(N_c)$ representation. The last equation presents two fundamental features: it is singular in the full collinear limit ($k_{\perp} \rightarrow 0$) and the soft momentum regimen ($x \rightarrow 0$). Moreover, if that differential probability is compared with the quark emission, the parton production enhancement is only present at the collinear and not in the small x region. On the other hand, although a power of alpha suppresses Eq. (2.20), given that such coupling decreases for $k_{\perp}^2 \gg \Lambda_{\text{QCD}}^2$, the large phase-space for the gluon radiation compensates such reduction: it is of order $\ln(Q^2/\Lambda_{\text{QCD}}^2)$ for the emission of any parton with $k_{\perp} \ll Q$, and of order $\ln(1/x)$ for the emission of a gluon with longitudinal momentum fraction ξ in the interval $x \ll \xi \ll 1$. Thus, for high-energy regimes where $Q^2 \gg \Lambda_{\text{QCD}}^2$ or $x \ll 1$, the radiative processes are not suppressed and needs to be resummed to all orders.

From the above, depending on the Q^2 and x values, the quark and gluon emission are mixed or not. The parton creation is an effect depending on the value of Q^2 . For increasing virtuality, more partons are visible, i.e., their density enhances. Moreover, a large Q^2 implies decreasing in α_s in such a way that partons interact weakly. Nevertheless, even if α_s is small, successive emissions need to be taken into account when $\ln Q^2$ is large so that $\alpha_s \ln Q^2 \sim \mathcal{O}(1)$. That condition implies the resummation of higher-order terms. The DGLAP equation usually describes it in order to obtain information about the parton distribution inside a hadron [205–207].

The DGLAP formalism generates an increase of parton density when Q^2 grows, being typically proportional to $\ln Q^2$. However, the transverse area occupied by each parton is $\Sigma \sim 1/Q^2$, so

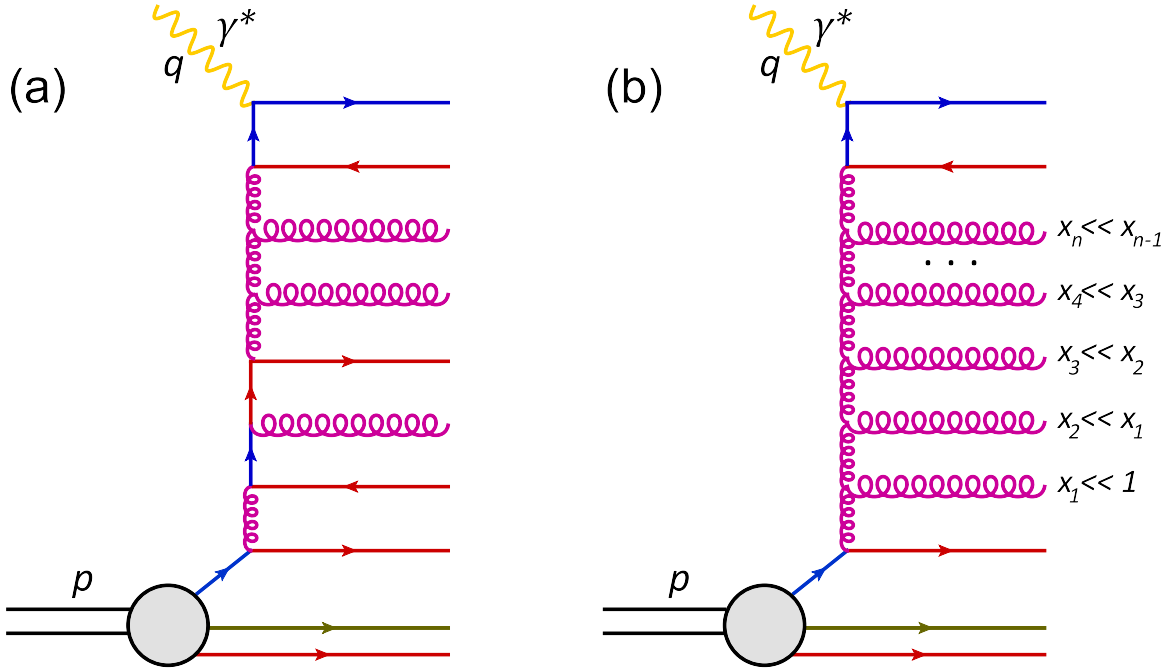


Figure 2.11: Parton production described by pQCD in a DIS configuration: (a) Evolution for high Q^2 at fixed x (*diluted system*) (b) Evolution for high Q^2 and small x (*dense system*).

that, for fixed and not too small x , an increment of density is compensated by the tiny area of partons, and the system becomes dilute. Figure 2.11(a) schematizes that situation: there is a mixture of quarks and gluons from the virtual photon's exchange. On the other hand, increasing energy implies a decrease in x . It implies that the transverse area for partons $\Sigma \sim 1/xp$ enhances, and corrections of the order $\alpha_s \ln(1/x) \sim 1$ are important. Moreover, from Eq. (2.20), small x means a high gluon production, and therefore, the system is a dense gluonic medium [214, 215]. Figure 2.11(b) shows the dense system.

The small x behaviour can be computed from Eq. (2.20), given that the emission probability is the same as the number of gluons, so that at leading order in α_s :

$$x \frac{dN_g}{dx}(Q^2) = \frac{\alpha_s C_F}{\pi} \int_{\Lambda_{\text{QCD}}^2}^{Q^2} \frac{dk_{\perp}^2}{k_{\perp}^2} = \frac{\alpha_s C_F}{\pi} \ln \left(\frac{Q^2}{\Lambda_{\text{QCD}}^2} \right), \quad (2.21)$$

where the infrared cutoff is introduced in order to account the confinement at low energies, where the parton has a minimal virtuality of order Λ_{QCD}^2 . Also, from the fact that Eqs. (2.20) and (2.21) are computed for $x \ll 1$, it is valid to assume that another gluon with $x_1 \ll x \ll 1$ can be emitted, and consequent gluons with longitudinal momentum fractions $x_2 \ll x_1 \ll x$, $x_3 \ll x_2 \ll x_1, \dots, x_n \ll x_{n-1} \ll x_{n-2}$ as is illustrated in Fig. 2.11(b). By adding n -th gluon emissions, Eq. (2.20) implies a contribution proportional to

$$\left(\frac{\alpha_s N_c}{\pi} \right)^n \int_x^1 \frac{dx_n}{x_n} \int_{x_n}^1 \frac{dx_{n-1}}{x_{n-1}} \dots \int_{x_2}^1 \frac{dx_1}{x_1} = \frac{1}{n!} \left(\frac{\alpha_s N_c}{\pi} \ln \frac{1}{x} \right)^n. \quad (2.22)$$

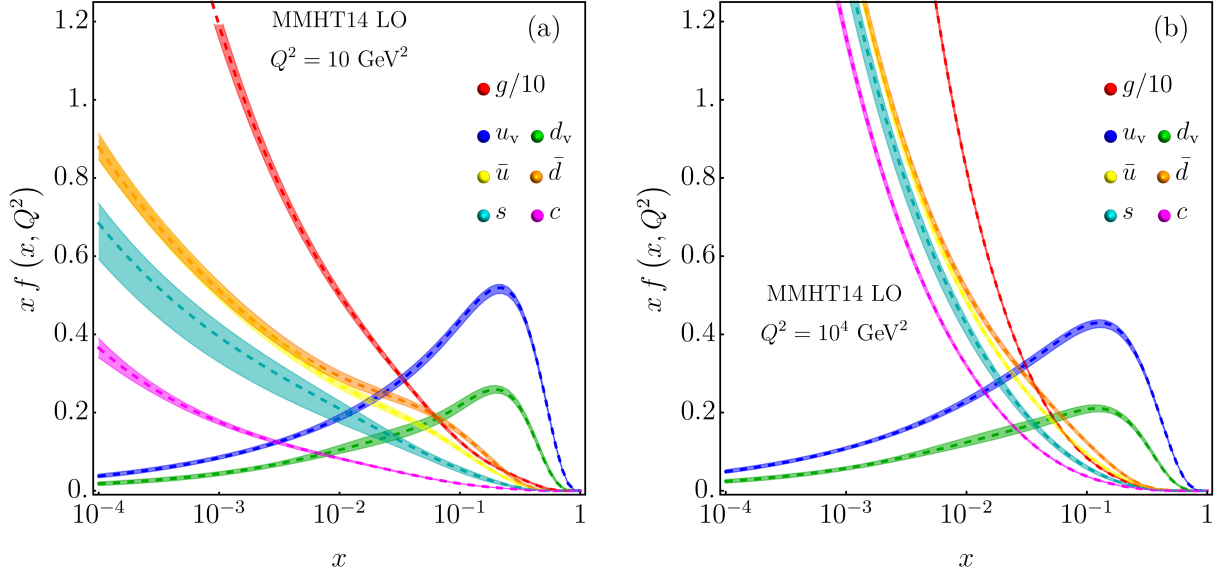


Figure 2.12: Parton distribution functions for the proton in the LHC for computed at LO as a function of the momentum fraction x at the scales (a) $Q^2 = 10 \text{ GeV}^2$ and (b) $Q^2 = 10^4 \text{ GeV}^2$. In each plot, the PDFs are shown for gluons (g), valence quarks (u_v, d_v), sea-quarks (\bar{u}, \bar{d}), strange quarks (s) and charm quarks (c). The error bands correspond to a confidence-level uncertainty of 68%. Note that the gluon PDF is scaled by a factor of 10.

For a large amount of gluons, the latter equation gives an exponential function, so that the *unintegrated gluon distribution* is

$$x \frac{dN_g}{dx dk_{\perp}^2} \sim \frac{\alpha_s C_F}{\pi} \frac{1}{k_{\perp}^2} \exp\left(\omega \frac{\alpha_s N_c}{\pi} Y\right), \quad (2.23)$$

where $\omega = 4 \log 2$ and $Y \equiv 1/x$ is the rapidity difference between the parent and the emitted gluon. A complete argumentation is found in the BFKL equation, where the kinematics of each gluon is considered, and arguments beyond a power counting are presented [216–218]. The *coherence time* in the BFKL formalism is defined as the parton lifetime $\Delta t \simeq 2k_z/k_{\perp}^2$ results proportional to x , which means that the first gluons in a cascade can be visualized as static color sources. Although the average color charge of the system is zero, the overlapping of color sources leads to fluctuations of color charge density, which increases with $1/x$.

Figures 2.12, 2.13 and 2.14 show the parton distribution functions for the proton as a function of the momentum fraction x computed in the LHC at LO, NLO, and NNLO, respectively. The analysis is made from hard scattering data at the scales $Q^2 = 10 \text{ GeV}^2$ and 100 GeV^2 with a 68% of confidence-level uncertainty, and the running coupling constant reference is chosen as $\alpha_s(M_Z^2) = 0.135$ (for LO), $\alpha_s(M_Z^2) = 0.120$ (for NLO) and $\alpha_s(M_Z^2) = 0.118$ (for NNLO), where M_Z is the Z -boson mass. [219]. In those figures, the PDFs are shown for gluons (g), valence quarks (u_v, d_v), sea-quarks (\bar{u}, \bar{d}), strange quarks (s) and charm quarks (c). Note that gluon production enhances at small x , which is indicated by scaling the corresponding PDF by a factor of 10. Moreover, as it was commented on, given the dense regime when the energy

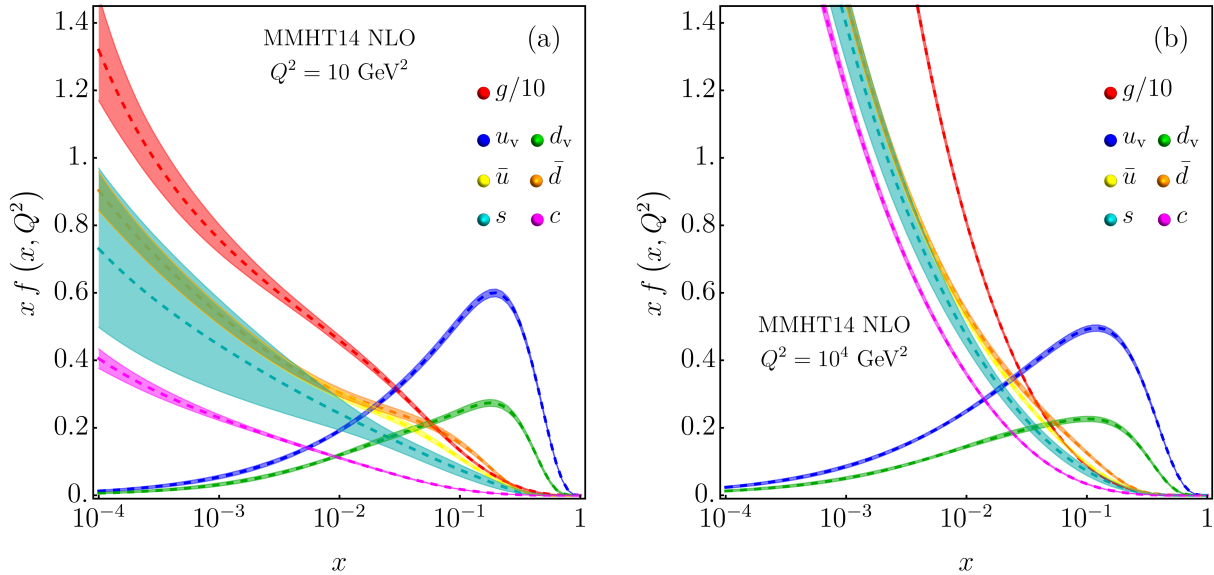


Figure 2.13: Parton distribution functions for the proton in the LHC for computed at NLO as a function of the momentum fraction x at the scales (a) $Q^2 = 10 \text{ GeV}^2$ and (b) $Q^2 = 10^4 \text{ GeV}^2$. In each plot, the PDFs are shown for gluons (g), valence quarks (u_v, d_v), sea-quarks (\bar{u}, \bar{d}), strange quarks (s) and charm quarks (c). The error bands correspond to a confidence-level uncertainty of 68%. Note that the gluon PDF is scaled by a factor of 10.

is increased, higher orders in the perturbation theory must be added in order to compute an accurate gluon distribution function. In particular, by comparison between Figs. 2.12(a), 2.13(a) and 2.14(a), it is clear that the gluon production reaches a saturation point when x decreases and more terms in the perturbative series are considered. Moreover, in Figs. 2.12(b), 2.13(b) and 2.14(b), a saturation point is not found, and the corrections provided by the NLO and NNLO do no change drastically the PDFs behavior.

The data is conclusive: at small x (or high-energy reactions), the proton is made mostly by gluons. Nevertheless, the results for large Q^2 suggest a non-saturation value, which has no physical grounds. In order to obtain a saturation regime, it is necessary to separate the gluon evolution. First, the Q^2 -evolution gives a picture of non-interacting gluons yielding linear effects in the BFKL formalism. However, even a considerable energy exchange from the virtual photons to partons leads a negligible interaction between the hadron constituents at the dilute regime, the Y -evolution (or $1/x$) implies a high-gluon density medium, and the coupling becomes significant, giving rise to non-linear effects [220–222].

To obtain an estimate of the saturation scale, one considers the dilute and dense regimes of gluon occupation numbers: in the former, $n \ll 1$ which is turned into order $n \sim \mathcal{O}(1)$ when gluons become to overlap, but given that their production is suppressed by $\alpha_s \ll 1$, their interactions are still weak. Increasing the density implies interactions of order $\alpha_s \sim 1$ and a large density of $n \sim \mathcal{O}(1/\alpha_s)$, where the non-linear effects stop the growth in the gluon number. Thus, from

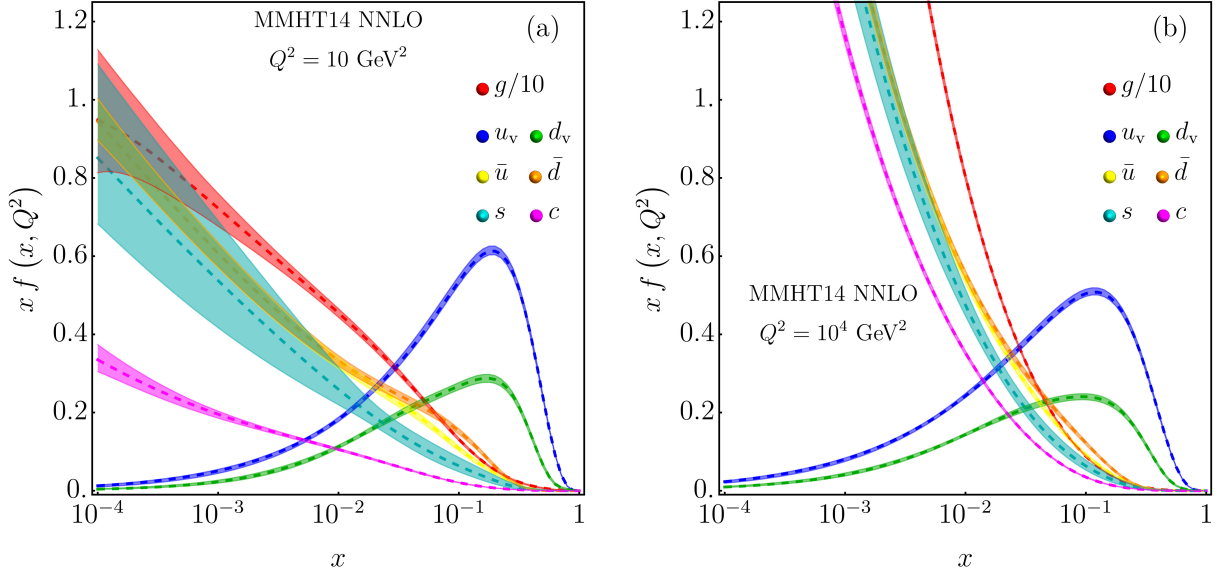


Figure 2.14: Parton distribution functions for the proton in the LHC for computed at NNLO as a function of the momentum fraction x at the scales (a) $Q^2 = 10 \text{ GeV}^2$ and (b) $Q^2 = 10^4 \text{ GeV}^2$. In each plot, the PDFs are shown for gluons (g), valence quarks (u_v, d_v), sea-quarks (\bar{u}, \bar{d}), strange quarks (s) and charm quarks (c). The error bands correspond to a confidence-level uncertainty of 68%. Note that the gluon PDF is scaled by a factor of 10.

the gluon occupation number $n(x, Q^2)$ defined as

$$\begin{aligned}
 n(x, Q^2) &\equiv \frac{\# \text{ of gluons with given } x \times \text{ occupied area by one gluon}}{\text{transverse area of the hadron}} \\
 &\simeq \frac{xg(x, Q^2)}{R^2 Q^2}, \tag{2.24}
 \end{aligned}$$

where it is assumed that the area per gluon is $\Sigma_g \sim 1/Q^2$ and the transverse (invariant) area of the hadron is $\Sigma_{\perp}^H \sim \pi R^2$, the gluon saturation scale $Q_s(x)$ is estimated to be [220, 223]:

$$n(x, Q^2 = Q_s^2(x)) \sim \frac{1}{\alpha_s} \implies Q_s^2(x) \simeq \alpha_s \frac{xg(x, Q_s^2(x))}{R^2}. \tag{2.25}$$

The above equation implies that gluons with momentum $k_{\perp} < Q_s(x)$ correspond to large occupation numbers but in a saturation scale such as they do not increase the number of gluons when x is decreased. On the other hand, gluons with $k_{\perp} \gg Q_s(x)$ remains in the dilute regime.

This analysis yields the basic concepts of the so-called Color Glass Condensate (CGC) as a state of the high-energy hadronic matter, which can be summarized as follows¹:

¹A detailed description from the theoretical and experimental perspectives can be found at the cited references throughout the current section and complemented with Refs. [77–83]. Although the CGC theory is of particular interest, its full treatment is outside the scope of this work.

- At high-energetic reactions, the hadron is most dominated by the presence of gluons, so that the medium is *colored* by the non-Abelian charges of $SU(3)$.
- The system behaves like a glass: the coherence time discussion shows that gluons with larger x are viewed as static sources (*fast gluons*) by the radiated gluons with small x (*slow gluons*). However, fast gluons can vary in a long time window set by their longitudinal momentum. Hence, for short time scales, the system is like a “solid”, but it is like a “liquid” for large times: that is the main characteristic of glass.
- The high saturated gluon occupation number adds its color charges coherently. The corresponding saturation scale is a multiparticle state of bosons in the Bose-Einstein’s condensate phase.

The CGC state is the starting point of the photon production mechanism proposed in this chapter: the gluons will be treated as on-shell particles. Their high-density makes them weakly coupled, and perturbation theory is then applicable for scales $Q_s^2(x) \gg \Lambda_{\text{QCD}}^2$.

2.4 Magnetic Fields in a Relativistic Heavy-Ion Collision

In Chapter 1, the effects of high temperatures and baryonic densities were studied as a key to understand QCD matter under extreme conditions, particularly the chiral symmetry restoration and the QCD-phase diagram were presented. On the other hand, Sec. 2.3 shows that ultrarelativistic systems have severe implications for the parton distribution functions, yielding a gluonic dense medium known as the CGC. In principle, this novel dynamics can be measured in heavy-ion collision experiments, which give rise to another phenomenon that probes the QCD in an additional limiting scenario: the presence of intense magnetic fields in a deconfined medium. In order to introduce the properties of such magnetic fields, this section is devoted to its theoretical study. The framework presented here summarizes Refs. [73–76] and an extension of these results is given in Sec. 2.6.2.

The existence of strongly interacting matter in the presence of intense magnetic fields has become of interest, given its implications in fundamental theoretical and experimental phenomena. The so-called magnetic catalysis, where the magnetic field acts as a catalyst for the dynamical fermion mass generation from flavor symmetry breaking, is an excellent example [224–228]. Also, the QCD-topological invariants encoded in the winding number related to symmetries \mathcal{P} and \mathcal{CP} are affected by external intense magnetic fields [72]. Moreover, it has been suggested that signals of the deconfinement and the chiral phase transition may be found by measuring the imbalance of charged particles emission along the direction of the magnetic field provided by a nonzero chirality [72, 229]. Similarly, intense magnetic fields have an impact in the QCD-phase diagram [230–233], the spontaneous creation of axial currents [234, 235], the formation of π^0 domain walls [236], and the color superconducting phases [237, 238], among others [239–243].

The idea behind the intense magnetic fields created in heavy-ion collisions is simple: for non-central events, i.e., collisions with an impact parameter b , the non-colliding hadrons (protons)

move as free charges with opposite directions. The electric current associated with these protons leads to the creation of a magnetic field perpendicular to the protons direction of motion. The magnetic field evolution for hadron collisions starts with the Boltzmann equation for the phase-space distribution function $f(x, p)$:

$$p^\mu \frac{\partial}{\partial x^\mu} f = C[f], \quad (2.26)$$

where $C[f]$ is the so-called *collision integral* which connects the dynamics of the colliding particles, where the particles are considered on-shell with 4-momentum p^μ and 4-position x^μ . The effects of a background electromagnetic field can be achieved by introducing the field tensor $F_{\mu\nu}$:

$$p^\mu \left(\frac{\partial}{\partial x^\mu} - F_{\mu\nu} \frac{\partial}{\partial p^\nu} \right) f = C[f]. \quad (2.27)$$

If the particles are constrained by an interaction potential U , the equation for a test particle with distribution $f(\mathbf{r}, \mathbf{p}, t)$ is

$$\left[\frac{\partial}{\partial t} + \left(\frac{\mathbf{p}}{p_0} + \nabla_{\mathbf{p}} U \right) \nabla_{\mathbf{r}} + (-\nabla_{\mathbf{r}} U + e\mathbf{E} + e\mathbf{v} \times \mathbf{B}) \nabla_{\mathbf{p}} \right] f = C_{\text{coll}}(f, f_1, \dots, f_N). \quad (2.28)$$

Besides the Boltzmann equation, the charged particle dynamics is determined by the Maxwell (field) equations:

$$\nabla \times \mathbf{E} = -\frac{1}{c} \frac{\partial \mathbf{B}}{\partial t}, \quad \nabla \cdot \mathbf{B} = 0, \quad (2.29)$$

so that for a point-like charge modelled by the sources:

$$\begin{aligned} \rho(\mathbf{r}, t) &= e \delta[\mathbf{r} - \mathbf{r}(t)], \\ \mathbf{j}(\mathbf{r}, t) &= e \mathbf{v}(t) \delta[\mathbf{r} - \mathbf{r}(t)], \end{aligned} \quad (2.30)$$

the electric and magnetic field background is found to be

$$e\mathbf{E} = \frac{\text{sign}(e)\alpha \mathbf{R}(t) (1 - v^2/c^2)}{[(\mathbf{R}(t) \cdot \mathbf{v}/c)^2 + R^2(t) (1 - v^2/c^2)]^{3/2}} \quad (2.31a)$$

and

$$e\mathbf{B} = \frac{\text{sign}(e)\alpha [\mathbf{v} \times \mathbf{R}(t)] (1 - v^2/c^2)}{c [(\mathbf{R}(t) \cdot \mathbf{v}/c)^2 + R^2(t) (1 - v^2/c^2)]^{3/2}}, \quad (2.31b)$$

where $\alpha = e^2/4\pi$. The above equations are the well-known Linaard-Wiechert fields for a moving particle.

The presented formalism to account for the created electromagnetic fields is more on less standard, but several computational approaches address variations in the event generation. The

Ultrarelativistic Quantum Molecular Dynamics (UrQMD) is one of them, and it is discussed in Sec. 2.6.2. The Hadron String Dynamics (HSD) is also used, which corresponds to Kadanoff-Baym kinetic equations, where the nuclear collisions are modeled as quasiparticles with finite width [244, 245]. The latter was used by Voronyuk *et al.* to describe the space-time evolution of the magnetic field in non-central collisions [74], but other approaches from general considerations on the rapidity Y and charge distribution density $\varrho_{\pm}(\mathbf{x}'_{\perp})$ are implemented. For example, the charge distribution density inside the contracted nucleus is usually taken as:

$$\varrho_{\pm}(\mathbf{x}'_{\perp}) = \frac{2}{\frac{4}{3}\pi R^3} \sqrt{R^2 - (\mathbf{x}'_{\perp} \pm \mathbf{b}/2)^2} \theta_{\pm}(\mathbf{x}'_{\perp}), \quad (2.32)$$

with the normalization condition

$$\int d^2\mathbf{x}'_{\perp} \varrho_{\pm}(\mathbf{x}'_{\perp}) = 1, \quad (2.33)$$

where \mathbf{x}'_{\perp} is a vector transverse to the beam axis (\mathbf{e}_y) and the nuclei are considered as *pancake* shaped. The function $\theta_{\pm}(\mathbf{x}'_{\perp})$ are the nuclei's projections over the transverse plane separating spectators (no colliding hadrons) and participants (hadrons with at least one collision) so that:

$$\theta_{\pm}(\mathbf{x}'_{\perp}) = \theta \left[R^2 - (\mathbf{x}'_{\perp} \pm \mathbf{b}/2)^2 \right]. \quad (2.34)$$

The latter formalism is used by Kharzeev *et al.* by writing the Linaard-Wiechert potentials as function of Y as follows [72]:

$$e\mathbf{B}(\mathbf{x}) = Z\alpha \sinh(Y) \frac{(\mathbf{x}'_{\perp} - \mathbf{x}_{\perp}) \times \mathbf{e}_y}{[(\mathbf{x}'_{\perp} - \mathbf{x}_{\perp})^2 + (t \sinh Y - z \cosh Y)^2]^{3/2}}, \quad (2.35)$$

where Z is the nucleus charge.

In terms of the charge distribution density, the total magnetic field is given by:

$$\mathbf{B} = \mathbf{B}_s^+ + \mathbf{B}_s^- + \mathbf{B}_p^+ + \mathbf{B}_p^-, \quad (2.36)$$

where \mathbf{B}_s^{\pm} and \mathbf{B}_p^{\pm} is the magnetic field created by spectators and participants moving in directions $\pm \mathbf{e}_y$, respectively. By defining the proper time $\tau = (t^2 - y^2)^{1/2}$ and the space-time rapidity $\eta = \frac{1}{2} \log [(t + y)/(t - y)]$, the spectators' field is:

$$e\mathbf{B}_s^{\pm}(\tau, \eta, \mathbf{x}_{\perp}) = \pm Z\alpha \sinh(Y_0 \mp \eta) \times \int d^2\mathbf{x}'_{\perp} \varrho_{\pm}(\mathbf{x}'_{\perp}) [1 - \theta_{\mp}(\mathbf{x}'_{\perp})] \frac{(\mathbf{x}'_{\perp} - \mathbf{x}_{\perp}) \times \mathbf{e}_y}{[(\mathbf{x}'_{\perp} - \mathbf{x}_{\perp})^2 + \tau^2 \sinh(Y_0 \mp \eta)^2]^{3/2}}, \quad (2.37)$$

where is assumed that spectators do no scatter and continues traveling with the initial beam's rapidity Y_0 .

The participant's contribution is taken only from the original colliding hadrons, i.e., the produced particles after the reaction are neglected. Such consideration is validated because produced particles expand spherically, and the magnetic field created by them is minimal. Moreover, the number of charged particles (positive and negative) remains approximately equal than

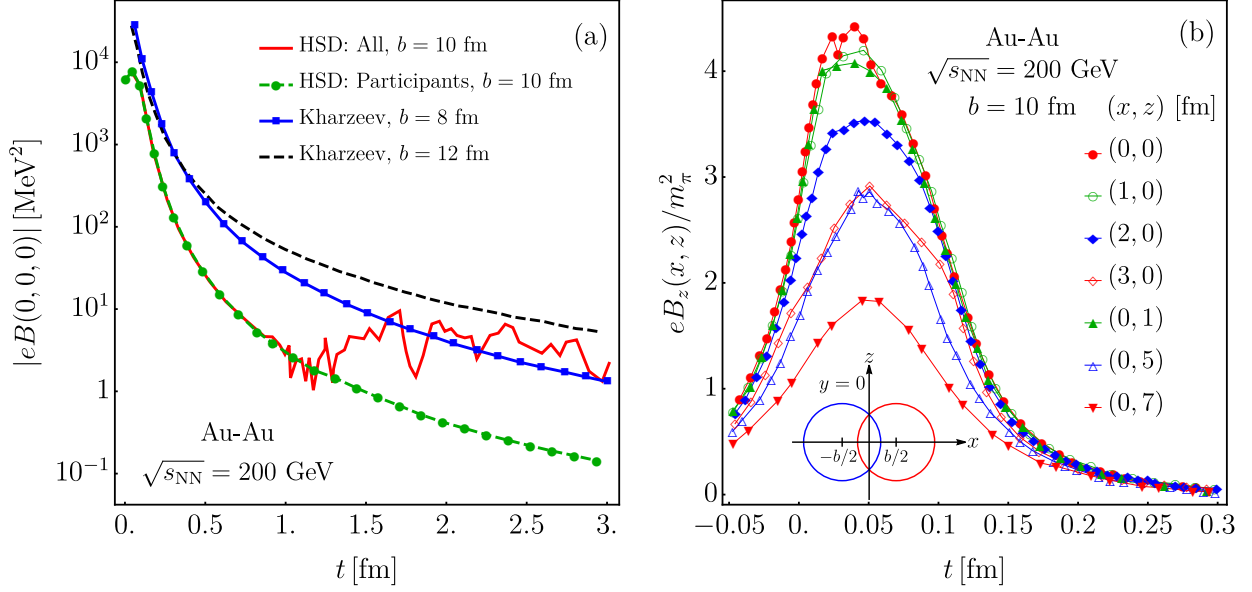


Figure 2.15: (a) Magnetic field space–time evolution at the center of the collision computed in Refs. [72,74] when the impact parameter b is changed. (b) Magnetic field in units of the squared pion mass m_π^2 in z -direction for several points (x, z) in the plane perpendicular to the charge’s motion with $b = 10$ fm [74]. The inset represents the geometry in the transverse plane ($y = 0$) of a noncentral heavy-ion collision.

before the collision. Therefore, by taking into account the normalized distribution of the participants along the collision axis:

$$f(Y) = \frac{a}{2 \sinh(aY_0)} e^{aY}, \quad -Y_0 \leq Y \leq Y_0, \quad (2.38)$$

where the parameter $a \approx 1/2$ is obtained from experimental data [246], the contribution of the participants to the magnetic field is

$$\begin{aligned} e\mathbf{B}_p^\pm(\tau, \eta, \mathbf{x}_\perp) &= \pm Z\alpha \int d^2\mathbf{x}'_\perp \int_{-Y_0}^{Y_0} dY f(Y) \sinh(Y \mp \eta) \varrho_\pm(\mathbf{x}'_\perp) \theta_\mp(\mathbf{x}'_\perp) \\ &\times \frac{(\mathbf{x}'_\perp - \mathbf{x}_\perp) \times \mathbf{e}_y}{[(\mathbf{x}'_\perp - \mathbf{x}_\perp)^2 + \tau^2 \sinh(Y \mp \eta)^2]^{3/2}}. \end{aligned} \quad (2.39)$$

Figure 2.15 shows the space-time evolution of the magnetic field in the approaches thus discussed for simulations of Au-Au collisions at $\sqrt{s_{NN}} = 200$ GeV with several impact parameters. In Fig. 2.15(a), the magnetic field at the collision’s center from the HSD and Kharzeev’s formalism is compared. The former separates the magnetic field originated by spectators from the spectators and participants. Both situations imply a rapid decay in the magnetic field strength with a peak of high intensity at the beginning of the collision. Moreover, Fig. 2.15(b) shows the magnetic field’s spatial profile in the transverse plane. The center’s variation to other directions is less than 20%, except for the boundaries of the nucleus overlap $x \approx b/2 \sim 5$ fm. Hence, the magnetic field is very homogeneous in the z -direction. Note that in Fig. 2.15(b), the vertical axis

is normalized to the squared pion mass m_π^2 , giving an estimate of the magnetic field strength $m_\pi^2 \sim 10^{18}$ Gauss.

The above results give the main features of the magnetic field in a heavy-ion collision: it has a very high intensity but is short-lived. That lifetime is crucial to the Chiral Magnetic Wave (CMW) framework to explain the elliptic flow dependence asymmetry for charged particles [247]. The CMW formalism needs magnetic fields with a minimum of 4 fm duration, but the models and data present a lifetime around 0.1 fm [248]. Models to improve the magnetic field pulse time based on the effects of the QCD-medium conductivity have been proposed. Still, for realistic values of the parameters, there is not an appreciable difference [75].

The presented discussion seeds the proposal for a source of photons in the early stages of a heavy-ion collision: a dense medium made of on-shell gluons with a strong magnetic background opens the photon production channel by gluon fusion and gluon splitting. The development of those channels and their impact on the photon invariant momentum distribution and the elliptic flow is presented in the following sections.

2.5 Prompt Photon Production by Gluon Fusion in a Magnetized Medium

As was commented on the previous sections, at the early stages of a heavy-ion collision two important scenarios have to be taken into account: the high gluon abundance and the existence of intense magnetic fields. In order to take into account such phenomenology, the photon production from gluon fusion is proposed as a source of prompt photons. The lowest order process in the strong, and electromagnetic couplings comes from an amplitude made out of a quark triangle diagram with two gluons and one photon attached to each one of the vertices of the triangle. Given that the electromagnetic interaction differentiates the particle charge, both quark and anti-quark triangles have to be considered.

The magnetic field acts over the fermionic loop, and therefore, the quark propagator in coordinate representation is

$$S(x, x') = \Phi(x, x') \int \frac{d^4 p}{(2\pi)^4} e^{-ip \cdot (x-x')} S(p), \quad (2.40)$$

where the *phase factor* is given by

$$\Phi(x, x') = \exp \left\{ i|q_f| \int_{x'}^x d\xi^\mu \left[A_\mu + \frac{1}{2} F_{\mu\nu} (\xi - x')^\nu \right] \right\}, \quad (2.41)$$

with $|q_f| = n|e|$, where n and e are the fractional quark's charge and electron charge, respectively [249]. The Fourier transform of the translationally invariant part of the propagator in the

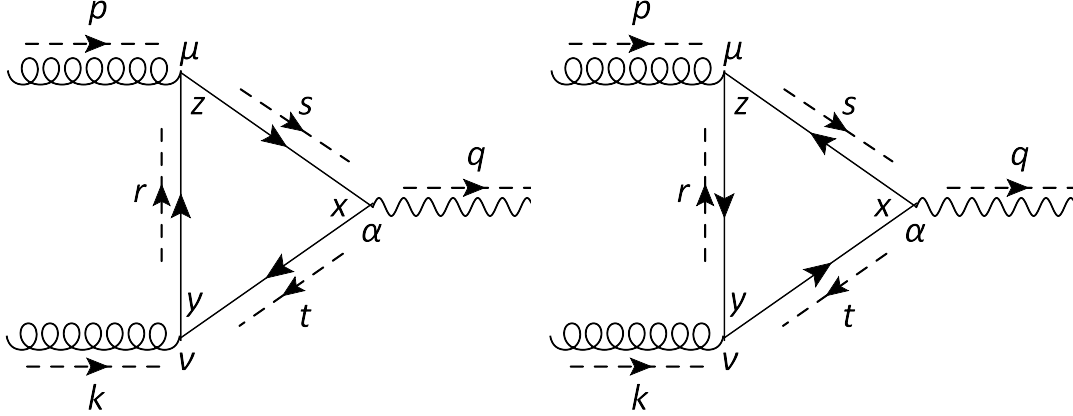


Figure 2.16: Feynman diagrams contributing to the production of a photon with four-momentum q^μ from the fusion of gluons with four-momentum p^μ and k^μ . Note the charge flow in each diagram, which differentiates the quark from the antiquark. The fermion lines represent the magnetized propagator of Eq. (2.42).

Schwinger's proper-time formalism is given by

$$iS(p) = \int_0^\infty \frac{d\tau}{\cos(|q_f B| \tau)} \exp \left\{ i\tau \left[p_\parallel^2 - p_\perp^2 \frac{\tan(|q_f B| \tau)}{|q_f B| \tau} - m_f^2 + i\epsilon \right] \right\} \\ \times \left[(\cos(|q_f B| \tau) + \gamma_1 \gamma_2 \sin(|q_f B| \tau)) (m_f + \not{p}_\parallel) - \frac{\not{p}_\perp}{\cos(|q_f B| \tau)} \right], \quad (2.42)$$

where m_f is the fermion mass. To simplify the calculations, a constant and homogeneous magnetic field along the \hat{z} -direction is chosen. Such a magnetic field, in the symmetric gauge, can be obtained from the vector potential

$$A^\mu = \frac{B}{2}(0, -y, x, 0). \quad (2.43)$$

Also, for a 4-momentum p^μ its parallel and transverse parts with respect to the magnetic field are defined as

$$p_\parallel^\mu = (p_0, 0, 0, p_3) \rightarrow p_\parallel^2 = p_0^2 - p_3^2, \quad (2.44a)$$

$$p_\perp^\mu = (0, p_1, p_2, 0) \rightarrow p_\perp^2 = p_1^2 + p_2^2, \quad (2.44b)$$

thus

$$p^2 = p_\parallel^2 - p_\perp^2. \quad (2.44c)$$

The Feynman diagrams which contribute to the process where two gluons with four-momentum p^μ and k^μ produced a photon with four-momentum q^μ are represented in Fig. 2.16. The quark

lines into the triangle describe the magnetized fermion propagator so that one diagram schematics the quark's contribution whereas the other the antiquark's part. Hence, the total amplitude is given by

$$\begin{aligned} \widetilde{\mathcal{M}} &= - \int d^4x d^4y d^4z \int \frac{d^4r}{(2\pi)^4} \frac{d^4s}{(2\pi)^4} \frac{d^4t}{(2\pi)^4} e^{-it \cdot (y-x)} e^{-is \cdot (x-z)} e^{-ir \cdot (z-y)} e^{-ip \cdot z} e^{-ik \cdot y} e^{iq \cdot x} \\ &\times \left\{ \text{Tr} [iq_f \gamma_\alpha iS(s) ig \gamma_\mu t^c iS(r) ig \gamma_\nu t^d iS(t)] + \text{Tr} [iq_f \gamma_\alpha iS(t) ig \gamma_\nu t^d iS(r) ig \gamma_\mu t^c iS(s)] \right\} \\ &\times \Phi(x, y) \Phi(y, z) \Phi(z, x) \epsilon^\mu(\lambda_p) \epsilon^\nu(\lambda_k) \epsilon^\alpha(\lambda_q), \end{aligned} \quad (2.45)$$

where t^c, t^d are Gell-Mann matrices. The polarization vectors for the gluons and the photon are $\epsilon^\mu(\lambda_p) \epsilon^\nu(\lambda_k)$, and $\epsilon^\alpha(\lambda_q)$, respectively.

The product of phase factor has the form

$$\Phi(x, y) \Phi(y, z) \Phi(z, x) = \exp \left[-i \frac{|q_f B|}{2} \epsilon_{mj} (z-x)_m (x-y)_j \right], \quad (2.46)$$

where m, j are indices in the transverse space, and ϵ_{mj} is the 2D-Levi-Civita symbol [250–252]. The formal deduction of the Eq. (2.46) can be found in Appendix B.

The quark propagator is expressed in the well-know sum over Landau levels [226, 253]:

$$iS(p) = ie^{-p_\perp^2/|q_f B|} \sum_{n=0}^{+\infty} (-1)^n \frac{D_n(q_f B, p)}{p_\parallel^2 - m_f^2 - 2n|q_f B|}, \quad (2.47)$$

where $L_n^\alpha(x)$ are the associated Laguerre polynomials, the numerator is

$$D_n(q_f B, p) = 2(\not{p}_\parallel + m_f) \left[\mathcal{O}^- L_n^0 \left(\frac{2p_\perp^2}{|q_f B|} \right) - \mathcal{O}^+ L_{n-1}^0 \left(\frac{2p_\perp^2}{|q_f B|} \right) \right] + 4\not{p}_\perp L_{n-1}^1 \left(\frac{2p_\perp^2}{|q_f B|} \right). \quad (2.48)$$

and the operators \mathcal{O}^\pm are given by

$$\mathcal{O}^\pm = \frac{1}{2} (1 \pm i\gamma^1 \gamma^2). \quad (2.49)$$

Usually, these operators are written by specifying the sign of the electric charge as

$$\mathcal{O}^\pm = \frac{1}{2} [1 \pm i \text{sign}(q_f B) \gamma^1 \gamma^2], \quad (2.50)$$

so that \mathcal{O}^+ and \mathcal{O}^- are exchanged in Eq. (2.48) when the propagator passes from describing a fermion to describing an antifermion. Given that the definition of “particle” and “antiparticle” is a matter of choice it doesn't matter which sing of $(q_f B)$ is selected for the “particle”, because the contribution of the two fermions is considered.

To compute analytically Eq. (2.45), the magnetic field is taken as the dominant energy scale. If the gluons have soft momentum and by the fact that the system has not reached thermal

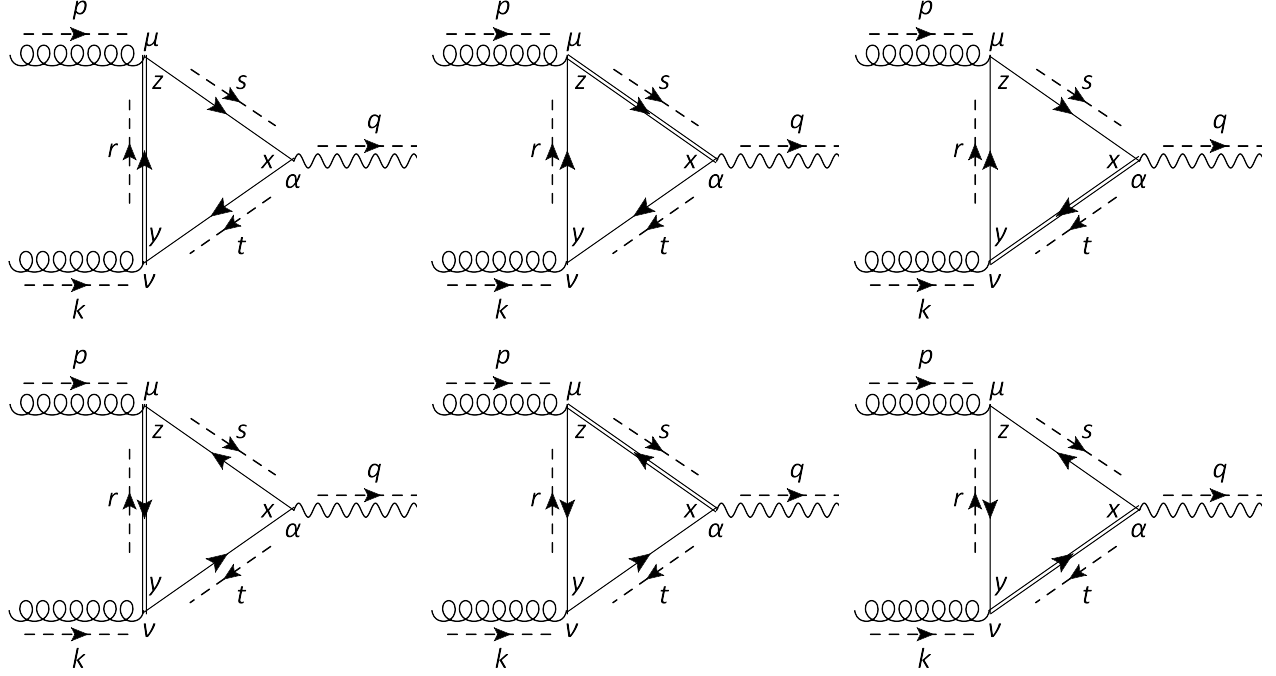


Figure 2.17: Feynman diagrams contributing to the process $gg \rightarrow \gamma$ in the presence of a magnetic field. The double lines represent that quark propagator in the 1LL, whereas the single lines represent the propagator in the LLL. The arrows in the propagators are the charge flow and the arrows on the sides represent the momentum direction.

equilibrium, it is a suitable approximation. Therefore, it is possible to set $m_f = 0$ and work with the contributions of the first Landau levels, i.e., with the Lowest Landau Level (LLL) and the first excited Landau level (1LL):

$$iS^{\text{1LL}}(p) = i \frac{e^{-p_{\perp}^2/|q_f B|}}{p_{\parallel}^2} \not{p}_{\parallel} \mathcal{O}^- \quad (2.51a)$$

$$iS^{\text{1LL}}(p) = -2i \frac{e^{-p_{\perp}^2/|q_f B|}}{p_{\parallel}^2 - 2|q_f B|} \left[\left(1 - \frac{2p_{\perp}^2}{|q_f B|} \right) \not{p}_{\parallel} \mathcal{O}^- - \not{p}_{\parallel} \mathcal{O}^+ + 2\not{p}_{\perp} \right]. \quad (2.51b)$$

It is necessary to consider at least one quark in the 1LL since if all the fermions are in the LLL the fermionic traces vanishes, and the process is not allowed (see Appendix C). The Feynman diagrams to be considered are shown in Fig. 2.17, where the quark/antiquark contribution is differentiated by the charge flow direction. Then, the leading order contribution of the amplitude

reads

$$\begin{aligned}
 \widetilde{\mathcal{M}} &= 8i(2\pi)^4 \delta^{(4)}(q - k - p) \delta^{cd} |q_f| g^2 \\
 &\times \int \frac{d^4 r}{(2\pi)^4} \frac{d^4 s}{(2\pi)^4} \frac{d^4 t}{(2\pi)^4} \epsilon^\mu(\lambda_p) \epsilon^\nu(\lambda_k) \epsilon^\alpha(\lambda_q) \\
 &\times \int d^4 w d^4 l e^{-il(r-t-k)} e^{-iw(r-s+p)} \exp \left\{ -i \frac{|q_f B|}{2} \epsilon_{mj} w_m l_j \right\} \exp \left\{ -\frac{r_\perp^2 + s_\perp^2 + t_\perp^2}{|q_f B|} \right\} \\
 &\times \text{Tr} \left\{ \frac{\gamma_1 \gamma_2 \gamma_\alpha \not{t}_\perp \gamma_\nu \not{t}_\parallel \gamma_\mu \not{s}_\parallel}{r_\parallel^2 s_\parallel^2 (t_\parallel^2 - 2|q_f B|)} + \frac{\gamma_1 \gamma_2 \gamma_\mu \not{s}_\perp \gamma_\alpha \not{t}_\parallel \gamma_\nu \not{t}_\parallel}{t_\parallel^2 r_\parallel^2 (s_\parallel^2 - 2|q_f B|)} + \frac{\gamma_1 \gamma_2 \gamma_\nu \not{t}_\perp \gamma_\mu \not{s}_\parallel \gamma_\alpha \not{t}_\parallel}{s_\parallel^2 t_\parallel^2 (r_\parallel^2 - 2|q_f B|)} \right\}. \quad (2.52)
 \end{aligned}$$

A second important approximation is to consider that in the denominators of Eq. (2.52) the term $|q_f B|$ is large with respect to the loop momenta, which implies that the calculations will be valid only for low photon energies. In this way, by considering that $2|q_f B| \gg t_\parallel^2, s_\parallel^2, r_\parallel^2$. After a straightforward calculation, the matrix element can be written as

$$\begin{aligned}
 \widetilde{\mathcal{M}} &= -i(2\pi)^4 \delta^{(4)}(q - k - p) \frac{q_f g^2 \delta^{cd} e^{f(p_\perp, k_\perp)}}{32\pi(2\pi)^8} \epsilon_\mu(\lambda_p) \epsilon_\nu(\lambda_k) \epsilon_\alpha(\lambda_q) \\
 &\times \left\{ \left(g_\parallel^{\mu\alpha} - \frac{p_\parallel^\mu p_\parallel^\alpha}{p_\parallel^2} \right) h^\nu(a) - \left(g_\parallel^{\mu\nu} - \frac{p_\parallel^\mu p_\parallel^\nu}{p_\parallel^2} \right) h^\alpha(a) + \left(g_\parallel^{\mu\nu} - \frac{k_\parallel^\mu k_\parallel^\nu}{k_\parallel^2} \right) h^\alpha(b) \right. \\
 &\left. - \left(g_\parallel^{\alpha\nu} - \frac{k_\parallel^\alpha k_\parallel^\nu}{k_\parallel^2} \right) h^\mu(b) + \left(g_\parallel^{\alpha\nu} - \frac{q_\parallel^\alpha q_\parallel^\nu}{q_\parallel^2} \right) h^\mu(c) - \left(g_\parallel^{\mu\alpha} - \frac{q_\parallel^\mu q_\parallel^\alpha}{q_\parallel^2} \right) h^\nu(c) \right\}, \quad (2.53)
 \end{aligned}$$

where

$$h^\mu(a) = -\frac{i}{\pi} \epsilon_{ij} a^i g_\perp^{j\mu}, \quad (2.54a)$$

$$a_i = p_i + 2k_i + i\epsilon_{im} p_m, \quad (2.54b)$$

$$b_i = 2p_i + k_i - i\epsilon_{im} k_m, \quad (2.54c)$$

$$c_i = k_i - p_i + i\epsilon_{im} (p_m + k_m), \quad (2.54d)$$

and

$$f(p_\perp, k_\perp) = \frac{1}{8|q_f B|} [p_m - k_m + i\epsilon_{mj} (p_j + k_j)]^2 - \frac{1}{2|q_f B|} (p_m^2 + k_m^2 + 2i\epsilon_{jm} p_m k_j). \quad (2.54e)$$

For details see Appendix D.

To obtain the invariant photon momentum distribution, the squared of Eq. (2.53) is required. Here, the three lightest flavors are considered. Moreover, in view of the tensor structure for the matrix elements, only a longitudinal polarization for the gluons and the photon needs to be evaluated. Thus, the process probability is given by

$$\sum_{\text{pol},f} |\widetilde{\mathcal{M}}|^2 = (2\pi)^4 \delta^{(4)}(q - k - p) \mathcal{V} \Delta\tau \sum_{\text{pol},f} |\mathcal{M}|^2, \quad (2.55)$$

where

$$\sum_{\text{pol},f} |\mathcal{M}|^2 = \frac{2\alpha_{\text{em}}\alpha_s^2 q_{\perp}^2}{\pi\omega_q^2} \sum_f q_f^2 (2\omega_p^2 + \omega_k^2 + \omega_p\omega_k) \exp \left\{ -\frac{q_{\perp}^2}{|q_f B| \omega_q^2} (\omega_p^2 + \omega_k^2 + \omega_p\omega_k) \right\}. \quad (2.56)$$

The factor $\mathcal{V} \Delta\tau$ represents the space-time volume where the reaction takes place, i.e., the overlap spatial region $\mathcal{V}(t)$ at time t and the time interval $\Delta\tau$ where the magnetic field can be taken as having a constant intensity $B(t)$. The full calculation is presented in Appendix E.

In order to write Eq. (2.56) which only depends on the photon momentum q_{\perp}^2 , the energy-momentum conservation for massless gluons and photons was implemented without considering the dispersive properties of the magnetized medium. A simple calculation of such conserved quantity implies that the gluons and the photon have parallel spatial momenta. Explicitly, this condition is taken as

$$\begin{aligned} p^{\mu} &= \omega_p(1, \hat{p}) = (\omega_p/\omega_q) q^{\mu}, \\ k^{\mu} &= \omega_k(1, \hat{k}) = (\omega_k/\omega_q) q^{\mu}, \end{aligned} \quad (2.57)$$

which can be relaxed if the magnetic mass acquired by the gluons is computed. This is the main motivation for the study of the Gluon Polarization Tensor presented in Chapter 3.

2.5.1 Photon invariant momentum distribution and elliptic flow

The magnetic invariant photon momentum distribution is easily computed from the probability amplitude above discussed. Explicitly, it is given by the expression:

$$\omega_q \frac{dN^{\text{mag}}}{d^3q} = \frac{\chi \mathcal{V} \tau_s}{2(2\pi)^3} \int \frac{d^3p}{(2\pi)^3 2\omega_p} \int \frac{d^3k}{(2\pi)^3 2\omega_k} n(\omega_p) n(\omega_k) (2\pi)^4 \delta^{(4)}(q - k - p) \sum_{\text{pol},f} |\mathcal{M}|^2, \quad (2.58)$$

where $n(\omega)$ represent the distribution of gluons obtained from the shattered *glasma*, and χ is a factor to account for the fact that the overlap region in a semicentral collision is not the full nuclear volume. At first approximation, the gluon distribution can be modeled as a Bose-Einstein-like number occupation, so that the temperature is replaced for the saturation energy scale Λ_s [254]:

$$n(\omega) = \frac{\kappa}{e^{\omega/\Lambda_s} - 1}. \quad (2.59)$$

Therefore, Eq. (2.58) gives (see Appendix E):

$$\begin{aligned} \frac{1}{2\pi\omega_q} \frac{dN^{\text{mag}}}{d\omega_q} &= \chi \mathcal{V} \Delta\tau \frac{\alpha_{\text{em}} \alpha_s^2 \pi}{2(2\pi)^6 \omega_q} \sum_f q_f^2 \int_0^{\omega_q} d\omega_p (2\omega_p^2 + \omega_q^2 - \omega_p \omega_q) e^{-g_f(\omega_p, \omega_q)} \\ &\times \left\{ I_0 [g_f(\omega_p, \omega_q)] - I_1 [g_f(\omega_p, \omega_q)] \right\} n(\omega_p) n(|\omega_q - \omega_p|), \end{aligned} \quad (2.60)$$

where I_0, I_1 are the modified Bessel function of the first kind, and

$$g_f(\omega_p, \omega_q) = \frac{\omega_p^2 + \omega_q^2 - \omega_p \omega_q}{2 |q_f B|}. \quad (2.61)$$

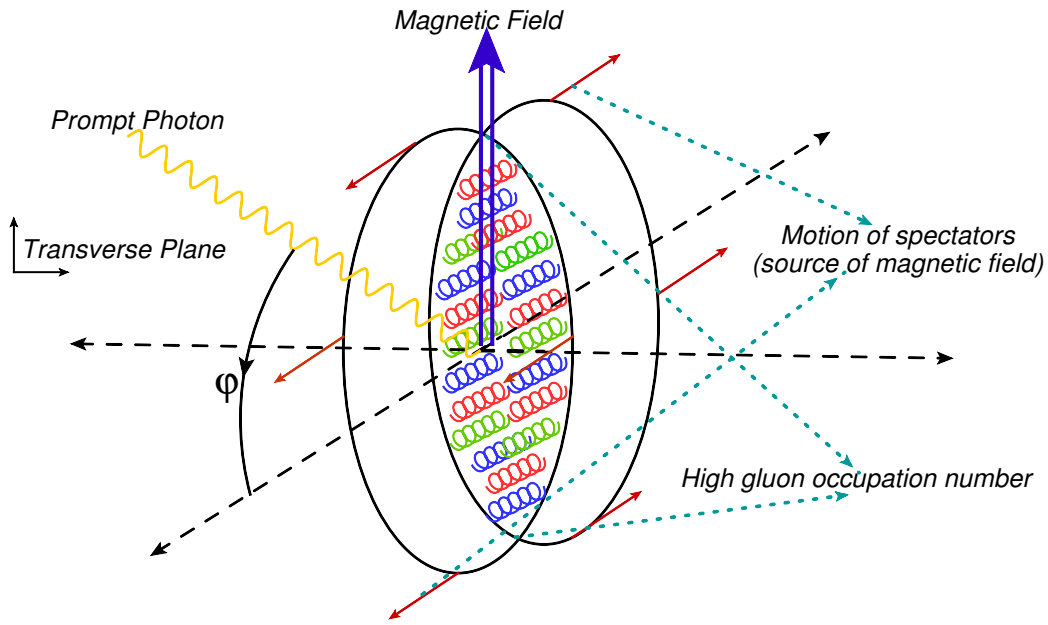


Figure 2.18: Geometry of the heavy-ion collision: The magnetic field lies on the transverse plane and the photon momentum q_{\perp} lies in the reaction plane.

The elliptic flow coefficient v_2 is obtained from the Fourier decomposition of Eq. (2.60). It is necessary to point out that the magnitude of the photon momentum q_{\perp} , which is transverse to the magnetic field is defined with the geometry presented in Fig. 2.18. Thus, azimuthal distribution with respect to the reaction plane is

$$\frac{dN^{\text{mag}}}{d\varphi} = \frac{N^{\text{mag}}}{2\pi} \left[1 + \sum_{n=1}^{\infty} 2v_n(\omega_q) \cos(n\varphi) \right], \quad (2.62)$$

where the total number of photons, N^{mag} , is given by

$$N^{\text{mag}} = \int d^3q \frac{dN^{\text{mag}}}{d^3q}. \quad (2.63)$$

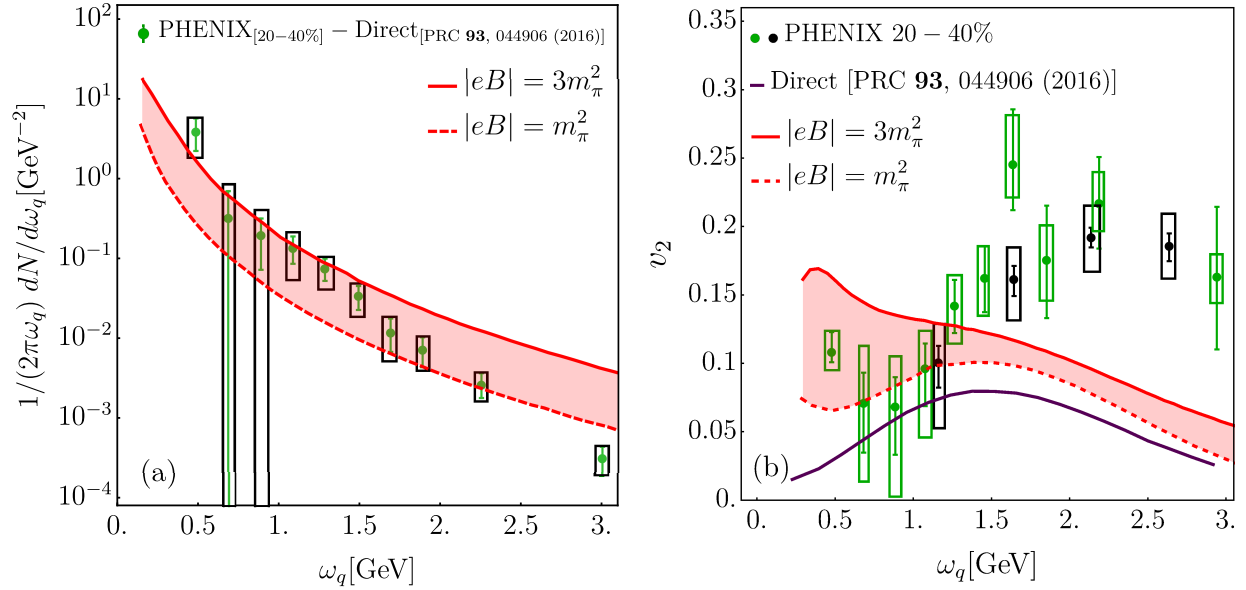


Figure 2.19: (a) Photon invariant momentum distribution obtained from Eq. (2.60) compared with the difference between the PHENIX data [64] and direct photons from Ref. [71]. (b) Harmonic coefficient v_2 computed from Eq. (2.65) compared with PHENIX data [65] and the elliptic flow of the direct photons from Ref. [71]. The green (black) points and errors are experimental measurements with the conversion (calorimeter) method. In both figures, the band shows variations of the parameter $|eB|$ within the indicated ranges.

The calculation of v_2 for a central rapidity can be found in Appendix E and its final expression is

$$\begin{aligned}
 v_2^{\text{mag}}(\omega_q) &= \chi \frac{\alpha_{\text{em}} \alpha_s^2 \pi \mathcal{V} \Delta \tau}{2(2\pi)^5 N_{\text{mag}}} \sum_f q_f^2 \int_0^{\omega_q} d\omega'_q \int_0^{\omega'_q} d\omega_p \left(2\omega_p^2 + \omega_q'^2 - \omega_p \omega_q' \right) e^{-g_f(\omega_p, \omega_q')} \\
 &\times \left\{ I_0 [g_f(\omega_p, \omega_q)] - \left[1 + \frac{1}{g_f(\omega_p, \omega_q)} \right] I_1 [g_f(\omega_p, \omega_q)] \right\} n(\omega_p) n(|\omega_q' - \omega_p|).
 \end{aligned} \tag{2.64}$$

The results for the photon production and elliptic flow are shown in Fig. 2.19. The plots are built as a function of the photon transverse momentum $q_\perp = \omega_q$, for central rapidity and the centrality range 20% – 40%. The value of parameters are: $\alpha_s = 0.3$, $\Lambda_s = 2 \text{ GeV}$, $\kappa = 3$, $\Delta \tau = 1.5 \text{ fm}$, $\chi = 0.8$, $\mathcal{V} = 4\pi R^2/3$, with $R = 7 \text{ fm}$ (corresponding to the Au nuclear radius), and the external magnetic field intensity is in the range $m_\pi^2 \leq |eB| \leq 3m_\pi^2$.

In Fig. 2.19(a) the photon invariant momentum distribution obtained from Eq. (2.60) is compared with the difference between the PHENIX and the direct photons of Ref. [71], therefore, the magnetic contribution has to be understood as an excess (missed photons) over calculations without magnetic field effects. As can be seen, the magnetic contribution helps to better describe the experimental data for intermediate and low energies, but for higher values of the photon

transverse moment. The latter can be attributed to a combination of the gluon distribution which does not contain a power like tail which is known to better describe the numerical solutions for this kind of distribution [255], and to the low momentum approximation $2|q_f B| \gg t_{\parallel}^2, s_{\parallel}^2, r_{\parallel}^2$.

On the other hand, Fig. 2.19(b) displays the harmonic flow coefficient v_2 for the same parameter configuration of the photon yield. To compare with experimental data, having as a baseline a state-of-the-art calculation accounting for many of the well-described sources of photons, it was taken into account that the v_2 is a weighted average given by

$$v_2(\omega_q) = \frac{\frac{dN^{\text{mag}}}{d\omega_q}(\omega_q)v_2^{\text{mag}}(\omega_q) + \frac{dN^{\text{direct}}}{d\omega_q}(\omega_q)v_2^{\text{direct}}(\omega_q)}{\frac{dN^{\text{mag}}}{d\omega_q}(\omega_q)v_2^{\text{mag}}(\omega_q) + \frac{dN^{\text{direct}}}{d\omega_q}(\omega_q)}, \quad (2.65)$$

where $N^{\text{direct}}(\omega_q)$ and $v_2^{\text{mag}}(\omega_q)$ are obtained from Ref. [71].

For low photon momenta, the magnetic contribution improves the harmonic flow description, so that, in comparison with the pure direct photon formalism (purple line), the addition of magnetic photons lies in the error bars reported by PHENIX. Moreover, for a magnetic field $|eB| \sim m_{\pi}^2$, there is a desirable functional behavior that reproduces the overall data distribution. The good fit together with the functional form can be explained from the fact that the existence of a magnetic field breaks the translational symmetry, thus, a preferential direction to elliptic flux is created. It cannot be expected that for higher photon energies the predictions are in agreement with the experiment, for the same reason discussed in the yield description: the simplified denominators of Eq. (2.52) and the absence of a tail for the gluon distribution preclude the possibility to get a correct description in that regime.

In a heavy-ion collision, the particle flow can be attributed to fluctuations in the internal fireball velocities [254, 256–258]. The sudden change of pressure in different directions between the interaction region and vacuum when the glasma is shattered is an important factor to take into account, therefore, in order to study the impact of its expansive effects, a flow velocity factor is introduced in the expression through

$$\omega_{p,k} \rightarrow (p, k) \cdot u, \quad (2.66a)$$

with a constant four-velocity given by

$$u^{\mu} = \gamma(1, \beta), \quad \gamma = \frac{1}{\sqrt{1 - \beta^2}}. \quad (2.66b)$$

Figure 2.20 displays the photon invariant momentum distribution and the harmonic coefficient v_2 when the flow velocity of Eq. (2) is considered with a value of $\beta=0.25$. The inclusion of this velocity shifts the momentum to higher energies and increases the response in the magnetic field dependence for both observables. Hence, lower magnetic fields can generate the same behavior with the inclusion of the velocity flow. As it was expected, the cases with and without flow cannot ensure the data description for high photon energies because of the simplifications named before.

It is necessary to point out that the results presented in Figs. 2.19 and 2.20 are obtained by considering qualitatively three fundamental scenarios in the proposed phenomenology: the magnetic

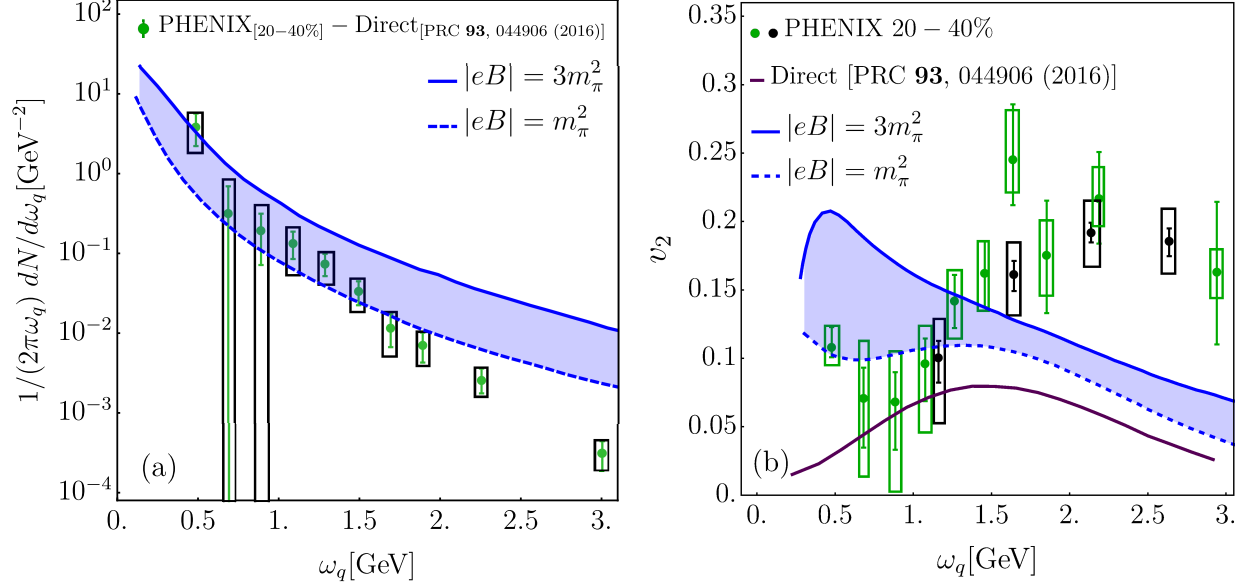


Figure 2.20: Impact of the flow velocity with $\beta = 0.25$ for (a) Photon invariant momentum distribution obtained from Eq. (2.60) compared with the difference between the PHENIX data [64] and direct photons from Ref. [71]. (b) Harmonic coefficient v_2 computed from Eq. (2.65) compared with PHENIX data [65] and the elliptic flow of the direct photons from Ref. [71]. The green (black) points and errors are measures with the conversion (calorimeter) method. In both figures, the band shows variations of the parameter $|eB|$ within the indicated ranges.

field is constant over all collision time, the space-temporal volume is assumed fixed and the centrality is not computed from first principles. Those assumptions allow having only a rough picture of the gluon fusion mechanism. In the next section, these issues are avoided by simulating computationally the heavy-ion collision, which gives the evolution in time and space of the magnetic field as well as the correct interaction volume and corresponding centrality.

Nevertheless, the prompt photon production by gluon fusion mediated by a magnetized medium seems to be a reasonable source of photon radiation to explain the discrepancy between the current calculations and the experimental measurements of the invariant momentum distribution. Certainly, to have a better picture and impact of the proposed mechanism, in particular, the v_2 tail at higher momenta, the energy scale restricted to a high magnetic field has to be relaxed, which implies to include the contribution of several Landau Levels. This is a work in process.

2.6 Centrality Dependence of the Photon Production by Gluon Fusion and Gluon Splitting in a Magnetized Medium

In this section, the centrality dependence of the photon production by the process $gg \rightarrow \gamma$ (gluon fusion) as well as the gluon splitting, i.e., $g \rightarrow g\gamma$ is presented. The latter comes from the

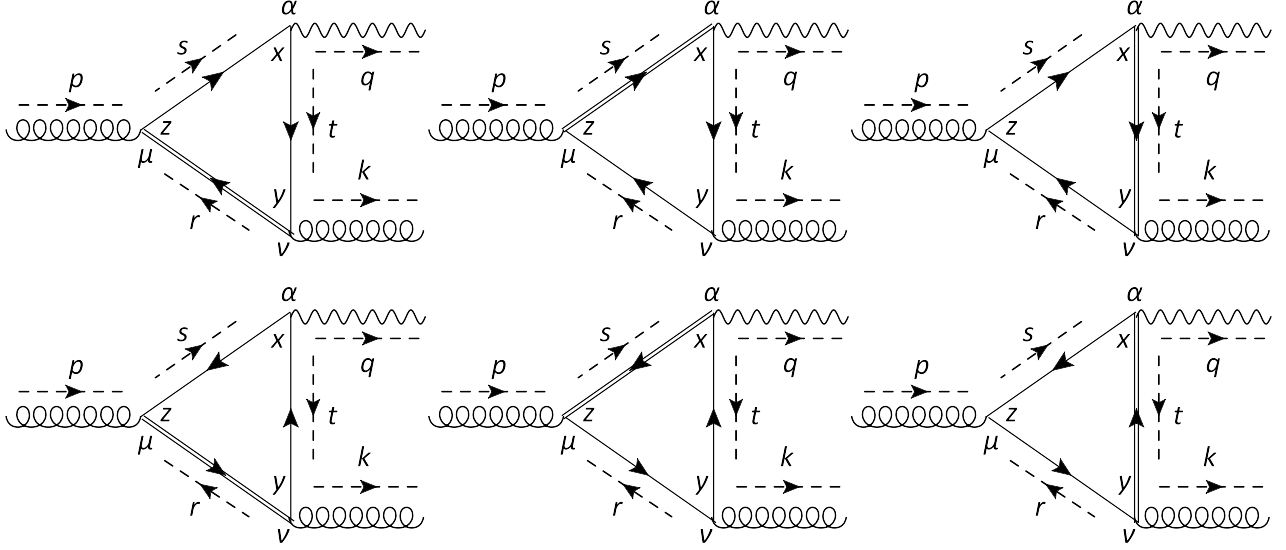


Figure 2.21: Feynman diagrams contributing to the process $g \rightarrow g\gamma$ in the presence of a magnetic field. The double lines represent that quark propagator in the 1LL, whereas the single lines represent the propagator in the LLL. The arrows in the propagators are the charge flow and the arrows on the sides represent the momentum direction.

fact that at order $\alpha_{\text{em}}\alpha_s^2$ this process has to be taken into account.

As was commented on the previous section, the results obtained from the gluon fusion in a magnetized medium can only give a rough description for the observables of interest, given that the centrality is modeled by a phenomenological parameter and the magnetic field evolution together with the space-temporal interaction volume were considered constant. Here, an estimate of the upper limit for the time evolution of the magnetic field intensity and the volume produced by the collision participants and spectators can be obtained, and therefore, a more realistic scenario can be achieved.

Figure 2.21 shows the Feynman diagrams which contribute to the process $g \rightarrow g\gamma$, at the same order in $|q_f B|$ than the process $gg \rightarrow \gamma$, namely, in the fermionic triangle two quarks are in the LLL and one in the 1LL.

2.6.1 Photon invariant momentum distribution and elliptic flow from gluon fusion and gluon splitting channels

By a direct application of Feynman rules it is evident that the matrix element $\mathcal{M}_{g \rightarrow g\gamma}$ is related to $\mathcal{M}_{gg \rightarrow \gamma}$ by the crossing symmetry

$$\mathcal{M}_{g \rightarrow g\gamma}(p, k, q) = \mathcal{M}_{gg \rightarrow \gamma}(p, -k, q), \quad (2.67)$$

where $\mathcal{M}_{gg \rightarrow \gamma}$ is given by Eq. (2.53).

To find the total photon invariant momentum distribution, both processes have to be squared, and after summing and averaging over the initial state and summing over the final state particle polarization and color, they have to be added. To do this, note that there aren't any diagrams which indicate interference between the pair of channels, therefore, they can be summed incoherently, obtaining

$$\overline{\sum_{c,p,f} |\widetilde{\mathcal{M}}|^2} = \mathcal{V} \Delta \tau (2\pi)^4 \overline{\sum_{c,p,f}} \left[\delta^{(4)}(q - k - p) |\mathcal{M}_{gg \rightarrow \gamma}|^2 + \delta^{(4)}(q + k - p) |\mathcal{M}_{g \rightarrow g\gamma}|^2 \right], \quad (2.68)$$

The energy-momentum conservation gives the same condition for the particle momenta of Eq. (2.57), thus, the observables can be computed in terms of the energy components ($\omega_p, \omega_k, \omega_q$) so that the three particles have parallel spatial-momentum. The invariant photon momentum distribution is given by

$$\omega_q \frac{dN^{\text{mag}}}{d^3q} = \frac{(2\pi)^4 \mathcal{V} \Delta \tau}{2(2\pi)^3} \int \frac{d^3p}{(2\pi)^3 2\omega_p} \int \frac{d^3k}{(2\pi)^3 2\omega_k} \left\{ \delta^{(4)}(q - k - p) n(\omega_k) \overline{\sum_{c,p,f}} |\mathcal{M}_{gg \rightarrow \gamma}|^2 + \delta^{(4)}(q + k - p) [1 + n(\omega_k)] \overline{\sum_{c,p,f}} |\mathcal{M}_{g \rightarrow g\gamma}|^2 \right\} n(\omega_p), \quad (2.69)$$

where the initial state gluon with energy ω_k comes weighed with an occupation factor $n(\omega_k)$, whereas the final state one comes weighed with an enhanced occupation factor $1 + n(\omega_k)$. Explicitly, the last equation reads

$$\begin{aligned} \frac{1}{2\pi\omega_q} \frac{dN^{\text{mag}}}{d\omega_q} &= \mathcal{V} \Delta \tau \frac{\alpha_{\text{em}} \alpha_s^2 \pi}{2(2\pi)^6 \omega_q} \sum_f q_f^2 \int_0^{\omega_q} d\omega_p (2\omega_p^2 + \omega_q^2 - \omega_p \omega_q) e^{-g_f(\omega_p, \omega_q)} \\ &\times \left\{ I_0 [g_f(\omega_p, \omega_q)] - I_1 [g_f(\omega_p, \omega_q)] \right\} \left\{ n(|\omega_q - \omega_p|) + [1 + n(|\omega_q - \omega_p|)] \right\} n(\omega_p), \end{aligned} \quad (2.70)$$

where $g_f(\omega_p, \omega_q)$ is given in Eq. (2.61). The deduction of Eq. (2.70) is presented in Appendix F. Moreover, the expression for the total v_2 can be found and reads

$$\begin{aligned} v_2^{\text{mag}}(\omega_q) &= \frac{\alpha_{\text{em}} \alpha_s^2 \pi \mathcal{V} \Delta \tau}{2(2\pi)^5 N^{\text{mag}}} \sum_f q_f^2 \int_0^{\omega_q} d\omega'_q \int_0^{\omega'_q} d\omega_p (2\omega_p^2 + \omega_q'^2 - \omega_p \omega_q') e^{-g_f(\omega)} \\ &\times \left\{ I_0 [g_f(\omega)] - \left[1 + \frac{1}{g_f(\omega)} \right] I_1 [g_f(\omega)] \right\} \left\{ n(|\omega'_q - \omega_p|) + [1 + n(|\omega'_q - \omega_p|)] \right\} n(\omega_p), \end{aligned} \quad (2.71)$$

with $g_f(\omega) = g_f(\omega_p, \omega'_q)$.

2.6.2 Magnetic Field Strength and Space Time Volume from UrQMD

The UrQMD is a microscopic model that simulates ultra-relativistic heavy-ion collisions in the energy range from 100 MeV to 200 GeV [259, 260]. The model has integrated a Monte Carlo

simulation package for $p + p$, $p + A$ and $A + A$ interactions.

In general terms, the model solves a large set of coupled integro-differential equations for the time-evolution of the phase-space densities $f_i(x, p)$, where x and p represents the classical position and momentum of the i -th particle specie (N, Λ, Δ , etc). The density f_i is assumed to satisfy a non-relativistic Boltzmann equation:

$$\frac{df_i(x, p)}{dt} = \frac{\partial p}{\partial t} \frac{\partial f_i(x, p)}{\partial p} + \frac{\partial x}{\partial t} \frac{\partial f_i(x, p)}{\partial x} + \frac{\partial f_i(x, p)}{\partial t} = \mathbf{St}f_i(x, p) \quad (2.72)$$

where $\mathbf{St}f_i(x, p)$ represents the collision term or particle source which connects the species i and j . Such terms contains information of covariant propagation hadrons on classical trajectories, stochastic binary scatterings, color string formation and resonance decays.

For $A + A$ collisions, the model considers binary and ternary interactions by taking into account the real part of the in-medium G-matrix, which includes a non-relativistic density-dependent Skyrme-type potential given by

$$V = \frac{1}{2!} t_1 \sum_{i \neq j} \delta(\mathbf{x}_i - \mathbf{x}_j) + \frac{1}{3!} t_2 \sum_{i \neq j \neq k} \delta(\mathbf{x}_i - \mathbf{x}_j) \delta(\mathbf{x}_j - \mathbf{x}_k), \quad (2.73)$$

as well as Coulomb and Yukawa interactions for more than fifty baryon species and five meson nonets (45 mesons). Moreover, the exchange of electric and baryonic charge, strangeness and four momentum is included for baryon-baryon collisions at low energies in the t -channel. The meson-baryon and the meson-meson interactions appears when $\sqrt{s} > 3$ GeV through formation and decay of resonances in the s -channel, whereas the t -channel for meson-baryon and meson-meson are explicitly given above $\sqrt{s} = 6$ GeV. The anti-particles are implemented by the charge conjugation which ensures baryon-antibaryon symmetry.

The cross-sections enter as a pure geometrical input: if b is the impact parameter of two hadrons, the collision will occurs if $b < \sqrt{\sigma_{\text{tot}}/\pi}$, where σ_{tot} is the total cross-section for both hadrons, which depends on the isospins of colliding particles, their flavor and the center of mass energy. Such total and elastic cross-sections are modeled (above of the resonance energy $p_{\text{lab}} > 2$ GeV/c) by parameters of the CERN-HERA fit, given by

$$\sigma_{\text{tot,el}}(p) = A + Bp^n + C \ln^2 p + D \ln p, \quad (2.74)$$

where p is the laboratory momentum [261]. If there are no experimental data to give a reasonable fit for the cross-sections, the additive quark model and detailed balance arguments are used to extrapolate such functions. Figure 2.22 shows the several stages of a heavy-ion collision simulated with UrQMD. As can it noticed, the Lorentz contraction of both nuclei is taken into account, as well as the color string formation, centrality (nucleons which do not collide), and the hadronic final states.

For the present work, the UrQMD was used to compute the space-time evolution of the interaction volume and the magnetic field strength by varying the centrality class and the colliding species. This procedure allows performing a systematic study of the photon excess coming from gluon fusion and splitting with a better estimate of the space-time volume $\mathcal{V}\Delta\tau$ and the time

profile for the magnetic field which consist to an improvement to the results presented in the last section.

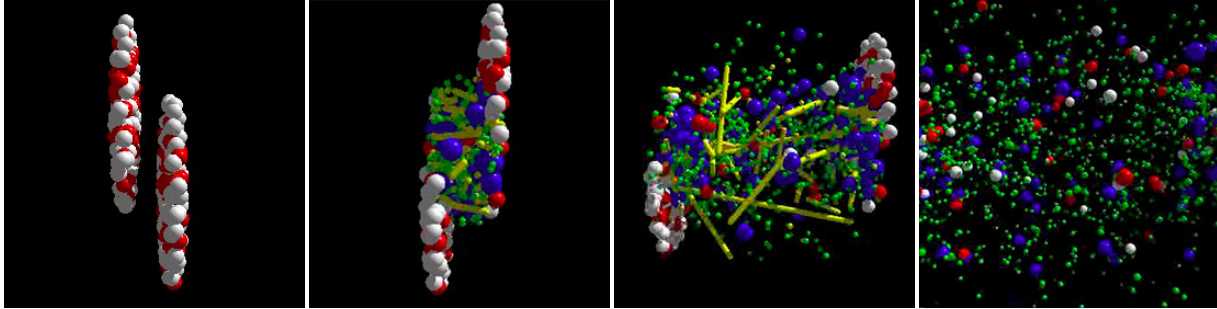


Figure 2.22: Stages of a UrQMD simulation for a Pb+Pb collision at CERN/SPS energies.

First, the magnetic field is computed event-by-event at the point \mathbf{x} at time t by using the Linaard-Wiechert potential generated by non-accelerated charges moving along the beam direction, namely

$$e\mathbf{B}(\mathbf{x}, t) = \alpha_{em} \sum_j \frac{(1 - v_j^2) \mathbf{v}_j \times \mathbf{R}_j}{R_j^3 \left[1 - \frac{(\mathbf{v}_j \times \mathbf{R}_j)^2}{R_j^2} \right]^{3/2}}, \quad (2.75)$$

where $\mathbf{R}_j = \mathbf{x} - \mathbf{x}_j(t)$, $\mathbf{x}_j(t)$ is the position of the j -th charge moving with velocity \mathbf{v}_j , R_j is the magnitude of \mathbf{R}_j and the sum runs over charged particles in each event [262]. The charges which produce the magnetic field are classified into two categories: participants and spectators. The former is defined as the number of nucleons that undergo at least one collision, and therefore, nucleons that do not participate in any collision and travel undeflected close to the beam direction, are defined as spectators. Furthermore, the centrality is defined as the fraction of the geometrical cross-section that overlaps for a given impact parameter b . This quantity is proportional to b^2/R_A^2 , where R_A is the radii of the nucleus that collide.

Figure 2.23 shows the magnetic field strength at the center of the interaction region, i.e., $\mathbf{x} = 0$, produced by the spectators [(a), (c), (e)] and participants + spectators [(b), (d), (f)] for different centrality classes in an Au-Au reaction for $\sqrt{s_{NN}} = 200$ GeV. As it was expected, central collisions (0 – 20%) have fewer spectators, therefore, in comparison with the peripheral classes, the magnetic field produced reach lower values. Moreover, the UrQMD allows calculating the spatial components for the magnetic field, being $|eB|_x$ and $(|eB|_y, |eB|_z)$ the parallel and perpendicular directions with respect to the collision axis., respectively.

The results are in agreement with the fact that in the beam-direction the magnetic field has to be small whereas its magnitude should be appreciable for the other components. Figures 2.23 (a), (c), (e) implies that in peripheral collisions the magnetic field is predominantly oriented at the z -direction, but for central ones, it has a comparable component at the y -axis. This will impact on the observable description, given that the calculation assumes a magnetic field in one preferential direction.

In contrast to the field generated by the spectators, in Figs. 2.23 (b), (d), (f) it can be seen the

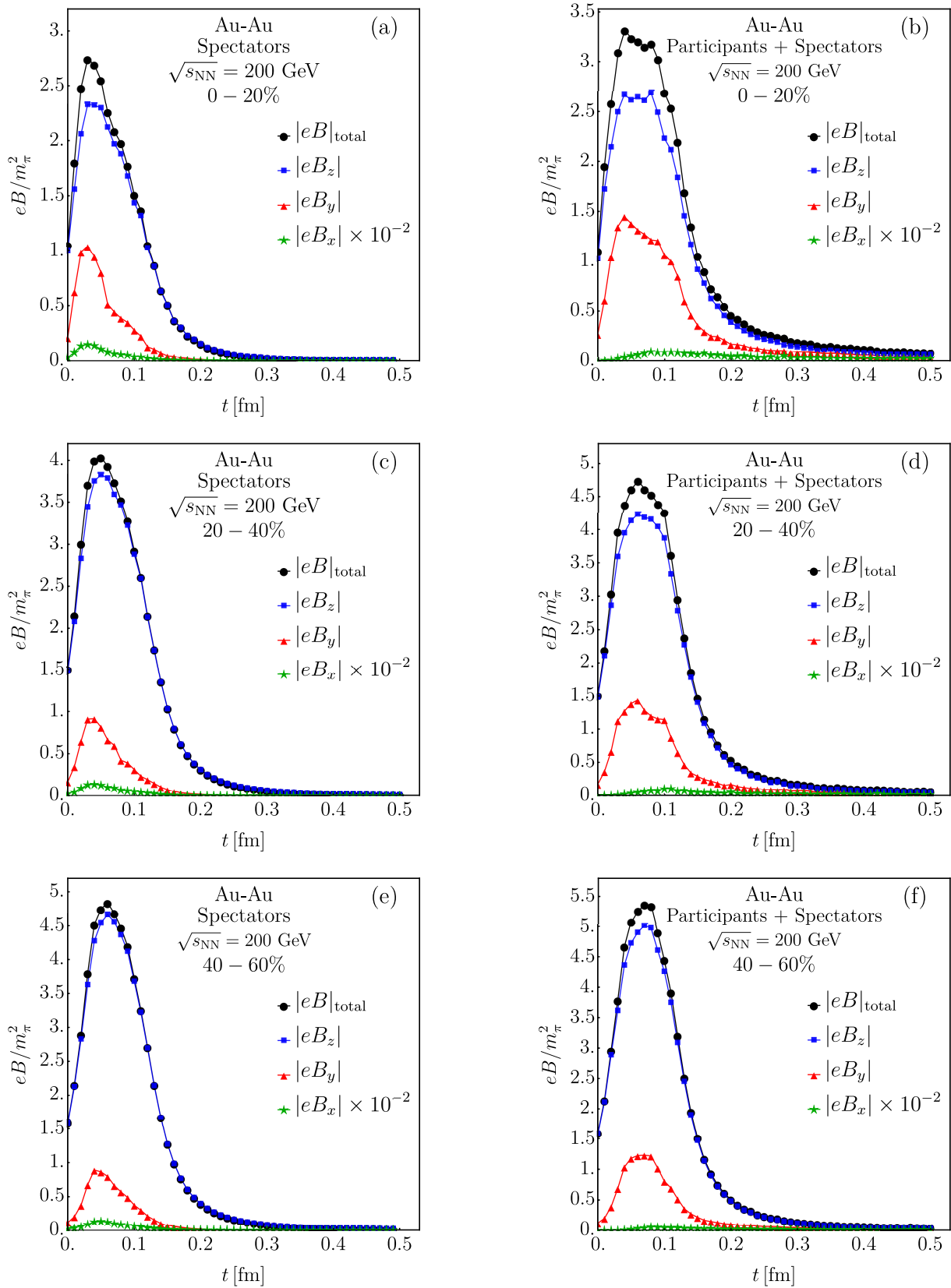


Figure 2.23: Magnetic field strength for directions parallel (\hat{x}) and perpendicular (\hat{y}, \hat{z}) to the collision axis for three centrality classes in an Au-Au reaction. The magnetic field is produced by spectators [(a), (c), (e)] and participants + spectators [(b), (d), (f)].

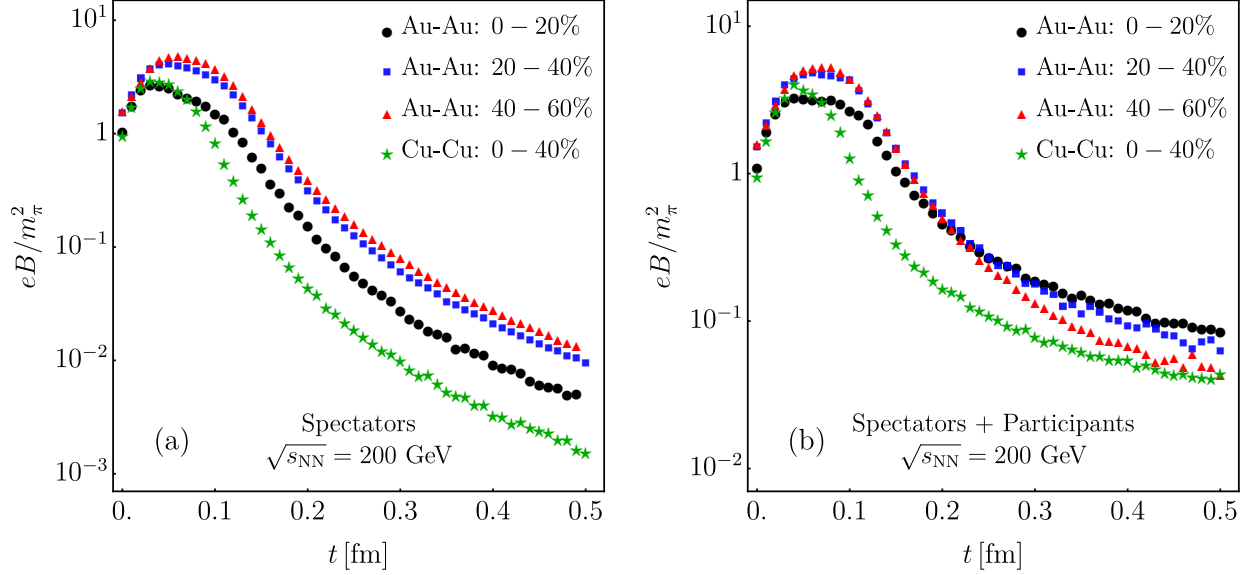


Figure 2.24: Magnetic field intensity in units of pion mass squared (m_π^2) at the center of the interaction region ($\mathbf{x} = 0$) for several centrality classes and two colliding species with $\sqrt{s_{NN}} = 200$ GeV. The magnetic field is assumed to be produced by (a) spectators and (b) spectators + participants.

magnetic field strength created by spectators and participants at $\mathbf{x} = 0$. Although in peripheral collisions the main contribution is still in the z -direction, the peak of intensity has an appreciable contribution in the y -axis. Thus, it can be expected deviations in the yield or the harmonic coefficient when the model takes into account both sources.

To complete the panorama and contrast it with the field produced by other colliding species, Fig. 2.24 shows the total magnetic field produced by Au-Au collisions at different centralities, compared with Cu-Cu simulations with a centrality of 0 – 40%, at $\sqrt{s_{NN}} = 200$ GeV. In agreement with the previous results, peripheral collisions imply a higher magnetic field, so much for participants in Fig. 2.24(a) as well as for participants and spectators in Fig. 2.24(b). Furthermore, the fact that in Cu-Cu collisions the magnetic field is understood in terms of the number of charges which can be spectators or participants: copper has 29 protons whereas gold has 79. Nevertheless, the considered centrality class produces a similar average field strength for the former compared to the latter for the most central collisions.

As it was commented on Sec. 2.4, a fundamental characteristic of the magnetic field in heavy-ion collisions is its short duration. As can be inferred from Figs. 2.23 and 2.24, the magnetic pulse is short-lived and it disappears around $t \sim 0.3$ fm. This means that possible thermal effects, implied by hydrodynamical simulations, start on average after the time interval when the magnetic pulse is important. Hence, this window of time allows calculating the interaction volume where the magnetic effects are relevant. Such volume is computed with the formula:

$$\mathcal{V}(t) = 2t\pi r_A^2 \left(\frac{N_{\text{part}}}{2N} \right)^{2/3}, \quad (2.76)$$

which corresponds to two times the volume of a cylinder with a circular basis of radius r_A and

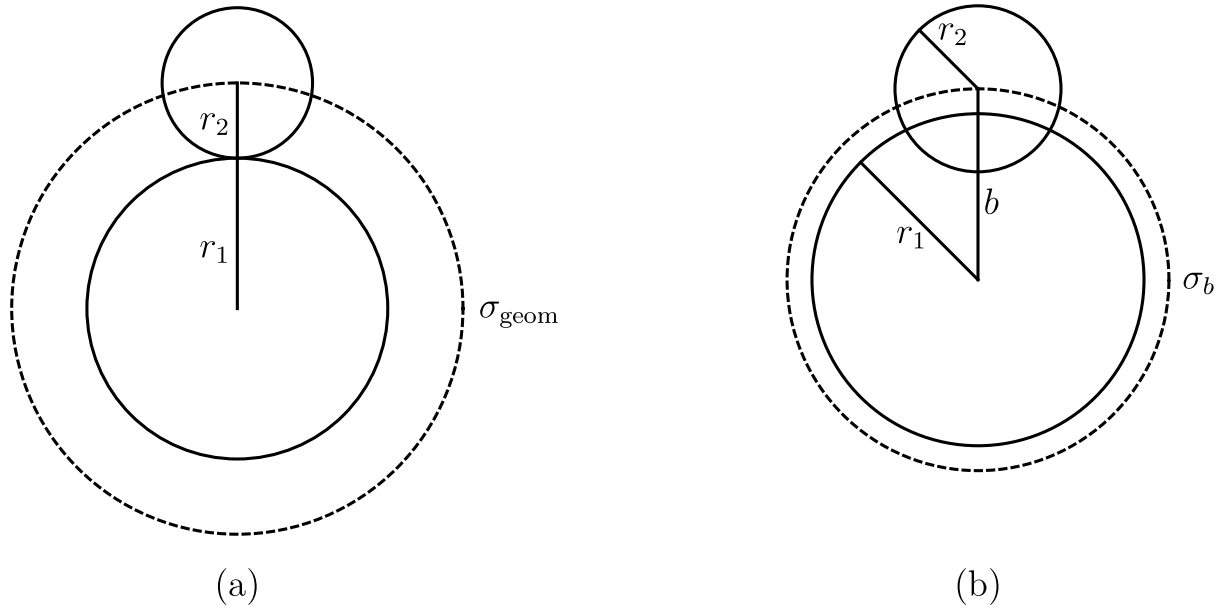


Figure 2.25: Cross-sections (dashed lines) for two colliding nuclei of radii r_1 and r_2 in (a) a maximal peripheral collision (*geometrical cross-section*), and (b) a peripheral collision with impact parameter b .

height t (the time of the magnetic pulse duration). The last term accounts for the overlap area in the collision region and can be justified by considering the cross-sections from Fig. 2.25: (a) the geometric cross-section σ_{geom} , defined as the area of the circle with radius $r_1 + r_2$ in a maximum peripheral collision, and (b) the cross-section σ_b for a peripheral collision with impact parameter b [263]. Such a fraction reads:

$$f = \frac{\sigma_b}{\sigma_{\text{geom}}} = \frac{\pi b^2}{\pi (r_1 + r_2)^2}. \quad (2.77)$$

If the colliding nuclei are of the same species, then $r_1 = r_2 = R$, and by assuming that σ_b describes an effective nucleus of radius b , the relation of the nuclear radius $r = r_0 N^{1/3}$, whith N is the number of nucleons per ion and $r_0 \approx 1.25$ fm, yields

$$f = \left(\frac{b}{2R} \right)^2 = \left(\frac{N_{\text{part}}}{2N} \right)^{2/3}, \quad (2.78)$$

where it was assumed that the effective nucleus has a number of particles that participate in the collision given by N_{part} . A more detailed analysis can be performed in order to get a better estimate of f , in terms of the nuclear overlap integral and generalizations of the geometric cross-section [264].

Figure 2.26(a) shows the number of participants N_{part} as a function of the collision time, obtained from UrQMD simulations for Au-Au collisions for the centrality classes 0-20%, 20-40% and 40-60%, and for Cu-Cu collisions with centrality 0-40% at $\sqrt{s_{\text{NN}}} = 200$ GeV. As was expected, central collisions (0-20%) have a higher number of participants than peripheral ones (40-60%),

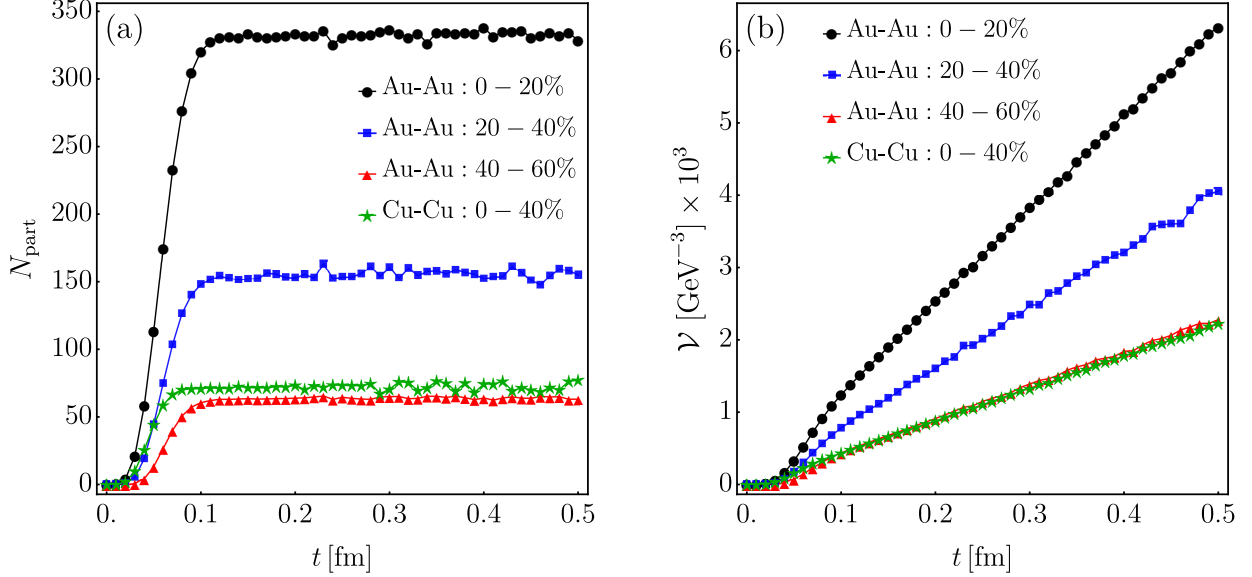


Figure 2.26: (a) Number of participants as function of the time for Au-Au and Cu-Cu collisions in different centrality classes. (b) Interaction volume eAu-Au and Cu-Cu collisions in different centrality classes. Both results are obtained by considering $\sqrt{s_{\text{NN}}} = 200$ GeV.

and the number of particles that participates of at least one collision suddenly increases from zero (at the beginning of the collision) to a certain value in which such number saturates.

The time evolution of the interaction volume \mathcal{V} computed from Eq. (2.76) is shown in Fig. 2.26(b) for the same centrality classes and energy of Fig. 2.26(a). A linear increase of \mathcal{V} as a function of t is expected from Eq. (2.76) so that the slope is related to the number of participants, which has a step-function form. Interestingly, although Cu ions are smaller than Au nuclei, peripheral Cu-Cu reactions in the range of 0-40% have basically the same interacting volume that Au-Au collisions in a region of smaller centrality. The impact of the magnetic field and volume on the photon invariant momentum distribution and the elliptic flow coefficient is presented in the next section.

2.6.3 Photon Invariant Distribution and Harmonic Coefficient with UrQMD simulations

In order to compute the invariant momentum distribution and the elliptic flow from the processes $gg \rightarrow \gamma$ and $g \rightarrow g\gamma$, UrQMD results for the magnetic field and interaction volume (centrality) were included into the phenomenology described by Eqs. (2.70) and (2.71). The rest of the parameters are chosen as follows: $\alpha_s = 0.3$, $\Lambda_s = 2$ GeV, and $\eta = 3$. Figure 2.27 shows the invariant momentum distribution and for Au+Au collisions at $\sqrt{s_{\text{NN}}} = 200$ GeV in the 0-20%, 20-40% and 40-60% centrality ranges and Cu+Cu collisions in the 0-40% centrality range at the same energy. The magnetic field contribution is assumed to be generated by (a)spectators and (b) spectators + participants.

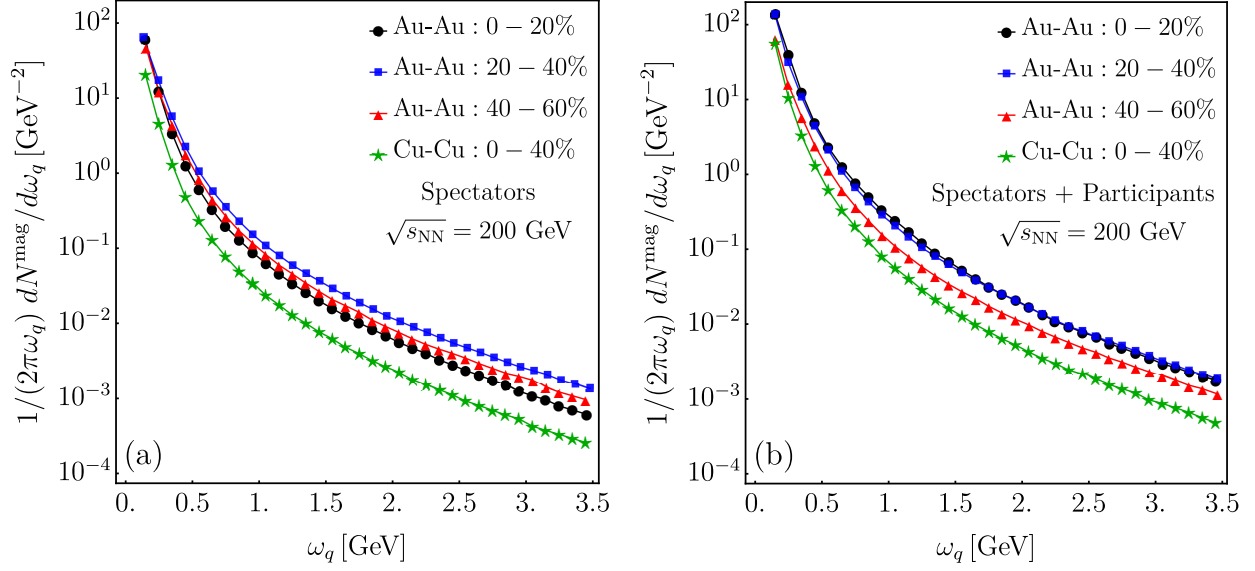


Figure 2.27: Invariant momentum distribution Au+Au collisions in the 0-20%, 20-40% and 40-60% centrality classes and Cu+Cu collisions in the 0-40% centrality class at $\sqrt{s_{\text{NN}}} = 200$ GeV considering the magnetic field generated by (a) participants and (b) participants and spectators.

The total photon yield is calculated by adding the yields for all time intervals within $\Delta\tau$, i.e., if $\Delta\tau$ is divided in small intervals of size Δt_i , the final output is given by

$$\frac{dN^{\text{mag}}}{d\omega_q} = \sum_{i=1} \left[\frac{dN^{\text{mag}}}{d\omega_q} \right]_i, \quad (2.79)$$

where $\left[\frac{dN^{\text{mag}}}{d\omega_q} \right]_i$ is the yield corresponding to the i th-time interval Δt_i (0.01 fm), computed from Eq. (2.60). The results confirm that a higher magnetic field intensity implies an enhancement of photon production. Nevertheless, despite the result of Eq. (2.60) which indicates that the volume and centrality implies a hierarchy between the momentum distribution with different centrality classes, that is to say, less \mathcal{V} and χ give small number of photons, Figs. 2.27(a) and 2.27(b) do not reflect such behavior. This can be understood from the fact that the integration volume has an opposite effect in centrality classes in with respect to the magnetic field. Therefore, the combination of both effects does not show a monotonically increasing (or decreasing) yield when the centrality is changed. Moreover, even when the Cu-Cu collisions has less interaction volume than Au-Au, the similarity between their magnetic fields (Fig. 2.24), N_{part} and \mathcal{V} (Fig. 2.26) make the photon production to be of the same order for the two species.

Figure 2.28 displays the pure magnetic contribution to the harmonic coefficient v_2 , for Au+Au collisions in the 0-20%, 20-40% and 40-60% centrality classes and Cu+Cu collisions in the 0-40% centrality class at $\sqrt{s_{\text{NN}}} = 200$ GeV. As it was previously mentioned, the elliptic flow needs to be considered as a weighted average. In that way, by accounting the time-variation of the yield,

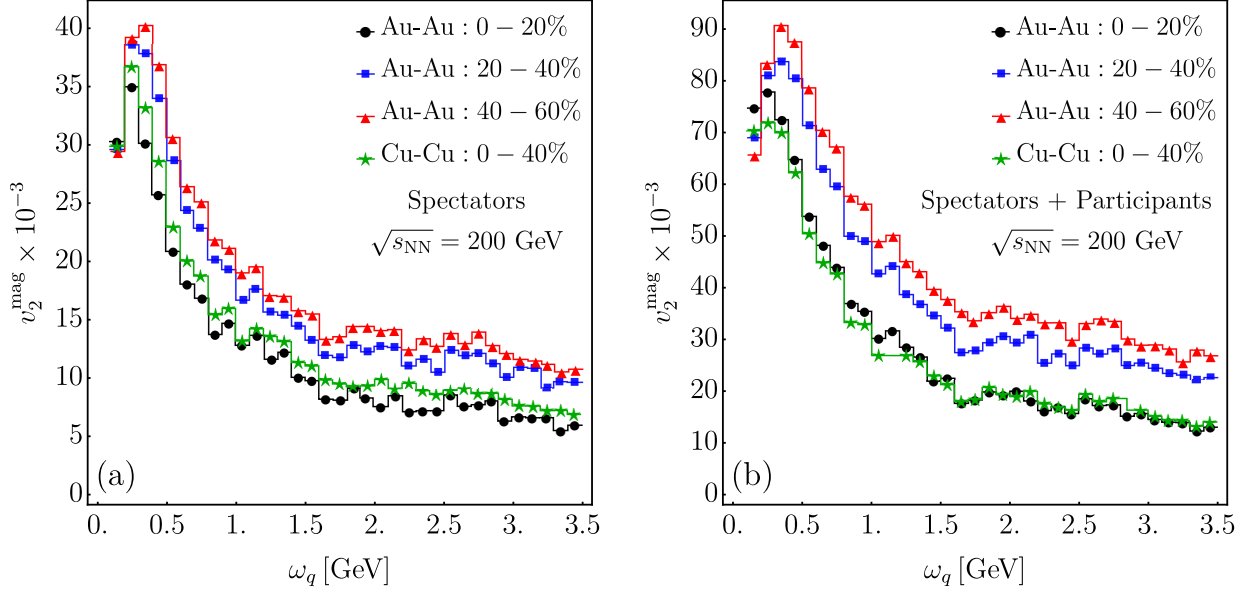


Figure 2.28: Harmonic coefficient v_2^{mag} for Au+Au collisions in the 0-20%, 20-40% and 40-60% centrality classes and Cu+Cu collisions in the 0-40% centrality class at $\sqrt{s_{\text{NN}}} = 200$ GeV considering the magnetic field generated by (a) participants and (b) participants and spectators.

the elliptic flow takes the form

$$v_2^{\text{mag}}(\omega_q) = \frac{\sum_{i=1} \left[\frac{dN^{\text{mag}}}{d\omega_q}(\omega_q) \right]_i [v_2^{\text{mag}}(\omega_q)]_i}{\sum_{i=1} \left[\frac{dN^{\text{mag}}}{d\omega_q} \right]_i} \quad (2.80)$$

where $[v_2^{\text{mag}}(\omega_q)]_i$ is the harmonic coefficient corresponding to the i th-time interval $\Delta\tau_i$, given by Eq. (2.64). Notice that including the contribution to the magnetic field strength coming from the spectators and participants, produces an increase of $[v_2^{\text{mag}}(\omega_q)]$. Here, the hierarchy between centrality classes at least for Au-Au collisions is clear, but in comparison with Cu-Cu simulations, there is still a non-direct relation between centrality and the curve height. Again, it can be argued that this effect comes from internal competitions among the parameters in each time interval.

2.6.4 Comparison with PHENIX data

Figure 2.29 shows the difference between PHENIX data [64, 265] and the hydrodynamical calculation of Ref. [71] compared to invariant yield produced by the processes $gg \rightarrow \gamma$ and $g \rightarrow g\gamma$ considering the contribution to the magnetic field strength produced by the spectators and spectators+participants in Au-Au collisions at $\sqrt{s_{\text{NN}}} = 200$ GeV for (a) the 0-20% and (b) the 20-40% centrality classes.

It can be noticed that when considering the magnetic field produced only by spectators the theoretical yield compares better to peripheral than to central collisions. In fact, for peripheral

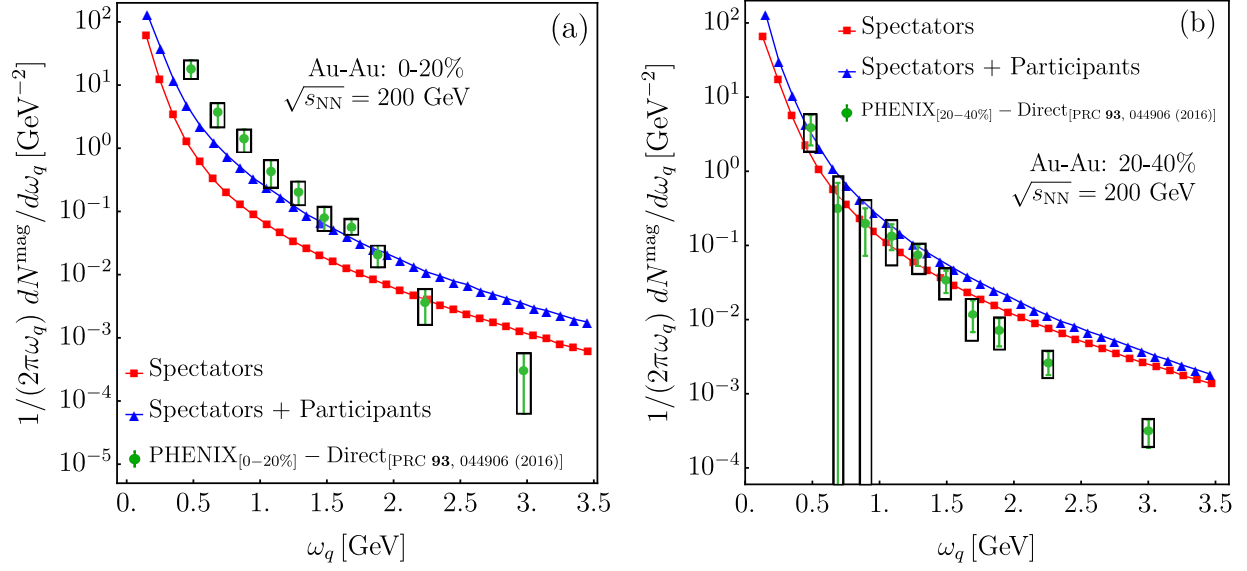


Figure 2.29: Difference between PHENIX data [64, 265] and the hydrodynamical calculation of Ref. [71] for Au-Au collisions at $\sqrt{s_{NN}} = 200$ GeV compared to the calculation of the invariant yield considering contribution to the magnetic field strength produced by the spectators, and spectators + participants for (a) the 0-20% and (b) 20-40% centrality classes.

collisions, both scenarios of magnetic field generation (spectators and spectators+participants) give a better data description. Such behavior comes from the orientation and intensity of the total magnetic field in that kind of reactions, which is predominantly aligned to the z -axis for non-central simulations [Figs. 2.23(c) and (d)], but has an important component in the y -axis when the centrality is recovered [Fig. 2.23(a)]. Additionally, the magnitude of the magnetic field produced in central collisions at the transverse plane direction is lower than the produced in the peripheral reactions. Then, the theoretical assumption for the present calculation, $\mathbf{B} = B\hat{z}$, and the hierarchy of the energy scales are not well justified for all the centrality classes. Moreover, as can be seen from Fig. 2.23 if only the spectators magnetic field is considered, the named approximation is accurate.

Figure 2.30 shows v_2 as a weighted average accounting for the magnetic and direct photons:

$$v_2(\omega_q) = \frac{\sum_{i=1}^m \left[\frac{dN}{d\omega_q} \right]_i [v_2^{\text{mag}}(\omega_q)]_i + \frac{dN^{\text{direct}}}{d\omega_q}(\omega_q) v_2^{\text{direct}}(\omega_q)}{\sum_{i=1}^m \left[\frac{dN}{d\omega_q} \right]_i + \frac{dN^{\text{direct}}}{d\omega_q}(\omega_q)}, \quad (2.81)$$

where $dN^{\text{direct}}/d\omega_q$ and v_2^{direct} are the (ω_q -dependent) spectrum and second harmonic coefficient of direct photons from Ref. [65], respectively, compared to the experimental data for Au+Au collisions at $\sqrt{s_{NN}} = 200$ GeV in the 20-40% centrality class from Ref. [265].

For the sake of completeness, the magnetic field generated by both spectators and participants+spectators is also shown. Notice that the magnetic field contribution improves the agreement with experimental data for the low part of the spectrum helping to describe the rise of v_2 as the photon energy decreases. The results indicate that a magnetic field created by participants+spectators are far from the central value of the experimental data, but it gives a better

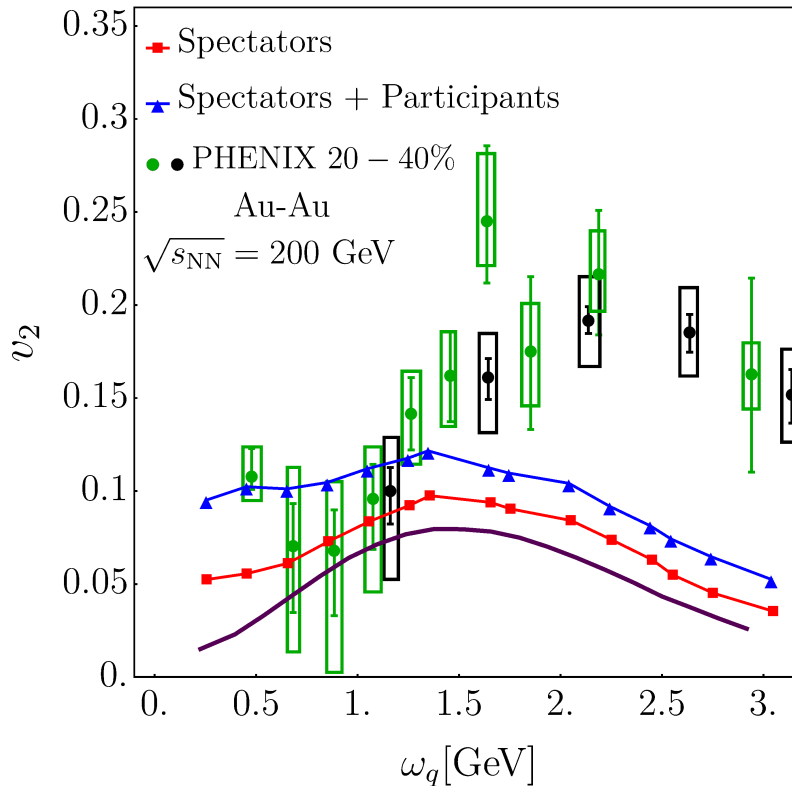


Figure 2.30: Harmonic coefficient v_2 computed from Eq. (2.81) compared with PHENIX data [65] and the elliptic flow of the direct photons from Ref. [71]. The green (black) points and errors are experimental measurements with the conversion (calorimeter) method corresponding to Au+Au collisions at $\sqrt{s_{NN}} = 200$ GeV in the 20-40% centrality class. The red (blue) curve takes into account the magnetic elliptic flow when the field is generated by the spectators (spectators+participants).

description of most data points at low transverse momentum. As it was mentioned in Sec. 2.5, the model cannot reproduce the data at higher photon energies, given that the formalism in the presented form assumes that the magnetic field is the dominant energy scale. Nonetheless, the addition of processes driven by magnetic fields allows enhancing the hydrodynamical predictions. The current calculations can be improved by relaxing the named approximation and by considering an arbitrary direction of the magnetic field as well as a better glasma occupation function.

2.7 Conclusion

In this chapter, the photon production from gluon fusion and gluon splitting was proposed as a magnetic-field driven channel to improve the current state-of-art of the so-called *photon puzzle* presented in Sec. 2.2. The collision's early stages provide the phenomenology, which allows proposing such a mechanism: as it was exposed in Sec. 2.3, the ultra-relativistic limit reached

by the colliding ions implies that gluons dominate the parton distribution function inside the constituent hadrons. Such gluons with small longitudinal momentum fractions (high-energy regime) are promoted to the mass-shell by processes involving larger virtualities. Therefore, a perturbative analysis of real particles is allowed. Moreover, as shown in Sec. 2.4, the production of intense magnetic fields at the beginning of the collision makes the Color Glass Condensate a strongly magnetized medium. The scales associated with the production of a large number of small momentum gluons coming from the shattering of the glasma. Additionally, a magnetic field's existence gives an initial asymmetry that evolves to an azimuthal anisotropy encoded in an appreciable elliptic flow at low photon momenta.

By working to lowest order in perturbation theory, the channels presented in Figs. 2.17 and 2.21, together with the assumption that in a strong magnetic field, the virtual quarks remain in the lowest and first-excited Landau levels, the probability amplitude of each process is computed analytically. It is worth to mention that the magnetic field is chosen as the dominant energy scale so that the approximation $2|q_f B| \gg t_{\parallel}^2, s_{\parallel}^2, r_{\parallel}^2$ is applied. The invariant momentum distribution and the elliptic flow were computed so that the former has to be understood as a yield over the hydrodynamical calculations, and the latter is an average-weighted term.

In the first approximation, the magnetic field and the reaction volume were taken as constants, and an external parameter introduces the centrality. Figure 2.19 shows that photons coming from the gluon fusion improve the hydrodynamic's framework's theoretical predictions considerably (within the error bar uncertainties). If a flow velocity factor is introduced in order to account for the medium expansion, the agreement with the experimental data becomes better, as shown in Fig.2.20. However, given the strong-field approximation, the theoretical curve falls to describe the data above $p_{\perp} > 1$ GeV. That may be because the gluon distribution does not contain a power-like tail, which is known better to define the numerical solutions for this kind of distribution.

In order to obtain predictions in a more realistic scenario, in Sec. 2.6, the space-time evolution of the magnetic field, the reaction volume, and their centrality dependence were simulated with the UrQMD model. Additionally, the gluon splitting mechanism is added to the gluon fusion, given that such diagrams belong to the same order in perturbation theory. As it was expected, the simulated magnetic field is found to be a magnitude around $1m_{\pi}^2 \lesssim |q_f B| \lesssim 4m_{\pi}^2$, and a lifetime around 0.2 fm. The centrality and the colliding species are fundamental to the magnetic field's strength and the number of participants, as Figs. 2.23 and 2.26 suggest. The results of Figs. 2.29 and 2.30 show again an agreement for the lower part of the spectra, and it is better for peripheral collisions. The comparison improves when the magnetic field strength includes the contribution of both spectators and participants. Hence, the magnetic field-driven photon emission for a magnetized and dense glasma appears to be an excellent candidate for better explaining the experimental data within a clear and well-accepted phenomenology.

At this point, it is necessary to mention that the presented calculation still has to be improved. First, the gluon occupation number may depend on the space-temporal coordinates and have a functional form beyond a simple Bose-Einstein like statistics. Moreover, the approximation fails when considering a magnetic field with constant orientation: the UrQMD simulations show a non-negligible magnetic field contribution at other directions for some centralities. Also, the

condition $2|q_f B| \gg t_{\parallel}^2, s_{\parallel}^2, r_{\parallel}^2$ have to be relaxed to calculate the matrix elements. Those improvements are being currently explored and will be reported elsewhere.

“Is the purpose of theoretical physics to be no more than a cataloging of all the things that can happen when particles interact with each other and separate? Or is it to be an understanding at a deeper level in which there are things that are not directly observable (as the underlying quantized fields are) but in terms of which we shall have a more fundamental understanding?”

– Julian Schwinger

Chapter 3

Gluon Polarization Tensor in Magnetized and Thermomagnetic Media

In the last chapter, the photon production from gluon fusion and gluon splitting in a magnetized medium seems essential to improve the experimental data. The core of such a description is the virtual quarks interaction with the external magnetic field, which opens the particle production channel. From that point of view, before a gluon fuses or splits, such particles can be strongly affected by the magnetic field since virtual quarks can drive processes with a single initial and final gluon. In particular, the self-energy or polarization tensor leads to modifications in the dispersion relation. The existence of a magnetic mass breaks the usual mass-shell condition, which is crucial for the analytic calculation of the probability amplitude. Moreover, the validity of Eq. (2.57) which ensures that the three-momentum for gluons and photons has to be parallel is no longer valid; therefore, one can expect more involved integrals for the photon invariant momentum distribution and the elliptic flow.

The polarization tensor encodes the interaction of the gluon (and photon) with the magnetized medium in a perturbative approximation. Attempts to compute the self-energy were performed in the strong field limit: the fermion propagator is written as a sum of Landau Levels so that only the lowest Landau level contributes to the tensor [88, 266]. Such calculation is analytical and finite. On the other hand, when the magnetic field is not the dominant energy scale, all the Landau levels must be taken into account. These kinds of calculations are approximately performed with numerical methods by truncating the sum at a desired order in the magnetic field [267, 268]. However, to gain a more in-depth insight, an analytical approach for the infinite sum over Landau levels is desirable.

Although the gluon abundance in thermal stages of heavy-ion collisions is lower than in the glasma state, the thermal corrections to the gluon mass encoded in the polarization tensor are also interesting, which has been computed and extensively studied both at zero and finite temperature [85, 269–271]. Nonetheless, in a thermalized or magnetic medium, the energy scale

comparison can also be given in terms of the square of the gluon momentum components as well as on the fermion mass. The boost and Lorentz invariance breaks imply a tensor with dependence on the parallel or transverse momentum separately. Thus, the magnetic mass can be different if some direction's momentum is small compared with other projections.

This chapter is divided into two parts: the first one is dedicated to computing the gluon polarization tensor in a magnetized medium by performing the analytic sum over all Landau levels. The tensor structure is reorganized, obtaining a self-energy written in terms of a transverse basis in the sense of the Ward-Takahashi identity. Such manipulation leads to the appearance of spurious terms that are not transverse, and they are appropriately eliminated. The existence of spurious tensors implies that the usual projection method can be plagued with non-physical contributions. Finally, the gluon polarization tensor is computed analytically for the strong and weak field limits.

The second part is devoted to computing the Debye mass or modifications on the gluon dispersion relation. In that calculation, the gluon is assumed to be in a thermalized and strongly magnetized medium. The analysis is performed by considering hierarchies between the fermion mass, the momentum squared, the temperature, and the magnetic field, namely $p^2 \ll m_f^2 \ll T^2$ and $m_f^2 \ll p^2 \ll T^2$. The results show that depending on which momentum component goes to zero first, the tensorial basis's coefficients are different.

The information presented here is based on the findings of the following articles [4–6]:

- Alejandro Ayala, Jorge David Castaño-Yepes, M. Loewe and Enrique Muñoz, *Gluon polarization tensor in a magnetized medium: Analytic approach starting from the sum over Landau levels*, Phys. Rev. D **101**, 036016 (2020).
- Alejandro Ayala, Jorge Castaño-Yepes, C. A. Dominguez, S. Hernandez-Ortiz, L. A. Hernandez, M. Loewe, D. Manreza Paret, and R. Zamora, *Thermal corrections to the gluon magnetic Debye mass*, Rev. Mex. Fis. **66** (4), 446–461 (2020).
- Alejandro Ayala, Jorge David Castaño-Yepes, L. A. Hernández, Jordi Salinas, R. Zamora. *Gluon polarization tensor and dispersion relation in a weakly magnetized medium..* preprint arXiv:2009.00830.

3.1 Magnetized Gluon Polarization Tensor from the Sum of All Landau Levels

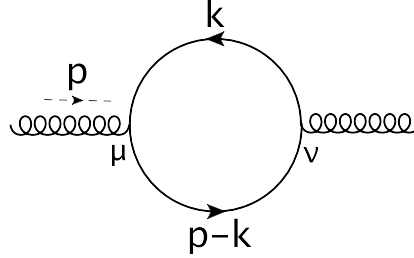


Figure 3.1: One-loop diagram representing the gluon polarization tensor.

Starting from the one-loop contribution to the gluon polarization tensor, which is depicted in Fig. 3.1, the object to be calculated is given explicitly by

$$i\Pi_{ab}^{\mu\nu} = -\frac{1}{2} \int \frac{d^4k}{(2\pi)^4} \text{Tr} \{igt_b\gamma^\nu iS^{(n)}(k)igt_a\gamma^\mu iS^{(m)}(q)\} + \text{C.C.}, \quad (3.1)$$

where g is the strong coupling, and C.C. refers to the *charge conjugate* contribution, that is, the contribution where the flow of charge within the loop is in the opposite direction. The factor $1/2$ accounts for the symmetry factor, which in the presence of the external magnetic field comes about given that the two contributing diagrams, with the opposite flow of charge, are not equivalent.

The quark propagator is denoted by $S(k)$, and $t_{a,b}$ are the generators of the color group in the fundamental representation. The fermion propagator in the presence of a magnetic field $\vec{B} = B\hat{z}$ can be written in terms of a sum over Landau levels in the same way that in Eq. (2.47), which has the form [226, 253]:

$$iS(p) = ie^{-p_\perp^2/|q_f B|} \sum_{n=0}^{+\infty} (-1)^n \frac{D_n(q_f B, p)}{p_\parallel^2 - m_f^2 - 2n|q_f B|}, \quad (3.2)$$

where m_f and q_f are the quark mass and electric charge, respectively, and

$$\begin{aligned} D_n(q_f B, p) &= 2(\not{p}_\parallel + m_f)\mathcal{O}^- L_n^0\left(\frac{2p_\perp^2}{|q_f B|}\right) - 2(\not{p}_\parallel + m_f)\mathcal{O}^+ L_{n-1}^0\left(\frac{2p_\perp^2}{|q_f B|}\right) \\ &+ 4\not{p}_\perp L_{n-1}^1\left(\frac{2p_\perp^2}{|q_f B|}\right). \end{aligned} \quad (3.3)$$

with $L_n^\alpha(x)$ the generalized Laguerre polynomials whose index n label the n -th Landau level, and

$$\mathcal{O}^{(\pm)} = \frac{1}{2} [1 \pm i\gamma^1\gamma^2 \text{sign}(q_f B)]. \quad (3.4)$$

The convention for the squared four-momentum p^μ , expressed in terms of the square of its parallel and perpendicular (with respect to the magnetic field direction) components, is given by

$$p^2 = p_{\parallel}^2 - p_{\perp}^2 = (p_0^2 - p_3^2) - (p_1^2 + p_2^2). \quad (3.5)$$

By replacing Eqs. (3.1) and (3.2), after performing the sum over all Landau levels, the gluon polarization tensor can be written in terms of four tensor structures, given by

$$i\Pi^{\mu\nu} = -\frac{i}{8\pi^2}g^2 \int d^2x f_0(x_1, x_2) \sum_{i=1}^4 f_i^{\mu\nu}(x_1, x_2), \quad (3.6)$$

where on the right-hand side, the factor δ_{ab} coming from using the relation $(t^{ab}) = \delta_{ab}/2$ was omitted, and correspondingly, for notation simplicity, removed the color indices on the left-hand side. Moreover, $(x_1, x_2) \in (0, \infty)$ are Schwinger parameters, with $d^2x = dx_1 dx_2$ and

$$\begin{aligned} f_0(x_1, x_2) &= \exp\left[\frac{x_1 x_2}{x_1 + x_2} p_{\parallel}^2 - m_f^2(x_1 + x_2)\right] \\ &\times \exp\left[-\frac{\tanh(|q_f B| x_1) \tanh(|q_f B| x_2)}{\tanh(|q_f B| x_1) + \tanh(|q_f B| x_2)} \frac{p_{\perp}^2}{|q_f B|}\right], \end{aligned} \quad (3.7a)$$

$$\begin{aligned} f_1^{\mu\nu}(x_1, x_2) &= |q_f B| \coth[|q_f B|(x_1 + x_2)] \\ &\times \left[\left(\frac{x_1 x_2}{(x_1 + x_2)^3} p_{\parallel}^2 + \frac{m_f^2}{x_1 + x_2} \right) g^{\mu\nu} - \frac{2x_1 x_2}{(x_1 + x_2)^3} p_{\parallel}^{\mu} p_{\parallel}^{\nu} \right], \end{aligned} \quad (3.7b)$$

$$f_2^{\mu\nu}(x_1, x_2) = |q_f B| \frac{\cosh[|q_f B|(x_2 - x_1)]}{\sinh[|q_f B|(x_1 + x_2)]} \left[\frac{x_1 x_2}{(x_1 + x_2)^3} p_{\parallel}^2 + \frac{m_f^2}{x_1 + x_2} + \frac{1}{(x_1 + x_2)^2} \right] g_{\perp}^{\mu\nu}, \quad (3.7c)$$

$$\begin{aligned} f_3^{\mu\nu}(x_1, x_2) &= \frac{|q_f B|}{2(x_1 + x_2)^2 \sinh^2[|q_f B|(x_1 + x_2)]} \\ &\times \left[x_1 \sinh(2|q_f B|x_2) + x_2 \sinh(2|q_f B|x_1) \right] \left(p_{\parallel}^{\mu} p_{\perp}^{\nu} + p_{\parallel}^{\nu} p_{\perp}^{\mu} \right), \end{aligned} \quad (3.7d)$$

$$\begin{aligned} f_4^{\mu\nu}(x_1, x_2) &= \frac{|q_f B|^2}{(x_1 + x_2) \sinh^2[|q_f B|(x_1 + x_2)]} \\ &\times \left[\left(1 - \frac{\tanh(|q_f B|x_1) \tanh(|q_f B|x_2)}{|q_f B| [\tanh(|q_f B|x_1) + \tanh(|q_f B|x_2)]} p_{\perp}^2 \right) g^{\mu\nu} \right. \\ &\left. - g_{\perp}^{\mu\nu} - \frac{2 \tanh(|q_f B|x_1) \tanh(|q_f B|x_2)}{|q_f B| [\tanh(|q_f B|x_1) + \tanh(|q_f B|x_2)]} p_{\perp}^{\mu} p_{\perp}^{\nu} \right]. \end{aligned} \quad (3.7e)$$

For calculation details, see Appendix G.

3.1.1 Tensor Basis

In order to give a direct physical interpretation of the obtained results, the correct choice of a tensorial basis is fundamental. That basis has to obey the following fundamental properties:

- All the tensors should be symmetric under the exchange of its Lorentz indices.
- It has to be constructed from external products of independent four-vectors which are related to the physical observables.

From the above, the gluon polarization tensor will be described in terms of the gluon four-momentum p^μ , the magnetic field direction b^μ , and the metric tensor $g^{\mu\nu}$. Given that there are no more dynamical variables in the present problem, the named vectors have to be enough to construct the tensorial basis.

The propagator of Eq. (3.2) comes from an analysis in where the external magnetic field is assumed to be oriented in the z -axis so that without loss of generality one can choose along this direction. Moreover, due to the breaking of Lorentz invariance by the vector b^μ (magnetic field), it is convenient to split the metric itself into parallel and perpendicular (with respect to the magnetic field direction) components, that is

$$g^{\mu\nu} = g_{\parallel}^{\mu\nu} + g_{\perp}^{\mu\nu}, \quad (3.8)$$

where

$$g_{\parallel}^{\mu\nu} = \text{diag}(1, 0, 0, -1), \quad (3.9)$$

and

$$g_{\perp}^{\mu\nu} = \text{diag}(0, -1, -1, 0). \quad (3.10)$$

Thus, the most general symmetric tensor can be constructed out of combinations of the independent tensors

$$p^\mu p^\nu, b^\mu b^\nu, p^\mu b^\nu + p^\nu b^\mu, g^{\mu\nu}. \quad (3.11)$$

However, notice that in QCD, $\Pi^{\mu\nu}$ must satisfy the generalized Ward-Takahashi identity namely, the *transversality* condition [84]

$$p_\mu p_\nu \Pi^{\mu\nu} = 0. \quad (3.12)$$

Therefore, since Eq. (3.12), implies a relation between the coefficients of the tensors to express $\Pi^{\mu\nu}$, only three *transverse* tensors turn out to be independent. Explicitly, the polarization tensor can be written as

$$\Pi^{\mu\nu} = a A^{\mu\nu} + b B^{\mu\nu} + c C^{\mu\nu} + d D^{\mu\nu}. \quad (3.13)$$

where the constants in front of each tensorial structure are determined from the gauge invariance of Eq. (3.12), i.e.,

$$\begin{aligned} p_\mu p_\nu \Pi^{\mu\nu} &= a(p_\mu p_\nu A^{\mu\nu}) + b(p_\mu p_\nu B^{\mu\nu}) \\ &+ c(p_\mu p_\nu C^{\mu\nu}) + d(p_\mu p_\nu D^{\mu\nu}) = 0. \end{aligned} \quad (3.14)$$

The latter means that only three of the four constants (a, b, c, d) have to be independent of each other, thus, one of the tensors of Eq. (3.14) is distributed among the rest of the tensor structures. That procedure results in only three tensors being needed to span the whole tensor $\Pi^{\mu\nu}$. A useful orthonormal basis where each element is transverse to satisfy the condition of Eq. (3.12) in a QED-like form ($p_\mu \Pi^{\mu\nu} = 0$) is

$$\mathcal{P}_{\parallel}^{\mu\nu} = g_{\parallel}^{\mu\nu} - \frac{p_{\parallel}^{\mu} p_{\parallel}^{\nu}}{p_{\parallel}^2}, \quad (3.15)$$

$$\mathcal{P}_{\perp}^{\mu\nu} = g_{\perp}^{\mu\nu} + \frac{p_{\perp}^{\mu} p_{\perp}^{\nu}}{p_{\perp}^2}, \quad (3.16)$$

$$\mathcal{P}_0^{\mu\nu} = g^{\mu\nu} - \frac{p^{\mu} p^{\nu}}{p^2} - \mathcal{P}_{\parallel}^{\mu\nu} - \mathcal{P}_{\perp}^{\mu\nu}. \quad (3.17)$$

The selected basis can be regarded as a natural factorization of the whole space into parallel and transverse structures, with respect to the magnetic field four-vector b^μ . To illustrate this, without loss of generality, the magnetic field direction can be chosen as

$$b^\mu = (0, \mathbf{b}) = (0, 0, 0, 1), \quad (3.18)$$

so that

$$\mathbf{b} = \frac{1}{2} \nabla \times (-y, x, 0) \equiv \nabla \times \mathbf{a}, \quad (3.19)$$

and therefore, by written the vector potential as $\mathbf{A} = B\mathbf{a}$, from the well-known definition $F^{\mu\nu} = \partial^\mu A^\nu - \partial^\nu A^\mu$, the following relation is found:

$$p_\alpha p_\beta F^{\alpha\mu} F^{\beta\nu} = B^2 \begin{pmatrix} 0 & 0 & 0 & 0 \\ 0 & p_2^2 & -p_1 p_2 & 0 \\ 0 & -p_1 p_2 & p_1^2 & 0 \\ 0 & 0 & 0 & 0 \end{pmatrix}. \quad (3.20)$$

Also, from Eq. (3.16)

$$p_{\perp}^2 \mathcal{P}_{\perp}^{\mu\nu} = \begin{pmatrix} 0 & 0 & 0 & 0 \\ 0 & -p_2^2 & p_1 p_2 & 0 \\ 0 & p_1 p_2 & -p_1^2 & 0 \\ 0 & 0 & 0 & 0 \end{pmatrix}, \quad (3.21)$$

therefore

$$B^2 p_\perp^2 \mathcal{P}_\perp^{\mu\nu} = -p_\alpha p_\beta F^{\alpha\mu} F^{\beta\nu}, \quad (3.22)$$

which shows that the choice of b^μ impacts directly the factorization of the metric into transverse and a parallel structures. Therefore, this basis can be used to rearrange the tensor structures of Eqs. (3.7) (see Appendix H) as

$$\begin{aligned} i\Pi^{\mu\nu} &= -\frac{i}{8\pi^2} g^2 \int d^2x f_0(x_1, x_2) \left[\Pi_\parallel(x_1, x_2) \mathcal{P}_\parallel^{\mu\nu} + \Pi_\perp(x_1, x_2) \mathcal{P}_\perp^{\mu\nu} + \Pi_0(x_1, x_2) \mathcal{P}_0^{\mu\nu} \right] \\ &- \frac{i}{8\pi^2} g^2 \int d^2x f_0(x_1, x_2) \left[A_1(x_1, x_2) g_\parallel^{\mu\nu} + A_2(x_1, x_2) g_\perp^{\mu\nu} \right], \end{aligned} \quad (3.23)$$

where

$$\Pi_\parallel = |q_f B| \left[\frac{2x_1 x_2 \coth[|q_f B|(x_1 + x_2)]}{(x_1 + x_2)^3} p_\parallel^2 - \frac{x_1 \sinh(2|q_f B|x_2) + x_2 \sinh(2|q_f B|x_1)}{2(x_1 + x_2)^2 \sinh^2[|q_f B|(x_1 + x_2)]} p_\perp^2 \right] \quad (3.24)$$

$$\begin{aligned} \Pi_\perp &= |q_f B| \left[\frac{x_1 \sinh(2|q_f B|x_2) + x_2 \sinh(2|q_f B|x_1)}{2(x_1 + x_2)^2 \sinh^2[|q_f B|(x_1 + x_2)]} p_\parallel^2 \right. \\ &\left. - \frac{2 \sinh(|q_f B|x_1) \sinh(|q_f B|x_2)}{(x_1 + x_2) \sinh^3[|q_f B|(x_1 + x_2)]} p_\perp^2 \right] \end{aligned} \quad (3.25)$$

$$\Pi_0 = |q_f B| \frac{x_1 \sinh(2|q_f B|x_2) + x_2 \sinh(2|q_f B|x_1)}{2(x_1 + x_2)^2 \sinh^2[|q_f B|(x_1 + x_2)]} p^2, \quad (3.26)$$

$$\begin{aligned} A_1 &= |q_f B| \left[\frac{x_1 \sinh(2|q_f B|x_2) + x_2 \sinh(2|q_f B|x_1)}{2(x_1 + x_2)^2 \sinh^2[|q_f B|(x_1 + x_2)]} p_\perp^2 \right. \\ &+ \frac{\coth[|q_f B|(x_1 + x_2)]}{(x_1 + x_2)^3} (m_f^2(x_1 + x_2)^2 - x_1 x_2 p_\parallel^2) \\ &+ \frac{|q_f B|}{(x_1 + x_2) \sinh^2[|q_f B|(x_1 + x_2)]} \\ &\left. \times \left(1 - \frac{\tanh(|q_f B|x_1) \tanh(|q_f B|x_2)}{|q_f B| [\tanh(|q_f B|x_1) + \tanh(|q_f B|x_2)]} p_\perp^2 \right) \right], \end{aligned} \quad (3.27)$$

and

$$\begin{aligned} A_2 &= |q_f B| \left[\frac{\cosh[|q_f B|(x_2 - x_1)]}{(x_1 + x_2)^3 \sinh[|q_f B|(x_1 + x_2)]} [x_1 x_2 p_\parallel^2 + (x_1 + x_2) + m_f^2(x_1 + x_2)^2] \right. \\ &\left. - \frac{x_1 \sinh(2|q_f B|x_2) + x_2 \sinh(2|q_f B|x_1)}{2(x_1 + x_2)^2 \sinh^2[|q_f B|(x_1 + x_2)]} p_\parallel^2 + \frac{\sinh(|q_f B|x_1) \sinh(|q_f B|x_2)}{(x_1 + x_2) \sinh^3[|q_f B|(x_1 + x_2)]} p_\perp^2 \right]. \end{aligned} \quad (3.28)$$

Equation (3.23) has a serious issue regarding the appearance of terms that are proportional to $g_{\parallel}^{\mu\nu}$ and $g_{\perp}^{\mu\nu}$, which implies a non-transverse structure for the polarization tensor. That situation makes that any calculation based on the projection procedure to compute the coefficients corresponding to each tensor structure is plagued with spurious terms, and therefore, a numerical evaluation of $\Pi^{\mu\nu}$ cannot give the truly physical coefficients [85,267,268]. Explicitly, a projection method yields

$$\tilde{\Pi}_{\parallel} = \Pi_{\mu\nu} \mathcal{P}_{\parallel}^{\mu\nu} = \Pi_{\parallel} + A_1, \quad (3.29a)$$

$$\tilde{\Pi}_{\perp} = \Pi_{\mu\nu} \mathcal{P}_{\perp}^{\mu\nu} = \Pi_{\perp} + A_2, \quad (3.29b)$$

and

$$\tilde{\Pi}_0 = \Pi_{\mu\nu} \mathcal{P}_0^{\mu\nu} = \Pi_0 - \frac{p_{\perp}^2}{p^2} A_1 + \frac{p_{\parallel}^2}{p^2} A_2, \quad (3.29c)$$

where Π_{\parallel} , Π_{\perp} and Π_0 are given by Eqs. (3.24)-(3.26) and A_1 , A_2 are given by Eqs. (3.27)-(3.28). Thus, it is necessary to show that A_1 and A_2 vanishes.

3.1.2 Elimination of spurious tensors

The elimination the so-called spurious terms is done by following the procedure shown in Ref. [272]. First, the x parameters are scaled in the form

$$x_i \rightarrow \lambda z_i, \quad (3.30)$$

with $(\lambda, z_i) \in \mathbb{R}$. Therefore, the integral that involves the coefficient A_1 can be written as

$$\begin{aligned} \mathcal{I}_{A_1} &= -\lambda \frac{\partial}{\partial \lambda} \int \frac{d^2 z}{(z_1 + z_2)^2} \coth[\lambda |q_f B| (z_1 + z_2)] \exp \left[\lambda \left(\frac{z_1 z_2}{z_1 + z_2} p_{\parallel}^2 - m_f^2 (z_1 + z_2) \right) \right] \\ &\times \exp \left[-\frac{\tanh(\lambda |q_f B| z_1) \tanh(\lambda |q_f B| z_2)}{\tanh(\lambda |q_f B| z_1) + \tanh(\lambda |q_f B| z_2)} \frac{p_{\perp}^2}{|q_f B|} \right]. \end{aligned} \quad (3.31)$$

Scaling back $\lambda z_1 \rightarrow x_i$ gives:

$$\begin{aligned} \mathcal{I}_{A_1} &= -\lambda \frac{\partial}{\partial \lambda} \int \frac{d^2 x}{(x_1 + x_2)^2} \coth[|q_f B| (x_1 + x_2)] \exp \left[\frac{x_1 x_2}{x_1 + x_2} p_{\parallel}^2 - m_f^2 (x_1 + x_2) \right] \\ &\times \exp \left[-\frac{\tanh(|q_f B| x_1) \tanh(|q_f B| x_2)}{\tanh(|q_f B| x_1) + \tanh(|q_f B| x_2)} \frac{p_{\perp}^2}{|q_f B|} \right], \end{aligned} \quad (3.32)$$

and thus, the derivative is applied to a function independent of λ . Therefore $\mathcal{I}_{A_1} = 0$.

The implementation of the same argument for \mathcal{I}_{A_2} is more involved, given that the function is not a trivial combination of coefficients for p_{\parallel}^2 and p_{\perp}^2 . After the λ -scaling, the integral is

$$\mathcal{I}_{A_2} = \lambda^2 \int \frac{d^2 z}{\lambda (z_1 + z_2)^2} I(\lambda z_1, \lambda z_2), \quad (3.33)$$

where

$$\begin{aligned}
I(\lambda z_1, \lambda z_2) &= f_0(\lambda z_1, \lambda z_2) \left[\frac{\cosh[\lambda |q_f B| (z_2 - z_1)]}{\sinh[\lambda |q_f B| (z_1 + z_2)]} \left(\frac{z_1 z_2}{z_1 + z_2} p_{\parallel}^2 + m_f^2 (z_1 + z_2) + \frac{1}{\lambda} \right) \right. \\
&\quad - \frac{z_1 \sinh(2\lambda |q_f B| z_2) + z_2 \sinh(2\lambda |q_f B| z_1)}{2 \sinh^2[\lambda |q_f B| (z_1 + z_2)]} p_{\parallel}^2 \\
&\quad \left. + \frac{(z_1 + z_2) \sinh(\lambda |q_f B| z_1) \sinh(\lambda |q_f B| z_2)}{\sinh^3[\lambda |q_f B| (z_1 + z_2)]} p_{\perp}^2 \right], \tag{3.34}
\end{aligned}$$

from which by expanding in a Taylor series around $\lambda = 0$ it is possible to find that

$$\begin{aligned}
\int I(\lambda z_1, \lambda z_2) d\lambda &= -\frac{1}{|q_f B| (z_1 + z_2) \lambda} \\
&+ \frac{2 |q_f B|^2 (z_1 + z_2)^2 (z_1^2 - 4z_1 z_2 + z_2^2) + 3 (z_1 z_2 p^2 - m^2 (z_1 + z_2)^2)^2}{6 |q_f B| (z_1 + z_2)^3} \lambda \\
&+ \frac{\lambda^2}{6 |q_f B| (z_1 + z_2)^4} \left[(3p^4 z_1^2 z_2^2 - 3m^2 p^2 z_1 z_2 (z_1 + z_2)^2 + m^4 (z_1 + z_2)^4) (z_1 + z_2)^2 m^2 \right. \\
&\quad \left. - z_1 z_2 (p^6 z_1^2 z_2^2 - 2 |q_f B|^2 (z_1 + z_2)^2 (p^2 (z_1 - z_2)^2 - p_{\perp}^2 z_1 z_2)) \right] \\
&+ \frac{\lambda^3}{1080 |q_f B| (z_1 + z_2)^5} \left[45 (p^2 z_1 z_2 - m^2 (z_1 + z_2)^2)^4 \right. \\
&\quad + 8 |q_f B|^4 (z_1 + z_2)^4 (z_1^4 + 4z_1^3 z_2 - 24z_1^2 z_2^2 + 4z_1 z_2^3 + z_2^4) \\
&\quad - 60 |q_f B|^2 (z_1 + z_2)^2 (p^2 z_1 z_2 - m^2 (z_1 + z_2)^2) (m^2 (z_1 + z_2)^2 (z_1^2 - 4z_1 z_2 + z_2^2) \\
&\quad \left. + z_1 z_2 (p^2 (3z_1^2 - 4z_1 z_2 + 3z_2^2) - 6p_{\perp}^2 z_1 z_2)) \right] + \mathcal{O}(\lambda^4), \tag{3.35}
\end{aligned}$$

where the desired scaling properties are recovered and hold for all orders in λ . This means that is possible to write

$$\int I(\lambda z_1, \lambda z_2) d\lambda = -\frac{1}{|q_f B| (z_1 + z_2) \lambda} + h(\lambda z_1, \lambda z_2), \tag{3.36}$$

thus

$$\begin{aligned}
I(\lambda z_1, \lambda z_2) &= \frac{\partial}{\partial \lambda} \left[-\frac{1}{|q_f B| (z_1 + z_2) \lambda} + h(\lambda z_1, \lambda z_2) \right] \\
&= \frac{\partial}{\partial \lambda} \left[-\frac{1}{|q_f B| (x_1 + x_2)} + h(x_1, x_2) \right] = 0, \tag{3.37}
\end{aligned}$$

and therefore, $\mathcal{I}_{A_2} = 0$.

The above argument is valid for all values of λ . Consequently, the result can be taken as general.

3.1.3 Obtaining the Vacuum Polarization Tensor

It is well established that the polarization tensor in the vacuum contains divergences that have to be isolated from the matter contribution. The simplest way to eliminate such singularities is by identifying the vacuum contribution in the appropriate limits. To perform this, note that at least two vacua can be defined, in terms of the physical quantities of the problem:

- A vacuum where $p^\mu = 0$ and $B = 0$, corresponding to a situation where particles and magnetic field appear simultaneously.
- A vacuum with $B = 0$ and $p^\mu \neq 0$, representing a situation where the external field is turned on with pre-existing gluons with four-momentum p^μ .

By looking at the computed equations for the polarization tensor, it can be noticed that the magnetic field and the transverse momentum appear within the combination $p_\perp^2 / |q_f B|$ and thus, p_\perp^2 and B cannot be set to zero simultaneously. For this reason, in this work the second vacuum definition is adopted, so that from Eq. (3.23):

$$\begin{aligned}
 i\Pi^{\mu\nu}(p, |q_f B| \rightarrow 0) &= -\frac{i}{8\pi^2} g^2 \int d^2x \exp \left[\frac{x_1 x_2}{x_1 + x_2} p^2 - m_f^2 (x_1 + x_2) \right] \\
 \times \left[\frac{2x_1 x_2}{(x_1 + x_2)^4} p^2 \left(g^{\mu\nu} - \frac{p^\mu p^\nu}{p^2} \right) + \frac{1}{(x_1 + x_2)^3} \left((x_1 + x_2) m_f^2 - \frac{x_1 x_2}{x_1 + x_2} p^2 + 1 \right) g^{\mu\nu} \right].
 \end{aligned} \tag{3.38}$$

The last equation points out to the fact that the elimination of spurious tensors is of great importance, given that even in the vacuum the tensor is not transverse. The method to eliminate such contributions also applies to Eq. (3.38), i.e., by scaling the Schwinger parameters, the coefficient of $g^{\mu\nu}$ is

$$\begin{aligned}
 \mathcal{I} &= \lambda^2 \int \frac{d^2z}{\lambda^2 (z_1 + z_2)^3} \left(m^2 (z_1 + z_2) - \frac{z_1 z_2}{z_1 + z_2} p^2 + \frac{1}{\lambda} \right) e^{\lambda \left[\frac{z_1 z_2}{z_1 + z_2} p^2 - m_f^2 (z_1 + z_2) \right]} \\
 &= -\lambda \frac{\partial}{\partial \lambda} \int \frac{d^2x}{(x_1 + x_2)^3} e^{\frac{x_1 x_2}{x_1 + x_2} p^2 - m_f^2 (x_1 + x_2)} \\
 &= 0.
 \end{aligned} \tag{3.39}$$

The above leads to identify the vacuum gluon polarization tensor as

$$\begin{aligned}
 i\Pi_{\text{vac}}^{\mu\nu}(p) &= -\frac{ig^2 p^2}{8\pi^2} \int d^2x \frac{2x_1 x_2}{(x_1 + x_2)^4} \exp \left[\frac{x_1 x_2}{x_1 + x_2} p^2 - m_f^2 (x_1 + x_2) \right] \left(g^{\mu\nu} - \frac{p^\mu p^\nu}{p^2} \right) \\
 &\equiv -\frac{ig^2}{8\pi^2} \int d^2x \Pi_{\text{vac}}(x_1, x_2) \left(\mathcal{P}_0^{\mu\nu} + \mathcal{P}_\parallel^{\mu\nu} + \mathcal{P}_\perp^{\mu\nu} \right)
 \end{aligned} \tag{3.40}$$

so that the finite magnetized gluon polarization tensor reads

$$\begin{aligned}
i\Pi^{\mu\nu} &= -\frac{ig^2}{8\pi^2} \int d^2x f_0(x_1, x_2) \left\{ \left[\Pi_0(x_1, x_2) - \tilde{\Pi}(x_1, x_2) \right] \mathcal{P}_0^{\mu\nu} \right. \\
&\quad \left. + \left[\Pi_{\parallel}(x_1, x_2) - \tilde{\Pi}(x_1, x_2) \right] \mathcal{P}_{\parallel}^{\mu\nu} + \left[\Pi_{\perp}(x_1, x_2) - \tilde{\Pi}(x_1, x_2) \right] \mathcal{P}_{\perp}^{\mu\nu} \right\}, \tag{3.41}
\end{aligned}$$

where

$$\tilde{\Pi}(x_1, x_2) \equiv \Pi_{\text{vac}}(x_1, x_2) \exp \left[\frac{\tanh(|q_f B| x_1) \tanh(|q_f B| x_2)}{\tanh(|q_f B| x_1) + \tanh(|q_f B| x_2)} \frac{p_{\perp}^2}{|q_f B|} - \frac{x_1 x_2}{x_1 + x_2} p_{\perp}^2 \right]. \tag{3.42}$$

In the following, the analysis is facilitated by performing the change of variables in Eq. (3.41) given by

$$x_1 \equiv \frac{s(1-y)}{m_f^2}, \quad x_2 \equiv \frac{sy}{m_f^2}, \tag{3.43a}$$

$$\rho_{\parallel, \perp}^2 \equiv \frac{p_{\parallel, \perp}^2}{m_f^2}, \quad \mathcal{B} \equiv \frac{|q_f B|}{m_f^2}, \tag{3.43b}$$

so that the magnetic contribution of Eq. (3.41) becomes

$$\begin{aligned}
i\Pi_{\text{mag}}^{\mu\nu} &= -\frac{ig^2 m_f^2 \mathcal{B}}{8\pi^2} \int_0^1 dy \int_0^\infty ds e^{s(y(1-y)\rho_{\parallel}^2 - 1)} \exp \left[-\frac{\cosh(\mathcal{B}s) - \cosh[\mathcal{B}s(2y-1)]}{2 \sinh(\mathcal{B}s)} \frac{\rho_{\perp}^2}{\mathcal{B}} \right] \\
&\times \left\{ \frac{(1-y)\mathcal{B} \sinh(2\mathcal{B}s y)}{\mathcal{B} \sinh^2(\mathcal{B}s)} \rho^2 \mathcal{P}_0^{\mu\nu} + \left[2y(1-y) \coth(\mathcal{B}s) \rho_{\parallel}^2 - \frac{(1-y) \sinh(2\mathcal{B}s y)}{\sinh^2(\mathcal{B}s)} \rho_{\perp}^2 \right] \mathcal{P}_{\parallel}^{\mu\nu} \right. \\
&\left. + \left[\frac{(1-y) \sinh(2\mathcal{B}s y)}{\sinh^2(\mathcal{B}s)} \rho_{\parallel}^2 - \frac{\cosh(\mathcal{B}s) - \cosh[\mathcal{B}s(2y-1)]}{\sinh^3(\mathcal{B}s)} \rho_{\perp}^2 \right] \mathcal{P}_{\perp}^{\mu\nu} \right\}. \tag{3.44}
\end{aligned}$$

To check the validity of the computed expressions, the strong and weak magnetic field limits are studied.

3.1.4 Strong Field Limit

The polarization tensor in an environment with extreme conditions is of special interest both for theoretical and experimental points of view. Particularly, in the QDE sector, the pair production is expected from the Schwinger effect, i.e., the electron-positron creation when an intense electric field is present [273,274]. Moreover, if the electric field varies in time, a strong magnetic field can be generated which interacts with the fermionic vacuum [275].

In the QCD sector, as it was established in Chapter 2, strong magnetic fields are created in the early stages of peripheral heavy-ion collisions where the gluon high occupation state, the *glasma*, is achieved. Thus, the gluons which form such overpopulated phase moves in a magnetized medium, so that its cloud of virtual quarks can modify the gluon properties.

In order to get the consequences of a strong magnetic field on the polarization tensor, note that if \mathcal{B} is the dominant energy scale

$$\begin{aligned} \mathcal{B} \coth(\mathcal{B}s) &\sim \mathcal{B}, \\ \frac{\mathcal{B} \sinh(2\mathcal{B}sy)}{2 \sinh^2(\mathcal{B}s)} &\sim 0, \\ \frac{\cosh(\mathcal{B}s) - \cosh[\mathcal{B}s(2y-1)]}{2 \sinh(\mathcal{B}s)} &\sim \frac{1}{2\mathcal{B}} \end{aligned} \quad (3.45)$$

which hold for all s and $0 < y < 1$. Therefore

$$i\Pi^{\mu\nu} = -\frac{ig^2 m_f^2 \mathcal{B} \rho_{\parallel}^2}{4\pi^2} e^{-\rho_{\perp}^2/2\mathcal{B}} \int_0^1 dy y(1-y) \int_0^{\infty} ds \exp[s(y(1-y)\rho_{\parallel}^2 - 1)] \mathcal{P}_{\parallel}^{\mu\nu}. \quad (3.46)$$

For the kinematical region such that $y(1-y)\rho_{\parallel}^2 < 1$, the integration over s can be performed, yielding

$$\begin{aligned} i\Pi^{\mu\nu} &= \frac{ig^2 m_f^2 \mathcal{B}}{4\pi^2} e^{-\rho_{\perp}^2/2\mathcal{B}} \int_0^1 dy \frac{y(1-y)}{y(1-y) - \rho_{\parallel}^{-2}} \mathcal{P}_{\parallel}^{\mu\nu} \\ &\equiv \frac{ig^2 m_f^2 \mathcal{B}}{4\pi^2} e^{-\rho_{\perp}^2/2\mathcal{B}} I(\rho_{\parallel}^2) \mathcal{P}_{\parallel}^{\mu\nu}. \end{aligned} \quad (3.47)$$

This result is the same that the one obtained in Ref. [88] by considering only the Lowest Landau Level (LLL) contribution of Eq. (3.2), namely, $n = 0$. A direct calculation starting from the LLL, shows that the polarization tensor is finite and it has not the vacuum piece given by Eq. (3.40). Moreover, the integral over the variable y can be performed analytically, yielding

$$I(x) \equiv \int_0^1 dy \frac{y(1-y)}{y(1-y) - x} = 1 - \frac{4x}{\sqrt{4x-1}} \arctan\left(\frac{1}{\sqrt{4x-1}}\right). \quad (3.48)$$

On the other hand, if the spurious terms were not eliminated, the strong magnetic field limit would be

$$i\Pi^{\mu\nu} = \frac{ig^2 m_f^2 \mathcal{B}}{4\pi^2} e^{-\rho_{\perp}^2/2\mathcal{B}} [I(\rho_{\parallel}^2) + I_1(\rho_{\parallel}^2)] \mathcal{P}_{\parallel}^{\mu\nu}, \quad (3.49)$$

where

$$I_1(x) = \int_0^1 dy \frac{1}{y(1-y)x - 1} = -\frac{4}{\sqrt{x(x-4)}} \arctan\left(\frac{\sqrt{x}}{\sqrt{4-x}}\right). \quad (3.50)$$

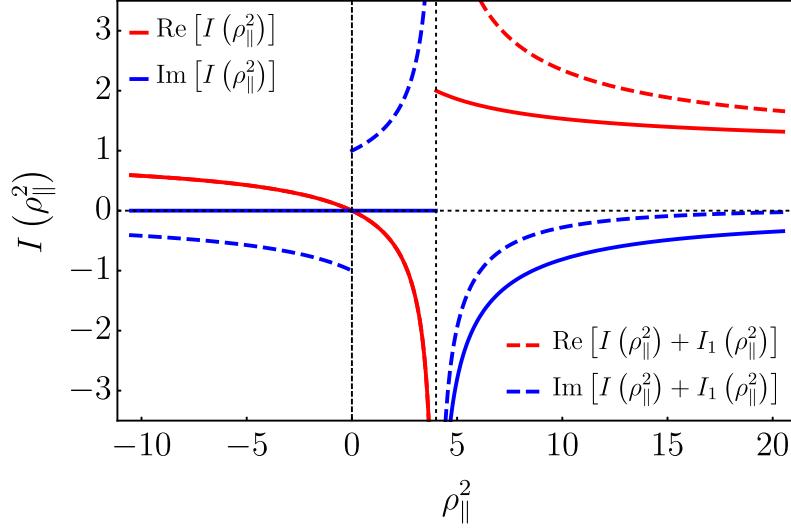


Figure 3.2: Real and imaginary parts of the function $I(\rho_{\parallel}^2)$ defined in Eq. (3.47) compared with the result including the spurious contribution of $I_1(\rho_{\parallel}^2)$ from Eq. (3.49).

Figure 3.2 shows the real and imaginary parts of Eq. (3.47) compared with the result of Eq. (3.49) as a function of ρ_{\parallel}^2 . The former has a discontinuity at the threshold value $\rho_{\parallel}^2 = 4$ or equivalently at $p_{\parallel}^2 = 4m_f^2$, whereas for the latter this is located at $\rho_{\parallel}^2 = 0$. Such discontinuities have the interpretation of pair production: the gluon (photon) reaches sufficient energy to decay into a pair quark-antiquark (electron-positron), which in some reference frame has the value $p_0 = 2m_f$. The main characteristic of this phenomenon is the appearance of an imaginary part in the polarization tensor, related to the decay probability. Thus, it is clear that the threshold of the spurious term located at $\rho_{\parallel}^2 = 0$ cannot represent a physical situation given the mass-energy conservation.

3.1.5 Weak Field Limit

The hierarchy of energy scales in this limit is taken as $|eB| < m_f^2$, then, a power series of Eq. (3.44) around $\mathcal{B} = 0$ can be performed, obtaining:

$$\begin{aligned}
i\Pi^{\mu\nu} &= -\frac{ig^2m_f^2\mathcal{B}^2}{8\pi^2} \int_0^1 dy \int_0^\infty ds \frac{2sy(1-y)}{3} \exp[s(y(1-y)\rho^2 - 1)] \\
&\times \left\{ \rho^2 [sy^2(1-y)^2\rho_{\perp}^2 + 2y^2 - 1] \mathcal{P}_0^{\mu\nu} + [sy^2(1-y)^2\rho_{\perp}^2\rho^2 + 2(1-y^2)\rho_{\perp}^2 + \rho^2] \mathcal{P}_{\parallel}^{\mu\nu} \right. \\
&+ \left. [sy^2(1-y)^2\rho_{\perp}^2\rho^2 + (1+y)\rho_{\perp}^2 - (1-y^2)\rho_{\parallel}^2 + y^2\rho^2] \mathcal{P}_{\perp}^{\mu\nu} \right\} \\
&- \frac{ig^2m_f^2\rho^2}{8\pi^2} \int_0^1 dy \int_0^\infty ds \frac{2y(1-y)}{s} \exp[s(y(1-y)\rho^2 - 1)] \left(\mathcal{P}_{\parallel}^{\mu\nu} + \mathcal{P}_{\perp}^{\mu\nu} + \mathcal{P}_0^{\mu\nu} \right), \tag{3.51}
\end{aligned}$$

where the vacuum term is explicitly given by the integral proportional to $\mathcal{P}_{\parallel}^{\mu\nu} + \mathcal{P}_{\perp}^{\mu\nu} + \mathcal{P}_0^{\mu\nu}$.

The integration over the variables s and y is performed analytically, so that, after subtracting the vacuum contribution, the gluon polarization tensor for a weak magnetic field is given by

$$i\Pi_{\text{weak } \mathcal{B}}^{\mu\nu} = -\frac{ig^2 m_f^2 \mathcal{B}^2}{6\pi^2} \left[\hat{\Pi}_{\parallel}(\rho^2) \mathcal{P}_{\parallel}^{\mu\nu} + \hat{\Pi}_{\perp}(\rho^2) \mathcal{P}_{\perp}^{\mu\nu} + \hat{\Pi}_0(\rho^2) \mathcal{P}_0^{\mu\nu} \right], \quad (3.52)$$

whith

$$\begin{aligned} \hat{\Pi}_{\parallel} = & \frac{1}{4-\rho^2} \left[1 - \frac{(\rho^2-10)(\rho^2-3)\rho_{\perp}^2}{4-\rho^2} + \frac{6\rho_{\perp}^2}{\rho^2} + \left(12 \frac{10+(\rho^2-6)\rho^2}{(4-\rho^2)^{3/2}(\rho^2)^{5/2}} \rho_{\perp}^2 \right. \right. \\ & \left. \left. + 2 \frac{\rho^2(\rho^2+2)-12}{\sqrt{4-\rho^2}(\rho^2)^{5/2}} \rho_{\perp}^2 + 2 \frac{(\rho^2-2)\sqrt{(4-\rho^2)\rho^2}}{(4-\rho^2)\rho^2} \right) \arctan \left(\frac{\sqrt{\rho^2}}{\sqrt{4-\rho^2}} \right) \right], \end{aligned} \quad (3.53)$$

$$\begin{aligned} \hat{\Pi}_{\perp} = & \frac{1}{4-\rho^2} \left[\frac{3\rho_{\perp}^2}{2\rho^2} - \frac{(\rho^2-10)(\rho^2-3)\rho_{\perp}^2}{4-\rho^2} - \frac{3\rho_{\parallel}^2}{\rho^4} + \frac{(\rho^2-3)\sqrt{(4-\rho^2)\rho^2}}{\sqrt{4-\rho^2}(\rho^2)^{3/2}} \right. \\ & \left. + \left(12 \frac{10+(\rho^2-6)\rho^2}{(4-\rho^2)^{3/2}(\rho^2)^{5/2}} \rho_{\perp}^2 + 3 \frac{(\rho^2-2)\sqrt{(4-\rho^2)\rho^2}}{(4-\rho^2)\rho^4} \rho_{\perp}^2 - \frac{\rho^2(\rho^2+2)-12}{\sqrt{4-\rho^2}(\rho^2)^{5/2}} \rho_{\parallel}^2 \right. \right. \\ & \left. \left. + \frac{12+(\rho^2-6)\rho^2}{\sqrt{4-\rho^2}(\rho^2)^{3/2}} \right) \arctan \left(\frac{\sqrt{\rho^2}}{\sqrt{4-\rho^2}} \right) \right], \end{aligned} \quad (3.54)$$

$$\begin{aligned} \hat{\Pi}_0 = & \frac{1}{4-\rho^2} \left[2 \frac{(\rho^2-3)\sqrt{(4-\rho^2)\rho^2}}{\sqrt{4-\rho^2}(\rho^2)^{3/2}} - \frac{(\rho^2-10)(\rho^2-3)\rho_{\perp}^2}{4-\rho^2} - 1 + \left(2 \frac{12+(\rho^2-6)\rho^2}{\sqrt{4-\rho^2}(\rho^2)^{3/2}} \right. \right. \\ & \left. \left. + 12 \frac{10+(\rho^2-6)\rho^2}{(4-\rho^2)^{3/2}(\rho^2)^{5/2}} \rho_{\perp}^2 + -2 \frac{(\rho^2-2)\sqrt{(4-\rho^2)\rho^2}}{(4-\rho^2)\rho^2} \right) \arctan \left(\frac{\sqrt{\rho^2}}{\sqrt{4-\rho^2}} \right) \right]. \end{aligned} \quad (3.55)$$

Figure 3.3 displays the coefficients of Eqs. (3.53)-(3.55) as a function of ρ for fixed values of ρ_{\parallel}^2 and ρ_{\perp}^2 . The spurious coefficients contribution is also plotted for comparison reasons. In the same way that in the strong magnetic field limit, the coefficients A_1 and A_2 have unphysical thresholds at $\rho^2 = 0$, producing notable deviations from the correct structures. On the other hand, the weak approximation has a threshold at $\rho^2 = 4$, in contrast with the strong field limit where the pair production is governed by $\rho_{\parallel}^2 = 4$. This feature indicates that all the directions are important in the polarization tensor dynamics, however, as Figs. 3.3(a)-(b) shows, the tensor structure parallel to the magnetic field dominates over the other directions.

3.1.6 Thresholds for an arbitrary magnetic field

As was commented on the previous sections, the polarization tensor thresholds are related to the probability of producing a fermion pair from a gluon or photon. In the strong as well as in the

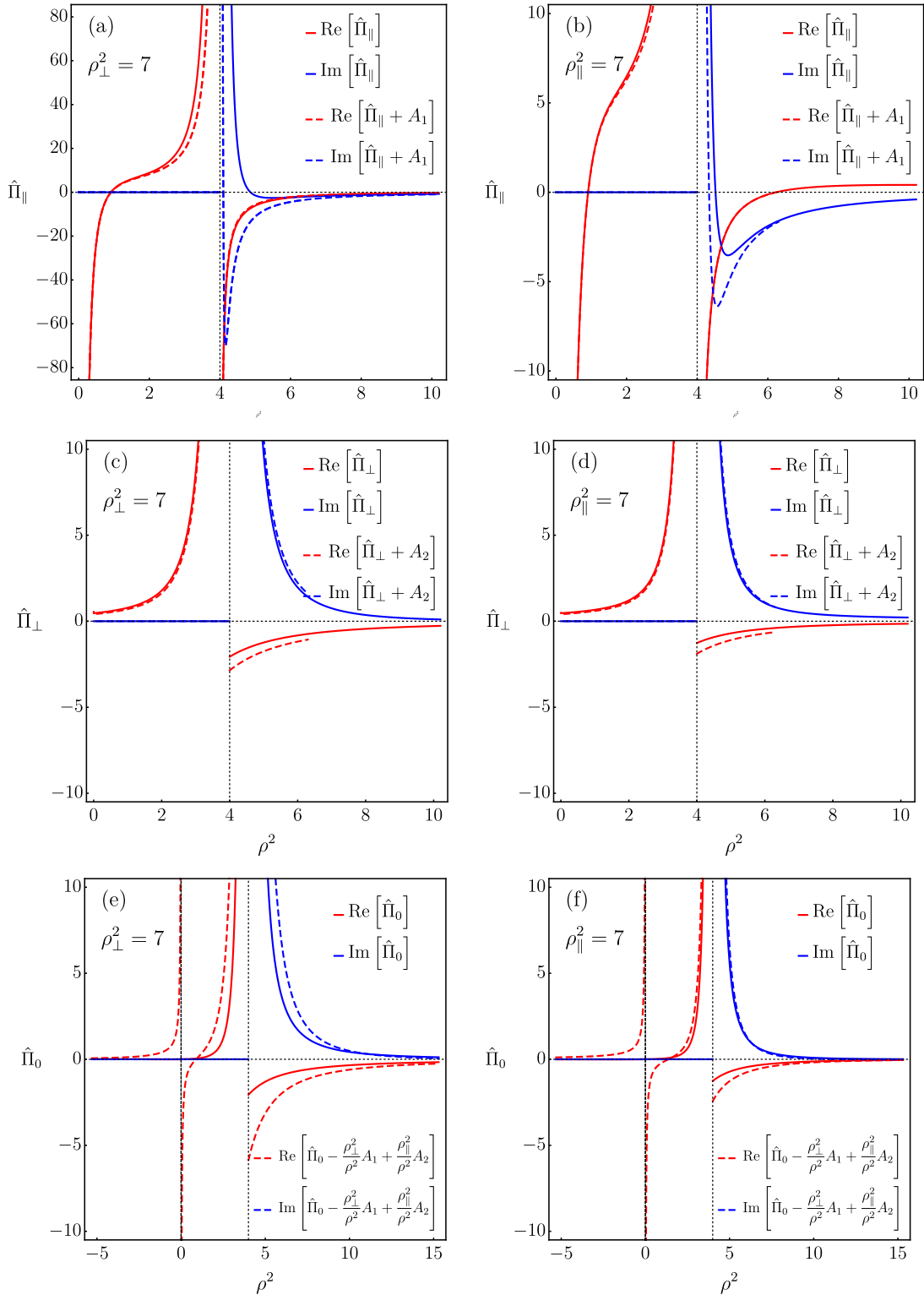


Figure 3.3: Real and imaginary parts of the coefficients $\hat{\Pi}_{\parallel}$, $\hat{\Pi}_{\perp}$ and $\hat{\Pi}_0$ from Eqs. (3.53)-(3.55) as functions of ρ^2 for fixed values of ρ_{\parallel}^2 and ρ_{\perp}^2 . For comparison, these coefficients are also plotted including the spurious contributions from A_1 and A_2 , given by Eqs. (3.29a)-(3.29c).

weak field limit, there is just one value of ρ^2 where such particle production can be reached. The existence of more of these singular points is related to the analytic behavior of the hyperbolic functions in Eq. (3.44). For example, its term proportional to $\coth(\mathcal{B}s)$ is

$$\begin{aligned} \mathcal{K} &= \int_0^1 dy \int_0^\infty ds y(1-y) \mathcal{B} \coth(\mathcal{B}s) \exp \left[s (y(1-y)\rho_{\parallel}^2 - 1) \right] \\ &\times \exp \left[-\frac{\cosh(\mathcal{B}s) - \cosh[\mathcal{B}s(2y-1)]}{2 \sinh(\mathcal{B}s)} \frac{\rho_{\perp}^2}{\mathcal{B}} \right]. \end{aligned} \quad (3.56)$$

such that if $\mathcal{B} \gg 1$

$$\begin{aligned} &\mathcal{B} \coth(\mathcal{B}s) \exp \left[-\frac{\cosh(\mathcal{B}s) - \cosh[\mathcal{B}s(2y-1)]}{2 \sinh(\mathcal{B}s)} \frac{\rho_{\perp}^2}{\mathcal{B}} \right] \\ &= \mathcal{B} \frac{1 + e^{-2\mathcal{B}s}}{1 - e^{-2\mathcal{B}s}} \exp \left\{ \frac{-1 - e^{-2\mathcal{B}s} + e^{-2\mathcal{B}s(y-1)} + e^{-2\mathcal{B}s y}}{2\mathcal{B}(1 - e^{-2\mathcal{B}s})} \rho_{\perp}^2 \right\} \\ &\approx \mathcal{B} \frac{1 + e^{-2\mathcal{B}s}}{1 - e^{-2\mathcal{B}s}} + \mathcal{O}(\rho_{\perp}^2). \end{aligned} \quad (3.57)$$

Using that

$$\frac{1}{1 - e^{-2\mathcal{B}s}} = \sum_{n=0}^{\infty} e^{-2n\mathcal{B}s}, \quad (3.58)$$

it is easy to prove that

$$\frac{1 + e^{-2\mathcal{B}s}}{1 - e^{-2\mathcal{B}s}} = 1 + 2 \sum_{n=1}^{\infty} e^{-2n\mathcal{B}s}, \quad (3.59)$$

so that, the dominant term in Eq. (3.56) is given by

$$\begin{aligned} \mathcal{K} &= \mathcal{B} \int_0^1 dy \int_0^\infty ds y(1-y) \left\{ e^{s(y(1-y)\rho_{\parallel}^2 - 1)} + 2 \sum_{n=1}^{\infty} \exp \left[s (y(1-y)\rho_{\parallel}^2 - 2n\mathcal{B} - 1) \right] \right\} \\ &= \frac{\mathcal{B}}{\rho_{\parallel}^2} I(\rho_{\parallel}^2) + 8\mathcal{B} J(\rho_{\parallel}^2), \end{aligned} \quad (3.60)$$

where $I(x)$ is defined in Eq. (3.47) and

$$J(x) \equiv - \sum_{n=1}^{\infty} \frac{\arctan \left(\frac{\sqrt{x}}{\sqrt{4(2n\mathcal{B}+1)-x}} \right)}{\sqrt{x} [4(2n\mathcal{B}+1) - x]}. \quad (3.61)$$

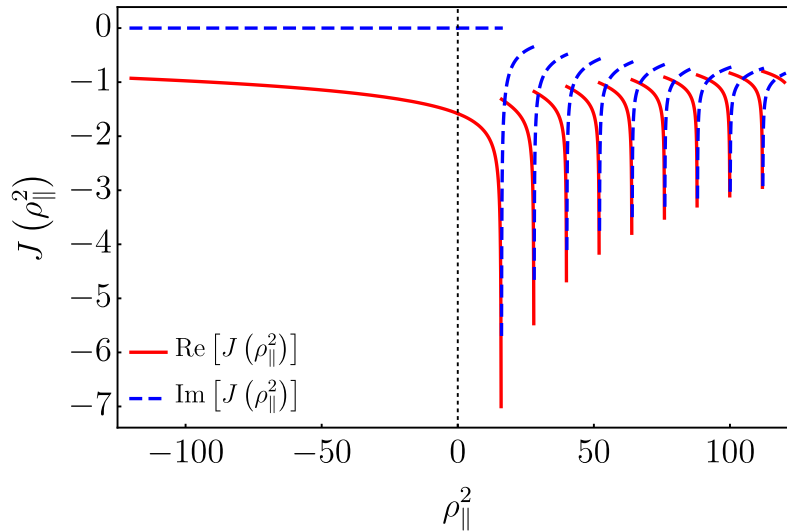


Figure 3.4: Real and imaginary parts of the function $J(\rho_{\parallel}^2)$ defined in Eq. (3.61) for $\mathcal{B} = 1.5$ and added up to $n_{\max} = 100$. Notice the emergence of different resonant thresholds when the quark magnetic mass includes consecutive Landau levels.

Figure 3.4 shows several thresholds of the function $J(\rho_{\parallel}^2)$ in a broad range of ρ_{\parallel}^2 for a maximum value of n , $n_{\max} = 100$. Those singularities appear from Eq. (3.61) when $p_{\parallel}^2 = 4m_{(Bn)f}^2$; thus, if n labels the n -th Landau level, the pair production is allowed when the gluon momentum not only reaches twice the fermion mass but rather the magnetic mass as well. It can be visualized with a classical picture in which the fermion jumps to the next orbit corresponding to the next Landau Level. The infinite sequence of thresholds is a crucial point to be analyzed. First, the resonant condition with the magnetic field implies that non-linear screening properties become essential in a magnetized medium. Such a regime impacts directly onto the direction of motion for the gauge bosons (photons or gluons); hence, one can expect deviations from the original propagation, which may modify the predictions for the flow coefficients. Second, at the resonant condition, the polarization tensor becomes divergent, and this implies that the probability of decay in two fermions is also infinite. The latter can be fixed by considering magnetic corrections to the gluon and quark propagators so that the divergence is adequately treated. A calculation that takes into account the named treatment is work in progress.

The next section is dedicated to understanding the effect of the temperature in the gluon polarization tensor. Its computation in a thermomagnetic medium is carried out by considering the strong magnetic field approximation. The thermal corrections to the so-called magnetic Debye mass are discussed.

3.2 Gluon Polarization Tensor in a Hot and Strongly Magnetized Medium

It is interesting to explore a situation where the dynamics of quarks and gluons evolves in a magnetized medium with a finite temperature. Recently, ab-initio calculations combined with astrophysical observations suggest that the core of neutron stars could be composed of free quarks and gluons, which corresponds to a scenario of low temperature and high magnetic field [276]. To analyze the gluon polarization tensor in a thermo-magnetic medium, it is necessary to take into account the problem's relevant energy scales: the squared fermion-mass m_f^2 , the squared four-momentum p^2 , the temperature T , and the magnetic field strength $|q_f B|$. Also, the breaking of boost and rotational invariance makes the polarization tensor depend separately on the gluon momentum's longitudinal and perpendicular components. Therefore, in this section, the interplay between the different hierarchies and momentum projections are analyzed.

3.2.1 Gluon Polarization Tensor in the High Temperature and Strong Magnetic Field Limits

At finite temperature, the loss of boost invariance is achieved in terms of the vector u^μ that defines the medium's reference frame. Thus, the full-transverse tensor $g^{\mu\nu} - p^\mu p^\nu / p^2$ splits into (three dimensional) transverse $\Pi_T^{\mu\nu}$ and longitudinal $\Pi_L^{\mu\nu}$ structures, such that

$$-g^{\mu\nu} + \frac{p^\mu p^\nu}{p^2} = \Pi_L^{\mu\nu} + \Pi_T^{\mu\nu}, \quad (3.62)$$

with

$$\begin{aligned} \Pi_T^{\mu\nu} &= -g^{\mu\nu} + \frac{q^0}{\mathbf{p}^2} (p^\mu u^\nu + u^\mu p^\nu) - \frac{1}{\mathbf{p}^2} (p^\mu p^\nu + p^2 u^\mu u^\nu), \\ \Pi_L^{\mu\nu} &= -\frac{p^0}{\mathbf{p}^2} (p^\mu u^\nu + u^\mu p^\nu) + \frac{1}{\mathbf{p}^2} \left[\frac{(p^0)^2}{p^2} p^\mu p^\nu + p^2 u^\mu u^\nu \right], \end{aligned} \quad (3.63)$$

where, in the medium's reference frame, $u^\mu = (1, 0, 0, 0)$.

In the strong magnetic field limit, only the tensorial structure $\mathcal{P}_\parallel^{\mu\nu}$ survives which is given by Eq. (3.47). Such tensorial dominance remains even in the thermalized case when $|q_f B| \gg T^2$. This can be understood from the fact that in a strong magnetized field with finite temperature, the fermion-antifermion pair is created in the same Landau Level (the lowest one) in such a way that if $|q_f B|$ is the dominant scale, neither the virtual quark nor the antiquark has enough thermal energy to transit between Landau levels; thus, no other tensor appear in $\Pi^{\mu\nu}$.

It is worth of mentioning that the last prescription is only valid for specific vectors u^μ . There exist the possibility of a non-trivial behavior in a given reference frame in such a manner that an electric field appears. The simultaneous treatment of magnetic and electric field effects on medium's properties has been recently considered in the context of asymmetric collisions or

event-by-event fluctuations in heavy-ion reactions [277]. Electromagnetic effects have also been studied using chiral kinetic theory with Landau level transitions induced by both boosts and rotations [278].

Now, by defining the temperature dependent part of the polarization tensor $\tilde{\Pi}^{\mu\nu}$ as

$$\tilde{\Pi}^{\mu\nu} = \tilde{P}^L \Pi_L^{\mu\nu} + \tilde{P}^T \Pi_T^{\mu\nu}, \quad (3.64)$$

the coefficients \tilde{P}^L and \tilde{P}^T It can be computed through the projections:

$$\begin{aligned} \Pi_{\mu\nu}^L \tilde{\Pi}^{\mu\nu} &= \tilde{P}^L \\ \Pi_{\mu\nu}^T \tilde{\Pi}^{\mu\nu} &= 2\tilde{P}^T. \end{aligned} \quad (3.65)$$

To calculate the above expressions, the quark loop in Fig. 3.1 is assumed to be in the LLL, so that the Eq. (3.1) becomes

$$\begin{aligned} i\Pi^{\mu\nu} &= -g^2 \sum_f \int \frac{d^2 k_\perp}{(2\pi)^2} \exp\left[-\frac{k_\perp^2}{|q_f B|}\right] \exp\left[-\frac{(p_\perp - k_\perp)^2}{|q_f B|}\right] \\ &\times \int \frac{d^2 k_\parallel}{(2\pi)^2} \frac{\text{Tr}[\gamma^\nu (m_f - \not{k}_\parallel) \mathcal{O}^+ \gamma^\mu (m_f - (\not{k} - \not{p})_\parallel) \mathcal{O}^+]}{[k_\parallel^2 - m_f^2][(k - p)_\parallel^2 - m_f^2]}, \end{aligned} \quad (3.66)$$

which, after the perpendicular integration yields

$$\begin{aligned} i\Pi^{\mu\nu} &= -g^2 \sum_f \left(\frac{\pi |q_f B|}{4\pi^2}\right) \exp\left(-\frac{p_\perp^2}{2|q_f B|}\right) \\ &\times \int \frac{d^2 k_\parallel}{(2\pi)^2} \frac{[m_f^2 - k_\parallel \cdot (k - p)_\parallel] g^{\mu\nu} + k_\parallel^\mu (k - p)_\parallel^\nu + k_\parallel^\nu (k - p)_\parallel^\mu}{[k_\parallel^2 - m_f^2][(k - p)_\parallel^2 - m_f^2]}. \end{aligned} \quad (3.67)$$

The temperature effects are included by means the Matsubara imaginary-time formalism:

$$\int \frac{d^4 k}{(2\pi^4)} f(k) \rightarrow iT \sum_{n=-\infty}^{\infty} \int \frac{d^3 k}{(2\pi^3)} f(i\tilde{\omega}_n, \vec{k}), \quad (3.68)$$

where the fermion Matsubara frequencies are $\tilde{\omega}_n = (2n + 1)\pi T$, $k_0 = i\tilde{\omega}_n$ and $q_4 = iq_0 = \omega$. The thermal vacuum has to be isolated, and as one can expect, it results in the pure magnetic contribution of Eq. (3.47). Details are shown in Appendix I.

It is convenient to introduce the Hard Thermal Loop (HTL) approximation [147, 279] which only considers terms where $k \sim T$. Thus, in the high-temperature limits, the sum can be performed in two cases:

- (a) For $p^2 \ll m_f^2 \ll T^2$:

When the external momentum p is considered as the smallest energy scale, in the HTL approximation, the terms p^2 and $k \cdot p$ can be neglected in each of the numerators. The integral over k_3 is shown in Appendix J obtaining that

$$\tilde{P}^L = \frac{g^2}{8\pi^2} \sum_f |q_f B| \exp\left(-\frac{p_\perp^2}{2|q_f B|}\right) \left[\frac{p_0^2(p_\perp^2 + 2p_3^2)}{\mathbf{p}^2 p^2} - 1 \right] \left[\ln\left(\frac{\pi^2 T^2}{m_f^2}\right) - 2\gamma_e \right] \quad (3.69)$$

and

$$\tilde{P}^T = \frac{g^2}{8\pi^2} \sum_f |q_f B| \exp\left(-\frac{p_\perp^2}{2|q_f B|}\right) \frac{p_\perp^2}{\mathbf{p}^2} \left[\ln\left(\frac{\pi^2 T^2}{m_f^2}\right) - 2\gamma_e \right]. \quad (3.70)$$

(b) For $m_f^2 \ll p^2 \ll T^2$:

In this limit, the fermion mass can be ignored and maintain the HTL approximation such that:

$$\tilde{P}^L = \frac{g^2}{64\pi^2} \sum_f |q_f B| \exp\left(-\frac{p_\perp^2}{2|q_f B|}\right) \left(2p_0^2 + p^2 + \frac{p_0^2 p_3^2}{p^2} \right) \left(\frac{p_3^2}{\mathbf{p}^2 p_\parallel^2} \right) \left(\frac{p_3}{T} \right), \quad (3.71)$$

and

$$\tilde{P}^T = -\frac{g^2}{64\pi^2} \sum_f |q_f B| \exp\left(-\frac{p_\perp^2}{2|q_f B|}\right) \left(\frac{p_\perp^2 p_3^2}{p_\parallel^2 \mathbf{p}^2} \right) \left(\frac{p_3}{T} \right). \quad (3.72)$$

The calculation of Eqs. (3.71) and (3.72) can be found in Appendix K.

3.2.2 Correction to the gluon Debye mass

The Debye mass $m_D \equiv p_0$ is defined as the solution of the following equation:

$$\left[p^2 - \tilde{P}^{L,T}(p_0, p_\perp, p_3) \right]_{\mathbf{p}=0} = 0, \quad (3.73)$$

which can be obtained from the coefficients computed in the last section. Notice that in Eqs. (3.69) and (3.70) the result may differ depending on whether the parallel or perpendicular momentum component, with respect to the magnetic field, is taken first to zero. This behavior is due to the breaking of the spatial isotropy and is the analog to the purely thermal case, where the limits when either p_0 or $|\mathbf{p}|$ goes first to zero, do not commute, due to the loss of Lorentz (boost) invariance.

To implement how the momentum components go to zero, the parameter a is included to ensure that p_0 and p_3 have different vanishing rates., i.e., $p_3^2 = ap_\perp^2$. Thus, the matter contribution in Eqs. (3.69) and (3.70) can be written as

$$\tilde{P}^L = \frac{g^2}{8\pi^2} \sum_f |q_f B| \exp\left(-\frac{p_\perp^2}{2|q_f B|}\right) \left[\ln\left(\frac{\pi^2 T^2}{m_f^2}\right) - 2\gamma_e \right] \left[\frac{(1+2a)p_0^2}{(1+a)(p_0^2 - (1+a)p_\perp^2)} - 1 \right], \quad (3.74)$$

and

$$\tilde{P}^T = \frac{g^2}{8\pi^2} \sum_f |q_f B| \exp\left(-\frac{p_\perp^2}{2|q_f B|}\right) \left[\ln\left(\frac{\pi^2 T^2}{m_f^2}\right) - 2\gamma_e \right] \left[\frac{1}{1+a} \right]. \quad (3.75)$$

The discussed limits are:

- (i) $p_\perp \rightarrow 0$ and p_3 finite or $a \rightarrow 0$:

In this case, Eqs. (3.74) and (3.75) become

$$\begin{aligned} \tilde{P}^L &= \frac{g^2}{8\pi^2} \sum_f |q_f B| \left(\frac{p_0^2}{p_\parallel^2} \right) \left[\ln\left(\frac{\pi^2 T^2}{m_f^2}\right) - 2\gamma_e \right] \\ \tilde{P}^T &= 0, \end{aligned} \quad (3.76)$$

which shows that transverse modes are not screened. By taking $p_3 \rightarrow 0$ in the first of Eqs. (3.76), the longitudinal mode develops a Debye mass given by

$$(m_D^2)_L = \frac{g^2}{8\pi^2} \sum_f |q_f B| \left[\ln\left(\frac{\pi^2 T^2}{m_f^2}\right) - 2\gamma_e \right]. \quad (3.77)$$

- (ii) $p_3 \rightarrow 0$ and p_\perp finite:

In this other case, Eqs. (3.74) and (3.75) become

$$\begin{aligned} \tilde{P}^L &= \frac{g^2}{8\pi^2} \sum_f |q_f B| \left[\ln\left(\frac{\pi^2 T^2}{m_f^2}\right) - 2\gamma_e \right] \left(\frac{p_0^2}{p_0^2 - p_\perp^2} - 1 \right) \\ \tilde{P}^T &= \frac{g^2}{8\pi^2} \sum_f |q_f B| \left[\ln\left(\frac{\pi^2 T^2}{m_f^2}\right) - 2\gamma_e \right], \end{aligned} \quad (3.78)$$

so that by taking $p_\perp \rightarrow 0$, $\tilde{P}^L = 0$ and this time it is the transverse modes which develop a Debye mass given by

$$(m_D^2)_T = \frac{g^2}{8\pi^2} \sum_f |q_f B| \left[\ln\left(\frac{\pi^2 T^2}{m_f^2}\right) - 2\gamma_e \right], \quad (3.79)$$

whereas the longitudinal one is not screened. Note that for these limits $(m_D^2)_L = (m_D^2)_T$.

- (iii) p_3 and $p_\perp \rightarrow 0$ at the same rate:

In this last case, Eqs. (3.74) and (3.75) become

$$\tilde{P}^L = \tilde{P}^T = \frac{g^2}{16\pi^2} \sum_f |q_f B| \left[\ln\left(\frac{\pi^2 T^2}{m_f^2}\right) - 2\gamma_e \right] \quad (3.80)$$

and both the longitudinal and transverse modes develop a Debye mass given by

$$(m_D^2)_L = (m_D^2)_T = \frac{g^2}{16\pi^2} \sum_f |q_f B| \left[\ln \left(\frac{\pi^2 T^2}{m_f^2} \right) - 2\gamma_E \right]. \quad (3.81)$$

Notice that when p_3 and p_\perp vanish at the same rate, both modes are screened and the Debye mass of the longitudinal mode is equal to that of the transverse mode. Finally, the sum of both transverse and longitudinal masses in the three cases gives:

$$(m_D^2)_L + (m_D^2)_T = \frac{g^2}{8\pi^2} \sum_f |q_f B| \left[\ln \left(\frac{\pi^2 T^2}{m_f^2} \right) - 2\gamma_E \right]. \quad (3.82)$$

3.3 Gluon Polarization Tensor in a Weakly Magnetized Medium

As discussed in previous sections, the magnetic field in heavy-ion collisions is estimated to have an intensity comparable to the pion-mass squared. Nevertheless, the magnetic field intensity decreases in a short time, and it cannot be considered as the dominant energy scale, which enforces to perform calculations in a weak magnetic field approximation. An example of such a situation can be found in Ref. [280], where heavy quarkonia's properties immersed in a thermal medium of quarks and gluons are computed by assuming a weak magnetic field background.

Clearly, in a QCD-medium, the magnetic field effects are directly encoded in the quark's (real or virtual) dynamics, which implies that the fermion propagator has to be appropriately written in the desired approximation. The computation of charged fermion and scalar propagators in the weak field limit were computed as an expansion of the full magnetized propagator of Eq. (2.47) [232, 281]. Moreover, the general expression shown in Eq. (3.41) can be expanded in powers of $|q_f B|$, by considering that momentum and fermion mass are the higher energy scales. Thus, it is natural to assume that the expression of the gluon one-loop self-energy starting from the fermion propagator in a weak magnetic field yields the same results as the ones obtained from the power series expansion of the general polarization tensor result. However, as it will be shown in this section, the former procedure has crucial subtleties regarding gauge invariance encoded in the transversality properties of the polarization tensor.

3.3.1 Weak Field Approximation of the Fermion Propagator Revisited

An expression for the fermion propagator when the magnetic field is considered as the weakest energy scale is provided in Ref. [281]. Nonetheless, although the calculation is correct, the procedure to find it is hard to read, obscuring the origin of the results. Here, a straightforward and more intuitive procedure is presented.

Starting from the Landau Levels representation of the fermion propagator:

$$iS(p) = ie^{-p_{\perp}^2/|q_f B|} \sum_{n=0}^{\infty} (-1)^n \frac{D_n(q_f B, p)}{p_{\parallel}^2 - m_f^2 - 2n|q_f B|}, \quad (3.83)$$

where $D_n(q_f B, p)$ is given by Eq. (2.48):

$$D_n(q_f B, p) = 2(p_{\parallel} + m_f) \left[\mathcal{O}^- L_n^0 \left(\frac{2p_{\perp}^2}{|q_f B|} \right) - \mathcal{O}^+ L_{n-1}^0 \left(\frac{2p_{\perp}^2}{|q_f B|} \right) \right] + 4p_{\perp} L_{n-1}^1 \left(\frac{2p_{\perp}^2}{|q_f B|} \right), \quad (3.84)$$

and the operators \mathcal{O}^{\pm} are given in Eq. (2.49), the denominators in Eq. (3.83) can be promoted to a geometric series, by assuming that $|q_f B|$ is the smaller scale, namely,

$$\frac{1}{p_{\parallel}^2 - m_f^2 - 2n|q_f B|} = \frac{1}{p_{\parallel}^2 - m_f^2} \sum_{k=0}^{\infty} \left(\frac{2n|q_f B|}{p_{\parallel}^2 - m_f^2} \right)^k. \quad (3.85)$$

From the above, three sums are identified:

$$\begin{aligned} s_1 &= \frac{2ie^{-\alpha}}{p_{\parallel}^2 - m_f^2} \sum_{n=0}^{\infty} (-1)^n \frac{L_n^0(2\alpha)}{1 - \frac{2n|q_f B|}{p_{\parallel}^2 - m_f^2}} \\ &= \frac{2ie^{-\alpha}}{p_{\parallel}^2 - m_f^2} \sum_{k=0}^{\infty} \left(\frac{2|q_f B|}{p_{\parallel}^2 - m_f^2} \right)^k \sum_{n=0}^{\infty} (-1)^n n^k L_n^0(2\alpha), \end{aligned} \quad (3.86a)$$

$$\begin{aligned} s_2 &= -\frac{2ie^{-\alpha}}{p_{\parallel}^2 - m_f^2} \sum_{n=1}^{\infty} (-1)^n \frac{L_{n-1}^0(2\alpha)}{1 - \frac{2n|q_f B|}{p_{\parallel}^2 - m_f^2}} \\ &= -\frac{2ie^{-\alpha}}{p_{\parallel}^2 - m_f^2} \sum_{k=0}^{\infty} \left(\frac{2|q_f B|}{p_{\parallel}^2 - m_f^2} \right)^k \sum_{n=1}^{\infty} (-1)^n n^k L_{n-1}^0(2\alpha), \end{aligned} \quad (3.86b)$$

$$\begin{aligned} s_3 &= \frac{4ie^{-\alpha}}{p_{\parallel}^2 - m_f^2} \sum_{n=1}^{\infty} (-1)^n \frac{L_{n-1}^1(2\alpha)}{1 - \frac{2n|q_f B|}{p_{\parallel}^2 - m_f^2}} \\ &= \frac{4ie^{-\alpha}}{p_{\parallel}^2 - m_f^2} \sum_{k=0}^{\infty} \left(\frac{2|q_f B|}{p_{\parallel}^2 - m_f^2} \right)^k \sum_{n=1}^{\infty} (-1)^n n^k L_{n-1}^1(2\alpha). \end{aligned} \quad (3.86c)$$

with $\alpha = p_{\perp}^2/|q_f B|$. The sum in n can easily be computed with the help of the following identities:

$$e^{-\alpha} \sum_{n=0}^{\infty} (-1)^n e^{-2in\alpha} L_n^0(2\alpha) = \frac{e^{i\alpha}}{2 \cos \alpha} e^{-i\alpha \tan \alpha}, \quad (3.87a)$$

$$e^{-\alpha} \sum_{n=0}^{\infty} (-1)^n e^{-2i(n+1)v} L_n^1(2\alpha) = \frac{1}{4 \cos^2 v} e^{-i\alpha \tan v}, \quad (3.87b)$$

so that

$$e^{-\alpha} \sum_{n=0}^{\infty} (-1)^n n^k L_n^0(2\alpha) = \frac{1}{(-2i)^k} \lim_{v \rightarrow 0} \frac{\partial^k}{\partial v^k} \left(\frac{e^{iv}}{2 \cos v} e^{-i\alpha \tan v} \right), \quad (3.88a)$$

$$e^{-\alpha} \sum_{n=0}^{\infty} (-1)^n (n+1)^k e^{-2i(n+1)v} L_n^1(2\alpha) = \frac{1}{(-2i)^k} \lim_{v \rightarrow 0} \frac{\partial^k}{\partial v^k} \left(\frac{1}{4 \cos^2 v} e^{-i\alpha \tan v} \right). \quad (3.88b)$$

Therefore,

$$s_1 = \frac{i}{p_{\parallel}^2 - m_f^2} \lim_{v \rightarrow 0} \sum_{k=0}^{\infty} \left(\frac{i |q_f B|}{p_{\parallel}^2 - m_f^2} \right)^k \frac{\partial^k}{\partial v^k} \left(\frac{e^{iv}}{\cos v} e^{-i\alpha \tan v} \right) \equiv \frac{i}{p_{\parallel}^2 - m_f^2} \sigma_1, \quad (3.89a)$$

$$s_2 = \frac{i}{p_{\parallel}^2 - m_f^2} \lim_{v \rightarrow 0} \sum_{k=0}^{\infty} \left(\frac{i |q_f B|}{p_{\parallel}^2 - m_f^2} \right)^k \frac{\partial^k}{\partial v^k} \left(\frac{e^{-iv}}{\cos v} e^{-i\alpha \tan v} \right) \equiv \frac{i}{p_{\parallel}^2 - m_f^2} \sigma_2, \quad (3.89b)$$

and

$$s_3 = -\frac{i}{p_{\parallel}^2 - m_f^2} \lim_{v \rightarrow 0} \sum_{k=0}^{\infty} \left(\frac{i |q_f B|}{p_{\parallel}^2 - m_f^2} \right)^k \frac{\partial^k}{\partial v^k} \left(\frac{e^{-i\alpha \tan v}}{\cos^2 v} \right) \equiv -\frac{i}{p_{\parallel}^2 - m_f^2} \sigma_3. \quad (3.89c)$$

The sum in k has not a closed-form, but it can be expanded at the desired order in the parameters $(|q_f B|, p_{\parallel}^2, p_{\perp}^2, m_f^2)$ by simple evaluation. For example, for $k_{\max} = 10$ and together with the definitions $x = p_{\perp}^2 / (p_{\parallel}^2 - m_f^2)$ and $\mathfrak{B} = |q_f B| / (p_{\parallel}^2 - m_f^2)$, one get:

$$\begin{aligned} \sigma_1 &= (1 + x + x^2 + x^3 + x^4 + x^5 + x^6 + x^7 + x^8 + x^9 + x^{10} + \dots) \\ &- (1 + 2x + 3x^2 + 4x^3 + 5x^4 + 6x^5 + 7x^6 + 8x^7 + 9x^8 + 10x^9 + 11x^{10} + \dots) \mathfrak{B} \\ &- 2x (1 + 4x + 10x^2 + 20x^3 + 35x^4 + 56x^5 + 84x^6 + 120x^7 + 165x^8 + 220x^9 \\ &+ 286x^{10} + \dots) \mathfrak{B}^2 + 2 (1 + 8x + 30x^2 + 80x^3 + 175x^4 + 336x^5 + 588x^6 + 960x^7 \\ &+ 1485x^8 + 2200x^9 + 3146x^{10} + \dots) \mathfrak{B}^3 + 8x (2 + 17x + 77x^2 + 252x^3 + 672x^4 \\ &+ 1554x^5 + 3234x^6 + 6204x^7 + 11154x^8 + 19019x^9 + 31031x^{10} + \dots) \mathfrak{B}^4 \\ &- 8 (2 + 34x + 231x^2 + 1008x^3 + 3360x^4 + 9324x^5 + 22638x^6 + 49632x^7 + 100386x^8 \\ &+ 190190x^9 + 341341x^{10} + \dots) \mathfrak{B}^5 - 16x (17 + 248x + 1760x^2 + 8480x^3 + 31790x^4 \\ &+ 99704x^5 + 273416x^6 + 674960x^7 + 1530815x^8 + 3237520x^9 + 6456736x^{10} + \dots) \mathfrak{B}^6 \\ &+ \mathcal{O}(\mathfrak{B}^7), \end{aligned} \quad (3.90a)$$

$$\begin{aligned}
\sigma_2 = & (1 + x + x^2 + x^3 + x^4 + x^5 + x^6 + x^7 + x^8 + x^9 + x^{10} + \dots) \\
& + (1 + 2x + 3x^2 + 4x^3 + 5x^4 + 6x^5 + 7x^6 + 8x^7 + 9x^8 + 10x^9 + 11x^{10} + \dots) \mathfrak{B} \\
& - 2x (1 + 4x + 10x^2 + 20x^3 + 35x^4 + 56x^5 + 84x^6 + 120x^7 + 165x^8 + 220x^9 \\
& + 286x^{10} + \dots) \mathfrak{B}^2 - 2 (1 + 8x + 30x^2 + 80x^3 + 175x^4 + 336x^5 + 588x^6 + 960x^7 \\
& + 1485x^8 + 2200x^9 + 3146x^{10} + \dots) \mathfrak{B}^3 + 8x (2 + 17x + 77x^2 + 252x^3 + 672x^4 \\
& + 1554x^5 + 3234x^6 + 6204x^7 + 11154x^8 + 19019x^9 + 31031x^{10} + \dots) \mathfrak{B}^4 \\
& - 8 (2 + 34x + 231x^2 + 1008x^3 + 3360x^4 + 9324x^5 + 22638x^6 + 49632x^7 + 100386x^8 \\
& + 190190x^9 + 341341x^{10} + \dots) \mathfrak{B}^5 - 16x (17 + 248x + 1760x^2 + 8480x^3 + 31790x^4 \\
& + 99704x^5 + 273416x^6 + 674960x^7 + 1530815x^8 + 3237520x^9 + 6456736x^{10} + \dots) \mathfrak{B}^6 \\
& + \mathcal{O}(\mathfrak{B}^7), \tag{3.90b}
\end{aligned}$$

and

$$\begin{aligned}
\sigma_3 = & (1 + x + x^2 + x^3 + x^4 + x^5 + x^6 + x^7 + x^8 + x^9 + x^{10} + \dots) \\
& - 2 (1 + 4x + 10x^2 + 20x^3 + 35x^4 + 56x^5 + 84x^6 + 120x^7 + 165x^8 + 220x^9 \\
& + 286x^{10} + \dots) \mathfrak{B}^2 + 8 (2 + 17x + 77x^2 + 252x^3 + 672x^4 + 1554x^5 + 3234x^6 \\
& + 6204x^7 + 11154x^8 + 19019x^9 + 31031x^{10} + \dots) \mathfrak{B}^4 - 16 (17 + 248x + 1760x^2 \\
& + 8480x^3 + 31790x^4 + 99704x^5 + 273416x^6 + 674960x^7 + 1530815x^8 + 3237520x^9 \\
& + 6456736x^{10}) \mathfrak{B}^6 + \mathcal{O}(\mathfrak{B}^8). \tag{3.90c}
\end{aligned}$$

The power series of x in Eqs. (3.90) can be recognized as polynomial expressions:

$$\begin{aligned}
\sigma_1 = & \frac{1}{1-x} - \frac{\mathfrak{B}}{(1-x)^2} - \frac{2x\mathfrak{B}^2}{(1-x)^4} + \frac{2(3x+1)\mathfrak{B}^3}{(1-x)^5} + \frac{8x(3x+2)\mathfrak{B}^4}{(1-x)^7} \\
& - \frac{8(15x^2+18x+2)\mathfrak{B}^5}{(1-x)^8} - \frac{16x(45x^2+78x+17)\mathfrak{B}^6}{(1-x)^{10}} + \mathcal{O}(\mathfrak{B}^7), \tag{3.91a}
\end{aligned}$$

$$\begin{aligned}
\sigma_2 = & \frac{1}{1-x} + \frac{\mathfrak{B}}{(1-x)^2} - \frac{2x\mathfrak{B}^2}{(1-x)^4} - \frac{2(3x+1)\mathfrak{B}^3}{(1-x)^5} + \frac{8x(3x+2)\mathfrak{B}^4}{(1-x)^7} \\
& + \frac{8(15x^2+18x+2)\mathfrak{B}^5}{(1-x)^8} - \frac{16x(45x^2+78x+17)\mathfrak{B}^6}{(1-x)^{10}} + \mathcal{O}(\mathfrak{B}^7), \tag{3.91b}
\end{aligned}$$

and

$$\begin{aligned}
\sigma_3 = & \frac{1}{1-x} - \frac{2\mathfrak{B}^2}{(1-x)^4} + \frac{8(3x+2)\mathfrak{B}^4}{(1-x)^7} - \frac{16(45x^2+78x+17)\mathfrak{B}^6}{(1-x)^{10}} + \mathcal{O}(\mathfrak{B}^8). \tag{3.91c}
\end{aligned}$$

Thus, the fermion propagator is obtained by replacing Eqs. (3.91) into Eqs. (3.89) and Eqs. (3.86), by taking into account the tensor structure given by

$$\psi = \psi_{\parallel} - \psi_{\perp}, \tag{3.92a}$$

$$\mathcal{O}^+ + \mathcal{O}^- = 1, \quad (3.92b)$$

and

$$\mathcal{O}^+ - \mathcal{O}^- = i \operatorname{sign}(q_f B) \gamma^1 \gamma^2, \quad (3.92c)$$

so that up to order $\mathcal{O}(\mathfrak{B}^6)$ reads

$$\begin{aligned} iS(p) &= \frac{i}{1-x} \frac{\not{p} + m_f}{p_{\parallel}^2 - m_f^2} \\ &- \left[\frac{\mathfrak{B}}{(1-x)^2} - \frac{2(3x+1)\mathfrak{B}^3}{(1-x)^5} + \frac{8(15x^2+18x+2)\mathfrak{B}^5}{(1-x)^8} \right] \operatorname{sign}(q_f B) \gamma^1 \gamma^2 \frac{\not{p}_{\parallel} + m_f}{p_{\parallel}^2 - m_f^2} \\ &- i \left[\frac{2\mathfrak{B}^2}{(1-x)^4} - \frac{8(3x+2)\mathfrak{B}^4}{(1-x)^7} - \frac{16(45x^2+78x+17)\mathfrak{B}^6}{(1-x)^{10}} \right] \frac{x(\not{p}_{\parallel} + m_f) - \not{p}_{\perp}}{p_{\parallel}^2 - m_f^2}, \end{aligned} \quad (3.93)$$

which after substituting x and \mathfrak{B} yields

$$\begin{aligned} iS(p) &= \frac{i(\not{p} + m_f)}{p^2 - m_f^2} - \mathcal{G}_1(p, B) \operatorname{sign}(q_f B) \gamma^1 \gamma^2 (\not{p}_{\parallel} + m_f) \\ &- 2i(p_{\parallel}^2 - m_f^2) \mathcal{G}_2(p, B) \left[\frac{p_{\perp}^2}{p_{\parallel}^2 - m_f^2} (\not{p}_{\parallel} + m_f) - \not{p}_{\perp} \right], \end{aligned} \quad (3.94)$$

where

$$\begin{aligned} \mathcal{G}_1(p, B) &\equiv \frac{|q_f B|}{(p^2 - m_f^2)^2} - 2 \frac{3p_{\perp}^2 + p_{\parallel}^2 - m_f^2}{(p^2 - m_f^2)^5} |q_f B|^3 \\ &+ 8 \frac{15p_{\perp}^4 + 18p_{\perp}^2(p_{\parallel}^2 - m_f^2) + 2(p_{\parallel}^2 - m_f^2)^2}{(p^2 - m_f^2)^8} |q_f B|^5, \end{aligned} \quad (3.95a)$$

and

$$\begin{aligned} \mathcal{G}_2(p, B) &\equiv \frac{|q_f B|^2}{(p^2 - m_f^2)^4} - 4 \frac{3p_{\perp}^2 - 2(p_{\parallel}^2 - m_f^2)}{(p^2 - m_f^2)^7} |q_f B|^4 \\ &- 8 \frac{45p_{\perp}^4 + 78(p_{\parallel}^2 - m_f^2) + 17(p_{\parallel}^2 - m_f^2)^2}{(p^2 - m_f^2)^{10}} |q_f B|^6. \end{aligned} \quad (3.95b)$$

Notice that Eq. (3.94) also can be obtained from the propagator in the Schwinger proper-time representation given by

$$\begin{aligned} iS(p) &= i \int_0^{\infty} d\tau \exp \left[\tau \left(p_{\parallel}^2 - p_{\perp}^2 \frac{\tanh(\tau |q_f B|)}{\tau |q_f B|} - m_f^2 \right) \right] \\ &\times \left\{ [m_f + \not{p}_{\parallel}] [1 + i\gamma^1 \gamma^2 \tanh(\tau |q_f B|) \operatorname{sign}(q_f B)] - \frac{\not{p}_{\perp}}{\cosh(\tau |q_f B|)^2} \right\}, \end{aligned} \quad (3.96)$$

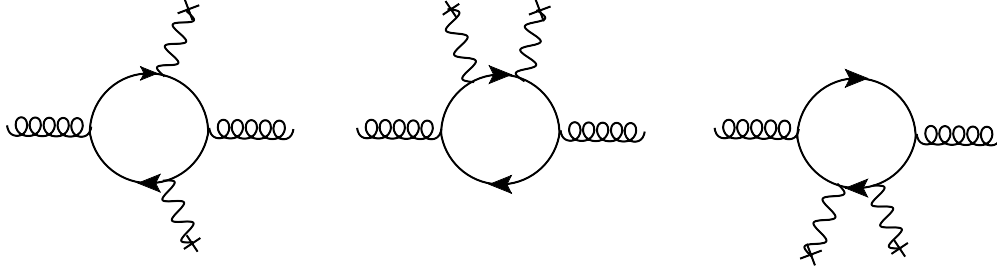


Figure 3.5: Feynman diagrams contributing to the one-loop gluon polarization tensor in the weak field limit up to $\mathcal{O}(|q_f B|^2)$. From the left to the right: $i\Pi_{(1,1)}^{\mu\nu}$, $i\Pi_{(2,0)}^{\mu\nu}$ and $i\Pi_{(0,2)}^{\mu\nu}$.

by performing a Taylor's series expansion for $\tau|q_f B| \sim 0$ and then integrating over the proper time parameter τ . Such a method reveals that the dominant region for the integration over the proper-time parameter is the small τ region and that, in order to obtain analytical results, this region can be extended to cover the whole original domain $0 \leq \tau \leq \infty$.

3.3.2 One-Loop Gluon Polarization Tensor

From the definition of the one-loop gluon polarization tensor:

$$i\Pi_{ab}^{\mu\nu}(p) = - \int \frac{d^4k}{(2\pi)^4} \text{Tr} \{igt_b \gamma^\nu iS(k)igt_a \gamma^\mu iS(k-p)\} + \text{C.C.}, \quad (3.97)$$

and from the fermion propagator up to order $\mathcal{O}(|q_f B|^2)$:

$$\begin{aligned} iS(k) &= i \frac{\not{k} + m_f}{k^2 - m^2} - |q_f B| \frac{\gamma^1 \gamma^2 (\not{k}_\parallel + m_f)}{(k^2 - m_f^2)^2} \text{sign}(q_f B) \\ &\quad - |q_f B|^2 \frac{2ik_\perp^2}{(k^2 - m_f^2)^4} \left[m_f + \not{k}_\parallel + \not{k}_\perp \left(\frac{m_f^2 - k_\parallel^2}{k_\perp^2} \right) \right] \\ &\equiv iS^{(0)}(k) + iS^{(1)}(k) + iS^{(2)}(k), \end{aligned} \quad (3.98)$$

where $iS^{(n)}(k)$ represent the contribution of order $\mathcal{O}(|q_f B|^n)$. The magnetized gluon polarization tensor comprises three non-vanishing contributions: one coming from a trace involving the product $S^{(1)} \times S^{(1)}$ (denoted by $i\Pi_{(1,1)}^{\mu\nu}$), other with the product $S^{(2)} \times S^{(0)}$ (denoted by $i\Pi_{(2,0)}^{\mu\nu}$), and its counterpart $S^{(0)} \times S^{(2)}$ (denoted by $i\Pi_{(0,2)}^{\mu\nu}$). The $S^{(0)} \times S^{(0)}$ term originates the vacuum contribution.

The magnetic contributions written in the basis $(\mathcal{P}_\parallel^{\mu\nu}, \mathcal{P}_\perp^{\mu\nu}, \mathcal{P}_0^{\mu\nu})$ defined in Eqs. (3.15)-(3.17)

have the following explicit form (for details see Appendix L):

$$\begin{aligned}
i\Pi_{(1,1)}^{\mu\nu} &= -\frac{2i|q_f B|^2 g^2}{16\pi^2} \int_0^1 dy \int_0^\infty ds sy(1-y) \exp\left[-s(m_f^2 + y(y-1)p^2)\right] \\
&\times \left\{ 2y(1-y)p_{\parallel}^2 \mathcal{P}_{\parallel}^{\mu\nu} + g_{\parallel}^{\mu\nu} [m_f^2 - y(1-y)p_{\parallel}^2] + g_{\perp}^{\mu\nu} \left[-m_f^2 - \frac{1}{s} - y(1-y)p_{\parallel}^2\right] \right\}, \quad (3.99)
\end{aligned}$$

$$\begin{aligned}
i\Pi_{(2,0)}^{\mu\nu} + i\Pi_{(0,2)}^{\mu\nu} &= -\frac{2}{3} \left(\frac{i}{16\pi^2}\right) g^2 |q_f B|^2 \int_0^1 dy \int_0^\infty ds s \exp\left[-s(m_f^2 + y(y-1)p^2)\right] \\
&\times \left\{ g_{\parallel}^{\mu\nu} \left[-\frac{1}{s} + sy^3(y-1)^3 p_{\parallel}^2 p_{\perp}^2 - sy^3(y-1)^3 p_{\perp}^4 - y(y-1)(1+2y(y-1))p_{\perp}^2 \right. \right. \\
&\quad \left. \left. + y(y-1)(1+2y(y-1))p_{\parallel}^2 + m_f^2(1-3y(y-1) + sy^2(y-1)^2 p_{\perp}^2) \right] \right. \\
&\quad \left. + g_{\perp}^{\mu\nu} \left[\frac{1+3y(y-1)}{s} + sy^3(y-1)^3 p_{\parallel}^2 p_{\perp}^2 - sy^3(y-1)^3 p_{\perp}^4 + y(y-1)p_{\perp}^2 \right. \right. \\
&\quad \left. \left. + y(1+y^2(y-2))p_{\parallel}^2 + m_f^2(1-3y(y-1) + sy^2(y-1)^2 p_{\perp}^2) \right] \right. \\
&\quad \left. + \mathcal{P}_0^{\mu\nu} [-4y^2(y-1)^2 p^2 - 2sy^3(y-1)^3 p^2 p_{\perp}^2] \right. \\
&\quad \left. + \mathcal{P}_{\parallel}^{\mu\nu} [-2y(y-1)(1+3y(y-1))p_{\parallel}^2 + 4y^2(y-1)^2 p_{\perp}^2 - 2sy^3(y-1)^3 p^2 p_{\perp}^2] \right. \\
&\quad \left. + \mathcal{P}_{\perp}^{\mu\nu} [-4y^2(y-1)^2 p_{\parallel}^2 + 2y(1+y^2(y-2))p_{\perp}^2 - 2sy^3(y-1)^3 p^2 p_{\perp}^2] \right\}. \quad (3.100)
\end{aligned}$$

Therefore, the gluon polarization tensor in a weak magnetized field is given by

$$\begin{aligned}
i\Pi^{\mu\nu} &= -\frac{2}{3} \left(\frac{i}{16\pi^2} \right) g^2 |q_f B|^2 \int_0^1 dy \int_0^\infty ds s \exp \left[-s(m_f^2 + y(y-1)p^2) \right] \\
&\times \left\{ g_{\parallel}^{\mu\nu} \left[-\frac{1}{s} + sy^3(y-1)^3 p_{\parallel}^2 p_{\perp}^2 - sy^3(y-1)^3 p_{\perp}^4 - y(y-1)(1+2y(y-1))p_{\perp}^2 \right. \right. \\
&\quad \left. \left. + y(y-1)p_{\parallel}^2 + m_f^2 (1 + sy^2(y-1)^2 p_{\perp}^2) \right] \right. \\
&\quad \left. + g_{\perp}^{\mu\nu} \left[\frac{1+6y(y-1)}{s} + sy^3(y-1)^3 p_{\parallel}^2 p_{\perp}^2 - sy^3(y-1)^3 p_{\perp}^4 + y(y-1)p_{\perp}^2 \right. \right. \\
&\quad \left. \left. - y(y-1)(1+2y(y-1))p_{\parallel}^2 + m_f^2 (1+6y(y-1) + sy^2(y-1)^2 p_{\perp}^2) \right] \right. \\
&\quad \left. + \mathcal{P}_0^{\mu\nu} [-4y^2(y-1)^2 p^2 - 2sy^3(y-1)^3 p^2 p_{\perp}^2] \right. \\
&\quad \left. + \mathcal{P}_{\parallel}^{\mu\nu} [-2y(y-1)p_{\parallel}^2 + 4y^2(y-1)^2 p_{\perp}^2 - 2sy^3(y-1)^3 p^2 p_{\perp}^2] \right. \\
&\quad \left. + \mathcal{P}_{\perp}^{\mu\nu} [-4y^2(y-1)^2 p_{\parallel}^2 + 2y(1+y^2(y-2))p_{\perp}^2 - 2sy^3(y-1)^3 p^2 p_{\perp}^2] \right\}. \quad (3.101)
\end{aligned}$$

Note that the last expression has the form

$$\Pi^{\mu\nu} = P_{\parallel} \mathcal{P}_{\parallel}^{\mu\nu} + P_{\perp} \mathcal{P}_{\perp}^{\mu\nu} + P_0 \mathcal{P}_0^{\mu\nu} + A_1 g_{\parallel}^{\mu\nu} + A_2 g_{\perp}^{\mu\nu}, \quad (3.102)$$

which as in the case of an arbitrary magnetic field contains terms proportional to $g_{\parallel}^{\mu\nu}$ and $g_{\perp}^{\mu\nu}$. That fact breaks the gauge invariance of the tensor, given that the presence of such coefficients implies a non-transverse structure. Nevertheless, coefficients A_1 and A_2 vanish when the integration over s and y is performed. Hence, the full transverse gluon polarization tensor is

$$\begin{aligned}
i\Pi^{\mu\nu} &= -\frac{2}{3} \left(\frac{i}{16\pi^2} \right) g^2 |q_f B|^2 \int_0^1 dy \int_0^\infty ds s \exp \left[-s(m_f^2 + y(y-1)p^2) \right] \\
&\times \left\{ \mathcal{P}_0^{\mu\nu} [-4y^2(y-1)^2 p^2 - 2sy^3(y-1)^3 p^2 p_{\perp}^2] \right. \\
&\quad \left. + \mathcal{P}_{\parallel}^{\mu\nu} [-2y(y-1)p_{\parallel}^2 + 4y^2(y-1)^2 p_{\perp}^2 - 2sy^3(y-1)^3 p^2 p_{\perp}^2] \right. \\
&\quad \left. + \mathcal{P}_{\perp}^{\mu\nu} [-4y^2(y-1)^2 p_{\parallel}^2 + 2y(1+y^2(y-2))p_{\perp}^2 - 2sy^3(y-1)^3 p^2 p_{\perp}^2] \right\}. \quad (3.103)
\end{aligned}$$

Noticeably, the integrals over s and y can be computed analytically with the constraint $0 \leq p^2 \leq 4m_f^2$, obtaining the coefficients for each tensor structure:

$$\begin{aligned}
P_0 &= \frac{ig^2 |q_f B|^2}{6\pi^2} \left\{ \frac{p^2 - 6m^2}{p^2 (p^2 - 4m^2)} + \frac{(p^2 - 10m^2)(p^2 - 3m^2)}{p^4 (p^2 - 4m^2)^2} p_{\perp}^2 \right. \\
&\quad \left. + \left[\frac{8m^2 (p^2 - 3m^2)}{(p^2)^{3/2} (4m^2 - p^2)^{3/2}} - \frac{12m^2 (10m^4 + (p^2 - 6m^2)p^2)}{(4m^2 - p^2)^{5/2} (p^2)^{5/2}} p_{\perp}^2 \right] \arctan \left(\sqrt{\frac{p^2}{4m_f^2 - p^2}} \right) \right\}, \quad (3.104a)
\end{aligned}$$

$$\begin{aligned}
P_{\parallel} = & \frac{ig^2 |q_f B|^2}{6\pi^2} \left\{ -\frac{p_{\parallel}^2}{(4m^2 - p^2) p^2} - \frac{(p^2 - 6m^2)p_{\perp}^2}{p^4 (p^2 - 4m^2)} + \frac{(p^2 - 10m^2)(p^2 - 3m^2)p_{\perp}^2}{p^4 (p^2 - 4m^2)^2} \right. \\
+ & \left[\frac{-2(p^2 - 2m^2)p_{\parallel}^2}{(4m^2 - p^2)^{3/2} (p^2)^{3/2}} - \frac{8m^2(p^2 - 3m^2)p_{\perp}^2}{(4m^2 - p^2)^{3/2} (p^2)^{5/2}} - \frac{12m^2(10m^4 + (p^2 - 6m^2)p^2)}{(4m^2 - p^2)^{5/2} (p^2)^{5/2}} p_{\perp}^2 \right] \\
\times & \left. \arctan \left(\sqrt{\frac{p^2}{4m_f^2 - p^2}} \right) \right\}, \tag{3.104b}
\end{aligned}$$

$$\begin{aligned}
P_{\perp} = & \frac{ig^2 |q_f B|^2}{6\pi^2} \left\{ \frac{(p^2 - 6m^2)p_{\parallel}^2}{p^4 (p^2 - 4m^2)} - \frac{(6m^2 + p^2)p_{\perp}^2}{2(4m^2 - p^2)p^4} + \frac{(p^2 - 10m^2)(p^2 - 3m^2)p_{\perp}^2}{p^4 (p^2 - 4m^2)^2} \right. \\
+ & \left[\frac{8m^2(p^2 - 3m^2)p_{\parallel}^2}{(4m^2 - p^2)^{3/2} (p^2)^{5/2}} + \frac{2(6m^4 - p^4)p_{\perp}^2}{(4m^2 - p^2)^{3/2} (p^2)^{5/2}} - \frac{12m^2(10m^4 + (p^2 - 6m^2)p^2)}{(4m^2 - p^2)^{5/2} (p^2)^{5/2}} p_{\perp}^2 \right] \\
\times & \left. \arctan \left(\sqrt{\frac{p^2}{4m_f^2 - p^2}} \right) \right\}. \tag{3.104c}
\end{aligned}$$

which is the same result of Eqs. (3.53)-(3.55).

3.3.3 Gluon Dispersion Relation and Polarizations

The dispersion relation or Debye mass is defined in Eq. (3.73) which is equivalent to

$$p_0^2 = P_i(p_0) \Big|_{p_{\perp}=0, p_3=0}, \tag{3.105}$$

is computed for the coefficients of Eqs. (3.104). Figure 3.6 shows the intersections of the functions that give the coefficients P_0 and P_{\perp} at order $\mathcal{O}(B^2)$, at all orders (defined by Eq. (3.44)) and the parabola $(p_0/m_f)^2$. The coefficient P_{\parallel} is not shown because it has the trivial solution $m_D = 0$ in both approximations. As can be noticed, the presented weak field approximation, besides the physical solution $m_D = 0$, generates a finite gluon mass for both modes. However, when Eq. (3.105) is solved with the expression for all orders in $|q_f B|$, that finite mass disappears, which demonstrates its spurious nature.

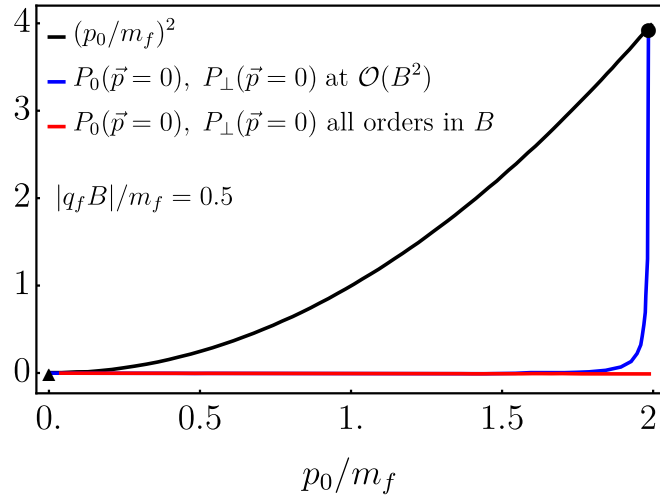


Figure 3.6: Gluon magnetic mass for the coefficients P_0 and P_\perp found by the intersection of the functions at the left and right-side of Eq. (3.105) for a fixed value of the magnetic field and for $\alpha_s = g^2/4\pi = 0.3$. The triangle represents the physical expected mass whereas the circle is a spurious mass.

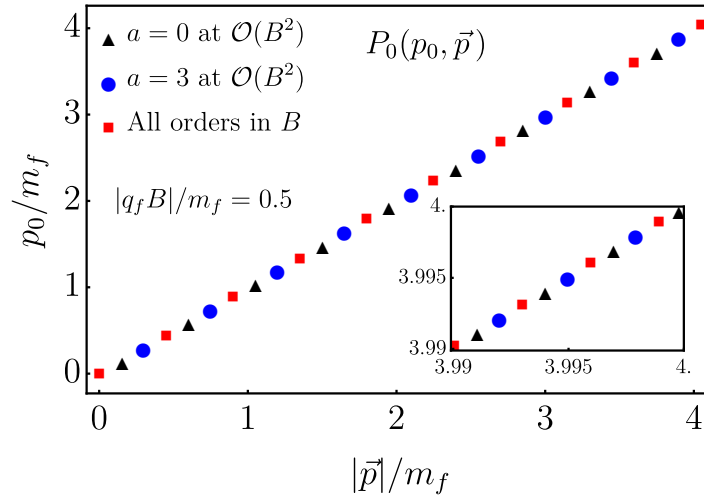


Figure 3.7: Dispersion relation for the mode P_0 obtained with the weak field expansion up to order $\mathcal{O}(B^2)$ and compared with the general expression at all orders (massless regime). The figure is constructed with the condition $p_3^2 = ap_\perp^2$ for two values of a and a fixed value of $|q_f B|$. The inset shows a complete agreement with the motion along the light cone.

The non-physical features are also found in the dispersion relation for the polarization tensor modes. Note that the presence of an external magnetic field breaks Lorentz invariance, which means that the coefficients depend separately on p_\parallel^2 and p_\perp^2 . Given that the modes do not rely only on p_0^2 , an analysis has to be made in order to find whether the gluon moves or not along the light-cone. The on-shell condition is studied by the three-momentum parametrization $p_3^2 = ap_\perp^2$, giving the motion along the transverse plane for $a = 0$, and along the magnetic field direction when $a \rightarrow \infty$.

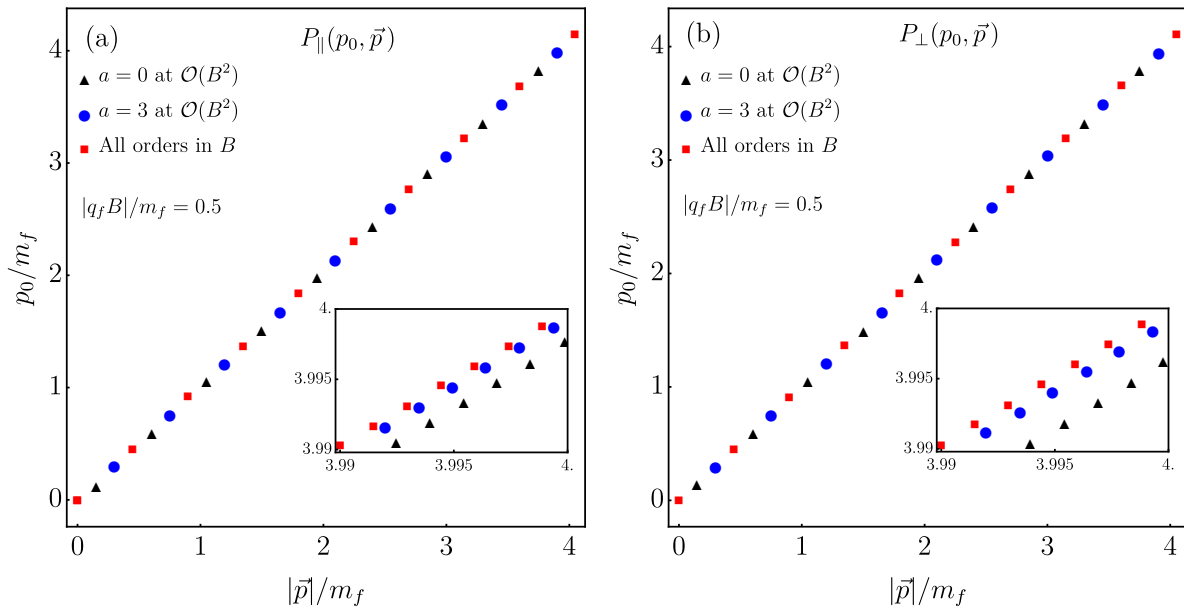


Figure 3.8: Dispersion relation for the modes P_{\parallel} and P_{\perp} obtained with the weak field expansion up to order $\mathcal{O}(B^2)$ and compared with the general expression at all orders (massless regime). The figure is constructed with the condition $p_3^2 = ap_{\perp}^2$ for two values of a and a fixed value of $|q_f B|$. The inset shows deviations with respect to the motion along the light cone.

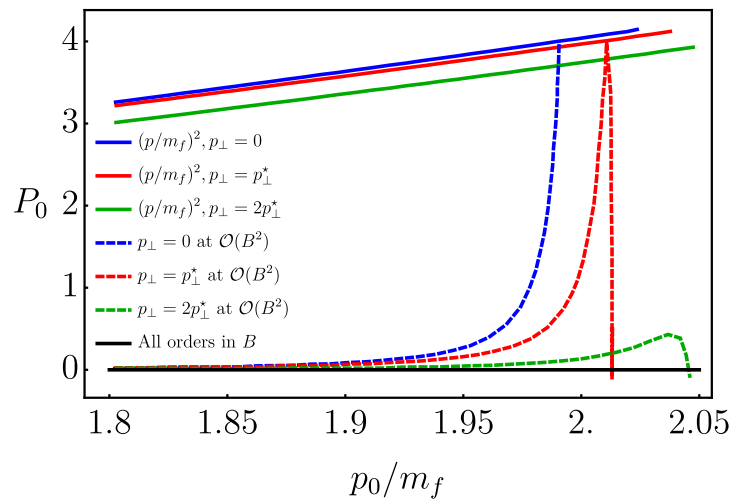


Figure 3.9: Solutions of Eq. (3.105) for the mode P_0 as a function of p_0/m_f for several values of p_{\perp} with the constriction $p_3^2 = ap_{\perp}^2$. The plot compares the coefficient obtained from the approximation up to $\mathcal{O}(B^2)$ with the result obtained to all orders in B . As can be noticed the former gives a spurious solution for $p_{\perp} \leq p_{\perp}^* \simeq 0.1209m_f$, which disappears when the latter is considered. The same behavior is present in the coefficient P_{\perp} .

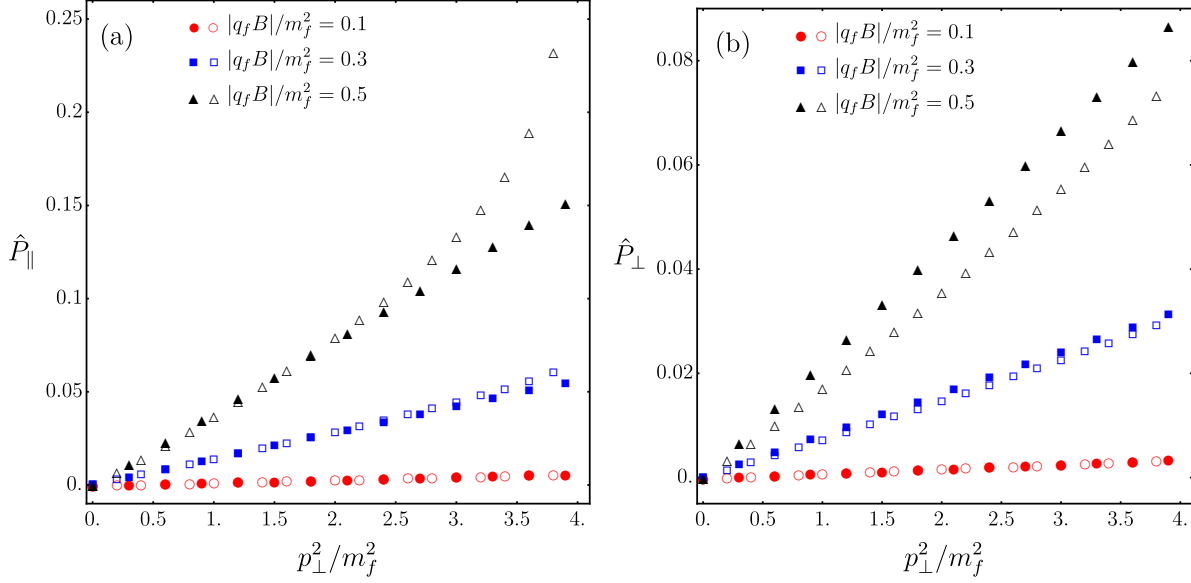


Figure 3.10: Normalized tensor coefficients \hat{P}_{\parallel} and \hat{P}_{\perp} with the on-shell condition $p^2 = 0$ as a function of p_{\perp}^2/m_f^2 computed from the weak field expansion given by Eqs. (3.104b)-(3.104c) (full symbols) and compared with the general expressions found in Eq. (3.44) (open symbols) for three values of $|q_f B|$.

Figures 3.7 and 3.8 shows the dispersion relation for the mode P_0 and P_{\parallel} and P_{\perp} , respectively, computed from Eqs. (3.104) and compared with the expression to all orders in $|q_f B|$ by considering a motion in the transverse plane ($a = 0$) as well as in an arbitrary direction (set by $a = 3$). To ensure physically acceptable results, the spurious solution of Eq. (3.105) is ignored. The massless regime, i.e., when the gluon moves along the light-cone, is represented by the red squares, and therefore, only the mode P_0 reproduce such behavior. As can be noticed, even discarding the finite Debye mass, the approximation up to $\mathcal{O}(B^2)$ for P_{\parallel} and P_{\perp} have slight deviations with respect to the exact result, and the light cone is approached to from below.

As in the case of Debye mass, the solution of Eq. (3.105) with the coefficients given by Eqs. (3.104b) and (3.104c) develops spurious results when the transverse momentum is lower than a critical value $p_{\perp} = p_{\perp}^* \simeq 0.1209 m_f$. As an example, Fig. 3.9 shows the dispersion relation for the mode P_0 for several values of p_{\perp} . Such extra solution is not present in the coefficient P_{\parallel} and is eliminated by considering the magnetic field expansion to all orders. Thus, as far as the gluons' propagation properties are concerned, the approximation for the gluon polarization tensor to the lowest non-trivial order in B is reliably provided if the second (spurious) solution, corresponding to a finite gluon mass, is discarded.

Figure 3.10 shows the normalized coefficients $\hat{P}_{\parallel} \equiv (8\pi^2/g^2 m_f^2) P_{\parallel}$ and $\hat{P}_{\perp} \equiv (8\pi^2/g^2 m_f^2) P_{\perp}$ for the on-shell condition $p^2 = 0$ to analyze the strength of the polarization modes. Such a condition for real gluons implies that the mode P_0 vanishes, and the coefficients P_{\parallel} and P_{\perp} become only functions of p_{\perp}^2 . The approximation to order B^2 and all orders in B are compared for three values of $|q_f B|$. The results in Fig. 3.10(a) show that the polarization tensor has a more prominent projection on its parallel component, and the approximation of Eq. (3.104b) is valid

for an extended range of $|q_f B|$ and p_\perp^2/m_f^2 . In contrast, Fig. 3.10(b) implies that Eq. (3.104c) is accurate if small p_\perp^2/m_f^2 or $|q_f B|$ values are considered.

3.4 Conclusion

In this chapter, the gluon-dominated medium's screening effects were computed from the gluon polarization tensor in a magnetized background. Such a calculation was performed in several approximations in order to focus on the study at the relevant energy scales. The calculation presented in Sec. 3.1 shows how the resummation of all Landau levels in the fermion propagator splits the polarization tensor into three tensorial structures that encode the translational symmetry breaking. Moreover, the procedure gives the appearance of non-transverse structures proportional to $g_{\parallel}^{\mu\nu}$ and $g_{\perp}^{\mu\nu}$. Those non-transverse structures imply that a tensor coefficients calculation starting from projections over the tensor basis may be plagued with non-trivial spurious terms, making it challenging to analyze the gluon properties. However, a method to systematically eliminate the spurious contribution is provided, and the final expression satisfies the Ward-Takahashi identities. On the other hand, by analyzing the tensor coefficients, several thresholds indicate resonances of the gluon momentum with the external magnetic field Landau levels attributed to pair production. The strong field limit indicates that in a magnetized medium gluons processes the birefringence effect, given the noticeable differences between the tensor coefficients. The birefringence is then associated with the vacuum fluctuations due to the spontaneous emergence of virtual electron-positron (quark-antiquark) pairs that act as dipoles, in analogy with dielectric crystals.

The analysis of both temperature and magnetic field on the gluon screening properties are presented in Sec. 3.2. The lowest Landau level approximation, together with the HTL approximations, they were used to find the Debye's mass correction. At the $T = 0$ limit, it is shown that the pair-production is oriented along the magnetic field direction. Indeed, since the chromoelectric field thrusts the quark/antiquark motion, only a polarization vector with a component along the external magnetic field can push the virtual pair motion. If temperature $T \ll |q_f B|$ (to ensure thermal fluctuations do not induce transitions between higher Landau levels), the vacuum contribution is isolated, useful for a renormalization group analysis of the gluon polarization tensor. In this hierarchy, temperature and magnetic field effects factorize due to the dimensional reduction in the LLL. The energy scale comparison shows that the final expression is free from infrared divergences, and the Debye mass per mode depends separately on what momentum (longitudinal or transversal) goes first to zero. If the rate is equal, both modes develop the same Debye mass.

Finally, Sec. 3.3 presents the gluon polarization tensor for zero temperature in a weakly magnetized medium. The fermion propagator expansion is revisited to clarify the method presented in previous works. The calculation presents the non-transverse structures again, which after integration over the Schwinger parameters, vanishes. Nevertheless, the weak field limit shows non-physical results in the dispersion relation and the Debye mass by comparison with the general expression. The origin of spurious solutions is identified as a feature of the approximation at order B^2 , and they are eliminated by resumming all the magnetic contributions.

High-Temperature Approximation for the One-Loop Boson and Fermion Effective Potentials

High-Temperature Bosonic Potential

To compute the high-temperature approximation for the bosonic potential, the starting point is Eq. (1.72):

$$V_b^{(1)} = \frac{1}{2\pi} \int dk k^2 \left[\frac{\sqrt{k^2 + m_b^2}}{2} + T \ln \left(1 - e^{-\sqrt{k^2 + m_b^2}/T} \right) \right], \quad (\text{A.1})$$

where the first terms correspond to the vacuum contributions. Such a term is computed via dimensional regularization by the following well-known result:

$$\int \frac{d^{d-2\epsilon} k}{(2\pi)^{d-2\epsilon}} \frac{1}{(k^2 - m_b^2)^n} = i(-1)^n \frac{(m^2)^{2-\epsilon-n}}{(4\pi)^{2-\epsilon}} \frac{\Gamma(n-2+\epsilon)}{\Gamma(n)}, \quad (\text{A.2})$$

so that $d = 3$ and $n = -1/2$. Thus, by introducing the regulator $\tilde{\mu}^{3-d}$ the vacuum piece is:

$$\begin{aligned} V_{\text{vac}}^{(1)\text{b}} &= \frac{\tilde{\mu}^{3-d}}{2} \int \frac{d^d k}{(2\pi)^d} \sqrt{k^2 + m_b^2} \\ &= -\frac{m_b^4}{32\pi^2} \Gamma(\epsilon - 2) \left(\frac{4\pi\tilde{\mu}^2}{m_b^2} \right)^\epsilon. \end{aligned} \quad (\text{A.3})$$

A power series around $\epsilon = 0$ yields:

$$V_{\text{vac}}^{(1)\text{b}} = -\frac{m_b^4}{64\pi^2} \left[\ln \left(\frac{4\pi\tilde{\mu}^2}{m_b^2} \right) - \gamma_e + \frac{3}{2} + \frac{1}{\epsilon} \right], \quad (\text{A.4})$$

where the divergence can be absorbed in the so-called Minimal Subtraction scheme (MS) with the renormalization scale $\tilde{\mu} = ae^{-1/2}$, giving the result:

$$V_{\text{vac}}^{(1)\text{b}} = -\frac{m_b^4}{64\pi^2} \left[\ln \left(\frac{4\pi a^2}{m_b^2} \right) - \gamma_e + 1 \right]. \quad (\text{A.5})$$

The matter contribution to the boson-effective potential is

$$V_{\text{matt}}^{(1)\text{b}} = \frac{T}{2\pi^2} \int dk k^2 \ln \left(1 - e^{-\sqrt{k^2+m_b^2}/T} \right), \quad (\text{A.6})$$

which performing the substitution $x = k\beta$, $y = m_b\beta$ with $\beta = 1/T$ gives:

$$V_{\text{matt}}^{(1)\text{b}} = \frac{1}{2\pi^2\beta^4} \int_0^\infty dx x^2 \ln \left(1 - e^{-\sqrt{x^2+y^2}} \right). \quad (\text{A.7})$$

To find the integral, the method developed by Dolan and Jackiw is used [282]. That method consists of promoting the integral to a second-order differential equation with the quantities:

$$\frac{\partial}{\partial y^2} V_{\text{matt}}^{(1)\text{b}} = \frac{1}{4\pi^2\beta^4} \int_0^\infty dx \frac{x^2}{\sqrt{x^2+y^2}} \frac{1}{\exp \left(\sqrt{x^2+y^2} \right) - 1}, \quad (\text{A.8})$$

and

$$\frac{\partial^2}{\partial (y^2)^2} V_{\text{matt}}^{(1)\text{b}} = -\frac{1}{8\pi^2\beta^4} \int_0^\infty \frac{dx}{\sqrt{x^2+y^2}} \frac{1}{\exp \left(\sqrt{x^2+y^2} \right) - 1}, \quad (\text{A.9})$$

with the boundary conditions:

$$V_{\text{matt}}^{(1)\text{b}} \Big|_{y^2=0} = -\frac{\pi}{90\beta^4} \quad (\text{A.10})$$

and

$$\frac{\partial}{\partial y} V_{\text{matt}}^{(1)\text{b}} \Big|_{y^2=0} = \frac{1}{24\beta^4}. \quad (\text{A.11})$$

The second-derivative is found by using the following regularized integral:

$$I_\epsilon(y) = \int_0^\infty dx \frac{x^{-\epsilon}}{(x^2+a^2)^{1/2}} \frac{1}{\exp \left(\sqrt{x^2+y^2} \right) - 1}, \quad \epsilon < -1, \quad (\text{A.12})$$

which can be written in terms of the series:

$$\sum_{n=1}^{\infty} \frac{y}{y^2+n^2} = -\frac{1}{2y} + \frac{1}{2}\pi \coth \pi y, \quad (\text{A.13})$$

so that:

$$I_\epsilon(y) = I_\epsilon^{(1)}(y) + I_\epsilon^{(2)}(y), \quad (\text{A.14})$$

where

$$I_\epsilon^{(1)}(y) = \int_0^\infty dx x^{-\epsilon} \sum_n \frac{1}{x^2 + y^2 + 4\pi^2 n^2}, \quad n = 0, \pm 1, \pm 2, \dots \quad (\text{A.15})$$

and

$$I_\epsilon^{(2)}(y) = -\frac{1}{2} \int_0^\infty dx \frac{x^{-\epsilon}}{(x^2 + y^2)^{1/2}}. \quad (\text{A.16})$$

For $I_\epsilon^{(1)}$, the integration over x gives:

$$\begin{aligned} I_\epsilon^{(1)} &= \frac{\pi}{2} \sec\left(\frac{\pi\epsilon}{2}\right) \sum_n \frac{1}{(y^2 + 4\pi^2 n^2)^{(1+\epsilon)/2}} \\ &= \frac{\pi}{2} \sec\left(\frac{\pi\epsilon}{2}\right) \left[\frac{1}{y^{1+\epsilon}} + \sum_{n=1}^\infty \frac{2}{(2\pi n)^{1+\epsilon}} + \sum_{n=1}^\infty \frac{2}{(2\pi n)^{1+\epsilon}} \left(\frac{1}{(1 + y^2/4\pi^2 n^2)^{(1+\epsilon)/2}} - 1 \right) \right], \end{aligned} \quad (\text{A.17})$$

which from the fact that $\sec(\pi\epsilon/2)$ is regular around $\epsilon = 0$ can be separated as

$$I_\epsilon^{(1)} = \frac{\pi}{2y} + 2^{-(1+\epsilon)} \pi^{-\epsilon} \zeta(1+\epsilon) + \tilde{I}(y) + \mathcal{O}(\epsilon), \quad (\text{A.18})$$

where $\zeta(x)$ is the Riemann zeta function and

$$\tilde{I}(y) = \frac{1}{2} \sum_{n=1}^\infty \frac{1}{n} \left[\left(1 + \frac{y^2}{4\pi^2 n^2} \right)^{-1/2} - 1 \right] \sim \mathcal{O}(y^2), \quad (\text{A.19})$$

in such a way that by performing a series expansion around $\epsilon = 0$ the integral is

$$I_\epsilon^{(1)}(y) = \frac{1}{2\epsilon} + \frac{\pi}{2y} + \frac{1}{2}(\gamma_e - \ln 2\pi) + \tilde{I}(y) + \mathcal{O}(\epsilon). \quad (\text{A.20})$$

For $I_\epsilon^{(2)}(y)$, the integration over x is direct:

$$\begin{aligned} I_\epsilon^{(2)}(y) &= -\frac{1}{2} \int_0^\infty dx \frac{x^{-\epsilon}}{\sqrt{x^2 + y^2}} \\ &= \frac{y^{-\epsilon}}{2\sqrt{\pi}} \Gamma\left(\frac{1}{2} - \frac{\epsilon}{2}\right) \Gamma\left(\frac{\epsilon}{2}\right), \end{aligned} \quad (\text{A.21})$$

so that when $\epsilon \sim 0$ behaves as:

$$I_\epsilon^{(2)}(y) = -\frac{1}{2\epsilon} + \frac{1}{2} \ln\left(\frac{y}{2}\right) + \mathcal{O}(\epsilon). \quad (\text{A.22})$$

In this way, the integral $I_\epsilon(y)$ when $\epsilon \rightarrow 0$ is

$$I(y) = \frac{\pi}{2y} + \frac{1}{2} \ln \left(\frac{y}{4\pi} \right) + \frac{\gamma_e}{2} + \tilde{I}(y), \quad (\text{A.23})$$

and therefore

$$\frac{\partial^2}{\partial(y^2)^2} V_{\text{matt}}^{(1)\text{b}} = -\frac{1}{8\pi^2\beta^4} \left[\frac{\pi}{2y} + \frac{1}{2} \ln \left(\frac{y}{4\pi} \right) + \frac{\gamma_e}{2} + \tilde{I}(y) \right]. \quad (\text{A.24})$$

Now, for a high-temperature approximation $y \ll 1$, so that $\tilde{I}(y)$ can be neglected. The effective potential is computed by integrating Eq. (A.24) with respect to y^2 :

$$\frac{\partial}{\partial y^2} V_{\text{matt}}^{(1)\text{b}} = -\frac{1}{8\pi^2\beta^4} \left(\pi y + \frac{\gamma_e}{2} y^2 + \frac{1}{4} y^2 \left[\ln \left(\frac{y^2}{16\pi^2} \right) - 1 \right] \right) + c_1, \quad (\text{A.25})$$

where the constant c_1 is given by the boundary condition of Eq. (A.11):

$$c_1 = \frac{\partial}{\partial y} V_{\text{matt}}^{(1)\text{b}} \Big|_{y^2=0} = \frac{1}{24\beta^4}. \quad (\text{A.26})$$

Performing again the integral over y^2 :

$$V_{\text{matt}}^{(1)\text{b}} = \frac{y^2}{24\beta^4} - \frac{1}{8\pi^2\beta^4} \left[\frac{2\pi y^3}{3} + \frac{1}{8} \left(2\gamma_e - \frac{3}{2} + \ln \left[\frac{y^2}{16\pi^2} \right] \right) \right] + c_2, \quad (\text{A.27})$$

with c_2 provided by the boundary condition of Eq. (A.10), namely:

$$c_2 = V_{\text{matt}}^{(1)\text{b}} \Big|_{y^2=0} = -\frac{\pi}{90\beta^4} \quad (\text{A.28})$$

Finally, by replacing the value of y and adding all terms, the bosonic high temperature-potential is found.

High-Temperature Fermionic Potential

For the high-temperature fermionic potential the vacuum and matter pieces are separated. Starting from Eq. (1.74):

$$\begin{aligned} V_f^{(1)} &= -\frac{1}{\pi^2} \int dk k^2 \sqrt{k^2 + m_f^2} \\ &+ \frac{T}{\pi^2} \int dk k^2 \left\{ \ln \left[1 + e^{-(\sqrt{k^2 + m_f^2} - \mu)/T} \right] + \ln \left[1 + e^{-(\sqrt{k^2 + m_f^2} + \mu)/T} \right] \right\}, \quad (\text{A.29}) \end{aligned}$$

it is easy to recognize the vacuum contribution, which has the same functional form as the bosonic vacuum. Therefore, by following the procedure of the last section is straightforward to find that

$$V_{\text{vac}}^{(1)\text{f}} = \frac{m_f^4}{16\pi^2} \left[\ln \left(\frac{4\pi a^2}{m_f^2} \right) - \gamma_e + 1 \right]. \quad (\text{A.30})$$

The matter contribution follows the differential equation method discussed above. Making the definitions $x = k\beta$, $y = m_b\beta$ and $z = \mu\beta$ such potential is given by

$$V_{\text{matt}}^{(1)\text{f}} = \frac{1}{\pi^2\beta^4} \int_0^\infty dx x^2 \left[\ln \left(1 + e^{-\sqrt{x^2+y^2}-z} \right) + \ln \left(1 + e^{-\sqrt{x^2+y^2}+z} \right) \right], \quad (\text{A.31})$$

so that

$$\frac{\partial V_{\text{matt}}^{(1)\text{f}}}{\partial y^2} = \frac{1}{2\pi^2\beta^4} \int_0^\infty dx \frac{x^2}{\sqrt{x^2+y^2}} \sum_{\sigma=\pm} \frac{1}{\exp(\sqrt{x^2+y^2} + \sigma z) + 1}, \quad (\text{A.32})$$

$$\frac{\partial^2 V_{\text{matt}}^{(1)\text{f}}}{\partial (y^2)^2} = \frac{1}{4\pi^2\beta^4} \int_0^\infty \frac{dx}{\sqrt{x^2+y^2}} \sum_{\sigma=\pm} \frac{1}{\exp(\sqrt{x^2+y^2} + \sigma z) + 1}. \quad (\text{A.33})$$

The last equations provide the boundary conditions:

$$V_{\text{matt}}^{(1)\text{f}} \Big|_{y^2=0} = -\frac{2}{\pi^2\beta^4} \left[\text{Li}_4(-e^{-z}) + \text{Li}_4(-e^z) \right] \quad (\text{A.34})$$

and

$$\frac{\partial V_{\text{matt}}^{(1)\text{f}}}{\partial y^2} \Big|_{y^2=0} = -\frac{1}{2\pi^2\beta^4} \left[\text{Li}_2(-e^{-z}) + \text{Li}_2(-e^z) \right], \quad (\text{A.35})$$

where $\text{Li}_s(x)$ is the polylogarithm function of order s .

To compute the second derivative it is useful to use the following identity:

$$\begin{aligned} & \sum_{n=-\infty}^{+\infty} \frac{4\pi^2}{[(2n+1)\pi + iz]^2 + x^2 + y^2} \\ &= \frac{2\pi^2}{\sqrt{x^2+y^2}} \left[1 - \frac{1}{\exp(\sqrt{x^2+y^2}-z)} - \frac{1}{\exp(\sqrt{x^2+y^2}+z)+1} \right], \end{aligned} \quad (\text{A.36})$$

so that the desired (regularized) integral is written as

$$J_\epsilon(y) = J_\epsilon^{(1)}(y) + J_\epsilon^{(2)}(y), \quad (\text{A.37})$$

with

$$J_\epsilon^{(1)}(y) = -2 \int_0^\infty dx \sum_{n=-\infty}^{+\infty} \frac{x^{-\epsilon}}{[(2n+1)\pi + iz]^2 + x^2 + y^2}, \quad (\text{A.38})$$

and

$$J_\epsilon^{(2)}(y) = \int_0^\infty dx \frac{x^{-\epsilon}}{\sqrt{x^2 + y^2}}. \quad (\text{A.39})$$

Note that $J_\epsilon^{(2)}(y)$ has the same functional form that Eq. (A.21); thus, the calculation of interest is about $J_\epsilon^{(1)}(y)$. After integrating over x the function $J_\epsilon^{(1)}(y)$ becomes

$$J_\epsilon^{(1)}(y) = -\pi \sec\left(\frac{\pi\epsilon}{2}\right) \sum_{n=-\infty}^{+\infty} \left\{ \frac{1}{[(2n+1)\pi + iz]^2 + y^2} \right\}^{\frac{1+\epsilon}{2}}, \quad (\text{A.40})$$

where the sum can be spitted into positive and negative n 's, yielding:

$$\begin{aligned} J_\epsilon^{(1)}(y) &= -\pi \sec\left(\frac{\pi\epsilon}{2}\right) \\ &\times \sum_{n=0}^{+\infty} \left\{ \frac{1}{([(2n+1)\pi + iz]^2 + y^2)^{\frac{1+\epsilon}{2}}} + \frac{1}{([(2n+1)\pi - iz]^2 + y^2)^{\frac{1+\epsilon}{2}}} \right\}. \end{aligned} \quad (\text{A.41})$$

The denominator can be simplified:

$$\frac{1}{([(2n+1)\pi \pm iz]^2 + y^2)^{\frac{1+\epsilon}{2}}} = \frac{1}{(2\pi)^{1+\epsilon}} \frac{1}{[n + 1/2 \pm iz/2\pi]^{1+\epsilon}} \quad (\text{A.42})$$

$$\times \left[1 + \frac{y^2/4\pi^2}{(n + 1/2 \pm iz/2\pi)^2} \right]^{-\frac{1+\epsilon}{2}}, \quad (\text{A.43})$$

which from the binomial theorem becomes:

$$\begin{aligned} &\frac{1}{(2\pi)^{1+\epsilon}} \sum_{l=0}^{+\infty} \frac{(-1)^l}{(n + 1/2 \pm iz/2\pi)^{\epsilon+1}} \binom{\frac{\epsilon-1}{2} + l}{\frac{\epsilon-1}{2}} \frac{(y/2\pi)^{2l}}{(n + 1/2 \pm iz/2\pi)^{2l}} \\ &= \frac{1}{(2\pi)^{1+\epsilon}} \frac{1}{(n + 1/2 \pm iz/2\pi)^{\epsilon+1}} \\ &+ \frac{1}{(2\pi)^{1+\epsilon}} \sum_{l=1}^{+\infty} (-1)^l \binom{\frac{\epsilon-1}{2} + l}{\frac{\epsilon-1}{2}} \frac{(y/2\pi)^{2l}}{(n + 1/2 \pm iz/2\pi)^{2l+\epsilon+1}}. \end{aligned} \quad (\text{A.44})$$

Performing the sum over n :

$$J_\epsilon^{(1)}(y) = -\pi \frac{\sec\left(\frac{\pi\epsilon}{2}\right)}{(2\pi)^{1+\epsilon}} \sum_{\sigma=\pm} \left[\zeta\left(1 + \epsilon; \frac{1}{2} + \sigma \frac{iz}{2\pi}\right) + \tilde{J}_\sigma(y) \right], \quad (\text{A.45})$$

where $\zeta(s, x)$ is the Hurwitz zeta function of order s and

$$\tilde{J}_\sigma(y) \equiv \sum_{l=1}^{+\infty} \frac{(-1)^l}{(2\pi)^{2l}} \left(\frac{\epsilon-1}{2} + l \right) \zeta \left(2l + \epsilon + 1; \frac{1}{2} + \sigma \frac{iz}{2\pi} \right) y^{2l}. \quad (\text{A.46})$$

In the same way, as in the boson effective-potential calculation, a high-temperature approximation means $y \ll 1$; therefore, the function $\tilde{J}_s(y)$ can be neglected. Moreover, by expanding into power series around $\epsilon = 0$:

$$J_\epsilon^{(1)}(y) \approx -\frac{1}{\epsilon} + \ln(2\pi) + \frac{1}{2}\psi_0 \left(\frac{1}{2} + \frac{iz}{2\pi} \right) + \frac{1}{2}\psi_0 \left(\frac{1}{2} - \frac{iz}{2\pi} \right) + \mathcal{O}(\epsilon), \quad (\text{A.47})$$

with $\psi_0(x)$ the zeroth-order polygamma function.

After joining all the pieces, the second derivative has the form:

$$\frac{\partial^2 V_{\text{matt}}^{(1)\text{f}}}{\partial(y^2)^2} = \frac{1}{4\pi^2\beta^4} \left[\ln(2\pi) + \ln \left(\frac{2}{y} \right) + \frac{1}{2}\psi_0 \left(\frac{1}{2} + \frac{iz}{2\pi} \right) + \frac{1}{2}\psi_0 \left(\frac{1}{2} - \frac{iz}{2\pi} \right) \right], \quad (\text{A.48})$$

and by integration over y^2 :

$$\frac{\partial V_{\text{matt}}^{(1)\text{f}}}{\partial y^2} = \frac{y^2}{4\pi^2\beta^4} \left[\frac{1}{2} + \ln(2\pi) - \frac{1}{2} \ln \left(\frac{y^2}{4} \right) + \frac{1}{2}\psi_0 \left(\frac{1}{2} + \frac{iz}{2\pi} \right) + \frac{1}{2}\psi_0 \left(\frac{1}{2} - \frac{iz}{2\pi} \right) \right] + c_3, \quad (\text{A.49})$$

where c_3 is given by the boundary condition of Eq. (A.34). Finally, integrating the last equation:

$$\begin{aligned} V_{\text{matt}}^{(1)\text{f}} &= \frac{y^2}{4\pi^2\beta^4} \left\{ \frac{1}{2} \left[\ln(2\pi) + \frac{1}{2}\psi_0 \left(\frac{1}{2} + \frac{iz}{2\pi} \right) + \frac{1}{2}\psi_0 \left(\frac{1}{2} - \frac{iz}{2\pi} \right) \right] y^2 \right. \\ &\quad \left. + \frac{y^2}{4} \left[\frac{3}{2} - \ln \left(\frac{y^2}{4} \right) \right] + c_3 \right\} + c_4, \end{aligned} \quad (\text{A.50})$$

with c_4 obtained from Eq. (A.35).

The latter together with Eq. (A.30) defines the high-temperature fermionic potential given in Eq. (1.75).

Schwinger's Phase Factor

The Schwinger's phase factor is defined in Eq. (2.41):

$$\Phi(x, y) = \exp \left\{ i|q_f| \int_y^x d\xi^\mu \left[A_\mu + \frac{1}{2} F_{\mu\nu} (\xi - y)^\nu \right] \right\}, \quad (\text{B.1})$$

which is a translational and gauge noninvariant value. Given that $F_{\mu\nu} = \partial_\mu A_\nu - \partial_\nu A_\mu$, the gauge invariance allows to write the 4-potential for a constant magnetic field as:

$$A_\mu(x) = -\frac{1}{2} F_{\mu\nu} x^\nu + \partial_\mu \lambda(x), \quad (\text{B.2})$$

where $\lambda(x)$ is an arbitrary well behaved function provided by the choice of gauge. By replacing Eq. (B.2) in the integral of Eq. (B.1):

$$\begin{aligned} \mathcal{I}(x, y) &\equiv \int_y^x d\xi^\mu \left[A_\mu + \frac{1}{2} F_{\mu\nu} (\xi - y)^\nu \right] \\ &= \int_y^x d\xi^\mu \left[-\frac{1}{2} F_{\mu\nu} y^\nu + \partial_\mu \lambda(\xi) \right] \\ &= -\frac{1}{2} (x - y)^\mu F_{\mu\nu} y^\nu + \lambda(x) - \lambda(y), \end{aligned} \quad (\text{B.3})$$

but $x^\mu F_{\mu\nu} y^\nu = -x^\nu F_{\mu\nu} y^\mu$ and $y^\mu F_{\mu\nu} y^\nu = 0$, and therefore:

$$\mathcal{I}(x, y) = \frac{1}{2} y^\mu F_{\mu\nu} x^\nu + \lambda(x) - \lambda(y). \quad (\text{B.4})$$

From the above to find the term in the exponential of $\Phi(x, y)\Phi(y, z)\Phi(z, x)$ is

$$\begin{aligned} \mathcal{I}(x, y) + \mathcal{I}(y, z) + \mathcal{I}(z, x) &= \frac{1}{2} y^\mu F_{\mu\nu} x^\nu + \lambda(x) - \lambda(y) \\ &+ \frac{1}{2} z^\mu F_{\mu\nu} y^\nu + \lambda(y) - \lambda(z) \\ &+ \frac{1}{2} x^\mu F_{\mu\nu} z^\nu + \lambda(z) - \lambda(x), \end{aligned} \quad (\text{B.5})$$

where the cancellation of the λ functions resembles the gauge invariance. To get the desired result, the term $-x^\mu F_{\mu\nu} x^\nu = 0$ is added and given that $z^\mu F_{\mu\nu} y^\nu = -y^\mu F_{\mu\nu} z^\nu$, the exponential factor becomes:

$$\begin{aligned}\mathcal{I}(x, y) + \mathcal{I}(y, z) + \mathcal{I}(z, x) &= \frac{1}{2} F_{\mu\nu} (x^\mu z^\nu - y^\mu z^\nu - x^\mu x^\nu + y^\mu x^\nu) \\ &= \frac{1}{2} (x - y)^\mu F_{\mu\nu} (z - x)^\nu.\end{aligned}\tag{B.6}$$

Now, from the choice of A_μ in Eq. (2.43):

$$A^\mu = \frac{B}{2} (0, -y, x, 0),\tag{B.7}$$

the only non-vanishing terms of $F_{\mu\nu}$ are $F_{12} = -F_{21} = |B|$ which yields:

$$\mathcal{I}(x, y) + \mathcal{I}(y, z) + \mathcal{I}(z, x) = -\frac{|B|}{2} \epsilon_{mj} (z - x)_m (x - y)_j,\tag{B.8}$$

and finally:

$$\Phi(x, y)\Phi(y, z)\Phi(z, x) = \exp \left[-i \frac{|q_f B|}{2} \epsilon_{mj} (z - x)_m (x - y)_j \right],\tag{B.9}$$

which is the phase factor of Eq. (2.46).

Appendix C

Matrix element for the process $gg \rightarrow \gamma$ with all the quarks in the LLL

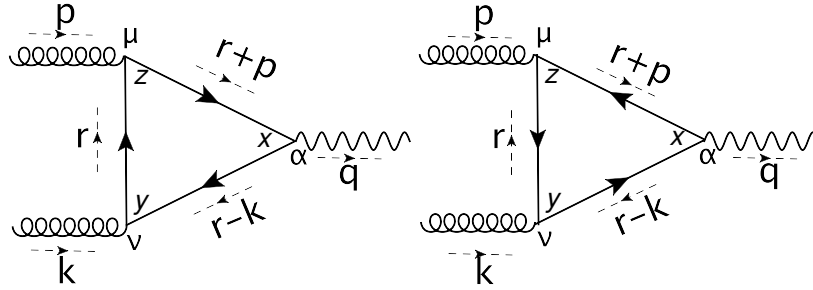


Figure C.1: Feynman diagrams contributing to the process $gg \rightarrow \gamma$ with all the fermions in the loop are in the LLL.

In the limit $m_f \rightarrow 0$ the trace which appears into Eq. (2.45) related to the left diagram shown in Fig. C.1 is given by

$$\text{Tr} \left\{ \gamma_\alpha (\not{r} + \not{p})_{\parallel} \mathcal{O}^+ \gamma_\mu \not{r}_{\parallel} \mathcal{O}^+ \gamma_\nu (\not{r} - \not{k})_{\parallel} \mathcal{O}^+ \right\}, \quad (\text{C.1})$$

which from the identities

$$\begin{aligned} \not{p}_{\parallel} \mathcal{O}^\pm &= \mathcal{O}^\pm \not{p}_{\parallel} \\ \mathcal{O}^\pm \gamma_\mu \mathcal{O}^\pm &= \mathcal{O}^\pm \gamma_\mu^{\parallel}, \end{aligned} \quad (\text{C.2})$$

and given that \mathcal{O}^\pm is idempotent and orthogonal to \mathcal{O}^\mp , the operator \mathcal{O}^+ can be moved to the left, such that:

$$\text{Tr} \left\{ \mathcal{O}^+ \gamma_\alpha^{\parallel} (\not{r} + \not{p})_{\parallel} \gamma_\mu^{\parallel} \not{r}_{\parallel} \gamma_\nu^{\parallel} (\not{r} - \not{k})_{\parallel} \right\}. \quad (\text{C.3})$$

The charge conjugate of Eq. (C.3) is related to the right diagram of Fig. C.1:

$$\begin{aligned}
& \text{Tr} \left\{ \gamma_\alpha (-\not{r} + \not{k})_{\parallel} \mathcal{O}^- \gamma_\nu (-\not{r}_{\parallel}) \mathcal{O}^- \gamma_\mu (-\not{r} - \not{p})_{\parallel} \mathcal{O}^- \right\} \\
&= -\text{Tr} \left\{ \mathcal{O}^- \gamma_\alpha^{\parallel} (\not{r} - \not{k})_{\parallel} \gamma_\nu^{\parallel} \not{r}_{\parallel} \gamma_\mu^{\parallel} (\not{r} + \not{p})_{\parallel} \right\} \\
&= -\text{Tr} \left\{ \mathcal{O}^- \gamma_\alpha^{\parallel} (\not{r} + \not{p})_{\parallel} \gamma_\mu^{\parallel} \not{r}_{\parallel} \gamma_\nu^{\parallel} (\not{r} - \not{k})_{\parallel} \right\}, \tag{C.4}
\end{aligned}$$

such that, the sum of both contributions is:

$$\frac{i}{2} \text{Tr} \left\{ \gamma_1 \gamma_2 \gamma_\alpha^{\parallel} (\not{r} + \not{p})_{\parallel} \gamma_\mu^{\parallel} \not{r}_{\parallel} \gamma_\nu^{\parallel} (\not{r} - \not{k})_{\parallel} \right\}. \tag{C.5}$$

The above expression, after the trace is performed is a product combinations of $g^{1\mu}$, $g^{2\mu}$, $g^{1\nu}$, $g^{2\nu}$, $g^{1\alpha}$, $g^{2\alpha}$, r_{\parallel}^1 , r_{\parallel}^2 , p_{\parallel}^1 , p_{\parallel}^2 and k_{\parallel}^1 , k_{\parallel}^2 , which by definition vanishes.

Appendix **D**

Calculation of \widetilde{M} for the process $gg \rightarrow \gamma$

For calculation of the amplitude for the process $gg \rightarrow \gamma$ depicted in Fig. 2.17 the starting point is Eq. (2.45):

$$\begin{aligned} \widetilde{\mathcal{M}} &= - \int d^4x d^4y d^4z \int \frac{d^4r}{(2\pi)^4} \frac{d^4s}{(2\pi)^4} \frac{d^4t}{(2\pi)^4} e^{-it \cdot (y-x)} e^{-is \cdot (x-z)} e^{-ir \cdot (z-y)} e^{-ip \cdot z} e^{-ik \cdot y} e^{iq \cdot x} \\ &\times \left\{ \text{Tr} [iq_f \gamma_\alpha iS(s) ig \gamma_\mu t^c iS(r) ig \gamma_\nu t^d iS(t)] + \text{Tr} [iq_f \gamma_\alpha iS(t) ig \gamma_\nu t^d iS(r) ig \gamma_\mu t^c iS(s)] \right\} \\ &\times \Phi(x, y) \Phi(y, z) \Phi(z, x) \epsilon^\mu(\lambda_p) \epsilon^\nu(\lambda_k) \epsilon^\alpha(\lambda_q), \quad , \end{aligned} \quad (\text{D.1})$$

where the phase factor $\Phi(x, y) \Phi(y, z) \Phi(z, x)$ is given by Eq. (2.46), namely:

$$\Phi(x, y) \Phi(y, z) \Phi(z, x) = \exp \left[-i \frac{|q_f B|}{2} \epsilon_{mj} (z-x)_m (x-y)_j \right]. \quad (\text{D.2})$$

By defining $w = z - x$ $l = x - y$ the coordinate integral of Eq. (D.1) is

$$\begin{aligned} &\int d^4x d^4w d^4l \exp \left\{ -\frac{i|q_f B|}{2} \epsilon_{mj} w_m l_j \right\} e^{ix(q-k-p)} e^{-il(r-t-k)} e^{-iw(p+r-s)} \\ &= (2\pi)^4 \delta^{(4)}(q-k-p) \int d^4w d^4l \exp \left\{ -\frac{i|q_f B|}{2} \epsilon_{mj} w_m l_j \right\} e^{-il(r-t-k)} e^{-iw(p+r-s)}. \end{aligned} \quad (\text{D.3})$$

The above can be separated into the transverse and longitudinal momentum components be-

cause $x \cdot p = x_{\parallel} \cdot p_{\parallel} - (x_1 p_1 + x_2 p_2) = x_{\parallel} \cdot p_{\parallel} - x_i p_i$, so that

$$\begin{aligned}
& (2\pi)^8 \delta^{(4)}(q - k - p) \delta^{(2)} \left[(k + t - r)_{\parallel} \right] \delta^{(2)} \left[(s - p - r)_{\parallel} \right] \\
& \times \prod_{m,j=1}^2 \int d^4 w_m d^4 l_j \exp \left\{ -\frac{i|q_f B|}{2} \epsilon_{mj} w_m l_j \right\} e^{i l_j (r-t-k)_j} e^{i w_m (p+r-s)_m} \\
& = (2\pi)^{10} \left(\frac{2}{q_f B} \right)^2 \delta^{(4)}(q - k - p) \delta^{(2)} \left[(k + t - r)_{\parallel} \right] \delta^{(2)} \left[(s - p - r)_{\parallel} \right] \\
& \times \prod_{j=1}^2 \int d^4 l_j \delta^{(2)} \left[-\frac{|q_f B|}{2} \epsilon_{mj} w_m l_j + (p + s - s)_m \right] e^{i l_j (r-t-k)_j} e^{i w_m (p+r-s)_m} \\
& = (2\pi)^{10} \left(\frac{2}{q_f B} \right)^2 \delta^{(4)}(q - k - p) \delta^{(2)} \left[(k + t - r)_{\parallel} \right] \delta^{(2)} \left[(s - p - r)_{\parallel} \right] \\
& \times \exp \left\{ \frac{2i}{|q_f B|} \epsilon_{mj} (p + r - s)_m (r - t - k)_j \right\}. \tag{D.4}
\end{aligned}$$

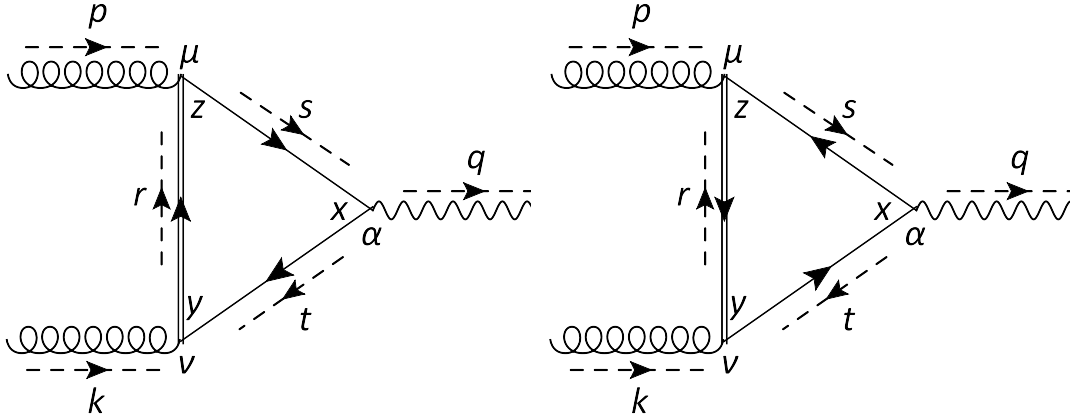


Figure D.1: Feynman diagrams contributing to the process when the fermion with momentum r is in the 1LL and the fermions with momentum s and t are in the LLL.

The leading order of the process is given by two quarks in the LLL and one in the 1LL, and for each fermion line in the 1LL there are two contributing diagrams. Thus, by replacing the propagators of Eqs. (2.51a) and (2.51b) the traces of Eq. (D.1) when the fermion with momentum r is in the 1LL and the fermions with momentum s and t (Fig. D.1) are:

$$\text{Tr} \left\{ i q_f \gamma_{\alpha} i S(s) i g \gamma_{\mu} t^d i S(r) i g \gamma_{\nu} t^c i S(t) \right\} = -16 i q_f g^2 \delta^{cd} \text{Tr} \left\{ \gamma_{\alpha} \not{s}_{\parallel} \mathcal{O}^{-} \gamma_{\mu} \not{t}_{\perp} \gamma_{\nu} \not{t}_{\parallel} \mathcal{O}^{-} \right\}, \tag{D.5a}$$

and

$$\text{Tr} \left\{ i q_f \gamma_{\alpha} i S(t) i g \gamma_{\nu} t^c i S(r) i g \gamma_{\mu} t^d i S(s) \right\} = 16 i q_f g^2 \delta^{cd} \text{Tr} \left\{ \gamma_{\alpha} \not{t}_{\parallel} \mathcal{O}^{+} \gamma_{\nu} \not{t}_{\perp} \gamma_{\mu} \not{s}_{\parallel} \mathcal{O}^{+} \right\}. \tag{D.5b}$$

From the properties of Eq. (C.2) it follows that:

$$\text{Tr} \left\{ \gamma_{\alpha} \not{s}_{\parallel} \mathcal{O}^{-} \gamma_{\mu} \not{t}_{\perp} \gamma_{\nu} \not{t}_{\parallel} \mathcal{O}^{-} \right\} = \text{Tr} \left\{ \gamma_{\alpha} \not{t}_{\parallel} \gamma_{\mu} \not{t}_{\perp} \gamma_{\nu} \not{s}_{\parallel} \mathcal{O}^{-} \right\}, \tag{D.6a}$$

and

$$\text{Tr} \left\{ \gamma_\alpha \not{t}_\parallel \mathcal{O}^+ \gamma_\nu \not{t}_\perp \gamma_\mu \not{s}_\parallel \mathcal{O}^+ \right\} = \text{Tr} \left\{ \gamma_\alpha^\parallel \not{s}_\parallel \gamma_\mu \not{t}_\perp \gamma_\nu \not{t}_\parallel \mathcal{O}^+ \right\}, \quad (\text{D.6b})$$

thus, the trace in Eq. (D.1) is

$$i \text{Tr} \left\{ \gamma^1 \gamma^2 \not{t}_\parallel \gamma_\nu \not{t}_\perp \gamma_\mu \not{s}_\parallel \gamma_\alpha^\parallel \right\}. \quad (\text{D.7})$$

The same procedure can be applied for the other diagrams so that

$$\begin{aligned} \widetilde{\mathcal{M}} &= 16i(2\pi)^{10} q_f g^2 \left(\frac{2}{q_f B} \right)^2 \delta^{cd} \\ &\times \int \frac{d^4 r}{(2\pi)^4} \frac{d^4 s}{(2\pi)^4} \frac{d^4 t}{(2\pi)^4} \delta^{(4)}(q - k - p) \delta^{(2)} \left[(k + t - r)_\parallel \right] \delta^{(2)} \left[(s - p - r)_\parallel \right] \\ &\times \exp \left\{ \frac{2i}{|q_f B|} \epsilon_{mj} (p + r - s)_m (r - t - k)_j \right\} \exp \left\{ -\frac{r_\perp^2 + s_\perp^2 + t_\perp^2}{|q_f B|} \right\} \\ &\times \text{Tr} \left\{ \frac{\gamma^1 \gamma^2 \not{t}_\parallel \gamma_\nu \not{t}_\perp \gamma_\mu \not{s}_\parallel \gamma_\alpha^\parallel}{t_\parallel^2 s_\parallel^2 (r_\parallel^2 - 2|q_f B|)} + \frac{\gamma^1 \gamma^2 \not{t}_\parallel \gamma_\mu \not{s}_\perp \gamma_\alpha \not{t}_\parallel \gamma_\nu^\parallel}{r_\parallel^2 t_\parallel^2 (s_\parallel^2 - 2|q_f B|)} + \frac{\gamma^1 \gamma^2 \not{s}_\parallel \gamma_\alpha \not{t}_\perp \gamma_\nu \not{t}_\parallel \gamma_\mu^\parallel}{r_\parallel^2 s_\parallel^2 (t_\parallel^2 - 2|q_f B|)} \right\} \\ &\times \epsilon^\mu(\lambda_p) \epsilon^\nu(\lambda_k) \epsilon^\alpha(\lambda_q). \end{aligned} \quad (\text{D.8})$$

Integration over t_\perp

The terms in the exponentials of Eq. (D.8) can be grouped as

$$-\frac{2i}{|q_f B|} \epsilon_{mj} (p + r - s)_m t_j - \frac{t_j^2}{|q_f B|} = -\frac{1}{|q_f B|} \left[(\tilde{t}_j + i\epsilon_{jm} (p + r - s)_m)^2 + (p + r - s)_m^2 \right], \quad (\text{D.9})$$

so that by defining

$$\tilde{t}_j = t_j + i\epsilon_{jm} (p + r - s)_m, \quad (\text{D.10})$$

the integration over t is given by

$$\int \frac{d^2 t_\parallel}{(2\pi)^2} \frac{d^2 \tilde{t}_j}{(2\pi)^2} \exp \left\{ -\frac{\tilde{t}_j^2}{|q_f B|} \right\} \text{Tr} \left\{ \frac{\gamma^1 \gamma^2 \not{s}_\parallel \gamma_\alpha \gamma^l [\tilde{t}_l - i\epsilon_{lm} (p + r - s)_m] \gamma_\nu \not{t}_\parallel \gamma_\mu^\parallel}{r_\parallel^2 s_\parallel^2 (t_\parallel^2 - 2|q_f B|)} + \dots \right\}. \quad (\text{D.11})$$

The odd powers do not contribute to the perpendicular integration, thus the first term of Eq. (D.11) becomes

$$-\frac{\pi |q_f B|}{(2\pi)^2} \exp \left\{ -\frac{(p + r - s)_m^2}{|q_f B|} \right\} \int \frac{d^2 t_\parallel}{(2\pi)^2} \text{Tr} \left\{ \frac{\gamma^1 \gamma^2 \not{s}_\parallel \gamma_\alpha \gamma^l [i\epsilon_{lm} (p + r - s)_m] \gamma_\nu \not{t}_\parallel \gamma_\mu^\parallel}{r_\parallel^2 s_\parallel^2 (t_\parallel^2 - 2|q_f B|)} \right\}. \quad (\text{D.12})$$

From the above:

$$\begin{aligned}
\widetilde{\mathcal{M}} &= 16i(2\pi)^8(\pi|q_f B|) \left(\frac{2}{q_f B}\right)^2 q_f g^2 \delta^{cd} \\
&\times \int \frac{d^4 r}{(2\pi)^4} \frac{d^4 s}{(2\pi)^4} \frac{d^2 t_{\parallel}}{(2\pi)^2} \delta^{(4)}(q-k-p) \delta^{(2)}\left[(t+k-r)_{\parallel}\right] \delta^{(2)}\left[(s-p-r)_{\parallel}\right] \\
&\times \exp\left\{-\frac{(p+r-s)_m^2}{|q_f B|}\right\} \exp\left\{-\frac{r_{\perp}^2 + s_{\perp}^2}{|q_f B|}\right\} \exp\left\{\frac{2i}{|q_f B|} \epsilon_{mj}(p+r-s)_m (r-k)_j\right\} \\
&\times \text{Tr} \left\{ \frac{\gamma^1 \gamma^2 \not{t}_{\parallel} \gamma_{\nu} \not{t}_{\perp} \gamma_{\mu} \not{s}_{\parallel} \gamma_{\alpha}}{t_{\parallel}^2 s_{\parallel}^2 (r_{\parallel}^2 - 2|q_f B|)} + \frac{\gamma^1 \gamma^2 \not{t}_{\parallel} \gamma_{\mu} \not{s}_{\perp} \gamma_{\alpha} \not{t}_{\parallel} \gamma_{\nu}}{r_{\parallel}^2 t_{\parallel}^2 (s_{\parallel}^2 - 2|q_f B|)} \right. \\
&\left. - \frac{\gamma^1 \gamma^2 \not{s}_{\parallel} \gamma_{\alpha} \gamma^l [i\epsilon_{lm}(p+r-s)_m] \gamma_{\nu} \not{t}_{\parallel} \gamma_{\mu}}{r_{\parallel}^2 s_{\parallel}^2 (t_{\parallel}^2 - 2|q_f B|)} \right\} \epsilon^{\mu}(\lambda_p) \epsilon^{\nu}(\lambda_k) \epsilon^{\alpha}(\lambda_q). \tag{D.13}
\end{aligned}$$

Integration over s_{\perp}

The terms in the exponential of Eq. (D.13) are

$$\begin{aligned}
&-\frac{1}{|q_f B|} [s_m^2 - 2(p+r)_m s_m + (p+r)_m^2 + s_m^2 + 2i\epsilon_{mj}(r-k)_j s_m] \\
&= -\frac{2}{|q_f B|} \left[\left(s_m + \frac{1}{2} [i\epsilon_{mj}(r-k)_j - (p+r)_m] \right)^2 + \frac{1}{2} (p+r)_m^2 \right. \\
&\left. - \frac{1}{4} [i\epsilon_{mj}(r-k)_j - (p+r)_m]^2 \right], \tag{D.14}
\end{aligned}$$

so that by defining $\tilde{s}_m = s_m + \frac{1}{2} [i\epsilon_{mj}(r-k)_j - (p+r)_m]$ the integration over s_{\perp} is easily performed in the same way as in Eq. (D.12), i.e., all the odd powers of s_{\perp} are ignored giving the following expression:

$$\begin{aligned}
&\frac{1}{(2\pi)^2} \frac{\pi|q_f B|}{2} \int \frac{d^2 s_{\parallel}}{(2\pi)^2} e^{-r_{\perp}^2/|q_f B|} \exp\left\{\frac{2i}{|q_f B|} \epsilon_{mj}(p+r)_m (r-k)_j\right\} \\
&\times \exp\left\{\frac{1}{2|q_f B|} [i\epsilon_{mj}(r-k)_j - (p+r)_m]^2 - \frac{1}{|q_f B|} (p+r)_m^2\right\} \\
&\times \text{Tr} \left\{ -\frac{\gamma^1 \gamma^2 \not{s}_{\parallel} \gamma_{\alpha} \gamma^l i\epsilon_{lm} [(p+r)_m + i\epsilon_{mj}(r-k)_j] \gamma_{\nu} \not{t}_{\parallel} \gamma_{\mu}}{2r_{\parallel}^2 s_{\parallel}^2 (t_{\parallel}^2 - 2|q_f B|)} \right. \\
&\left. + \frac{\gamma^1 \gamma^2 \not{t}_{\parallel} \gamma_{\nu} \not{t}_{\perp} \gamma_{\mu} \not{s}_{\parallel} \gamma_{\alpha}}{t_{\parallel}^2 s_{\parallel}^2 (r_{\parallel}^2 - 2|q_f B|)} - \frac{\gamma^1 \gamma^2 \not{t}_{\parallel} \gamma_{\mu} \gamma^l [i\epsilon_{lj}(r-k)_j - (p+r)_l] \gamma_{\alpha} \not{t}_{\parallel} \gamma_{\nu}}{2r_{\parallel}^2 t_{\parallel}^2 (s_{\parallel}^2 - 2|q_f B|)} \right\}. \tag{D.15}
\end{aligned}$$

By collecting results:

$$\begin{aligned}
\widetilde{\mathcal{M}} &= 8i(2\pi)^6 (\pi |q_f B|)^2 \left(\frac{2}{q_f B} \right)^2 q_f g^2 \delta^{cd} \\
&\times \int \frac{d^4 r}{(2\pi)^4} \frac{d^2 s_{\parallel}}{(2\pi)^2} \frac{d^2 t_{\parallel}}{(2\pi)^2} \delta^{(4)}(q - k - p) \delta^{(2)} \left[(t + k - r)_{\parallel} \right] \delta^{(2)} \left[(s - p - r)_{\parallel} \right] \\
&\times \exp \left\{ -\frac{r_{\perp}^2}{|q_f B|} \right\} \exp \left\{ \frac{2i}{|q_f B|} \epsilon_{mj} (p + r)_m (r - k)_j \right\} \\
&\times \exp \left\{ \frac{1}{2|q_f B|} [i\epsilon_{mj} (r - k)_j - (p + r)_m]^2 - \frac{1}{|q_f B|} (p + r)_m^2 \right\} \\
&\times \text{Tr} \left\{ \frac{\gamma^1 \gamma^2 \not{s}_{\parallel} \gamma_{\alpha} \gamma^l i\epsilon_{lm} [(p + r)_m + i\epsilon_{mj} (r - k)_j] \gamma_{\nu} \not{t}_{\parallel} \gamma_{\mu}^{\parallel}}{2r_{\parallel}^2 s_{\parallel}^2 (t_{\parallel}^2 - 2|q_f B|)} \right. \\
&+ \left. \frac{\gamma^1 \gamma^2 \not{t}_{\parallel} \gamma_{\nu} \not{r}_{\perp} \gamma_{\mu} \not{s}_{\parallel} \gamma_{\alpha}^{\parallel}}{t_{\parallel}^2 s_{\parallel}^2 (r_{\parallel}^2 - 2|q_f B|)} - \frac{\gamma^1 \gamma^2 \not{r}_{\parallel} \gamma_{\mu} \gamma^l [i\epsilon_{lj} (r - k)_j - (p + r)_l] \gamma_{\alpha} \not{t}_{\parallel} \gamma_{\nu}^{\parallel}}{2r_{\parallel}^2 t_{\parallel}^2 (s_{\parallel}^2 - 2|q_f B|)} \right\} \\
&\times \epsilon^{\mu}(\lambda_p) \epsilon^{\nu}(\lambda_k) \epsilon^{\alpha}(\lambda_q). \tag{D.16}
\end{aligned}$$

Integration over r_{\perp}

Similarly, at the last steps, the exponential factor is

$$\begin{aligned}
&-\frac{1}{|q_f B|} \left(r_m^2 - 2i\epsilon_{mj} (p + r)_m (r - k)_j - \frac{1}{2} [i\epsilon_{mj} (r - k)_j - (p + r)_m]^2 + (p + r)_m^2 \right) \\
&= -\frac{2}{|q_f B|} \left[r_m^2 + \frac{1}{2} c_m r_m \right] - \frac{1}{|q_f B|} \left[\frac{1}{2} (p_m^2 + k_m^2) + i\epsilon_{mj} p_m k_j \right] \\
&= -\frac{2}{|q_f B|} \left[r_m + \frac{1}{4} c_m \right]^2 + f(p_{\perp}, k_{\perp}), \tag{D.17}
\end{aligned}$$

where

$$\begin{aligned}
c_m &= p_m - k_m + i\epsilon_{mj} (p_j + k_j) \\
f(p_{\perp}, k_{\perp}) &= \frac{1}{8|q_f B|} [a_m]^2 - \frac{1}{2|q_f B|} (p_m^2 + k_m^2 + i\epsilon_{mj} p_m k_j). \tag{D.18}
\end{aligned}$$

Defining $\tilde{r}_m = r_m + \frac{1}{4} c_m$ and ignoring the linear terms of r_{\perp} the desired integral gives:

$$\begin{aligned}
&\frac{1}{(2\pi)^2} \frac{\pi |q_f B|}{2} \frac{1}{4} e^{f(p_{\perp}, k_{\perp})} \\
&\times \int \frac{d^2 r_{\parallel}}{(2\pi)^2} \text{Tr} \left\{ \frac{\gamma^1 \gamma^2 \not{s}_{\parallel} \gamma_{\alpha} \not{t}_{\parallel} \gamma_{\nu} \not{r}_{\parallel} \gamma_{\mu}^{\parallel}}{r_{\parallel}^2 s_{\parallel}^2 (t_{\parallel}^2 - 2|q_f B|)} + \frac{\gamma^1 \gamma^2 \not{r}_{\parallel} \gamma_{\mu} \not{t}_{\parallel} \gamma_{\alpha} \not{s}_{\parallel} \gamma_{\nu}^{\parallel}}{r_{\parallel}^2 t_{\parallel}^2 (s_{\parallel}^2 - 2|q_f B|)} - \frac{\gamma^1 \gamma^2 \not{t}_{\parallel} \gamma_{\nu} \not{r}_{\parallel} \gamma_{\mu} \not{s}_{\parallel} \gamma_{\alpha}^{\parallel}}{t_{\parallel}^2 s_{\parallel}^2 (r_{\parallel}^2 - 2|q_f B|)} \right\}, \tag{D.19}
\end{aligned}$$

where a, b, c , and $f(p_\perp, k_\perp)$ are given in Eq. (2.54).

To obtain Eq. (2.53) the approximation $2|q_f B| \gg t_\parallel^2, s_\parallel^2, r_\parallel^2$ is performed, so that it allows to compute the parallel momentum integrals in terms of a Feynman parametrization:

$$\frac{1}{AB} = \int_0^1 \frac{dx}{[xA + (1-x)B]}, \quad (\text{D.20})$$

in such a way that the only integrals are reduced to the following identities [84]:

$$\begin{aligned} \int \frac{d^d l}{(2\pi)^d} \frac{1}{(l^2 - \Delta)^n} &= \frac{(-1)^n}{(4\pi)^{d/2}} i \frac{\Gamma(n - d/2)}{\Gamma(n)} \left(\frac{1}{\Delta}\right)^{n-d/2} \\ \int \frac{d^d l}{(2\pi)^d} \frac{l^2}{(l^2 - \Delta)^n} &= \frac{(-1)^{n-1}}{(4\pi)^{d/2}} i \frac{d}{2} \frac{\Gamma(n - d/2 - 1)}{\Gamma(n)} \left(\frac{1}{\Delta}\right)^{n-d/2-1} \\ \int \frac{d^d l}{(2\pi)^d} \frac{l^\mu l^\nu}{(l^2 - \Delta)^n} &= \frac{(-1)^{n-1}}{(4\pi)^{d/2}} i \frac{d}{2} g^{\mu\nu} \frac{\Gamma(n - d/2 - 1)}{\Gamma(n)} \left(\frac{1}{\Delta}\right)^{n-d/2-1}. \end{aligned} \quad (\text{D.21})$$

Invariant Momentum Distribution and Flow Coefficient Calculation for the Process $gg \rightarrow \gamma$

To compute the invariant momentum distribution and the flow coefficient v_2 , the starting point is the energy-momentum conservation given by:

$$\begin{aligned}\omega_q &= \omega_p + \omega_k \\ \mathbf{q} &= \mathbf{p} + \mathbf{k},\end{aligned}\tag{E.1}$$

so that, if the particles are in the mass-shell, i.e., $|\mathbf{p}| = \omega_p$ it is easy to find that

$$\omega_q^2 = (\omega_p + \omega_k)^2 = \omega_p^2 + \omega_k^2 + 2\omega_p\omega_k \cos \delta,\tag{E.2}$$

where δ is the angle between the gluon's three-momentum. The above equation is satisfied only if $\delta = 0$, and therefore, the spatial momentum of the gluons are parallel.

Squared Matrix Element

From the tensorial structure of Eq. (2.53):

$$\begin{aligned}\Gamma^{\mu\nu\alpha} &= \left(g_{\parallel}^{\mu\alpha} - \frac{p_{\parallel}^{\mu} p_{\parallel}^{\alpha}}{p_{\parallel}^2} \right) h^{\nu}(a) - \left(g_{\parallel}^{\mu\nu} - \frac{p_{\parallel}^{\mu} p_{\parallel}^{\nu}}{p_{\parallel}^2} \right) h^{\alpha}(a) + \left(g_{\parallel}^{\mu\nu} - \frac{k_{\parallel}^{\mu} k_{\parallel}^{\nu}}{k_{\parallel}^2} \right) h^{\alpha}(b) \\ &- \left(g_{\parallel}^{\alpha\nu} - \frac{k_{\parallel}^{\alpha} k_{\parallel}^{\nu}}{k_{\parallel}^2} \right) h^{\mu}(b) + \left(g_{\parallel}^{\alpha\nu} - \frac{q_{\parallel}^{\alpha} q_{\parallel}^{\nu}}{q_{\parallel}^2} \right) h^{\mu}(c) - \left(g_{\parallel}^{\mu\alpha} - \frac{q_{\parallel}^{\mu} q_{\parallel}^{\alpha}}{q_{\parallel}^2} \right) h^{\nu}(c),\end{aligned}\tag{E.3}$$

where

$$\begin{aligned}
T_{\parallel}^{\mu\nu} &= g_{\parallel}^{\mu\nu} - \frac{q_{\parallel}^{\mu} q_{\parallel}^{\nu}}{q_{\parallel}^2} \\
S_{1\perp}^{\nu} &= h^{\nu}(a) - h^{\nu}(c) = \frac{i}{\pi} \epsilon_m^{\nu} (2p^m + k^m - i\epsilon^{mn} k^n) \\
S_{2\perp}^{\alpha} &= h^{\alpha}(b) - h^{\alpha}(a) = \frac{i}{\pi} \epsilon_m^{\alpha} (p^m - k^m - i\epsilon^{mn} (p^n + k^n)) \\
S_{3\perp}^{\mu} &= h^{\mu}(c) - h^{\mu}(b) = \frac{i}{\pi} \epsilon_m^{\mu} (-3p^m + i\epsilon^{mn} (p^n + 2k^n)), \tag{E.4}
\end{aligned}$$

the squared matrix element is

$$\begin{aligned}
\sum_{\text{pol}} \left| \widetilde{\mathcal{M}} \right|^2 &= \left| -i\pi^3 q_f g^2 \delta^{(4)}(q-p-k) e^{f(p,k)} \right|^2 \sum_{\text{pol}} \Gamma^{\mu\nu\alpha} \Gamma^{*\mu'\nu'\alpha'} \epsilon_{\mu} \epsilon_{\nu} \epsilon_{\alpha} \epsilon_{\mu'}^* \epsilon_{\nu'}^* \epsilon_{\alpha'}^* \\
&= - \left| -i\pi^3 q_f g^2 \delta^{(4)}(q-p-k) e^{f(p,k)} \right|^2 g_{\mu\mu'} g_{\nu\nu'} g_{\alpha\alpha'} \Gamma^{\mu\nu\alpha} \Gamma^{*\mu'\nu'\alpha'} \\
&= -(2\pi)^4 \delta^{(4)}(q-p-k) \mathcal{VT} \left| \pi^3 q_f g^2 e^{f(p,k)} \right|^2 \sum_i |S_{i\perp}|^2 \tag{E.5}
\end{aligned}$$

where where it has been used the fact that in an unpolarized cross section the Ward identity implies that [84]:

$$\sum_{\text{pol}} \epsilon_{\mu}^* \epsilon_{\nu} \rightarrow -g_{\mu\nu}. \tag{E.6}$$

together with the identity:

$$\left| \delta^{(4)}(q-p-k) \right|^2 = (2\pi)^4 \delta^{(4)}(q-p-k) \mathcal{VT}. \tag{E.7}$$

Note that after sum over flavours, Eq. (E.5) corresponds to Eq. (2.55).

On the other hand:

$$\begin{aligned}
|S_{1\perp}^{\nu}|^2 &= S_{1\perp}^{\nu} S_{\nu}^{1\perp*} \\
&= \frac{1}{\pi^2} \epsilon_m^{\nu} \epsilon_{\nu}^l (2p^m + k^m - i\epsilon^{mn} k^n) (2p_l + k_l + i\epsilon_{lj} k_j) \\
&= \frac{1}{\pi^2} \delta_m^l (2p^m + k^m - i\epsilon^{mn} k^n) (2p_l + k_l + i\epsilon_{lj} k_j) \\
&= -\frac{4p_{\perp}^2 + 2k_{\perp}^2 + 4p_{\perp} \cdot k_{\perp}}{\pi^2}, \tag{E.8}
\end{aligned}$$

where the following conventions were used:

$$p^m p_m = -p_1^2 - p_2^2 = -p_{\perp}^2 \tag{E.9a}$$

and

$$p^m k_m = -p_1 k_1 - p_2 k_2 = -p_{\perp} \cdot k_{\perp}. \tag{E.9b}$$

Similarly:

$$|S_{2\perp}^\alpha|^2 = -\frac{2(p_\perp^2 + k_\perp^2)}{\pi^2}, \quad (\text{E.10})$$

and

$$|S_{3\perp}^\mu|^2 = -\frac{10p_\perp^2 + 4k_\perp^2 + 4p_\perp \cdot k_\perp}{\pi^2}. \quad (\text{E.11})$$

By using Eq. (E.1) and the fact that the three-momentum for the involved particles are collinear it is straightforward to obtain the rule of Eq. (2.57):

$$\begin{aligned} p^\mu &= \omega_p(1, \hat{p}) = (\omega_p/\omega_q) q^\mu, \\ k^\mu &= \omega_k(1, \hat{k}) = (\omega_k/\omega_q) q^\mu, \end{aligned} \quad (\text{E.12})$$

in such a way that the quantities shown in Eqs. (E.8)- (E.11) can be written in terms of q_\perp^2 , namely:

$$\begin{aligned} p_\perp^2 &= \left(\frac{\omega_p}{\omega_q}\right)^2 q_\perp^2 \\ k_\perp^2 &= \left(\frac{\omega_k}{\omega_q}\right)^2 q_\perp^2, \end{aligned} \quad (\text{E.13})$$

so that after sum over flavors:

$$\begin{aligned} \sum_{\text{pol},f} |\widetilde{\mathcal{M}}|^2 &= (2\pi)^4 \delta^{(4)}(q - p - k) \mathcal{V}\mathcal{T} \frac{2\alpha_{\text{em}}\alpha_s^2 q_\perp^2}{\pi\omega_q^2} (2\omega_p^2 + \omega_k^2 + \omega_p\omega_k) \\ &\times \sum_f q_f^2 \exp\left\{-\frac{q_\perp^2}{|q_f B| \omega_q^2} (\omega_p^2 + \omega_k^2 + \omega_p\omega_k)\right\}, \end{aligned} \quad (\text{E.14})$$

which is the result of Eq. (2.56).

Invariant Momentum Distribution

From the invariant momentum distribution definition of Eq. (2.58) and from the squared matrix element of Eq. (2.56) it follows that:

$$\begin{aligned} \omega_q \frac{d^3 N}{d^3 q} &= \frac{1}{2(2\pi)^3} \int \frac{d^3 p}{2(2\pi)^3 \omega_p} \int \frac{d^3 k}{2(2\pi)^3 \omega_k} n(\omega_p) n(\omega_k) \sum_{\text{pol},f} |\widetilde{\mathcal{M}}|^2 \\ &= (2\pi)^4 \frac{\mathcal{V}\mathcal{T}}{2(2\pi)^3} \frac{2q_f^2 \alpha_{\text{em}} \alpha_s^2}{\pi\omega_q^2} q_\perp^2 \int \frac{d^3 p}{2(2\pi)^3 \omega_p} \int \frac{d^3 k}{2(2\pi)^3 \omega_k} n(\omega_p) n(\omega_k) \\ &\times \delta(\omega_q - \omega_p - \omega_k) \delta^{(3)}(\mathbf{q} - \mathbf{p} - \mathbf{k}) (2\omega_p^2 + \omega_k^2 + \omega_p\omega_k) \\ &\times \exp\left\{-\frac{q_\perp^2}{|q_f B| \omega_q^2} (\omega_p^2 + \omega_k^2 + \omega_p\omega_k)\right\}, \end{aligned} \quad (\text{E.15})$$

where in the last line the sum over f is implicit and it was used the fact that

$$\delta^{(4)}(P) = \delta^{(0)}(P^0) \delta^{(3)}(\mathbf{P}). \quad (\text{E.16})$$

By using the mass-shell condition for gluons and photon the integral of interest is given by:

$$\begin{aligned} I &= \int \frac{d^3p}{2(2\pi)^3|\mathbf{p}|} \int \frac{d^3k}{2(2\pi)^3|\mathbf{k}|} \delta(\omega_q - \omega_p - \omega_k) \delta^{(3)}(\mathbf{q} - \mathbf{p} - \mathbf{k}) \\ &\times n(|\mathbf{p}|) n(|\mathbf{k}|) (2|\mathbf{p}|^2 + |\mathbf{k}|^2 + \mathbf{p} \cdot \mathbf{k}) \exp \left\{ -\frac{q_\perp^2}{|q_f B| \omega_q^2} (|\mathbf{p}|^2 + |\mathbf{k}|^2 + \mathbf{p} \cdot \mathbf{k}) \right\} \\ &= \frac{1}{2(2\pi)^3} \int \frac{d^3p}{2(2\pi)^3|\mathbf{p}||\mathbf{q} - \mathbf{p}|} \delta\left(\omega_q - \omega_p - \sqrt{\mathbf{p}^2 + \mathbf{q}^2 - 2|\mathbf{p}||\mathbf{q}| \cos \alpha}\right) \\ &\times n(|\mathbf{p}|) n(|\mathbf{q} - \mathbf{p}|) (2|\mathbf{p}|^2 + |\mathbf{q} - \mathbf{p}|^2 + \mathbf{p} \cdot (\mathbf{q} - \mathbf{p})) \\ &\times \exp \left\{ -\frac{q_\perp^2}{|q_f B| \omega_q^2} (|\mathbf{p}|^2 + |\mathbf{q} - \mathbf{p}|^2 + \mathbf{p} \cdot (\mathbf{q} - \mathbf{p})) \right\}. \end{aligned} \quad (\text{E.17})$$

The integration over p is performed in a spherical coordinate system and given the momentum's collinearity condition:

$$\delta\left(\omega_q - \omega_p - \sqrt{\mathbf{p}^2 + \mathbf{q}^2 - 2|\mathbf{p}||\mathbf{q}| \cos \alpha}\right) = \frac{|\mathbf{q} - \mathbf{p}|}{\omega_p \omega_q} \delta(\cos \alpha - 1), \quad (\text{E.18})$$

it follows that:

$$\begin{aligned} \omega_q \frac{d^3N}{d^3q} &= \frac{q_f^2 \alpha_{\text{em}} \alpha_s^2 \mathcal{V} \mathcal{T}}{2(2\pi)^5} \frac{q_\perp^2}{\omega_q^3} \int d\omega_p (2\omega_p^2 + \omega_q^2 - \omega_p \omega_q) n(\omega_p) n(|\omega_q - \omega_p|) \\ &\times \exp \left\{ -\frac{q_\perp^2}{|q_f B| \omega_q^2} (\omega_p^2 + \omega_q^2 - \omega_p \omega_q) \right\}. \end{aligned} \quad (\text{E.19})$$

Now, given that:

$$\frac{\omega_q}{d^3q} = \frac{1}{d^2q_\perp dy} = \frac{1}{\omega_q d\omega_q d\theta dy}, \quad (\text{E.20})$$

with $q_\perp = \omega_q \sin \theta$, and θ the angle between \mathbf{q} and the magnetic field, the Eq. (E.19) becomes:

$$\frac{dN}{\omega_q d\omega_q d\theta dy} = \frac{q_f^2 \alpha_{\text{em}} \alpha_s^2 \mathcal{V} \mathcal{T}}{2(2\pi)^5} \frac{\sin^2 \theta}{\omega_q} \mathcal{I}(\omega_q, \theta), \quad (\text{E.21})$$

where

$$\begin{aligned} \mathcal{I}(\omega_q, \theta) &= \int d\omega_p (2\omega_p^2 + \omega_q^2 - \omega_p \omega_q) n(\omega_p) n(|\omega_q - \omega_p|) \\ &\times \exp \left\{ -\frac{\sin^2 \theta}{|q_f B|} (\omega_p^2 + \omega_q^2 - \omega_p \omega_q) \right\}. \end{aligned} \quad (\text{E.22})$$

From Eq. (E.21) the number of photons for central rapidity $\Delta y \simeq 1$ can be obtained as follows:

$$\frac{dN}{\omega_q d\omega_q} = \frac{q_f^2 \alpha_{\text{em}} \alpha_s^2 \mathcal{V}\mathcal{T}}{2(2\pi)^5 \omega_q} \int_0^{2\pi} d\theta \sin^2 \theta I(\omega_q, \theta). \quad (\text{E.23})$$

Finally, by using:

$$\int_0^{2\pi} d\theta \sin^2 \theta e^{-f(x) \sin^2 \theta} = \pi e^{-f(x)/2\theta} \left[I_0 \left(\frac{f(x)}{2} \right) - I_1 \left(\frac{f(x)}{2} \right) \right], \quad (\text{E.24})$$

with $I_k(x)$ the Bessel functions of order k , and sum over f the invariant momentum distribution of Eq. (2.60) is obtained.

Flow Coefficient

The photon angular distribution is obtained from Eq. (E.21):

$$\frac{dN}{d\theta} = \frac{q_f^2 \alpha_{\text{em}} \alpha_s^2 \mathcal{V}\mathcal{T}}{2(2\pi)^5} \sin^2 \theta \int_0^\infty d\omega_q I(\omega_q, \theta). \quad (\text{E.25})$$

The v_2 coefficient usually is measured from the collision plane (see Fig. 2.18), but in the present calculation the angle θ is referred to the magnetic field. Thus, in order to compare with the experimental data it is necessary to perform the shift $\theta = \pi/2 - \phi$ so that:

$$\begin{aligned} \frac{dN}{d\phi} &= \frac{q_f^2 \alpha_{\text{em}} \alpha_s^2 \mathcal{V}\mathcal{T}}{2(2\pi)^5} \cos^2 \phi \int_0^\infty d\omega_q I(\omega_q, \pi/2 - \phi) \\ &= \frac{N}{2\pi} \left[1 + \sum_n v_n(\omega_q) \cos(n\phi) \right]. \end{aligned} \quad (\text{E.26})$$

From the identity:

$$\int_0^{2\pi} d\phi \cos^2 \phi \cos(2\phi) e^{-f(x) \cos^2 \phi} = \pi e^{-f(x)/2} \left[I_0 \left(\frac{f(x)}{2} \right) - \frac{2 + f(x)}{f(x)} I_1 \left(\frac{f(x)}{2} \right) \right], \quad (\text{E.27})$$

the flow coefficient of Eq. (2.64) is achieved.

Appendix **F**

Proof of Eq. (2.70)

From three cross symmetry of Eq. (2.67):

$$\mathcal{M}_{g \rightarrow g\gamma}(p, k, q) = \mathcal{M}_{gg \rightarrow \gamma}(p, -k, q), \quad (\text{F.1})$$

and taking into account the result of Eq. (E.5) the problem is resumed to evaluate the expression given by

$$|e^{f(p, -k)}|^2 \sum_i |S_{i\perp}(-k)|^2, \quad (\text{F.2})$$

so that the sign change is reflected in quantities:

$$k_{\perp}^2 = \left(\frac{\omega_k}{\omega_q} \right)^2 q_{\perp}^2 \quad (\text{F.3a})$$

and

$$k_{\perp} \cdot p_{\perp} = -\frac{\omega_p \omega_k}{\omega_q^2} q_{\perp}^2, \quad (\text{F.3b})$$

then,

$$\begin{aligned} \sum_{\text{pol}, f} \left| \widetilde{\mathcal{M}}_{g \rightarrow g\gamma} \right|^2 &= (2\pi)^4 \delta^{(4)}(q - p + k) \mathcal{V}\mathcal{T} \frac{2\alpha_{\text{em}} \alpha_s^2 q_{\perp}^2}{\pi \omega_q^2} (2\omega_p^2 + \omega_k^2 - \omega_p \omega_k) \\ &\times \sum_f q_f^2 \exp \left\{ -\frac{q_{\perp}^2}{|q_f B| \omega_q^2} (\omega_p^2 + \omega_k^2 - \omega_p \omega_k) \right\}. \end{aligned} \quad (\text{F.4})$$

From the above, the integral in the invariant momentum distribution is:

$$\begin{aligned}
J &= \int \frac{d^3 p}{2(2\pi)^3 |\mathbf{p}|} \int \frac{d^3 k}{2(2\pi)^3 |\mathbf{k}|} \delta(\omega_q - \omega_p + \omega_k) \delta^{(3)}(\mathbf{q} - \mathbf{p} + \mathbf{k}) \\
&\times n(|\mathbf{p}|) [1 + n(|\mathbf{k}|)] (2|\mathbf{p}|^2 + |\mathbf{k}|^2 - \mathbf{p} \cdot \mathbf{k}) \exp \left\{ -\frac{q_\perp^2}{|q_f B| \omega_q^2} (|\mathbf{p}|^2 + |\mathbf{k}|^2 - \mathbf{p} \cdot \mathbf{k}) \right\}
\end{aligned} \tag{F.5}$$

The integration over $d^3 k$ implies $\mathbf{k} = \mathbf{p} - \mathbf{q}$, therefore:

$$\begin{aligned}
J &= \frac{1}{2(2\pi)^3} \int \frac{d^3 p}{2(2\pi)^3 |\mathbf{p}| |\mathbf{q} - \mathbf{p}|} \delta \left(\omega_q - \omega_p - \sqrt{\mathbf{p}^2 + \mathbf{q}^2 - 2|\mathbf{p}||\mathbf{q}| \cos \alpha} \right) \\
&\times n(|\mathbf{p}|) [1 + n(|\mathbf{q} - \mathbf{p}|)] (2|\mathbf{p}|^2 + |\mathbf{q} - \mathbf{p}|^2 + \mathbf{p} \cdot (\mathbf{q} - \mathbf{p})) \\
&\times \exp \left\{ -\frac{q_\perp^2}{|q_f B| \omega_q^2} (|\mathbf{p}|^2 + |\mathbf{q} - \mathbf{p}|^2 + \mathbf{p} \cdot (\mathbf{q} - \mathbf{p})) \right\},
\end{aligned} \tag{F.6}$$

which apart from the form of the gluon distributions has the same form than Eq. (E.17), so that the steps to compute such integral yields Eq. (2.70).

Derivation of tensor structures of Eqs. (3.7)

Recalling the general expression of the gluon polarization tensor of Eq. (3.1):

$$i\Pi_{(ab)}^{\mu\nu} = -\frac{1}{2} \int \frac{d^4k}{(2\pi)^4} \text{Tr} \{igt_b \gamma^\nu iS^{(n)}(k)igt_a \gamma^\mu iS^{(m)}(q)\} + \text{C.C.} \quad (\text{G.1})$$

The trace in the above expression involves two fermion propagator factors, each given by Eqs. (2.47)-(3.3), so that their product produces nine terms. By defining the function

$$\tilde{E}(p_\perp, k_\perp | q_f B) \equiv \exp \left[-\frac{k_\perp^2 + (k-p)_\perp^2}{|q_f B|} \right], \quad (\text{G.2})$$

such terms are explicitly given by

$$\begin{aligned} t_1^{\mu\nu} &= -g^2 \int \frac{d^4k}{(2\pi)^4} \tilde{E}(p_\perp, k_\perp | q_f B) \sum_{n,m=0}^{\infty} (-1)^{n+m} L_n^0 \left(\frac{2k_\perp^2}{|q_f B|} \right) L_m^0 \left[\frac{2(k-p)_\perp^2}{|q_f B|} \right] \\ &\times \frac{\text{Tr} \left\{ \gamma^\nu (\not{k}_\parallel + m_f) \mathcal{O}^- \gamma^\mu (\not{k}_\parallel - \not{p}_\parallel + m_f) \mathcal{O}^- \right\}}{\left[k_\parallel^2 - m_f^2 - 2n |q_f B| \right] \left[(k-p)_\parallel^2 - m_f^2 - 2m |q_f B| \right]} + \text{C.C.} \quad (\text{G.3}) \end{aligned}$$

$$\begin{aligned} t_2^{\mu\nu} &= g^2 \int \frac{d^4k}{(2\pi)^4} \tilde{E}(p_\perp, k_\perp | q_f B) \sum_{n,m=1}^{\infty} (-1)^{n+m} L_n^0 \left(\frac{2k_\perp^2}{|q_f B|} \right) L_{m-1}^0 \left[\frac{2(k-p)_\perp^2}{|q_f B|} \right] \\ &\times \frac{\text{Tr} \left\{ \gamma^\nu (\not{k}_\parallel + m_f) \mathcal{O}^- \gamma^\mu (\not{k}_\parallel - \not{p}_\parallel + m_f) \mathcal{O}^+ \right\}}{\left[k_\parallel^2 - m_f^2 - 2n |q_f B| \right] \left[(k-p)_\parallel^2 - m_f^2 - 2m |q_f B| \right]} + \text{C.C.} \quad (\text{G.4}) \end{aligned}$$

$$\begin{aligned}
t_3^{\mu\nu} &= -2g^2 \int \frac{d^4k}{(2\pi)^4} \tilde{E}(p_\perp, k_\perp | q_f B) \sum_{n=0, m=1}^{\infty} (-1)^{n+m} L_n^0 \left(\frac{2k_\perp^2}{|q_f B|} \right) L_{m-1}^1 \left[\frac{2(k-p)_\perp^2}{|q_f B|} \right] \\
&\times \frac{\text{Tr} \left\{ \gamma^\nu (\not{k}_\parallel + m_f) \mathcal{O}^- \gamma^\mu (\not{k}_\perp - \not{p}_\perp) \right\}}{\left[k_\parallel^2 - m_f^2 - 2n |q_f B| \right] \left[(k-p)_\parallel^2 - m_f^2 - 2m |q_f B| \right]} + \text{C.C.} \tag{G.5}
\end{aligned}$$

$$\begin{aligned}
t_4^{\mu\nu} &= g^2 \sum_{n=1, m=0}^{\infty} \int \frac{d^4k}{(2\pi)^4} \tilde{E}(p_\perp, k_\perp | q_f B) (-1)^{n+m} L_{n-1}^0 \left(\frac{2k_\perp^2}{|q_f B|} \right) L_m^0 \left[\frac{2(k-p)_\perp^2}{|q_f B|} \right] \\
&\times \frac{\text{Tr} \left\{ \gamma^\nu (\not{k}_\parallel + m_f) \mathcal{O}^+ \gamma^\mu (\not{k}_\parallel - \not{p}_\parallel + m_f) \mathcal{O}^- \right\}}{\left[k_\parallel^2 - m_f^2 - 2n |q_f B| \right] \left[(k-p)_\parallel^2 - m_f^2 - 2m |q_f B| \right]} + \text{C.C.} \tag{G.6}
\end{aligned}$$

$$\begin{aligned}
t_5^{\mu\nu} &= -g^2 \int \frac{d^4k}{(2\pi)^4} \tilde{E}(p_\perp, k_\perp | q_f B) \sum_{n=1, m=1}^{\infty} (-1)^{n+m} L_{n-1}^0 \left(\frac{2k_\perp^2}{|q_f B|} \right) L_{m-1}^0 \left[\frac{2(k-p)_\perp^2}{|q_f B|} \right] \\
&\times \frac{\text{Tr} \left\{ \gamma^\nu (\not{k}_\parallel + m_f) \mathcal{O}^+ \gamma^\mu (\not{k}_\parallel - \not{p}_\parallel + m_f) \mathcal{O}^+ \right\}}{\left[k_\parallel^2 - m_f^2 - 2n |q_f B| \right] \left[(k-p)_\parallel^2 - m_f^2 - 2m |q_f B| \right]} + \text{C.C.} \tag{G.7}
\end{aligned}$$

$$\begin{aligned}
t_6^{\mu\nu} &= 2g^2 \int \frac{d^4k}{(2\pi)^4} \tilde{E}(p_\perp, k_\perp | q_f B) \sum_{n=1, m=1}^{\infty} (-1)^{n+m} L_{n-1}^0 \left(\frac{2k_\perp^2}{|q_f B|} \right) L_{m-1}^1 \left[\frac{2(k-p)_\perp^2}{|q_f B|} \right] \\
&\times \frac{\text{Tr} \left\{ \gamma^\nu (\not{k}_\parallel + m_f) \mathcal{O}^+ \gamma^\mu (\not{k}_\perp - \not{p}_\perp) \right\}}{\left[k_\parallel^2 - m_f^2 - 2n |q_f B| \right] \left[(k-p)_\parallel^2 - m_f^2 - 2m |q_f B| \right]} + \text{C.C.} \tag{G.8}
\end{aligned}$$

$$\begin{aligned}
t_7^{\mu\nu} &= -2g^2 \int \frac{d^4k}{(2\pi)^4} \tilde{E}(p_\perp, k_\perp | q_f B) \sum_{n=1, m=0}^{\infty} (-1)^{n+m} L_{n-1}^1 \left(\frac{2k_\perp^2}{|q_f B|} \right) L_m^0 \left[\frac{2(k-p)_\perp^2}{|q_f B|} \right] \\
&\times \frac{\text{Tr} \left\{ \gamma^\nu \not{k}_\perp \gamma^\mu (\not{k}_\parallel - \not{p}_\parallel + m_f) \mathcal{O}^- \right\}}{\left[k_\parallel^2 - m_f^2 - 2n |q_f B| \right] \left[(k-p)_\parallel^2 - m_f^2 - 2m |q_f B| \right]} + \text{C.C.} \tag{G.9}
\end{aligned}$$

$$\begin{aligned}
t_8^{\mu\nu} &= 2g^2 \int \frac{d^4k}{(2\pi)^4} \tilde{E}(p_\perp, k_\perp | q_f B) \sum_{n=1, m=1}^{\infty} (-1)^{n+m} L_{n-1}^1 \left(\frac{2k_\perp^2}{|q_f B|} \right) L_{m-1}^0 \left[\frac{2(k-p)_\perp^2}{|q_f B|} \right] \\
&\times \frac{\text{Tr} \left\{ \gamma^\nu \not{k}_\perp \gamma^\mu (\not{k}_\parallel - \not{p}_\parallel + m_f) \mathcal{O}^+ \right\}}{\left[k_\parallel^2 - m_f^2 - 2n |q_f B| \right] \left[(k-p)_\parallel^2 - m_f^2 - 2m |q_f B| \right]} + \text{C.C.} \tag{G.10}
\end{aligned}$$

$$\begin{aligned}
t_9^{\mu\nu} &= 4g^2 \int \frac{d^4k}{(2\pi)^4} \tilde{E}(p_\perp, k_\perp |q_f B|) \sum_{n=1, m=1}^{\infty} (-1)^{n+m} L_{n-1}^1 \left(\frac{2k_\perp^2}{|q_f B|} \right) L_{m-1}^1 \left[\frac{2(k-p)_\perp^2}{|q_f B|} \right] \\
&\times \frac{\text{Tr} \left\{ \gamma^\nu \not{k}_\perp \gamma^\mu (\not{k}_\perp - \not{p}_\perp) \right\}}{\left[k_\parallel^2 - m_f^2 - 2n |q_f B| \right] \left[(k-p)_\parallel^2 - m_f^2 - 2m |q_f B| \right]} + \text{C.C.} \tag{G.11}
\end{aligned}$$

In order to perform the sum over Landau levels, a Schwinger parametrization is performed to the denominators:

$$\frac{1}{y} = \int_0^\infty e^{-yx} dx. \tag{G.12}$$

For the Eq. (G.3)

$$\begin{aligned}
t_1^{\mu\nu} &= -g^2 \int \frac{d^4k}{(2\pi)^4} \tilde{E}(p_\perp, k_\perp |q_f B|) \text{Tr} \left\{ \gamma^\nu (\not{k}_\parallel + m_f) \mathcal{O}^- \gamma^\mu (\not{k}_\parallel - \not{p}_\parallel + m_f) \mathcal{O}^- \right\} \\
&\times \sum_{n, m=0}^{\infty} \frac{(-1)^{n+m} L_n^0 \left(\frac{2k_\perp^2}{|q_f B|} \right) L_m^0 \left[\frac{2(k-p)_\perp^2}{|q_f B|} \right]}{\left[k_\parallel^2 - m_f^2 - 2n |q_f B| \right] \left[(k-p)_\parallel^2 - m_f^2 - 2m |q_f B| \right]} \\
&= -g^2 \int d^2x \int \frac{d^4k}{(2\pi)^4} \tilde{E}(p_\perp, k_\perp |q_f B|) \text{Tr} \left\{ \gamma^\nu (\not{k}_\parallel + m_f) \mathcal{O}^- \gamma^\mu (\not{k}_\parallel - \not{p}_\parallel + m_f) \mathcal{O}^- \right\} \\
&\times e^{\alpha(k_\parallel)x_1 + \beta(k_\parallel)x_2} \sum_{n, m=0}^{\infty} r_1^n L_n^0(s_1) r_2^m L_m^0(s_2) + \text{C.C.} \tag{G.13}
\end{aligned}$$

where

$$\alpha(k_\parallel) = k_\parallel^2 - m_f^2, \tag{G.14a}$$

$$\beta(k_\parallel) = (k_\parallel - p_\parallel)^2 - m_f^2, \tag{G.14b}$$

$$r_i = -e^{-2|q_f B|x_i}, \quad i = 1, 2, \tag{G.14c}$$

$$s_1 = \frac{2k_\perp^2}{|q_f B|}, \tag{G.14d}$$

and

$$s_2 = \frac{2(k-p)_\perp^2}{|q_f B|}. \tag{G.14e}$$

By using the generating function of the Laguerre Polynomials, given by

$$\sum_{n=0}^{\infty} r^n L_n^b(s) = \frac{1}{(1-r)^{b+1}} \exp\left(-\frac{r}{1-r}s\right), \quad (\text{G.15})$$

it can be found that

$$\begin{aligned} t_1^{\mu\nu} &= -g^2 \int \frac{d^2x}{\left(1 + e^{-2|q_f B|x_1}\right) \left(1 + e^{-2|q_f B|x_2}\right)} \int \frac{d^4k}{(2\pi)^4} \tilde{E}(p_{\perp}, k_{\perp} | q_f B) e^{\alpha(k_{\parallel})x_1 + \beta(k_{\parallel})x_2} \\ &\times \exp\left[n(x_1) \frac{2k_{\perp}^2}{|q_f B|}\right] \exp\left[n(x_2) \frac{2(k-p)_{\perp}^2}{|q_f B|}\right] \\ &\times \text{Tr} \left\{ \gamma^{\nu}(\not{k}_{\parallel} + m_f) \mathcal{O}^{-} \gamma^{\mu}(\not{k}_{\parallel} - \not{p}_{\parallel} + m_f) \mathcal{O}^{-} \right\} + \text{C.C.} \end{aligned} \quad (\text{G.16})$$

where it has been defined

$$n(x) \equiv \frac{1}{e^{2|q_f B|x} + 1}. \quad (\text{G.17})$$

Now, for the trace computation, note that

$$\left[\gamma_{\parallel}^{\mu}, \mathcal{O}^{(\pm)} \right] = 0, \quad (\text{G.18a})$$

$$\mathcal{O}^{(\pm)} \gamma^{\mu} \mathcal{O}^{(\pm)} = \mathcal{O}^{(\pm)} \gamma_{\parallel}^{\mu}, \quad (\text{G.18b})$$

and therefore

$$\begin{aligned} &4\text{Tr} \left\{ \gamma^{\nu}(\not{k}_{\parallel} + m_f) \gamma_{\parallel}^{\mu}(\not{k}_{\parallel} - \not{p}_{\parallel} + m_f) \mathcal{O}^{-} \right\} + \text{C.C.} \\ &= 4\text{Tr} \left\{ \gamma^{\nu}(\not{k}_{\parallel} + m_f) \gamma_{\parallel}^{\mu}(\not{k}_{\parallel} - \not{p}_{\parallel} + m_f) \right\} \\ &= 16 \left[(k_{\parallel} \cdot p_{\parallel} + m_f^2 - k_{\parallel}^2) g_{\parallel}^{\mu\nu} + 2k_{\parallel}^{\mu} k_{\parallel}^{\nu} - k_{\parallel}^{\mu} p_{\parallel}^{\nu} - k_{\parallel}^{\nu} p_{\parallel}^{\mu} \right]. \end{aligned} \quad (\text{G.19})$$

Putting all together

$$t_1^{\mu\nu} = -4g^2 \int \frac{\mathcal{I}_1(x_1, x_2) \mathcal{J}_1^{\mu\nu}(x_1, x_2)}{\left(1 + e^{-2|q_f B|x_1}\right) \left(1 + e^{-2|q_f B|x_2}\right)} d^2x, \quad (\text{G.20})$$

with

$$\mathcal{I}_1 = \int \frac{d^2k_{\perp}}{(2\pi)^2} \exp\left[-\frac{k_{\perp}^2 + (k-p)_{\perp}^2}{|q_f B|}\right] \exp\left[n(x_1) \frac{2k_{\perp}^2}{|q_f B|}\right] \exp\left[n(x_2) \frac{2(k-p)_{\perp}^2}{|q_f B|}\right] \quad (\text{G.21})$$

and

$$\mathcal{J}_1^{\mu\nu} = \int \frac{d^2 k_{\parallel}}{(2\pi)^2} e^{\alpha(k_{\parallel})x_1} e^{\beta(k_{\parallel})x_2} \left[(k_{\parallel} \cdot p_{\parallel} + m_f^2 - k_{\parallel}^2) g^{\mu\nu} + 2k_{\parallel}^{\mu} k_{\parallel}^{\nu} - k_{\parallel}^{\mu} p_{\parallel}^{\nu} - k_{\parallel}^{\nu} p_{\parallel}^{\mu} \right] \quad (\text{G.22})$$

The transverse integral \mathcal{I}_1 is performed by making the shift

$$k_{\perp} = q_{\perp} + \frac{1 - 2n(x_2)}{2[1 - n(x_1) - n(x_2)]} p_{\perp}, \quad (\text{G.23})$$

which turns the integral into a simple Gaussian form. It is straightforward to prove that

$$\begin{aligned} \mathcal{I}_1 &= \frac{\pi}{(2\pi)^2} \frac{|q_f B|}{\tanh(|q_f B| x_1) + \tanh(|q_f B| x_2)} \\ &\times \exp \left[-\frac{\tanh(|q_f B| x_1) \tanh(|q_f B| x_2)}{\tanh(|q_f B| x_1) + \tanh(|q_f B| x_2)} \frac{p_{\perp}^2}{|q_f B|} \right]. \end{aligned} \quad (\text{G.24})$$

For the parallel integral $\mathcal{J}_1^{\mu\nu}$, the appropriate shift is

$$l = k_{\parallel} - \frac{x_2}{x_1 + x_2} p_{\parallel}, \quad (\text{G.25})$$

and by performing a rotation to Euclidean space, the integral becomes of a Gaussian form in the variable $l_E^2 = l_4^2 + l_3^2$, and thus

$$\begin{aligned} \mathcal{J}_1^{\mu\nu} &= \frac{i\pi}{(2\pi)^2} \exp \left[\frac{x_1 x_2}{x_1 + x_2} p_{\parallel}^2 - m_f^2 (x_1 + x_2) \right] \\ &\times \left[\left(\frac{x_1 x_2}{(x_1 + x_2)^3} p_{\parallel}^2 + \frac{m_f^2}{x_1 + x_2} g^{\mu\nu} p \right) - \frac{2x_1 x_2}{(x_1 + x_2)^3} p_{\parallel}^{\mu} p_{\parallel}^{\nu} \right]. \end{aligned} \quad (\text{G.26})$$

Collecting terms

$$\begin{aligned} t_1^{\mu\nu} &= -\frac{i|q_f B|}{16\pi^2} g^2 \int d^2 x \frac{e^{|q_f B|(x_1+x_2)}}{\sinh[|q_f B|(x_1+x_2)]} \exp \left[\frac{x_1 x_2}{x_1 + x_2} p_{\parallel}^2 - m_f^2 (x_1 + x_2) \right] \\ &\times \exp \left[-\frac{\tanh(|q_f B| x_1) \tanh(|q_f B| x_2)}{\tanh(|q_f B| x_1) + \tanh(|q_f B| x_2)} \frac{p_{\perp}^2}{|q_f B|} \right] \\ &\times \left[\left(\frac{x_1 x_2}{(x_1 + x_2)^3} p_{\parallel}^2 + \frac{m_f^2}{x_1 + x_2} \right) g^{\mu\nu} p - \frac{2x_1 x_2}{(x_1 + x_2)^3} p_{\parallel}^{\mu} p_{\parallel}^{\nu} \right]. \end{aligned} \quad (\text{G.27})$$

Note that the term $t_5^{\mu\nu}$ of Eq. (G.7) has the same tensor structure as $t_1^{\mu\nu}$. By means of the variable shifts $m' = m - 1$ and $n' = n - 1$, which produce a factor $e^{-2|q_f B|(x_1+x_2)}$, this gives rise at the

same set of transverse and parallel integrals than for the case of $t_1^{\mu\nu}$, i.e.,

$$\begin{aligned}
t_5^{\mu\nu} &= -\frac{i|q_f B|}{16\pi^2} g^2 \int d^2x \frac{e^{-|q_f B|(x_1+x_2)}}{\sinh[|q_f B|(x_1+x_2)]} \exp\left[\frac{x_1 x_2}{x_1+x_2} p_{\parallel}^2 - m_f^2(x_1+x_2)\right] \\
&\times \exp\left[-\frac{\tanh(|q_f B|x_1) \tanh(|q_f B|x_2)}{\tanh(|q_f B|x_1) + \tanh(|q_f B|x_2)} \frac{p_{\perp}^2}{|q_f B|}\right] \\
&\times \left[\left(\frac{x_1 x_2}{(x_1+x_2)^3} p_{\parallel}^2 + \frac{m_f^2}{x_1+x_2}\right) g^{\mu\nu} p - \frac{2x_1 x_2}{(x_1+x_2)^3} p_{\parallel}^{\mu} p_{\parallel}^{\nu}\right]. \tag{G.28}
\end{aligned}$$

Adding up these two terms:

$$\begin{aligned}
t_1^{\mu\nu} + t_5^{\mu\nu} &= -\frac{i|q_f B|}{8\pi^2} g^2 \int d^2x \coth[|q_f B|(x_1+x_2)] \exp\left[\frac{x_1 x_2}{x_1+x_2} p_{\parallel}^2 - m_f^2(x_1+x_2)\right] \\
&\times \exp\left[-\frac{\tanh(|q_f B|x_1) \tanh(|q_f B|x_2)}{\tanh(|q_f B|x_1) + \tanh(|q_f B|x_2)} \frac{p_{\perp}^2}{|q_f B|}\right] \\
&\times \left[\left(\frac{x_1 x_2}{(x_1+x_2)^3} p_{\parallel}^2 + \frac{m_f^2}{x_1+x_2}\right) g^{\mu\nu} p - \frac{2x_1 x_2}{(x_1+x_2)^3} p_{\parallel}^{\mu} p_{\parallel}^{\nu}\right] \\
&\equiv -\frac{i}{8\pi^2} g^2 \int d^2x f_0(x_1, x_2) f_1^{\mu\nu}(x_1, x_2). \tag{G.29}
\end{aligned}$$

For the term $t_2^{\mu\nu}$ of Eq. (G.4) the trace involved is computed by using Eq. (G.18a) and the relation

$$\mathcal{O}^{(\pm)} \gamma^{\mu} \mathcal{O}^{(\mp)} = \mathcal{O}^{(\pm)} \gamma_{\perp}^{\mu}, \tag{G.30}$$

so that

$$\text{Tr} \left\{ \gamma_{\perp}^{\nu} (k_{\parallel} + m_f) \gamma^{\mu} (k_{\parallel} - \not{p}_{\parallel} + m_f) \right\} + \text{C.C.} = 4 (k_{\parallel} \cdot p_{\parallel} - k_{\parallel}^2 + m_f^2) g_{\perp}^{\mu\nu}. \tag{G.31}$$

This results implies that after introducing the Schwinger parametrization, the integration over the transverse momentum gives the same results as those in Eq. (G.24). Moreover, in order to apply Eq. (G.15) it is necessary to perform the shift $m' = m - 1$. That shift extracts a factor $-e^{-2|q_f B|x_2}$ from the sum, thus

$$\begin{aligned}
t_2^{\mu\nu} &= -\frac{4\pi|q_f B|}{(2\pi)^4} g^2 \int d^2x \exp\left[-\frac{\tanh(|q_f B|x_1) \tanh(|q_f B|x_2)}{\tanh(|q_f B|x_1) + \tanh(|q_f B|x_2)} \frac{p_{\perp}^2}{|q_f B|}\right] \\
&\times \frac{e^{-2|q_f B|x_2}}{\left(1 + e^{-2|q_f B|x_1}\right) \left(1 + e^{-2|q_f B|x_2}\right)} \frac{|q_f B|}{\tanh(|q_f B|x_1) + \tanh(|q_f B|x_2)} \\
&\times \int d^2k_{\parallel} (k_{\parallel} \cdot p_{\parallel} - k_{\parallel}^2 + m_f^2) e^{\alpha(k_{\parallel})x_1} e^{\beta(k_{\parallel})x_2} g_{\perp}^{\mu\nu}. \tag{G.32}
\end{aligned}$$

The parallel integration is carried out with the help of the momentum shift of Eq. (G.25) which

in Euclidean space gives

$$\begin{aligned}
t_2^{\mu\nu} &= -\frac{4i\pi^2 |q_f B|}{(2\pi)^2} g^2 \int d^2x \exp \left[\frac{x_1 x_2}{x_1 + x_2} p_{\parallel}^2 - m_f^2 (x_1 + x_2) \right] \\
&\times \exp \left[-\frac{\tanh(|q_f B| x_1) \tanh(|q_f B| x_2)}{\tanh(|q_f B| x_1) + \tanh(|q_f B| x_2)} \frac{p_{\perp}^2}{|q_f B|} \right] \\
&\times \frac{e^{-2|q_f B| x_2}}{(1 + e^{-2|q_f B| x_1}) (1 + e^{-2|q_f B| x_2})} \frac{|q_f B|}{\tanh(|q_f B| x_1) + \tanh(|q_f B| x_2)} \\
&\times \left[\frac{x_1 x_2}{(x_1 + x_2)^3} p_{\parallel}^2 + \frac{m_f^2}{x_1 + x_2} + \frac{1}{(x_1 + x_2)^2} \right] g_{\perp}^{\mu\nu}. \tag{G.33}
\end{aligned}$$

From the fact that the term $t_4^{\mu\nu}$ has the same tensor structure of $t_2^{\mu\nu}$, it is easy to show that both expressions are related to each other after the exchange $x_1 \leftrightarrow x_2$, so that

$$\begin{aligned}
t_4^{\mu\nu} &= -\frac{4i\pi^2 |q_f B|}{(2\pi)^2} g^2 \int d^2x \frac{e^{-2|q_f B| x_1}}{(1 + e^{-2|q_f B| x_1}) (1 + e^{-2|q_f B| x_2})} \\
&\times \exp \left[\frac{x_1 x_2}{x_1 + x_2} p_{\parallel}^2 - m_f^2 (x_1 + x_2) \right] \exp \left[-\frac{\tanh(|q_f B| x_1) \tanh(|q_f B| x_2)}{\tanh(|q_f B| x_1) + \tanh(|q_f B| x_2)} \frac{p_{\perp}^2}{|q_f B|} \right] \\
&\times \left[\frac{x_1 x_2}{(x_1 + x_2)^3} p_{\parallel}^2 + \frac{m_f^2}{x_1 + x_2} + \frac{1}{(x_1 + x_2)^2} \right] g_{\perp}^{\mu\nu}, \tag{G.34}
\end{aligned}$$

and therefore, after manipulating the exponential, it reads

$$\begin{aligned}
t_2^{\mu\nu} + t_4^{\mu\nu} &= -\frac{i |q_f B|}{8\pi^2} g^2 \int d^2x \frac{\cosh[|q_f B| (x_2 - x_1)]}{\sinh[|q_f B| (x_1 + x_2)]} \exp \left[\frac{x_1 x_2}{x_1 + x_2} p_{\parallel}^2 - m_f^2 (x_1 + x_2) \right] \\
&\times \exp \left[-\frac{\tanh(|q_f B| x_1) \tanh(|q_f B| x_2)}{\tanh(|q_f B| x_1) + \tanh(|q_f B| x_2)} \frac{p_{\perp}^2}{|q_f B|} \right] \\
&\times \left[\frac{x_1 x_2}{(x_1 + x_2)^3} p_{\parallel}^2 + \frac{m_f^2}{x_1 + x_2} + \frac{1}{(x_1 + x_2)^2} \right] g_{\perp}^{\mu\nu} \\
&\equiv -\frac{i}{8\pi^2} g^2 \int d^2x f_0(x_1, x_2) f_2^{\mu\nu}(x_1, x_2). \tag{G.35}
\end{aligned}$$

For the term $t_3^{\mu\nu}$, the trace is computed with the help of Eqs. (G.18a),(G.18b) and (G.30):

$$\text{Tr} \left\{ \gamma^{\nu} (\not{k}_{\parallel} + m_f) \mathcal{O}^{-} \gamma^{\mu} (\not{k}_{\perp} - \not{p}_{\perp}) \right\} + \text{C.C.} = 4 \left[k_{\parallel}^{\mu} (k_{\perp}^{\nu} - p_{\perp}^{\nu}) + k_{\parallel}^{\nu} (k_{\perp}^{\mu} - p_{\perp}^{\mu}) \right] \tag{G.36}$$

After introducing Schwinger's parametrization and using the generating function for the La-

guerre polynomials (with the shift $m' = m - 1$), it yields

$$\begin{aligned}
t_3^{\mu\nu} &= -\frac{8}{(2\pi)^4} g^2 \int d^2x \int d^4k \frac{e^{-2|q_f B|x_2} e^{\alpha(k_{\parallel})x_1} e^{\beta(k_{\parallel})x_2}}{\left(1 + 2e^{-2|q_f B|x_1}\right) \left(1 + 2e^{-2|q_f B|x_1}\right)^2} \\
&\times \exp\left[-\frac{k_{\perp}^2 + (k-p)_{\perp}^2}{|q_f B|}\right] \exp\left[n(x_1) \frac{2k_{\perp}^2}{|q_f B|}\right] \exp\left[n(x_2) \frac{2(k-p)_{\perp}^2}{|q_f B|}\right] \\
&\times \left[k_{\parallel}^{\mu} (k'_{\perp} - p'_{\perp}) + k'_{\parallel} (k_{\perp}^{\mu} - p_{\perp}^{\mu})\right].
\end{aligned} \tag{G.37}$$

The change of variable in Eq. (G.23) leads to the result

$$\begin{aligned}
t_3^{\mu\nu} &= -\frac{8}{(2\pi)^4} g^2 \int d^2x \int d^4k \frac{e^{-2|q_f B|x_2} [\mathcal{I}_2^{\mu\nu}(x_1, x_2) + \mathcal{I}_2^{\nu\mu}(x_1, x_2)]}{\left(1 + 2e^{-2|q_f B|x_1}\right) \left(1 + 2e^{-2|q_f B|x_1}\right)^2} \\
&\times \exp\left[-\frac{\tanh(|q_f B|x_1) \tanh(|q_f B|x_2) p_{\perp}^2}{\tanh(|q_f B|x_1) + \tanh(|q_f B|x_2) |q_f B|}\right],
\end{aligned} \tag{G.38}$$

where

$$\mathcal{I}_2^{\mu\nu} = \int d^2k_{\parallel} e^{\alpha(k_{\parallel})x_1} e^{\beta(k_{\parallel})x_2} \int d^2q_{\perp} e^{-\eta q_{\perp}^2} k_{\parallel}^{\mu} [q_{\perp}^{\nu} + (\sigma - 1)p_{\perp}^{\nu}], \tag{G.39}$$

with

$$\eta \equiv \frac{\tanh(|q_f B|x_1) + \tanh(|q_f B|x_2)}{|q_f B|}, \tag{G.40a}$$

and

$$\sigma \equiv \frac{\tanh(|q_f B|x_2)}{\tanh(|q_f B|x_1) + \tanh(|q_f B|x_2)}. \tag{G.40b}$$

The perpendicular integration has a simple Gaussian form for which the linear term in q_{\perp} integrates to zero, yielding

$$\mathcal{I}_2^{\mu\nu} = \frac{\pi(\sigma - 1)}{\eta} p_{\perp}^{\nu} \int d^2k_{\parallel} e^{\alpha(k_{\parallel})x_1} e^{\beta(k_{\parallel})x_2} k_{\parallel}^{\mu}. \tag{G.41}$$

The shift of variable in Eq. (G.25) also implies a Gaussian integration (in Euclidean space), where the linear terms in l vanish after integration. In this way

$$\begin{aligned}
\mathcal{I}_2^{\mu\nu} &= \frac{\pi^2(\sigma - 1)}{\eta} \frac{x_2}{(x_1 + x_2)^2} p_{\parallel}^{\mu} p_{\perp}^{\nu} \exp\left[\frac{x_1 x_2}{x_1 + x_2} p_{\parallel}^2 - m_f^2(x_1 + x_2)\right] \\
&= -\frac{i\pi^2 |q_f B| x_2}{(x_1 + x_2)^2} \frac{\tanh(|q_f B|x_1) p_{\parallel}^{\mu} p_{\perp}^{\nu}}{[\tanh(|q_f B|x_1) + \tanh(|q_f B|x_2)]^2}.
\end{aligned} \tag{G.42}$$

Putting together these results

$$\begin{aligned}
t_3^{\mu\nu} &= -\frac{i|q_f B| \pi^2}{(2\pi)^4} g^2 \int d^2x \frac{x_2 e^{|q_f B| x_1} \sinh(|q_f B| x_1)}{(x_1 + x_2)^2 \sinh^2[|q_f B| (x_1 + x_2)]} \\
&\times \exp\left[\frac{x_1 x_2}{x_1 + x_2} p_{\parallel}^2 - m_f^2(x_1 + x_2)\right] \exp\left[-\frac{\tanh(|q_f B| x_1) \tanh(|q_f B| x_2)}{\tanh(|q_f B| x_1) + \tanh(|q_f B| x_2)} \frac{p_{\perp}^2}{|q_f B|}\right] \\
&\times \left(p_{\parallel}^{\mu} p_{\perp}^{\nu} + p_{\parallel}^{\nu} p_{\perp}^{\mu}\right). \tag{G.43}
\end{aligned}$$

The structure $t_6^{\mu\nu}$ is obtained from $t_3^{\mu\nu}$ after the shift $n' = n - 1$ which means introducing a factor $-e^{-2|q_f B| x_1}$, thus

$$\begin{aligned}
t_6^{\mu\nu} &= -\frac{i|q_f B| \pi^2}{(2\pi)^4} g^2 \int d^2x \frac{x_2 e^{-|q_f B| x_1} \sinh(|q_f B| x_1)}{(x_1 + x_2)^2 \sinh^2[|q_f B| (x_1 + x_2)]} \\
&\times \exp\left[\frac{x_1 x_2}{x_1 + x_2} p_{\parallel}^2 - m_f^2(x_1 + x_2)\right] \exp\left[-\frac{\tanh(|q_f B| x_1) \tanh(|q_f B| x_2)}{\tanh(|q_f B| x_1) + \tanh(|q_f B| x_2)} \frac{p_{\perp}^2}{|q_f B|}\right] \\
&\times \left(p_{\parallel}^{\mu} p_{\perp}^{\nu} + p_{\parallel}^{\nu} p_{\perp}^{\mu}\right), \tag{G.44}
\end{aligned}$$

and therefore

$$\begin{aligned}
t_3^{\mu\nu} + t_6^{\mu\nu} &= -\frac{i|q_f B|}{8\pi^2} g^2 \int d^2x \frac{x_2 \cosh(|q_f B| x_1) \sinh(|q_f B| x_1)}{(x_1 + x_2)^2 \sinh^2[|q_f B| (x_1 + x_2)]} \\
&\times \exp\left[\frac{x_1 x_2}{x_1 + x_2} p_{\parallel}^2 - m_f^2(x_1 + x_2)\right] \exp\left[-\frac{\tanh(|q_f B| x_1) \tanh(|q_f B| x_2)}{\tanh(|q_f B| x_1) + \tanh(|q_f B| x_2)} \frac{p_{\perp}^2}{|q_f B|}\right] \\
&\times \left(p_{\parallel}^{\mu} p_{\perp}^{\nu} + p_{\parallel}^{\nu} p_{\perp}^{\mu}\right). \tag{G.45}
\end{aligned}$$

Coming now to the terms $t_7^{\mu\nu}$ and $t_8^{\mu\nu}$, it can be notice that they share a common tensor form. Starting from $t_3^{\mu\nu}$, the expression for $t_7^{\mu\nu}$ is obtained by replacing $x_1 \rightarrow x_2$ and $p \rightarrow -p$. Moreover, $t_8^{\mu\nu}$ is obtained from $t_7^{\mu\nu}$ by performing the shift $m' = m - 1$ which amounts to introducing a factor $-e^{-2|q_f B| x_2}$. Implementing these observations, the following results is obtained:

$$\begin{aligned}
t_7^{\mu\nu} + t_8^{\mu\nu} &= -\frac{i|q_f B|}{8\pi^2} g^2 \int d^2x \frac{x_1 \cosh(|q_f B| x_2) \sinh(|q_f B| x_2)}{(x_1 + x_2)^2 \sinh^2[|q_f B| (x_1 + x_2)]} \\
&\times \exp\left[\frac{x_1 x_2}{x_1 + x_2} p_{\parallel}^2 - m_f^2(x_1 + x_2)\right] \exp\left[-\frac{\tanh(|q_f B| x_1) \tanh(|q_f B| x_2)}{\tanh(|q_f B| x_1) + \tanh(|q_f B| x_2)} \frac{p_{\perp}^2}{|q_f B|}\right] \\
&\times \left(p_{\parallel}^{\mu} p_{\perp}^{\nu} + p_{\parallel}^{\nu} p_{\perp}^{\mu}\right), \tag{G.46}
\end{aligned}$$

then

$$\begin{aligned}
t_3^{\mu\nu} + t_6^{\mu\nu} + t_7^{\mu\nu} + t_8^{\mu\nu} &= -\frac{i|q_f B|}{8\pi^2} g^2 \int \frac{d^2 x}{2(x_1 + x_2)^2 \sinh^2[|q_f B|(x_1 + x_2)]} \\
&\times \exp\left[\frac{x_1 x_2}{x_1 + x_2} p_{\parallel}^2 - m_f^2(x_1 + x_2)\right] \exp\left[-\frac{\tanh(|q_f B|x_1) \tanh(|q_f B|x_2)}{\tanh(|q_f B|x_1) + \tanh(|q_f B|x_2)} \frac{p_{\perp}^2}{|q_f B|}\right] \\
&\times \left[x_1 \sinh(2|q_f B|x_2) + x_2 \sinh(2|q_f B|x_1)\right] \left(p_{\parallel}^{\mu} p_{\perp}^{\nu} + p_{\parallel}^{\nu} p_{\perp}^{\mu}\right) \\
&\equiv -\frac{i}{8\pi^2} g^2 \int d^2 x f_0(x_1, x_2) f_3^{\mu\nu}(x_1, x_2). \tag{G.47}
\end{aligned}$$

Finally, the trace in the term $t_9^{\mu\nu}$ is given by

$$\text{Tr} \left\{ \gamma^{\nu} \not{k}_{\perp} \gamma^{\mu} (\not{k}_{\perp} - \not{p}_{\perp}) \right\} = 4 \left[(k_{\perp} \cdot p_{\perp} + k_{\perp}^2) g^{\mu\nu} + 2k_{\perp}^{\mu} k_{\perp}^{\nu} - (p_{\perp}^{\mu} k_{\perp}^{\nu} + p_{\perp}^{\nu} k_{\perp}^{\mu}) \right]. \tag{G.48}$$

After introducing the Schwinger parametrization and performing the sum together with the shift in Eq. (G.23) is obtained that:

$$\begin{aligned}
t_9^{\mu\nu} &= -\frac{2}{(2\pi)^4} g^2 \int \frac{d^2 x}{\cosh^2(|q_f B|x_1) \cosh^2(|q_f B|x_2)} \\
&\times \exp\left[-\frac{\tanh(|q_f B|x_1) \tanh(|q_f B|x_2)}{\tanh(|q_f B|x_1) + \tanh(|q_f B|x_2)} \frac{p_{\perp}^2}{|q_f B|}\right] \int d^2 k_{\parallel} e^{\alpha(k_{\parallel})x_1} e^{\beta(k_{\parallel})x_2} \\
&\times \int d^2 q_{\perp} e^{-\eta q_{\perp}^2} \left[(q_{\perp}^2 + \sigma(\sigma - 1)p_{\perp}^2) g^{\mu\nu} + 2q_{\perp}^{\mu} q_{\perp}^{\nu} + 2\sigma(\sigma - 1)p_{\perp}^{\nu} p_{\perp}^{\mu} \right], \tag{G.49}
\end{aligned}$$

where the linear terms in q_{\perp} were ignored, and the variables η and σ are defined in Eqs. (G.40). In Euclidean space, by means of the change of variable given in Eq. (G.25), the parallel integral is easily performed, yielding

$$\begin{aligned}
t_9^{\mu\nu} &= -\frac{2i\pi}{(2\pi)^4} g^2 \int \frac{d^2 x}{(x_1 + x_2) \cosh^2(|q_f B|x_1) \cosh^2(|q_f B|x_2)} \mathcal{J}_2^{\mu\nu}(x_1, x_2) \\
&\times \exp\left[\frac{x_1 x_2}{x_1 + x_2} p_{\parallel}^2 - m_f^2(x_1 + x_2)\right] \exp\left[-\frac{\tanh(|q_f B|x_1) \tanh(|q_f B|x_2)}{\tanh(|q_f B|x_1) + \tanh(|q_f B|x_2)} \frac{p_{\perp}^2}{|q_f B|}\right], \tag{G.50}
\end{aligned}$$

where

$$\mathcal{J}_2^{\mu\nu} = \int d^2 q_{\perp} e^{-\eta q_{\perp}^2} \left[(q_{\perp}^2 + \sigma(\sigma - 1)p_{\perp}^2) g^{\mu\nu} + 2q_{\perp}^{\mu} q_{\perp}^{\nu} + 2\sigma(\sigma - 1)p_{\perp}^{\nu} p_{\perp}^{\mu} \right]. \tag{G.51}$$

The last integral has a simple Gaussian form and it is straightforward to compute it, yielding

$$\begin{aligned}
\mathcal{J}_2^{\mu\nu} &= \frac{\pi |q_f B|^2}{[\tanh(|q_f B|x_1) + \tanh(|q_f B|x_2)]^2} \\
&\times \left[\left(1 - \frac{\tanh(|q_f B|x_1) \tanh(|q_f B|x_2) p_{\perp}^2}{|q_f B| [\tanh(|q_f B|x_1) + \tanh(|q_f B|x_2)]} \right) g^{\mu\nu} - g_{\perp}^{\mu\nu} \right. \\
&\left. - \frac{2 \tanh(|q_f B|x_1) \tanh(|q_f B|x_2)}{|q_f B| [\tanh(|q_f B|x_1) + \tanh(|q_f B|x_2)]} p_{\perp}^{\nu} p_{\perp}^{\mu} \right]. \tag{G.52}
\end{aligned}$$

Putting all of this together, we get

$$\begin{aligned}
t_9^{\mu\nu} &= -\frac{i|q_f B|^2}{8\pi^2} \int \frac{d^2x}{(x_1 + x_2) \sinh^2[|q_f B|(x_1 + x_2)]} \\
&\times \exp\left[\frac{x_1 x_2}{x_1 + x_2} p_{\parallel}^2 - m_f^2(x_1 + x_2)\right] \exp\left[-\frac{\tanh(|q_f B|x_1) \tanh(|q_f B|x_2)}{\tanh(|q_f B|x_1) + \tanh(|q_f B|x_2)} \frac{p_{\perp}^2}{|q_f B|}\right] \\
&\times \left[\left(1 - \frac{\tanh(|q_f B|x_1) \tanh(|q_f B|x_2) p_{\perp}^2}{|q_f B| [\tanh(|q_f B|x_1) + \tanh(|q_f B|x_2)]}\right) g^{\mu\nu} - g_{\perp}^{\mu\nu} \right. \\
&\quad \left. - \frac{2 \tanh(|q_f B|x_1) \tanh(|q_f B|x_2)}{|q_f B| [\tanh(|q_f B|x_1) + \tanh(|q_f B|x_2)]} p_{\perp}^{\nu} p_{\perp}^{\mu} \right] \\
&\equiv -\frac{i}{8\pi^2} g^2 \int d^2x f_0(x_1, x_2) f_4^{\mu\nu}(x_1, x_2). \tag{G.53}
\end{aligned}$$

Appendix **H**

Tensor manipulation of Eqs. (3.7)

In order to obtain the tensor structure of Eq. (3.23), the terms $f_1^{\mu\nu}(x_1, x_2)$, $f_3^{\mu\nu}(x_1, x_2)$ and $f_4^{\mu\nu}(x_1, x_2)$ in Eqs. (3.7) have been factorized in a convenient way, so as to avoid the projection procedure which can lead non-physical contributions. The tensor $f_2^{\mu\nu}(x_1, x_2)$ remains unchanged and the manipulation is made by direct inspection.

For $f_1^{\mu\nu}(x_1, x_2)$:

$$\begin{aligned}
 f_1^{\mu\nu}(x_1, x_2) &= |q_f B| \coth[|q_f B|(x_1 + x_2)] \left[\left(\frac{x_1 x_2}{(x_1 + x_2)^3} p_{\parallel}^2 + \frac{m_f^2}{x_1 + x_2} \right) g_{\parallel}^{\mu\nu} - \frac{2x_1 x_2}{(x_1 + x_2)^3} p_{\parallel}^{\mu} p_{\parallel}^{\nu} \right] \\
 &= |q_f B| \coth[|q_f B|(x_1 + x_2)] \left[\left(\frac{x_1 x_2}{(x_1 + x_2)^3} p_{\parallel}^2 + \frac{m_f^2}{x_1 + x_2} \right) g_{\parallel}^{\mu\nu} \right. \\
 &\quad \left. + \frac{2x_1 x_2}{(x_1 + x_2)^3} \left(p_{\parallel}^2 g_{\parallel}^{\mu\nu} - p_{\parallel}^2 g_{\parallel}^{\mu\nu} - p_{\parallel}^{\mu} p_{\parallel}^{\nu} \right) \right] \\
 &= |q_f B| \frac{\coth[|q_f B|(x_1 + x_2)]}{(x_1 + x_2)^3} \left[2x_1 x_2 p_{\parallel}^2 \mathcal{P}_{\parallel}^{\mu\nu} + (m_f^2 (x_1 + x_2)^2 - x_1 x_2 p_{\parallel}^2) g_{\parallel}^{\mu\nu} \right].
 \end{aligned} \tag{H.1}$$

For $f_3^{\mu\nu}(x_1, x_2)$:

$$\begin{aligned}
 f_3^{\mu\nu}(x_1, x_2) &= \frac{|q_f B|}{2(x_1 + x_2)^2 \sinh^2[|q_f B|(x_1 + x_2)]} \\
 &\quad \times \left[x_1 \sinh(2|q_f B|x_2) + x_2 \sinh(2|q_f B|x_1) \right] \left(p_{\parallel}^{\mu} p_{\perp}^{\nu} + p_{\parallel}^{\nu} p_{\perp}^{\mu} \right),
 \end{aligned} \tag{H.2}$$

Notice that

$$p^{\mu} p^{\nu} = \left(p_{\parallel}^{\mu} - p_{\perp}^{\mu} \right) \left(p_{\parallel}^{\nu} - p_{\perp}^{\nu} \right) = p_{\parallel}^{\mu} p_{\parallel}^{\nu} + p_{\perp}^{\mu} p_{\perp}^{\nu} - \left(p_{\parallel}^{\mu} p_{\perp}^{\nu} + p_{\parallel}^{\nu} p_{\perp}^{\mu} \right), \tag{H.3}$$

therefore,

$$\begin{aligned}
\left(p_{\parallel}^{\mu} p_{\perp}^{\nu} + p_{\parallel}^{\nu} p_{\perp}^{\mu}\right) &= p_{\parallel}^{\mu} p_{\parallel}^{\nu} + p_{\perp}^{\mu} p_{\perp}^{\nu} - p^{\mu} p^{\nu} \\
&= p_{\parallel}^{\mu} p_{\parallel}^{\nu} + p_{\perp}^{\mu} p_{\perp}^{\nu} - p^{\mu} p^{\nu} + p^2 g^{\mu\nu} - p^2 g^{\mu\nu} \\
&= p^2 \left(g^{\mu\nu} - \frac{p^{\mu} p^{\nu}}{p^2}\right) + p_{\parallel}^{\mu} p_{\parallel}^{\nu} + p_{\perp}^{\mu} p_{\perp}^{\nu} - (p_{\parallel}^2 - p_{\perp}^2) \left(g_{\parallel}^{\mu\nu} + g_{\perp}^{\mu\nu}\right) \\
&= p^2 \left(g^{\mu\nu} - \frac{p^{\mu} p^{\nu}}{p^2}\right) - p_{\parallel}^2 \mathcal{P}_{\parallel}^{\mu\nu} + p_{\perp}^2 \mathcal{P}_{\perp}^{\mu\nu} - p_{\parallel}^2 g_{\perp}^{\mu\nu} + p_{\perp}^2 g_{\parallel}^{\mu\nu} \\
&= p^2 \left(g^{\mu\nu} - \frac{p^{\mu} p^{\nu}}{p^2} - \mathcal{P}_{\parallel}^{\mu\nu} - \mathcal{P}_{\perp}^{\mu\nu}\right) + p^2 \mathcal{P}_{\parallel}^{\mu\nu} + p^2 \mathcal{P}_{\perp}^{\mu\nu} \\
&\quad - p_{\parallel} \mathcal{P}_{\parallel}^{\mu\nu} + p_{\perp}^2 \mathcal{P}_{\perp}^{\mu\nu} - p_{\parallel}^2 g_{\perp}^{\mu\nu} + p_{\perp}^2 g_{\parallel}^{\mu\nu} \\
&= p^2 \mathcal{P}_0^{\mu\nu} - p_{\perp}^2 \mathcal{P}_{\parallel}^{\mu\nu} + p_{\parallel}^2 \mathcal{P}_{\perp}^{\mu\nu} - p_{\parallel}^2 g_{\perp}^{\mu\nu} + p_{\perp}^2 g_{\parallel}^{\mu\nu}.
\end{aligned} \tag{H.4}$$

Thus,

$$\begin{aligned}
f_3^{\mu\nu}(x_1, x_2) &= \frac{|q_f B| \left[x_1 \sinh(2|q_f B| x_2) + x_2 \sinh(2|q_f B| x_1) \right]}{2(x_1 + x_2)^2 \sinh^2[|q_f B|(x_1 + x_2)]} \\
&\quad \times \left(p^2 \mathcal{P}_0^{\mu\nu} - p_{\perp}^2 \mathcal{P}_{\parallel}^{\mu\nu} + p_{\parallel}^2 \mathcal{P}_{\perp}^{\mu\nu} - p_{\parallel}^2 g_{\perp}^{\mu\nu} + p_{\perp}^2 g_{\parallel}^{\mu\nu} \right).
\end{aligned} \tag{H.5}$$

Finally, for $f_4^{\mu\nu}(x_1, x_2)$, from

$$p_{\perp}^{\mu} p_{\perp}^{\nu} = p_{\perp}^{\mu} p_{\perp}^{\nu} + p_{\perp}^2 g_{\perp}^{\mu\nu} - p_{\perp}^2 g_{\perp}^{\mu\nu} = p_{\perp}^2 \mathcal{P}_{\perp}^{\mu\nu} - p_{\perp}^2 g_{\perp}^{\mu\nu}, \tag{H.6}$$

it can be obtained that

$$\begin{aligned}
f_4^{\mu\nu}(x_1, x_2) &= \frac{|q_f B|^2}{(x_1 + x_2) \sinh^2[|q_f B|(x_1 + x_2)]} \\
&\quad \times \left[\left(1 - \frac{\tanh(|q_f B| x_1) \tanh(|q_f B| x_2)}{|q_f B| [\tanh(|q_f B| x_1) + \tanh(|q_f B| x_2)]} p_{\perp}^2 \right) g^{\mu\nu} - g_{\perp}^{\mu\nu} \right. \\
&\quad - \frac{2 \tanh(|q_f B| x_1) \tanh(|q_f B| x_2)}{|q_f B| [\tanh(|q_f B| x_1) + \tanh(|q_f B| x_2)]} \mathcal{P}_{\perp}^{\mu\nu} \\
&\quad \left. + \frac{2 \tanh(|q_f B| x_1) \tanh(|q_f B| x_2)}{|q_f B| [\tanh(|q_f B| x_1) + \tanh(|q_f B| x_2)]} p_{\perp}^2 g_{\perp}^{\mu\nu} \right].
\end{aligned} \tag{H.7}$$

By collecting the common terms of the structures $\mathcal{P}_{\parallel}^{\mu\nu}$, $\mathcal{P}_{\perp}^{\mu\nu}$ and $\mathcal{P}_0^{\mu\nu}$, the coefficients of Eqs. (3.24)-(3.28) can be found.

Vacuum contribution in the HTL and LLL approximations

Here the thermal vacuum contribution of the gluon polarization tensor of Sec. 3.2 is computed in the LLL and HTL approximations. The result coincides with the obtained after performing the integration over k_0 in Eq. (3.67), which means that the pure magnetic contribution given in Eq. (3.47) remains at $T = 0$. Recalling Eq. (3.67):

$$\begin{aligned}
 i\Pi^{\mu\nu} &= -g^2 \sum_f \left(\frac{\pi|q_f B|}{4\pi^2} \right) \exp\left(-\frac{p_\perp^2}{2|q_f B|}\right) \\
 &\times \int \frac{d^2 k_\parallel}{(2\pi)^2} \frac{[m_f^2 - k_\parallel \cdot (k-p)_\parallel] g_\parallel^{\mu\nu} + k_\parallel^\mu (k-p)_\parallel^\nu + k_\parallel^\nu (k-p)_\parallel^\mu}{[k_\parallel^2 - m_f^2][(k-p)_\parallel^2 - m_f^2]}, \quad (\text{I.1})
 \end{aligned}$$

the component k_0 is isolated to apply the Matsubara formalism:

$$\begin{aligned}
 i\Pi^{\mu\nu} &= g^2 \sum_f \left(\frac{\pi|q_f B|}{4\pi^2} \right) \exp\left(-\frac{p_\perp^2}{2|q_f B|}\right) \int \frac{d^2 k_\parallel}{(2\pi)^2} \frac{1}{[k_\parallel^2 - m_f^2][(k-p)_\parallel^2 - m_f^2]} \\
 &\times \left[(m_f^2 + k_3^2 - k_3 p_3) g_\parallel^{\mu\nu} + 2(k_3^2 - k_3(p_3 + p_0)) \right. \\
 &\left. + k_0(p_0 g_\parallel^{\mu\nu} + 2(k_3 - p_3 - p_0)) + k_0^2(-g_\parallel^{\mu\nu} + 2) \right], \quad (\text{I.2})
 \end{aligned}$$

and by the introduction of the imaginary-time method with $p_0 = i\omega$ and $k_0 = i\tilde{\omega}_n$ the above equation becomes:

$$\begin{aligned}
i\Pi^{\mu\nu} &= ig^2 \sum_f \left(\frac{\pi |q_f B|}{4\pi^2} \right) \exp \left(-\frac{p_\perp^2}{2|q_f B|} \right) \\
&\times T \sum_{n=-\infty}^{\infty} \int \frac{dk_3}{(2\pi)^2} \left[\frac{(m_f^2 + k_3^2 - k_3 p_3) g_{\parallel}^{\mu\nu} + 2(k_3^2 - k_3(p_3 + i\omega))}{[\tilde{\omega}_n^2 + k_3^2 + m_f^2][(\tilde{\omega}_n - \omega)^2 + (k_3 - p_3)^2 + m_f^2]} \right. \\
&\quad - \frac{(i\tilde{\omega}_n)(i\omega g_{\parallel}^{\mu\nu} + 2(k_3 - p_3 - i\omega))}{[\tilde{\omega}_n^2 + k_3^2 + m_f^2][(\tilde{\omega}_n - \omega)^2 + (k_3 - p_3)^2 + m_f^2]} \\
&\quad \left. + \frac{(i\tilde{\omega}_n)^2(-g_{\parallel}^{\mu\nu} + 2)}{[\tilde{\omega}_n^2 + k_3^2 + m_f^2][(\tilde{\omega}_n - \omega)^2 + (k_3 - p_3)^2 + m_f^2]} \right]. \tag{I.3}
\end{aligned}$$

The Matsubara frequencies sums can be performed by the following identities [147]:

$$\begin{aligned}
I_0 &= T \sum_{n=-\infty}^{\infty} \frac{1}{[\tilde{\omega}_n^2 + k_3^2 + m_f^2][(\tilde{\omega}_n - \omega)^2 + (k_3 - p_3)^2 + m_f^2]} \\
&= - \sum_{s_1, s_2 = \pm 1} \frac{s_1 s_2}{4E_1 E_2} \left[\frac{1 - \tilde{f}(s_1 E_1) - \tilde{f}(s_2 E_2)}{i\omega - s_1 E_1 - s_2 E_2} \right] \\
I_1 &= T \sum_{n=-\infty}^{\infty} \frac{i\tilde{\omega}_n}{[\tilde{\omega}_n^2 + k_3^2 + m_f^2][(\tilde{\omega}_n - \omega)^2 + (k_3 - p_3)^2 + m_f^2]} \\
&= - \sum_{s_1, s_2 = \pm 1} \frac{s_1 s_2 (s_1 E_1)}{4E_1 E_2} \left[\frac{1 - \tilde{f}(s_1 E_1) - \tilde{f}(s_2 E_2)}{i\omega - s_1 E_1 - s_2 E_2} \right] \\
I_3 &= T \sum_{n=-\infty}^{\infty} \frac{(i\tilde{\omega}_n)^2}{[\tilde{\omega}_n^2 + k_3^2 + m_f^2][(\tilde{\omega}_n - \omega)^2 + (k_3 - p_3)^2 + m_f^2]} \\
&= - \sum_{s_1, s_2 = \pm 1} \frac{s_1 s_2 (s_1 E_1)(s_2 E_2 - i\omega)}{4E_1 E_2} \left[\frac{1 - \tilde{f}(s_1 E_1) - \tilde{f}(s_2 E_2)}{i\omega - s_1 E_1 - s_2 E_2} \right]. \tag{I.4}
\end{aligned}$$

where $E_1^2 = k_3^2 + m_f^2$, $E_2^2 = (k_3 - p_3)^2 + m_f^2$ and

$$\tilde{f}(x) = \frac{1}{(e^{x/T} + 1)}. \tag{I.5}$$

The vacuum pieces, i.e., the terms independent of the Fermi-Dirac distribution function \tilde{f} are

isolated and their contributions are given by:

$$\begin{aligned}
i\Pi_{\text{vac}}^{\mu\nu} &= -ig^2 \sum_f \left(\frac{\pi |p_f B|}{4\pi^2} \right) \exp \left(-\frac{p_{\perp}^2}{2|q_f B|} \right) \\
&\times \int \frac{dk_3}{(2\pi)^2} \left(\frac{1}{i\omega - E_1 - E_2} - \frac{1}{i\omega + E_1 + E_2} \right) \left[\frac{2 - g_{\parallel}^{\mu\nu}}{4} \left(\frac{i\omega}{E_2} - 1 \right) \right. \\
&\left. + \frac{(m_f^2 + k_3^2 - k_3 p_3) g_{\parallel}^{\mu\nu} + 2(k_3^2 - k_3(p_3 + i\omega))}{4E_1 E_2} - \frac{i\omega g_{\parallel}^{\mu\nu} + 2(k_3 - p_3 - i\omega)}{4E_2} \right].
\end{aligned} \tag{I.6}$$

The above result is the same obtained by performing the integration over k_0 in Eq. (3.67) and performing the analytic continuation $p_0 \rightarrow i\omega$.

Appendix J

Calculation of \tilde{P}^L and \tilde{P}^T when $q^2 \ll m_f^2 \ll T^2$

Here the explicit steps that lead to the results for the matter contributions in Eqs. (3.69) and (3.70) are shown. First, the temperature effects are introduced into the corresponding projections onto $\tilde{\Pi}^{\mu\nu}$, Eq. (3.65), using the Matsubara formalism of thermal field theory, obtaining:

$$\begin{aligned}
\tilde{P}^L &= -g^2 T \sum_{n=-\infty}^{\infty} \sum_f \left(\frac{\pi |q_f B|}{4\pi^2} \right) \exp \left(-\frac{p_{\perp}^2}{2 |q_f B|} \right) \\
&\times \int \frac{dk_3}{(2\pi)} \frac{1}{[\tilde{\omega}_n^2 + k_3^2 + m_f^2][(\tilde{\omega}_n - \omega)^2 + (k_3 - p_3)^2 + m_f^2]} \\
&\times \left\{ \left[4\tilde{\omega}_n(-\tilde{\omega}_n\omega - k_3 p_3) + 2\tilde{\omega}_n(\omega_n^2 + p_3^2) + 2\omega(\tilde{\omega}_n^2 + k_3^2 + m_f^2) \right] \frac{\omega}{\mathbf{p}^2} \right. \\
&+ \left[2(\tilde{\omega}_n^2\omega^2 + k_3^2 p_3^2 + 2\tilde{\omega}_n\omega k_3 p_3) - (\omega_n^2 + p_3^2)(\tilde{\omega}_n\omega + k_3 p_3 + m_f^2) \right] \frac{\omega^2}{\mathbf{p}^2 p^2} \\
&\left. + \left[\tilde{\omega}_n^2 + 2\tilde{\omega}_n\omega - k_3^2 + \tilde{\omega}_n\omega + k_3 p_3 - m_f^2 \right] \frac{p^2}{\mathbf{p}^2} \right\} \tag{J.1}
\end{aligned}$$

and

$$\begin{aligned}
\tilde{P}^T &= -g^2 T \sum_{n=-\infty}^{\infty} \sum_f \left(\frac{\pi |q_f B|}{4\pi^2} \right) \exp \left(-\frac{p_{\perp}^2}{2 |q_f B|} \right) \\
&\times \int \frac{dk_3}{(2\pi)} \frac{-\tilde{\omega}_n^2 + k_3^2 - m_f^2 - \tilde{\omega}_n\omega - k_3 p_3}{[\tilde{\omega}_n^2 + k_3^2 + m_f^2][(\tilde{\omega}_n - \omega)^2 + (k_3 - p_3)^2 + m_f^2]}. \tag{J.2}
\end{aligned}$$

To compute the matter contribution the following integral:

$$\int_{-\infty}^{\infty} dk_3 \frac{f(\tilde{E}_1)}{E_1} = \int_{-\infty}^{\infty} dk_3 \frac{1}{(k_3^2 + m_f^2)^{1/2}} \frac{1}{e^{\sqrt{(k_3^2 + m_f^2)}/T} + 1}, \quad (\text{J.3})$$

is performed by using the well-known result [283]:

$$f_n(\tilde{y}) = \frac{1}{\Gamma(n)} \int_0^{\infty} \frac{dx x^{n-1}}{\sqrt{x^2 + \tilde{y}^2}} \frac{1}{e^{\sqrt{x^2 + \tilde{y}^2}} + 1}, \quad (\text{J.4})$$

so that Eq. (J.3) correspondings to the case with $n = 1$ and $\tilde{y} = m_f/T$. In the limit where \tilde{y} is small, Eq. (J.4) becomes

$$f_1(m_f/T) = -\frac{1}{2} \ln \left(\frac{m_f}{\pi T} \right) - \frac{1}{2} \gamma_e + \dots, \quad (\text{J.5})$$

therefore

$$\int_{-\infty}^{\infty} dk_3 \frac{f(\tilde{E}_1)}{E_1} = -\ln \left(\frac{m_f}{\pi T} \right) - \gamma_e. \quad (\text{J.6})$$

Using the above expression it is straightforward to get

$$\tilde{P}^L = -\frac{g^2}{8\pi^2} \sum_f |q_f B| \exp \left(-\frac{p_{\perp}^2}{2|q_f B|} \right) \left[\frac{-\omega^2(p_{\perp}^2 + 2p_3^2)}{\mathbf{p}^2 p^2} - 1 \right] \left[\ln \left(\frac{m_f^2}{\pi^2 T^2} \right) + 2\gamma_e \right] \quad (\text{J.7})$$

and

$$\tilde{P}^T = -\frac{g^2}{8\pi^2} \sum_f |q_f B| \exp \left(-\frac{p_{\perp}^2}{2|q_f B|} \right) \left(\frac{p_{\perp}^2}{\mathbf{p}^2} \right) \left[\ln \left(\frac{m_f^2}{\pi^2 T^2} \right) + 2\gamma_e \right]. \quad (\text{J.8})$$

Finally, to obtain Eqs. (3.69) and (3.70) an analytical continuation $i\omega \rightarrow q_0$ is performed back to Minkowski space.

Calculation of \tilde{P}^L and \tilde{P}^T when $m_f^2 \ll p^2 \ll T^2$

The change of hierarchy implies that the momentum k is the largest energy scale, and the quark mass m_f is the smallest. The matter contribution is computed in the same fashion as Appendix J.

The temperature effects into the corresponding projections onto $\tilde{\Pi}^{\mu\nu}$, Eq. (3.65), are introduced by using the Matsubara formalism of thermal field theory, obtaining:

$$\begin{aligned}
\tilde{P}^L &= -g^2 T \sum_{n=-\infty}^{\infty} \sum_f \left(\frac{\pi |q_f B|}{4\pi^2} \right) \exp \left(-\frac{p_{\perp}^2}{2 |q_f B|} \right) \\
&\times \int \frac{dk_3}{(2\pi)} \frac{1}{[\tilde{\omega}_n^2 + k_3^2 + m_f^2][(\tilde{\omega}_n - \omega)^2 + (k_3 - p_3)^2 + m_f^2]} \\
&\times \left\{ \left[4\tilde{\omega}_n(-\tilde{\omega}_n\omega - k_3 p_3) + 2\tilde{\omega}_n(\omega_n^2 + p_3^2) + 2\omega(\tilde{\omega}_n^2 + k_3^2 + m_f^2) \right] \frac{\omega}{\mathbf{p}^2} \right. \\
&+ \left[2(\tilde{\omega}_n^2\omega^2 + k_3^2 p_3^2 + 2\tilde{\omega}_n\omega k_3 p_3) - (\omega_n^2 + p_3^2)(\tilde{\omega}_n\omega + k_3 p_3 + m_f^2) \right] \frac{\omega^2}{\mathbf{p}^2 p^2} \\
&\left. + \left[\tilde{\omega}_n^2 + 2\tilde{\omega}_n\omega - k_3^2 + \tilde{\omega}_n\omega + k_3 p_3 - m_f^2 \right] \frac{p^2}{\mathbf{p}^2} \right\} \quad (\text{K.1})
\end{aligned}$$

and

$$\begin{aligned}
\tilde{P}^T &= -g^2 T \sum_{n=-\infty}^{\infty} \sum_f \left(\frac{\pi |q_f B|}{4\pi^2} \right) \exp \left(-\frac{p_{\perp}^2}{2 |q_f B|} \right) \\
&\times \frac{p_{\perp}^2}{\mathbf{p}^2} \int \frac{dk_3}{(2\pi)} \frac{(-\tilde{\omega}_n^2 + k_3^2 - m_f^2 - \tilde{\omega}_n\omega - k_3 p_3)}{[\tilde{\omega}_n^2 + k_3^2 + m_f^2][(\tilde{\omega}_n - \omega)^2 + (k_3 - p_3)^2 + m_f^2]}. \quad (\text{K.2})
\end{aligned}$$

Note that since in the HTL approximation terms proportional to m_f^2 , $\tilde{\omega}_n$, and k_3 in the numer-

ators do not contribute, the calculation of Eqs. (K.1) and (K.2) involves only two kinds of sums over the Matsubara frequencies given in Eqs. (I.4), namely:

$$\chi_0 \equiv \sum_{s_1, s_2 = \pm 1} \frac{-s_1 s_2}{4E_1 E_2} \left[\frac{1 - \tilde{f}(s_1 E_1) - \tilde{f}(s_2 E_2)}{i\omega - s_1 E_1 - s_2 E_2} \right], \quad (\text{K.3})$$

and

$$\chi_1 \equiv \sum_{s_1, s_2 = \pm 1} \frac{s_1 s_2 E_1}{4E_2} \left[\frac{1 - \tilde{f}(s_1 E_1) - \tilde{f}(s_2 E_2)}{i\omega - s_1 E_1 - s_2 E_2} \right], \quad (\text{K.4})$$

so that $\chi_1 = -E_1^2 \chi_0$; thus, one should only find an expression for the sum in Eq. (K.4). In this approximation ($k > q > m_f$) Eq. (K.4) is given by

$$\chi_1 = \frac{-p_3}{2p_{\parallel}^2} \left[\frac{p_3 e^{k_3/T}}{T(e^{k_3/T} + 1)^2} + \frac{1}{2} \frac{p_3^2 e^{k_3/T} (e^{k_3/T} - 1)}{T^2 (e^{k_3/T} + 1)^3} + \dots \right], \quad (\text{K.5})$$

from which Eqs. (K.1) and (K.2) take the following form

$$\begin{aligned} \tilde{P}^L &= -g^2 T \sum_{n=-\infty}^{\infty} \sum_f \left(\frac{\pi |q_f B|}{4\pi^2} \right) \exp \left(-\frac{p_{\perp}^2}{2|q_f B|} \right) \\ &\times \int \frac{dk_3}{(2\pi)} \frac{1}{[\tilde{\omega}_n^2 + k_3^2 + m_f^2][(\tilde{\omega}_n - \omega)^2 + (k_3 - p_3)^2 + m_f^2]} \\ &\times \left\{ \left[-4\tilde{\omega}_n^2 \omega + 2\omega(\tilde{\omega}_n^2 + k_3^2) \right] \frac{\omega}{\mathbf{p}^2} + \left[2(\tilde{\omega}_n^2 \omega^2 + k_3^2 p_3^2) \right] \frac{\omega^2}{\mathbf{p}^2 p^2} + \left[\tilde{\omega}_n^2 - k_3^2 \right] \frac{p^2}{\mathbf{p}^2} \right\} \end{aligned} \quad (\text{K.6})$$

and

$$\begin{aligned} \tilde{P}^T &= -g^2 T \sum_{n=-\infty}^{\infty} \sum_f \left(\frac{\pi |q_f B|}{4\pi^2} \right) \exp \left(-\frac{p_{\perp}^2}{2|q_f B|} \right) \\ &\times \frac{p_{\perp}^2}{\mathbf{p}^2} \int \frac{dk_3}{(2\pi)} \left\{ \frac{-\tilde{\omega}_n^2 + k_3^2}{[\tilde{\omega}_n^2 + k_3^2 + m_f^2][(\tilde{\omega}_n - \omega)^2 + (k_3 - p_3)^2 + m_f^2]} \right\}. \end{aligned} \quad (\text{K.7})$$

Finally, by using Eqs. (K.6) and (K.7) the desired result is achieved.

Appendix **L**

Calculation of $i\Pi_{(1,1)}^{\mu\nu}$, $i\Pi_{(2,0)}^{\mu\nu}$ and $i\Pi_{(0,2)}^{\mu\nu}$

Calculation of $i\Pi_{(1,1)}^{\mu\nu}$

The contribution from $\Pi_{(1,1)}^{\mu\nu}$ is given by

$$i\Pi_{(1,1)}^{\mu\nu} = - \int \frac{d^4k}{(2\pi)^4} \text{Tr} \{igt_b \gamma^\nu iS^{(1)}(k-p)igt_a \gamma^\mu iS^{(1)}(k)\}, \quad (\text{L.1})$$

which is computed by introducing two Schwinger parameters x_1 and x_2 as follows:

$$\frac{1}{k^2 - m^2} = - \int_0^\infty dx e^{x(k^2 - m^2)}, \quad (\text{L.2})$$

so that, after the trace computation yields

$$\begin{aligned} i\Pi_{(1,1)}^{\mu\nu} &= 2|q_f B|^2 g^2 \int \frac{d^4k}{(2\pi)^4} \frac{1}{(k^2 - m_f^2)^2 [(k-p)^2 - m_f^2]^2} \\ &\times \left[k_{\parallel}^\nu (k_{\parallel}^\mu - p_{\parallel}^\mu) + k_{\parallel}^\mu (k_{\parallel}^\nu - p_{\parallel}^\nu) - (g_{\parallel}^{\mu\nu} - g_{\perp}^{\mu\nu}) (k_{\parallel} \cdot (k_{\parallel} - p_{\parallel}) - m_f^2) \right]. \end{aligned} \quad (\text{L.3})$$

By applying the Schwinger parametrization, the last equation is

$$\begin{aligned} i\Pi_{(1,1)}^{\mu\nu} &= 2|q_f B|^2 g^2 \frac{\partial}{\partial m_1^2} \frac{\partial}{\partial m_2^2} \int d^2x \int \frac{d^4k}{(2\pi)^4} \mathbb{E}(\mathbf{x}, \mathbf{m}, p, k) \\ &\times \left[k_{\parallel}^\nu (k_{\parallel}^\mu - p_{\parallel}^\mu) + k_{\parallel}^\mu (k_{\parallel}^\nu - p_{\parallel}^\nu) - (g_{\parallel}^{\mu\nu} - g_{\perp}^{\mu\nu}) [k_{\parallel} \cdot (k_{\parallel} - p_{\parallel}) - m_f^2] \right], \end{aligned} \quad (\text{L.4})$$

where

$$\mathbb{E}(\mathbf{x}, \mathbf{m}, p, k) \equiv \exp \left[(x_1 + x_2) \left(k - \frac{x_1}{x_1 + x_2} p \right)^2 + \frac{x_1 x_2}{x_1 + x_2} p^2 - (m_1^2 x_1 + m_2^2 x_2) \right]. \quad (\text{L.5})$$

The integral over k is performed after the change of variable

$$l = \left(k - \frac{x_1}{x_1 + x_2} p \right), \quad (\text{L.6})$$

so that by performing the derivatives with respect m_1 and m_2 , and by replacing $m_1 = m_2 = m_f$ it follows that

$$\begin{aligned} i\Pi_{(1,1)}^{\mu\nu} &= 2|q_f B|^2 g^2 \int \frac{d^4 l}{(2\pi)^4} \int d^2 x x_1 x_2 \exp \left[(x_1 + x_2)(l^2 - m_f^2) + \frac{x_1 x_2}{x_1 + x_2} p^2 \right] \\ &\times \left\{ 2l_{\parallel}^{\mu} l_{\parallel}^{\nu} - 2 \frac{x_1 x_2}{(x_1 + x_2)^2} p_{\parallel}^{\mu} p_{\parallel}^{\nu} - (g_{\parallel}^{\mu\nu} - g_{\perp}^{\mu\nu}) \left[l_{\parallel}^2 - \frac{x_1 x_2}{(x_1 + x_2)^2} p_{\parallel}^2 - m_f^2 \right] \right\}. \end{aligned} \quad (\text{L.7})$$

Now, from the fact that

$$p_{\parallel}^{\mu} p_{\parallel}^{\nu} = -p_{\parallel}^2 \mathcal{P}_{\parallel}^{\mu\nu} + p_{\parallel}^2 g_{\parallel}^{\mu\nu}, \quad (\text{L.8})$$

equation (L.7) is

$$\begin{aligned} i\Pi_{(1,1)}^{\mu\nu} &= 2|q_f B|^2 g^2 \int \frac{d^4 l}{(2\pi)^4} \int d^2 x x_1 x_2 \exp \left[(x_1 + x_2)(l^2 - m_f^2) + \frac{x_1 x_2}{x_1 + x_2} p^2 \right] \\ &\times \left\{ -2l_{\parallel}^{\mu} l_{\parallel}^{\nu} - 2 \frac{x_1 x_2}{(x_1 + x_2)^2} p_{\parallel}^2 \mathcal{P}_{\parallel}^{\mu\nu} + g_{\parallel}^{\mu\nu} \left(m_f^2 + l_{\parallel}^2 + \frac{x_1 x_2}{(x_1 + x_2)^2} p_{\parallel}^2 \right) \right. \\ &\left. - g_{\perp}^{\mu\nu} \left(m_f^2 + l_{\parallel}^2 - \frac{x_1 x_2}{(x_1 + x_2)^2} p_{\parallel}^2 \right) \right\}. \end{aligned} \quad (\text{L.9})$$

To carry out the integration on l_{\parallel} it is useful to make the replacement:

$$l_{\parallel}^{\mu} l_{\parallel}^{\nu} \rightarrow \frac{1}{2} g_{\parallel}^{\mu\nu} l_{\parallel}^2, \quad (\text{L.10})$$

so that the integral over l factorizes as $d^4 l = d^2 l_{\parallel} d^2 l_{\perp}$. By following the same procedure presented in Appendix G, i.e., a Wick's rotation allows compute the integral as a Gaussian one, to that:

$$\begin{aligned} i\Pi_{(1,1)}^{\mu\nu} &= -\frac{2i|q_f B|^2 g^2}{16\pi^2} \int d^2 x \frac{x_1 x_2}{(x_1 + x_2)^4} \exp \left[-(x_1 + x_2)m_f^2 + \frac{x_1 x_2}{x_1 + x_2} p^2 \right] \\ &\times \left\{ 2x_1 x_2 p_{\parallel}^2 \mathcal{P}_{\parallel}^{\mu\nu} + g_{\parallel}^{\mu\nu} (m_f^2 (x_1 + x_2)^2 - x_1 x_2 p_{\parallel}^2) \right. \\ &\left. + g_{\perp}^{\mu\nu} (-m_f^2 (x_1 + x_2)^2 - (x_1 + x_2) - x_1 x_2 p_{\parallel}^2) \right\}. \end{aligned} \quad (\text{L.11})$$

Finally, the variable changes $x_1 = s(1 - y)$ and $x_2 = sy$ gives the result shown in Eq. (3.99).

Calculation of $i\Pi_{(2,0)}^{\mu\nu}$ and $i\Pi_{(0,2)}^{\mu\nu}$

The second non-vanishing magnetic contribution is given by

$$i\Pi_{(2,0)}^{\mu\nu} = - \int \frac{d^4 k}{(2\pi)^4} \text{Tr} \{ i g t_b \gamma^{\nu} i S^{(0)}(q) i g t_a \gamma^{\mu} i S^{(2)}(k) \}, \quad (\text{L.12})$$

which after a Schwinger parametrization and the change of variable of Eq. (L.6) results in

$$\begin{aligned}
i\Pi_{(2,0)}^{\mu\nu} &= |q_f B|^2 g^2 \int \frac{d^4 l}{(2\pi)^4} \int d^2 x \exp \left[(x_1 + x_2)(l^2 - m_f^2) + \frac{x_1 x_2}{x_1 + x_2} p^2 \right] \\
&\times \left[\frac{x_2^2}{2!} \text{Tr} \left\{ \gamma^\nu \gamma^\alpha \gamma^\mu \gamma^\beta \left(l_\perp - \frac{x_2 p_\perp}{x_1 + x_2} \right)_\alpha \left(l_\perp + \frac{x_1 p_\perp}{x_1 + x_2} \right)_\beta \right\} \right. \\
&- \frac{x_2^3}{3!} \text{Tr} \left\{ \gamma^\nu \gamma^\alpha \gamma^\mu \gamma^\beta \left(l - \frac{x_2 p}{x_1 + x_2} \right)_\alpha \left(l + \frac{x_1 p}{x_1 + x_2} \right)_\beta \left(l_\perp + \frac{x_1 p_\perp}{x_1 + x_2} \right)^2 \right. \\
&\left. \left. + \gamma^\nu \gamma^\mu \left(l_\perp + \frac{x_1 p_\perp}{x_1 + x_2} \right)^2 m_f^2 \right\} \right] \\
&\equiv I_1^{\mu\nu} + I_2^{\mu\nu} + I_3^{\mu\nu}, \tag{L.13}
\end{aligned}$$

where

$$\begin{aligned}
I_1^{\mu\nu} &= |q_f B|^2 g^2 \frac{1}{2!} \int \frac{d^4 l}{(2\pi)^4} \int d^2 x x_2^2 \exp \left[(x_1 + x_2)(l^2 - m_f^2) + \frac{x_1 x_2}{x_1 + x_2} p^2 \right] \\
&\times \text{Tr} \left\{ \gamma^\nu \gamma^\alpha \gamma^\mu \gamma^\beta \left(l_\perp - \frac{x_2 p_\perp}{x_1 + x_2} \right)_\alpha \left(l_\perp + \frac{x_1 p_\perp}{x_1 + x_2} \right)_\beta \right\}, \tag{L.14a}
\end{aligned}$$

$$\begin{aligned}
I_2^{\mu\nu} &= -|q_f B|^2 g^2 \frac{1}{3!} \int \frac{d^4 l}{(2\pi)^4} \int d^2 x x_2^3 \exp \left[(x_1 + x_2)(l^2 - m_f^2) + \frac{x_1 x_2}{x_1 + x_2} p^2 \right] \\
&\times \text{Tr} \left\{ \gamma^\nu \gamma^\alpha \gamma^\mu \gamma^\beta \left(l - \frac{x_2 p}{x_1 + x_2} \right)_\alpha \left(l + \frac{x_1 p}{x_1 + x_2} \right)_\beta \left(l_\perp + \frac{x_1 p_\perp}{x_1 + x_2} \right)^2 \right\}, \tag{L.14b}
\end{aligned}$$

and

$$\begin{aligned}
I_3^{\mu\nu} &= -|q_f B|^2 g^2 \frac{m_f^2}{3!} \int \frac{d^4 l}{(2\pi)^4} \int d^2 x x_2^3 \exp \left[(x_1 + x_2)(l^2 - m_f^2) + \frac{x_1 x_2}{x_1 + x_2} p^2 \right] \\
&\times \text{Tr} \left\{ \gamma^\nu \gamma^\mu \left(l_\perp + \frac{x_1 p_\perp}{x_1 + x_2} \right)^2 \right\}. \tag{L.14c}
\end{aligned}$$

After computing the trace, $I_1^{\mu\nu}$ is

$$\begin{aligned}
I_1^{\mu\nu} &= 2 |q_f B|^2 g^2 \int \frac{d^4 l}{(2\pi)^4} \int d^2 x x_2^2 \exp \left[(x_1 + x_2)(l^2 - m_f^2) + \frac{x_1 x_2}{x_1 + x_2} p^2 \right] \\
&\times \left[g_{\parallel}^{\mu\nu} l_\perp^2 - \frac{x_1 x_2}{(x_1 + x_2)^2} (p^\nu p_\perp^\mu + p^\mu p_\perp^\nu - p_\perp^2 g^{\mu\nu}) \right], \tag{L.15}
\end{aligned}$$

and given that

$$p^\nu p_\perp^\mu + p^\mu p_\perp^\nu = p_\perp^2 \mathcal{P}_{\parallel}^{\mu\nu} - (p_\parallel^2 - 2p_\perp^2) \mathcal{P}_\perp^{\mu\nu} - p^2 \mathcal{P}_0^{\mu\nu} - p_\perp^2 g_{\parallel}^{\mu\nu} + (p_\parallel^2 - 2p_\perp^2) g_\perp^{\mu\nu}, \tag{L.16}$$

the integral becomes:

$$I_1^{\mu\nu} = 2 |q_f B|^2 g^2 \int \frac{d^4 l}{(2\pi)^4} \int d^2 x x_2^2 \exp \left[(x_1 + x_2)(l^2 - m_f^2) + \frac{x_1 x_2}{x_1 + x_2} p^2 \right] \\ \times \left[g_{\parallel}^{\mu\nu} l_{\perp}^2 + \frac{x_1 x_2}{(x_1 + x_2)^2} \left(p^2 \mathcal{P}_0^{\mu\nu} - p_{\perp} \mathcal{P}_{\parallel}^{\mu\nu} + (p_{\parallel}^2 - 2p_{\perp}^2) \mathcal{P}_{\perp}^{\mu\nu} - g_{\perp}^{\mu\nu} p^2 \right) \right], \quad (\text{L.17})$$

which can be promoted to Gaussian integrals over l , so that

$$I_1^{\mu\nu} = 2 \left(\frac{i}{16\pi^2} \right) |q_f B|^2 g^2 \int d^2 x x_2^2 \exp \left[-(x_1 + x_2) m_f^2 + \frac{x_1 x_2}{x_1 + x_2} p^2 \right] \\ \times \left[\frac{g_{\parallel}^{\mu\nu}}{(x_1 + x_2)^3} + \frac{x_1 x_2}{(x_1 + x_2)^4} \left(p^2 \mathcal{P}_0^{\mu\nu} - p_{\perp} \mathcal{P}_{\parallel}^{\mu\nu} + (p_{\parallel}^2 - 2p_{\perp}^2) \mathcal{P}_{\perp}^{\mu\nu} - g_{\perp}^{\mu\nu} p^2 \right) \right]. \quad (\text{L.18})$$

The integral $I_2^{\mu\nu}$, after trace operation is

$$I_2^{\mu\nu} = - |q_f B|^2 g^2 \frac{2}{3} \int \frac{d^4 l}{(2\pi)^4} \int d^2 x x_2^3 \exp \left[(x_1 + x_2)(l^2 - m_f^2) + \frac{x_1 x_2}{x_1 + x_2} p^2 \right] \left(l_{\perp} + \frac{x_1 p_{\perp}}{x_1 + x_2} \right)^2 \\ \times \left\{ -g^{\mu\nu} \left[l^2 - \frac{x_1 x_2}{(x_1 + x_2)^2} p^2 + \frac{x_1 - x_2}{x_1 + x_2} (l \cdot p) \right] + 2l^{\mu} l^{\nu} - \frac{2x_1 x_2}{(x_1 + x_2)^2} p^{\mu} p^{\nu} \right. \\ \left. + \frac{x_1 - x_2}{x_1 + x_2} (l^{\mu} p^{\nu} + l^{\nu} p^{\mu}) \right\}. \quad (\text{L.19})$$

By using Eq. (L.16) and discarding odd powers in l looks like

$$I_2^{\mu\nu} = - |q_f B|^2 g^2 \frac{2}{3} \int \frac{d^4 l}{(2\pi)^4} \int d^2 x x_2^3 \exp \left[(x_1 + x_2)(l^2 - m_f^2) + \frac{x_1 x_2}{x_1 + x_2} p^2 \right] \\ \times \left\{ \left(l_{\perp}^2 + \frac{x_1^2 p_{\perp}^2}{(x_1 + x_2)^2} \right) \left[g_{\parallel}^{\mu\nu} l_{\perp}^2 - g_{\perp}^{\mu\nu} l_{\parallel}^2 - \frac{x_1 x_2}{(x_1 + x_2)^2} g^{\mu\nu} p^2 \right. \right. \\ \left. \left. + \frac{2x_1 x_2}{(x_1 + x_2)^2} p^2 \left(\mathcal{P}_0^{\mu\nu} + \mathcal{P}_{\parallel}^{\mu\nu} + \mathcal{P}_{\perp}^{\mu\nu} \right) \right] \right. \\ \left. + \frac{x_1(x_1 - x_2)}{(x_1 + x_2)^2} l_{\perp}^2 \left[g_{\perp}^{\mu\nu} p^2 - p^2 \mathcal{P}_0^{\mu\nu} + p_{\perp}^2 \mathcal{P}_{\parallel}^{\mu\nu} - (p_{\parallel}^2 - 2p_{\perp}^2) \mathcal{P}_{\perp}^{\mu\nu} \right] \right\}, \quad (\text{L.20})$$

and the remaining integral over l yields

$$\begin{aligned}
I_2^{\mu\nu} &= -2 \left(\frac{i}{16\pi^2} \right) |q_f B|^2 g^2 \frac{1}{3} \int d^2x x_2^3 \exp \left[-(x_1 + x_2)m_f^2 + \frac{x_1 x_2}{x_1 + x_2} p^2 \right] \\
&\times \left\{ g_{\parallel}^{\mu\nu} \left[\frac{2}{(x_1 + x_2)^4} + \frac{x_1^2}{(x_1 + x_2)^5} p_{\perp}^2 \right] - g_{\perp}^{\mu\nu} \left[-\frac{1}{(x_1 + x_2)^4} - \frac{x_1^2}{(x_1 + x_2)^5} p_{\perp}^2 \right] \right. \\
&- \frac{x_1 x_2}{(x_1 + x_2)^2} \left[\frac{1}{(x_1 + x_2)^3} + \frac{x_1^2}{(x_1 + x_2)^4} p_{\perp}^2 \right] \left[g^{\mu\nu} p^2 - 2p^2 \left(\mathcal{P}_0^{\mu\nu} + \mathcal{P}_{\parallel}^{\mu\nu} + \mathcal{P}_{\perp}^{\mu\nu} \right) \right] \\
&\left. + \frac{x_1(x_1 - x_2)}{(x_1 + x_2)^5} \left[g_{\perp}^{\mu\nu} p^2 - p^2 \mathcal{P}_0^{\mu\nu} + p_{\perp}^2 \mathcal{P}_{\parallel}^{\mu\nu} - (p_{\parallel}^2 - 2p_{\perp}^2) \mathcal{P}_{\perp}^{\mu\nu} \right] \right\}. \tag{L.21}
\end{aligned}$$

For the integral $I_3^{\mu\nu}$ follows the same procedure: change the momentum integration by an integral over l , discard odd powers of l and promote the remaining integration as a Gaussian integral. That computation yields:

$$\begin{aligned}
I_3^{\mu\nu} &= -|q_f B|^2 g^2 \frac{2}{3} \int \frac{d^4l}{(2\pi)^4} \int d^2x x_2^3 \exp \left[(x_1 + x_2)(l^2 - m_f^2) + \frac{x_1 x_2}{x_1 + x_2} p^2 \right] \\
&\times \left(l_{\perp} + \frac{x_1 p_{\perp}}{x_1 + x_2} \right)^2 m_f^2 g^{\mu\nu} \\
&= -2 \left(\frac{i}{16\pi^2} \right) |q_f B|^2 g^2 \frac{1}{3} g^{\mu\nu} m_f^2 \\
&\times \int d^2x x_2^3 \exp \left[-(x_1 + x_2)m_f^2 + \frac{x_1 x_2}{x_1 + x_2} p^2 \right] \left[\frac{1}{(x_1 + x_2)^3} + \frac{x_1^2}{(x_1 + x_2)^4} p_{\perp}^2 \right] \tag{L.22}
\end{aligned}$$

Adding $I_1^{\mu\nu}$, $I_2^{\mu\nu}$ and $I_3^{\mu\nu}$ results in an expression for $i\Pi_{(2,0)}^{\mu\nu}$ in terms of (x_1, x_2) , which from $i\Pi_{(0,2)}^{\mu\nu}$ is obtained by the exchange $x_1 \leftrightarrow x_2$. Finally, the change of variable $x_1 = s(1 - y)$ and $x_2 = sy$ reproduces the result of Eq. (3.100).

Bibliography

- [1] Alejandro Ayala, Jorge David Castano-Yepes, JJ Cobos-Martínez, Saúl Hernández-Ortiz, Ana Julia Mizher, and Alfredo Raya. “Chiral symmetry transition in the linear sigma model with quarks: Counting effective QCD degrees of freedom from low to high temperature”. *Int. J. Mod. Phys. A*, 31(36):1650199, (2016).
- [2] Alejandro Ayala, Jorge David Castaño Yepes, C. A. Dominguez, L. A. Hernández, Saúl Hernández-Ortiz, and María Elena Tejeda-Yeomans. “Prompt photon yield and elliptic flow from gluon fusion induced by magnetic fields in relativistic heavy-ion collisions”. *Phys. Rev. D*, 96:014023, (2017).
- [3] Alejandro Ayala, Jorge David Castao-Yepes, Isabel Dominguez Jimenez, Jordi Salinas San Martn, and Mara Elena Tejeda-Yeomans. “Centrality dependence of photon yield and elliptic flow from gluon fusion and splitting induced by magnetic fields in relativistic heavy-ion collisions”. *Eur. Phys. J. A*, 56(2):53, (2020).
- [4] Alejandro Ayala, Jorge David Castaño Yepes, M. Loewe, and Enrique Muñoz. “Gluon polarization tensor in a magnetized medium: Analytic approach starting from the sum over Landau levels”. *Phys. Rev. D*, 101:036016, (2020).
- [5] Alejandro Ayala, Jorge Castaño Yepes, CA Dominguez, S Hernandez-Ortiz, LA Hernandez, M Loewe, D Manreza Paret, and R Zamora. “Thermal corrections to the gluon magnetic Debye mass”. *Rev. Mex. Fis.*, 66:446–461, (2020).
- [6] Alejandro Ayala, Jorge David Castaño-Yepes, LA Hernández, Jordi Salinas, and R Zamora. “Gluon polarization tensor and dispersion relation in a weakly magnetized medium”. *arXiv preprint arXiv:2009.00830*, (2020).
- [7] Murray Gell-Mann. “A Schematic Model of Baryons and Mesons”. *Phys. Lett.*, 8:214–215, (1964).
- [8] George Zweig. “Origins of the Quark Model”. In *4th International Conference on Baryon Resonances*, 7 (1980).
- [9] David J. Gross and Frank Wilczek. “Ultraviolet Behavior of Nonabelian Gauge Theories”. *Phys. Rev. Lett.*, 30:1343–1346, (1973).

-
- [10] H.David Politzer. “Reliable Perturbative Results for Strong Interactions?” *Phys. Rev. Lett.*, 30:1346–1349, (1973).
- [11] Kenneth G. Wilson. “Confinement of quarks”. *Phys. Rev. D*, 10:2445–2459, (1974).
- [12] Jeff Greensite. “*An introduction to the confinement problem*”, volume 821. Springer, 2011.
- [13] Walter Greiner, Stefan Schramm, and Eckart Stein. “*Quantum chromodynamics*”. Springer Science & Business Media, (2007).
- [14] I. Arsene and BRAHMS collaboration. “Quark gluon plasma and color glass condensate at RHIC? The Perspective from the BRAHMS experiment”. *Nucl. Phys. A*, 757:1–27, (2005).
- [15] B.B. Back and PHOBOS collaboration. “The PHOBOS perspective on discoveries at RHIC”. *Nucl. Phys. A*, 757:28–101, (2005).
- [16] John Adams and STAR collaboration. “Experimental and theoretical challenges in the search for the quark gluon plasma: The STAR Collaboration’s critical assessment of the evidence from RHIC collisions”. *Nucl. Phys. A*, 757:102–183, (2005).
- [17] K. Adcox and PHENIX collaboration. “Formation of dense partonic matter in relativistic nucleus-nucleus collisions at RHIC: Experimental evaluation by the PHENIX collaboration”. *Nucl. Phys. A*, 757:184–283, (2005).
- [18] Peter Jacobs and Xin-Nian Wang. “Matter in extremis: Ultrarelativistic nuclear collisions at RHIC”. *Prog. Part. Nucl. Phys.*, 54:443–534, (2005).
- [19] Francesco Becattini. “The Quark Gluon Plasma and relativistic heavy ion collisions in the LHC era”. *J. Phys. Conf. Ser.*, 527:012012, (2014).
- [20] Betty Bezverkhny Abelev and ALICE collaboration. “Performance of the ALICE Experiment at the CERN LHC”. *Int. J. Mod. Phys. A*, 29:1430044, (2014).
- [21] Morad Aaboud and ATLAS collaboration. “Dijet azimuthal correlations and conditional yields in pp and $p+Pb$ collisions at $\sqrt{s_{NN}} = 5.02$ TeV with the ATLAS detector”. *Phys. Rev. C*, 100(3):034903, (2019).
- [22] Maxime Guilbaud and CMS collaboration. “New insights of multi-particle azimuthal correlations with symmetric cumulants in $p - p$, p -Pb, and Pb-Pb collisions”. *Nucl. Phys. A*, 967:325–328, (2017).
- [23] Wei Li. “Collective flow from AA , pA to pp collisions – *Toward a unified paradigm*”. *Nucl. Phys. A*, 967:59–66, (2017).
- [24] Betty Bezverkhny Abelev and ALICE collaboration. “Multiplicity dependence of the average transverse momentum in pp , p -Pb, and Pb-Pb collisions at the LHC”. *Phys. Lett. B*, 727:371–380, (2013).
- [25] Benjamin Nachman and Michelangelo L. Mangano. “Observables for possible QGP signatures in central pp collisions”. *Eur. Phys. J. C*, 78:1–19, (2017).

-
- [26] Eleazar Cuautle Flores. “Are the collective phenomena a universal feature of the hadronic matter created in $p - p$, $p - A$ and $A - A$ colliding systems?” *Int. J. Mod. Phys. E*, 25(07):1642007, (2016).
- [27] Fu-Ming Liu and Klaus Werner. “On QGP Formation in pp Collisions at 7 TeV”. *J. Phys. G*, 38:124183, (2011).
- [28] MT AlFiky, OT ElSherif, and AM Hamed. “Quark gluon plasma formation in proton-proton collisions using PYTHIA”. *arXiv preprint arXiv:1902.05114*, (2019).
- [29] Edmond Iancu. “QCD in heavy ion collisions”. *arXiv preprint arXiv:1205.0579*, (2012).
- [30] Henning Heiselberg and Morten Hjorth-Jensen. “Phases of dense matter in neutron stars”. *Phys. Rept.*, 328:237–327, (2000).
- [31] N. Cabibbo and G. Parisi. “Exponential Hadronic Spectrum and Quark Liberation”. *Phys. Lett. B*, 59:67–69, (1975).
- [32] R. Hagedorn. “Statistical thermodynamics of strong interactions at high-energies”. *Nuovo Cim. Suppl.*, 3:147–186, (1965).
- [33] Kenji Fukushima. “Chiral Symmetry and Heavy-Ion Collisions”. *J. Phys. G*, 35:104020, (2008).
- [34] Gordon Baym. “Confinement of quarks in nuclear matter”. *Phys. A*, 96(1-2):131–135, (1979).
- [35] Helmut Satz. “Deconfinement and percolation”. *Nucl. Phys. A*, 642:130–142, (1998).
- [36] T. Hatsuda and T. Kunihiro. “Fluctuation Effects in Hot Quark Matter: Precursors of Chiral Transition at Finite Temperature”. *Phys. Rev. Lett.*, 55:158–161, (1985).
- [37] P. Gerber and H. Leutwyler. “Hadrons Below the Chiral Phase Transition”. *Nucl. Phys. B*, 321:387–429, (1989).
- [38] EG Drukarev and EM Levin. “Structure of nuclear matter and QCD sum rules”. *Progress in Particle and Nuclear Physics*, 27:77–134, (1991).
- [39] Thomas D. Cohen, R.J. Furnstahl, and David K. Griegel. “Quark and gluon condensates in nuclear matter”. *Phys. Rev. C*, 45:1881–1893, (1992).
- [40] Tetsuo Hatsuda and Su Houng Lee. “QCD sum rules for vector mesons in the nuclear medium”. *Phys. Rev. C*, 46(1):34, (1992).
- [41] Kenji Fukushima and Tetsuo Hatsuda. “The phase diagram of dense QCD”. *Rept. Prog. Phys.*, 74:014001, (2011).
- [42] M. Asakawa and K. Yazaki. “Chiral Restoration at Finite Density and Temperature”. *Nucl. Phys. A*, 504:668–684, (1989).

-
- [43] A. Barducci, R. Casalbuoni, S. De Curtis, Raoul Gatto, and Giulio Pettini. “Chiral Symmetry Breaking in QCD at Finite Temperature and Density”. *Phys. Lett. B*, 231:463–470, (1989).
- [44] A. Barducci, R. Casalbuoni, S. De Curtis, Raoul Gatto, and Giulio Pettini. “Chiral Phase Transitions in QCD for Finite Temperature and Density”. *Phys. Rev. D*, 41:1610, (1990).
- [45] A. Barducci, R. Casalbuoni, Giulio Pettini, and Raoul Gatto. “Chiral phases of QCD at finite density and temperature”. *Phys. Rev. D*, 49:426–436, (1994).
- [46] Frank Wilczek. “Application of the renormalization group to a second order QCD phase transition”. *Int. J. Mod. Phys. A*, 7:3911–3925, (1992). [Erratum: *Int.J.Mod.Phys.A* 7, 6951 (1992)].
- [47] Bertrand C Barrois. “Superconducting quark matter”. *Nucl. Phys. B*, 129(3):390–396, (1977).
- [48] D. Bailin and A. Love. “Superfluidity and Superconductivity in Relativistic Fermion Systems”. *Phys. Rept.*, 107:325, (1984).
- [49] M. Iwasaki and T. Iwado. “Superconductivity in the quark matter”. *Phys. Lett. B*, 350:163–168, (1995).
- [50] Mark G. Alford, Krishna Rajagopal, and Frank Wilczek. “QCD at finite baryon density: Nucleon droplets and color superconductivity”. *Phys. Lett. B*, 422:247–256, (1998).
- [51] R. Rapp, Thomas Schäfer, Edward V. Shuryak, and M. Velkovsky. “Diquark Bose condensates in high density matter and instantons”. *Phys. Rev. Lett.*, 81:53–56, (1998).
- [52] Philippe Chomaz. “The nuclear liquid gas phase transition and phase coexistence”. In *AIP Conference Proceedings*, volume 610, pages 167–181. American Institute of Physics, (2002).
- [53] P. Braun-Munzinger, J. Stachel, and Christof Wetterich. “Chemical freezeout and the QCD phase transition temperature”. *Phys. Lett. B*, 596:61–69, (2004).
- [54] Larry McLerran and Robert D. Pisarski. “Phases of cold, dense quarks at large N_c ”. *Nucl. Phys. A*, 796:83–100, (2007).
- [55] A. Andronic et al. “Hadron Production in Ultra-relativistic Nuclear Collisions: Quarkyonic Matter and a Triple Point in the Phase Diagram of QCD”. *Nucl. Phys. A*, 837:65–86, (2010).
- [56] Jacopo Ghiglieri, Juhee Hong, Aleksi Kurkela, Egang Lu, Guy D. Moore, and Derek Teaney. “Next-to-leading order thermal photon production in a weakly coupled quark-gluon plasma”. *JHEP*, 05:010, (2013).
- [57] Simon Turbide, Ralf Rapp, and Charles Gale. “Hadronic production of thermal photons”. *Phys. Rev. C*, 69:014903, (2004).
- [58] Ralf Rapp and Jochen Wambach. “Low mass dileptons at the CERN SPS: Evidence for chiral restoration?” *Eur. Phys. J. A*, 6:415–420, (1999).

-
- [59] W. Liu and R. Rapp. “Low-energy thermal photons from meson-meson bremsstrahlung”. *Nucl. Phys. A*, 796:101–121, (2007).
- [60] Jaroslav Adam and ALICE collaboration. “Direct photon production in Pb-Pb collisions at $\sqrt{s_{NN}} = \text{TeV}$ ”. *Phys. Lett. B*, 754:235–248, (2016).
- [61] Erwann Masson. “Direct Photon Measurements with the ALICE Experiment at the LHC”. *MDPI Proc.*, 10(1):1, (2019).
- [62] A. Adare and PHENIX collaboration. “Enhanced production of direct photons in Au+Au collisions at $\sqrt{s_{NN}} = 200 \text{ GeV}$ and implications for the initial temperature”. *Phys. Rev. Lett.*, 104:132301, (2010).
- [63] A. Adare and PHENIX collaboration. “Observation of direct-photon collective flow in $\sqrt{s_{NN}} = 200 \text{ GeV}$ Au+Au collisions”. *Phys. Rev. Lett.*, 109:122302, (2012).
- [64] A. Adare and PHENIX collaboration. “Centrality dependence of low-momentum direct-photon production in Au+Au collisions at $\sqrt{s_{NN}} = 200 \text{ GeV}$ ”. *Phys. Rev. C*, 91(6):064904, (2015).
- [65] A. Adare and PHENIX collaboration. “Azimuthally anisotropic emission of low-momentum direct photons in Au+Au collisions at $\sqrt{s_{NN}} = 200 \text{ GeV}$ ”. *Phys. Rev. C*, 94(6):064901, (2016).
- [66] M. Germain and ALICE collaboration. “Direct photon measurements in pp and Pb–Pb collisions with the ALICE experiment”. *Nucl. Phys. A*, 967:696–699, (2017).
- [67] Daniel Lohner and ALICE collaboration. “Measurement of Direct-Photon Elliptic Flow in Pb-Pb Collisions at $\sqrt{s_{NN}} = 2.76 \text{ TeV}$ ”. *J. Phys. Conf. Ser.*, 446:012028, (2013).
- [68] Peter Brockway Arnold, Guy D. Moore, and Laurence G. Yaffe. “Photon emission from quark gluon plasma: Complete leading order results”. *JHEP*, 12:009, (2001).
- [69] Jacopo Ghiglieri, Juhee Hong, Aleksi Kurkela, Egang Lu, Guy D Moore, and Derek Teaney. “Next-to-leading order thermal photon production in a weakly coupled quark-gluon plasma”. *Journal of High Energy Physics*, 2013(5):10, (2013).
- [70] Nathan P.M. Holt, Paul M. Hohler, and Ralf Rapp. “Thermal photon emission from the $\pi\rho\omega$ system”. *Nucl. Phys. A*, 945:1–20, (2016).
- [71] Jean-François Paquet, Chun Shen, Gabriel S. Denicol, Matthew Luzum, Björn Schenke, Sangyong Jeon, and Charles Gale. “Production of photons in relativistic heavy-ion collisions”. *Phys. Rev. C*, 93:044906, (2016).
- [72] Dmitri E. Kharzeev, Larry D. McLerran, and Harmen J. Warringa. “The Effects of topological charge change in heavy ion collisions: Event by event \mathcal{P} and \mathcal{CP} violation”. *Nucl. Phys. A*, 803:227–253, (2008).
- [73] V. Skokov, A.Yu. Illarionov, and V. Toneev. “Estimate of the magnetic field strength in heavy-ion collisions”. *Int. J. Mod. Phys. A*, 24:5925–5932, (2009).

-
- [74] V. Voronyuk, V. D. Toneev, W. Cassing, E. L. Bratkovskaya, V. P. Konchakovski, and S. A. Voloshin. “Electromagnetic field evolution in relativistic heavy-ion collisions”. *Phys. Rev. C*, 83:054911, (2011).
- [75] L. McLerran and V. Skokov. “Comments About the Electromagnetic Field in Heavy-Ion Collisions”. *Nucl. Phys. A*, 929:184–190, (2014).
- [76] Adam Bzdak and Vladimir Skokov. “Event-by-event fluctuations of magnetic and electric fields in heavy ion collisions”. *Phys. Lett. B*, 710:171–174, (2012).
- [77] Alfred H Mueller. “Parton saturation: an overview”. In *QCD Perspectives on Hot and Dense Matter*, pages 45–72. Springer, (2002).
- [78] Edmond Iancu and Raju Venugopalan. “The color glass condensate and high energy scattering in QCD”. In *Quark–Gluon Plasma 3*, pages 249–363. World Scientific, (2004).
- [79] Jamal Jalilian-Marian and Yuri V Kovchegov. “Saturation physics and deuteron–gold collisions at RHIC”. *Progress in Particle and Nuclear Physics*, 56(1):104–231, (2006).
- [80] Heribert Weigert. “Evolution at small x_{bj} : The color glass condensate”. *Progress in Particle and Nuclear Physics*, 55(2):461–565, (2005).
- [81] D.N. Triantafyllopoulos. “Pomeron loops in high energy QCD”. *Acta Phys. Polon. B*, 36:3593–3664, (2005).
- [82] Francois Gelis, Edmond Iancu, Jamal Jalilian-Marian, and Raju Venugopalan. “The Color Glass Condensate”. *Ann. Rev. Nucl. Part. Sci.*, 60:463–489, (2010).
- [83] T. LAPPI. “Small x physics and RHIC data”. *Int. J. Mod. Phys. E*, 20(1):1–43, (2011).
- [84] Michael Edward Peskin and Daniel V. Schroeder. *Quantum field theory. The Advanced Book Program*. Perseus Books Reading, Massachusetts, (1995).
- [85] Koichi Hattori and Daisuke Satow. “Gluon spectrum in a quark-gluon plasma under strong magnetic fields”. *Phys. Rev. D*, 97(1):014023, (2018).
- [86] R. Kobes, G. Kunstatter, and K. Mak. “Fermion damping in hot gauge theories”. *Phys. Rev. D*, 45:4632–4639, (1992).
- [87] Robert D. Pisarski. “Scattering amplitudes in hot gauge theories”. *Phys. Rev. Lett.*, 63:1129–1132, (1989).
- [88] Kenji Fukushima. “Magnetic-field induced screening effect and collective excitations”. *Phys. Rev. D*, 83:111501, (2011).
- [89] M. Gell-Mann. “Quarks”. *Acta Phys. Austriaca Suppl.*, 9:733–761, (1972).
- [90] M.Y. Han and Yoichiro Nambu. “Three Triplet Model with Double SU(3) Symmetry”. *Phys. Rev.*, 139:B1006–B1010, (1965).

-
- [91] Sidney Coleman. “*Aspects of symmetry: selected Erice lectures*”. Cambridge University Press, (1988).
- [92] Claude Itzykson and Jean-Bernard Zuber. “*Quantum field theory*”. Courier Corporation, (2012).
- [93] Michio Kaku. “*Quantum field theory: a modern introduction*”. Oxford Univ. Press, (1993).
- [94] H. Sazdjian. “Introduction to chiral symmetry in QCD”. *EPJ Web Conf.*, 137:02001, (2017).
- [95] John F Donoghue, Eugene Golowich, and Barry R Holstein. “*Dynamics of the standard model*”, volume 35. Cambridge University press, (2014).
- [96] Benjamin Svetitsky and Laurence G. Yaffe. “Critical Behavior at Finite Temperature Confinement Transitions”. *Nucl. Phys. B*, 210:423–447, (1982).
- [97] Robert D. Pisarski and Frank Wilczek. “Remarks on the chiral phase transition in chromodynamics”. *Phys. Rev. D*, 29:338–341, (1984).
- [98] Masataka Fukugita, Masanori Okawa, and Akira Ukawa. “Finite Size Scaling Study of the Deconfining Phase Transition in Pure SU(3) Lattice Gauge Theory”. *Nucl. Phys. B*, 337:181–232, (1990).
- [99] T. Biró, P. Lévai, and Csörgö. “Editorial”. *Eur. Phys. J. Spec. Top.*, 155:I–II, (2008).
- [100] Y Aoki, G Endrődi, Z Fodor, SD Katz, and KK Szabo. “The order of the quantum chromodynamics transition predicted by the standard model of particle physics”. *Nature*, 443(7112):675–678, (2006).
- [101] VI Yukalov and EP Yukalova. “Multichannel approach to clustering matter”. *Phys. A*, 243(3-4):382–414, (1997).
- [102] V.I. Yukalov and E.P. Yukalova. “Thermodynamics of strong interactions”. *Phys. Part. Nucl.*, 28:37–65, (1997).
- [103] C. Bernard and MILC collaboration. “QCD thermodynamics with three flavors of improved staggered quarks”. *Phys. Rev. D*, 71:034504, (2005).
- [104] M. Cheng and BNLRBC-Bielefeld collaboration. “Transition temperature in QCD”. *Phys. Rev. D*, 74:054507, (2006).
- [105] Szabolcs Borsanyi and Wuppertal-Budapest collaboration. “Is there still any T_c mystery in lattice QCD? Results with physical masses in the continuum limit III”. *JHEP*, (2010)(9):73, 2010.
- [106] Yasumichi Aoki and Wuppertal-Budapest collaboration. “The QCD transition temperature: results with physical masses in the continuum limit II”. *JHEP*, 2009(06):088, (2009).
- [107] Yasumichi Aoki, Z Fodor, SD Katz, and KK Szabo. “The QCD transition temperature: Results with physical masses in the continuum limit”. *Phys. Lett. B*, 643(1):46–54, (2006).

-
- [108] Alexei Bazavov. “Chiral transition temperature and aspects of deconfinement in 2+1 flavor QCD with the HISQ/tree action”. In *XXIX International Symposium on Lattice Field Theory*, volume 139, page 182. SISSA Medialab, (2012).
- [109] A. Bazavov and HotQCD collaboration. “Chiral and deconfinement aspects of the QCD transition”. *Phys. Rev. D*, 85:054503, (2012).
- [110] Tanmoy Bhattacharya and HotQCD collaboration. “QCD Phase Transition with Chiral Quarks and Physical Quark Masses”. *Phys. Rev. Lett.*, 113:082001, (2014).
- [111] Philippe de Forcrand. “Simulating QCD at finite density”. *PoS, LAT2009:010*, (2009).
- [112] Juergen Berges and Krishna Rajagopal. “Color superconductivity and chiral symmetry restoration at nonzero baryon density and temperature”. *Nucl. Phys. B*, 538:215–232, (1999).
- [113] M. A. Halasz, A. D. Jackson, R. E. Shrock, M. A. Stephanov, and J. J. M. Verbaarschot. “Phase diagram of QCD”. *Phys. Rev. D*, 58:096007, (1998).
- [114] O. Scavenius, Á. Mócsy, I. N. Mishustin, and D. H. Rischke. “Chiral phase transition within effective models with constituent quarks”. *Phys. Rev. C*, 64:045202, (2001).
- [115] N.G. Antoniou and A.S. Kapoyannis. “Bootstrapping the QCD critical point”. *Phys. Lett. B*, 563:165–172, (2003).
- [116] Yoshitaka Hatta and Takashi Ikeda. “Universality, the QCD critical / tricritical point and the quark number susceptibility”. *Phys. Rev. D*, 67:014028, (2003).
- [117] Alejandro Ayala. “Hadronic matter at the edge: A survey of some theoretical approaches to the physics of the QCD phase diagram”. *J. Phys. Conf. Ser.*, 761(1):012066, (2016).
- [118] Ana Julia Mizher, M.N. Chernodub, and Eduardo S. Fraga. “Phase diagram of hot QCD in an external magnetic field: possible splitting of deconfinement and chiral transitions”. *Phys. Rev. D*, 82:105016, (2010).
- [119] Gergely Endrödi. “Critical point in the QCD phase diagram for extremely strong background magnetic fields”. *JHEP*, 2015(7):173, (2015).
- [120] R. V. Gavai and Sourendu Gupta. “On the critical end point of QCD”. *Phys. Rev. D*, 71:114014, (2005).
- [121] Philippe de Forcrand and Slavo Kratochvila. “Finite density QCD with a canonical approach”. *Nucl. Phys. B Proc. Suppl.*, 153:62–67, (2006).
- [122] Sayantan Sharma. “QCD Thermodynamics on the Lattice”. *Adv. High Energy Phys.*, 2013:452978, (2013).
- [123] Heng-Tong Ding, Frithjof Karsch, and Swagato Mukherjee. “Thermodynamics of strong-interaction matter from Lattice QCD”. *Int. J. Mod. Phys. E*, 24(10):1530007, (2015).

-
- [124] J.T. Mitchell and PHENIX collaboration. “The RHIC Beam Energy Scan Program: Results from the PHENIX Experiment”. *PoS*, CPOD2013:003, (2013).
- [125] Hui Wang and STAR collaboration. “STAR Results from the RHIC Beam Energy Scan”. In *J. Phys. Conf. Ser.*, volume 458, page 012001. IOP Publishing, (2013).
- [126] L. Adamczyk and STAR collaboration. “Observation of an Energy-Dependent Difference in Elliptic Flow between Particles and Antiparticles in Relativistic Heavy Ion Collisions”. *Phys. Rev. Lett.*, 110:142301, (2013).
- [127] A. Adare and PHENIX collaboration. “Evolution of π^0 Suppression in Au + Au Collisions from $\sqrt{s_{\text{NN}}} = 39$ to 200 GeV”. *Phys. Rev. Lett.*, 109:152301, (2012).
- [128] M. A. Stephanov. “Non-Gaussian Fluctuations near the QCD Critical Point”. *Phys. Rev. Lett.*, 102:032301, (2009).
- [129] Sourendu Gupta. “Finding the critical end point of QCD: Lattice and experiment”. *PoS*, CPOD2009:025, (2009).
- [130] A. Bazavov et al. “Freeze-Out Conditions in Heavy Ion Collisions from QCD Thermodynamics”. *Phys. Rev. Lett.*, 109:192302, (2012).
- [131] R.V. Gavai and Sourendu Gupta. “Lattice QCD predictions for shapes of event distributions along the freezeout curve in heavy-ion collisions”. *Phys. Lett. B*, 696:459–463, (2011).
- [132] Marek Gazdzicki and NA49-NA61/SHINE Collaborations. “NA49/NA61: results and plans on beam energy and system size scan at the CERN SPS”. *J. Phys. G*, 38:124024, (2011).
- [133] Krishna Rajagopal and Frank Wilczek. “*The Condensed matter physics of QCD*”, pages 2061–2151. 11 (2000).
- [134] Mark G. Alford, Andreas Schmitt, Krishna Rajagopal, and Thomas Schäfer. “Color superconductivity in dense quark matter”. *Rev. Mod. Phys.*, 80:1455–1515, (2008).
- [135] Steven Gottlieb, W. Liu, D. Toussaint, R. L. Renken, and R. L. Sugar. “Chiral-symmetry breaking in lattice QCD with two and four fermion flavors”. *Phys. Rev. D*, 35:3972–3980, (1987).
- [136] Steven Gottlieb, W. Liu, D. Toussaint, R. L. Renken, and R. L. Sugar. “Estimating the chiral-symmetry-restoration temperature in two-flavor QCD”. *Phys. Rev. Lett.*, 59:1513–1516, (1987).
- [137] Steven A. Gottlieb, W. Liu, R.L. Renken, R.L. Sugar, and D. Toussaint. “QCD Thermodynamics With Eight Time Slices”. *Phys. Rev. D*, 41:622, (1990).
- [138] Andrei V. Smilga. “Physics of thermal QCD”. *Phys. Rept.*, (291):1–106, 1997.
- [139] Krishna Rajagopal. “*The Chiral phase transition in QCD: Critical phenomena and long wavelength pion oscillations*”. University of Oregon, 4 (1995).

-
- [140] Ling-Fong Li. “Spontaneous symmetry breaking and chiral symmetry”. *AIP Conf. Proc.*, 531(1):16–44, (2000).
- [141] Michael C. Birse. “Chiral symmetry in nuclei: Partial restoration and its consequences”. *J. Phys. G*, 20:1537–1576, (1994).
- [142] Tetsuo Hatsuda and Teiji Kunihiro. “Chiral symmetry restoration and the sigma meson”. *Soryushiron Kenkyu*, 102(5):173–178, (2000).
- [143] J. Goldstone. “Field Theories with Superconductor Solutions”. *Nuovo Cim.*, 19:154–164, (1961).
- [144] Y. Nambu and G. Jona-Lasinio. “Dynamical Model of Elementary Particles Based on an Analogy with Superconductivity. I”. *Phys. Rev.*, 122:345–358, (1961).
- [145] Y. Nambu and G. Jona-Lasinio. “Dynamical Model of Elementary Particles Based on an Analogy with Superconductivity. II”. *Phys. Rev.*, 124:246–254, (1961).
- [146] Murray Gell-Mann and M Levy. “The axial vector current in beta decay”. *Nuovo Cim.*, 16:705, (1960).
- [147] Michel Le Bellac. “*Thermal Field Theory*”. Cambridge Monographs on Mathematical Physics. Cambridge University Press, 3 (2011).
- [148] Y. Maezawa, S. Aoki, S. Ejiri, T. Hatsuda, N. Ishii, K. Kanaya, and N. Ukita. “Thermodynamics of two-flavor lattice QCD with an improved Wilson quark action at non-zero temperature and density”. *J. Phys. G*, 34:S651–654, (2007).
- [149] A. Bazavov and HotQCD collaboration. “Chiral crossover in QCD at zero and non-zero chemical potentials”. *Phys. Lett. B*, 795:15–21, (2019).
- [150] C. Sasaki, B. Friman, and K. Redlich. “Chiral phase transition in the presence of spinodal decomposition”. *Phys. Rev. D*, 77:034024, (2008).
- [151] B.-J. Schaefer, J. M. Pawłowski, and J. Wambach. “Phase structure of the Polyakov-quark-meson model”. *Phys. Rev. D*, 76:074023, (2007).
- [152] P. Kovács and Zs. Szép. “Influence of the isospin and hypercharge chemical potentials on the location of the critical end point in the μ_B – T phase diagram of the $SU(3)_L \times SU(3)_R$ chiral quark model”. *Phys. Rev. D*, 77:065016, (2008).
- [153] M. Loewe, F. Marquez, and C. Villavicencio. “Nonlocal Nambu–Jona-Lasinio model with a fractional Lorentzian regulator in the real time formalism”. *Phys. Rev. D*, 88:056004, (2013).
- [154] P. Costa, H. Hansen, M. C. Ruivo, and C. A. de Sousa. “How parameters and regularization affect the Polyakov–Nambu–Jona-Lasinio model phase diagram and thermodynamic quantities”. *Phys. Rev. D*, 81:016007, (2010).

-
- [155] H. Abuki, R. Anglani, R. Gatto, G. Nardulli, and M. Ruggieri. “Chiral crossover, deconfinement, and quarkyonic matter within a Nambu–Jona-Lasinio model with the Polyakov loop”. *Phys. Rev. D*, 78:034034, (2008).
- [156] Wei-jie Fu, Zhao Zhang, and Yu-xin Liu. “2 + 1 flavor Polyakov–Nambu–Jona-Lasinio model at finite temperature and nonzero chemical potential”. *Phys. Rev. D*, 77:014006, (2008).
- [157] P. Costa, M. C. Ruivo, and C. A. de Sousa. “Thermodynamics and critical behavior in the Nambu–Jona-Lasinio model of QCD”. *Phys. Rev. D*, 77:096001, (2008).
- [158] R. V. Gavai and Sourendu Gupta. “QCD at finite chemical potential with six time slices”. *Phys. Rev. D*, 78:114503, (2008).
- [159] Zoltan Fodor and Sandor D Katz. “Critical point of QCD at finite T and μ , lattice results for physical quark masses”. *Journal of High Energy Physics*, 2004(04):050, (2004).
- [160] Zoltan Fodor and Sandor D Katz. “Lattice determination of the critical point of QCD at finite T and μ ”. *Journal of High Energy Physics*, 2002(03):014, (2002).
- [161] Alejandro Ayala, Martin Hentschinski, L. A. Hernández, M. Loewe, and R. Zamora. “Superstatistics and the effective QCD phase diagram”. *Phys. Rev. D*, 98:114002, (2018).
- [162] B.-J. Schaefer and M. Wagner. “Three-flavor chiral phase structure in hot and dense QCD matter”. *Phys. Rev. D*, 79:014018, (2009).
- [163] Alejandro Ayala, L.A. Hernández, M. Loewe, Juan Cristobal Rojas, and R. Zamora. “On the critical end point in a two-flavor linear sigma model coupled to quarks”. *Eur. Phys. J. A*, 56(2):71, (2020).
- [164] Frithjof Karsch, Edwin Laermann, and A Peikert. “The pressure in 2, 2+ 1 and 3 flavour QCD”. *Physics Letters B*, 478(4):447–455, (2000).
- [165] Carlos Lourenço. “Quark matter production in heavy-ion collisions”. In *Lectures on Quark Matter*, pages 1–36. Springer, (2002).
- [166] Matthew Luzum and Hannah Petersen. “Initial state fluctuations and final state correlations in relativistic heavy-ion collisions”. *J Phys. G*, 41(6):063102, (2014).
- [167] Charles Gale, Sangyong Jeon, and Bjoern Schenke. “Hydrodynamic modeling of heavy-ion collisions”. *Int. J. Mod. Phys. A*, 28(11):1340011, (2013).
- [168] Arthur M. Poskanzer and S.A. Voloshin. “Methods for analyzing anisotropic flow in relativistic nuclear collisions”. *Phys. Rev. C*, 58:1671–1678, (1998).
- [169] Ulrich Heinz and Raimond Snellings. “Collective flow and viscosity in relativistic heavy-ion collisions”. *Annual Review of Nuclear and Particle Science*, 63:123–151, (2013).
- [170] Sangyong Jeon and Ulrich Heinz. “Introduction to hydrodynamics”. *Int. J. Mod. Phys. E*, 24(10):1530010, (2015).

-
- [171] Pasi Huovinen and Hannah Petersen. “Particlization in hybrid models”. *Eur. Phys. J. A*, 48:171, (2012).
- [172] S.A. Bass and A. Dumitru. “Dynamics of hot bulk QCD matter: From the quark gluon plasma to hadronic freezeout”. *Phys. Rev. C*, 61:064909, (2000).
- [173] D. Teaney, J. Lauret, and Edward V. Shuryak. “Flow at the SPS and RHIC as a quark gluon plasma signature”. *Phys. Rev. Lett.*, 86:4783–4786, (2001).
- [174] Tetsufumi Hirano, Ulrich W. Heinz, Dmitri Kharzeev, Roy Lacey, and Yasushi Nara. “Hadronic dissipative effects on elliptic flow in ultrarelativistic heavy-ion collisions”. *Phys. Lett. B*, 636:299–304, (2006).
- [175] Chiho Nonaka and Steffen A. Bass. “Space-time evolution of bulk QCD matter”. *Phys. Rev. C*, 75:014902, (2007).
- [176] Steffen A Bass, Mohamed Belkacem, Marcus Bleicher, Mathias Brandstetter, L Bravina, Christoph Ernst, Lars Gerland, M Hofmann, S Hofmann, Jens Konopka, et al. “Microscopic models for ultrarelativistic heavy ion collisions”. *Progress in Particle and Nuclear Physics*, 41:255–369, (1998).
- [177] M. Bleicher et al. “Relativistic hadron hadron collisions in the ultrarelativistic quantum molecular dynamics model”. *J. Phys. G*, 25:1859–1896, (1999).
- [178] Y. Nara, N. Otuka, A. Ohnishi, K. Niita, and S. Chiba. “Study of relativistic nuclear collisions at AGS energies from p + Be to Au + Au with hadronic cascade model”. *Phys. Rev. C*, 61:024901, (2000).
- [179] H. Sorge. “Flavor production in Pb (160-A/GeV) on Pb collisions: Effect of color ropes and hadronic rescattering”. *Phys. Rev. C*, 52:3291–3314, (1995).
- [180] Adam Takacs and Denes Molnar. “Suppression of elliptic flow without viscosity”. *arXiv preprint arXiv:1906.12311*, (2019).
- [181] Fred Cooper and Graham Frye. “Single-particle distribution in the hydrodynamic and statistical thermodynamic models of multiparticle production”. *Phys. Rev. D*, 10:186–189, (1974).
- [182] S. Ryu, J. F. Paquet, C. Shen, G.S. Denicol, B. Schenke, S. Jeon, and C. Gale. “Importance of the Bulk Viscosity of QCD in Ultrarelativistic Heavy-Ion Collisions”. *Phys. Rev. Lett.*, 115(13):132301, (2015).
- [183] K. Aamodt and ALICE collaboration. “Higher harmonic anisotropic flow measurements of charged particles in Pb-Pb collisions at $\sqrt{s_{NN}}=2.76$ TeV”. *Phys. Rev. Lett.*, 107:032301, (2011).
- [184] Serguei Chatrchyan and CMS collaboration. “Measurement of the elliptic anisotropy of charged particles produced in PbPb collisions at $\sqrt{s_{NN}}=2.76$ TeV”. *Phys. Rev. C*, 87(1):014902, (2013).

-
- [185] Serguei Chatrchyan and CMS collaboration. “Measurement of Higher-Order Harmonic Azimuthal Anisotropy in PbPb Collisions at $\sqrt{s_{NN}} = 2.76$ TeV”. *Phys. Rev. C*, 89(4):044906, (2014).
- [186] Snigdha Ghosh, Sushant K. Singh, Sandeep Chatterjee, Jane Alam, and Sourav Sarkar. “Initial conditions from the shadowed Glauber model for Pb + Pb collisions at $\sqrt{s_{NN}} = 2.76$ TeV”. *Phys. Rev. C*, 93:054904, (2016).
- [187] Jia Liu, Chun Shen, and Ulrich Heinz. “Pre-equilibrium evolution effects on heavy-ion collision observables”. *Phys. Rev. C*, 91:064906, (2015).
- [188] Peter F. Kolb and Ralf Rapp. “Transverse flow and hadrochemistry in Au + Au collisions at $\sqrt{s_{NN}} = 200$ GeV”. *Phys. Rev. C*, 67:044903, (2003).
- [189] Wojciech Broniowski, Wojciech Florkowski, Mikolaj Chojnacki, and Adam Kisiel. “Free-streaming approximation in early dynamics of relativistic heavy-ion collisions”. *Phys. Rev. C*, 80:034902, (2009).
- [190] Björn Schenke, Prithwish Tribedy, and Raju Venugopalan. “Fluctuating Glasma Initial Conditions and Flow in Heavy Ion Collisions”. *Phys. Rev. Lett.*, 108:252301, (2012).
- [191] Björn Schenke, Chun Shen, and Prithwish Tribedy. “Features of the IP-Glasma”. *Nuclear Physics A*, 982:435–438, (2019).
- [192] Pasi Huovinen and Pter Petreczky. “QCD equation of state and hadron resonance gas”. *Nucl. Phys. A*, 837(1):26 – 53, (2010).
- [193] S. Afanasiev and PHENIX collaboration. “Measurement of Direct Photons in Au+Au Collisions at $\sqrt{s_{NN}} = 200$ GeV”. *Phys. Rev. Lett.*, 109:152302, (2012).
- [194] A. Adare and PHENIX collaboration. “Direct photon production in $p+p$ collisions at $\sqrt{s}=200$ GeV at midrapidity”. *Phys. Rev. D*, 86:072008, (2012).
- [195] S. S. Adler and PHENIX collaboration. “Measurement of Direct Photon Production in $p+p$ Collisions at $\sqrt{s} = 200$ GeV”. *Phys. Rev. Lett.*, 98:012002, (2007).
- [196] J.F. Owens. “Large Momentum Transfer Production of Direct Photons, Jets, and Particles”. *Rev. Mod. Phys.*, 59:465, (1987).
- [197] P. Aurenche, R. Baier, M. Fontannaz, and D. Schiff. “Prompt Photon Production at Large $p(T)$ Scheme Invariant QCD Predictions and Comparison with Experiment”. *Nucl. Phys. B*, 297:661–696, (1988).
- [198] F. Aversa, P. Chiappetta, Mario Greco, and J.P. Guillet. “QCD Corrections to Parton-Parton Scattering Processes”. *Nucl. Phys. B*, 327:105, (1989).
- [199] P. Aurenche, J. Ph. Guillet, E. Pilon, M. Werlen, and M. Fontannaz. “Recent critical study of photon production in hadronic collisions”. *Phys. Rev. D*, 73:094007, (2006).

-
- [200] Serguei Chatrchyan and CMS collaboration. “Measurement of isolated photon production in pp and PbPb collisions at $\sqrt{s_{NN}} = 2.76$ TeV”. *Phys. Lett. B*, 710:256–277, (2012).
- [201] Daniel Lohner. *Anisotropic flow of direct photons in Pb-Pb collisions at 2.76 TeV per nucleon*. PhD thesis, PhD thesis, Heidelberg University, 2013.
- [202] Benjamin Bannier. *Systematic studies of soft direct photon production in Au+ Au collisions at $\sqrt{s_{NN}} = 200$ GeV*. PhD thesis, PhD thesis, Stony Brook University, (2014).
- [203] Benjamin Bannier and PHENIX Collaboration. “Systematic studies of the centrality dependence of soft photon production in Au+ Au collision with PHENIX”. *Nuclear Physics A*, 931:1189–1193, (2014).
- [204] J.D. Bjorken. “Hadron Final States in Deep Inelastic Processes”. *Lect. Notes Phys.*, 56:93, (1976).
- [205] V.N. Gribov and L.N. Lipatov. “Deep inelastic $e + p$ scattering in perturbation theory”. *Sov. J. Nucl. Phys.*, 15:438–450, (1972).
- [206] Guido Altarelli and Giorgio Parisi. “Asymptotic freedom in parton language”. *Nuclear Physics B*, 126(2):298–318, (1977).
- [207] Yuri L Dokshitzer. “Calculation of the structure functions for deep inelastic scattering and e^+e^- annihilation by perturbation theory in quantum chromodynamics”. *Zh. Eksp. Teor. Fiz*, 73:1216, (1977).
- [208] R Keith Ellis, W James Stirling, and Bryan R Webber. “*QCD and collider physics*”. Cambridge university press, 2003.
- [209] P Cortese et al. “ALICE: Physics performance report, volume I”. *J. Phys. G*, 30:1517–1763, (2004).
- [210] Christian Wolfgang Fabjan et al. “ALICE: Physics performance report, volume II”. *J. Phys. G*, 32:1295–2040, (2006).
- [211] Dmitri Kharzeev and Eugene Levin. “Manifestations of high density QCD in the first RHIC data”. *Physics Letters B*, 523(1-2):79–87, (2001).
- [212] F. Gelis. “Color Glass Condensate and Glasma”. *Int. J. Mod. Phys. A*, 28:1330001, (2013).
- [213] Harrison B Prosper and Michael Danilov. “*Techniques and concepts of high-energy physics*”, volume 566. Springer Science & Business Media, (2012).
- [214] Edmond Iancu, Andrei Leonidov, and Larry McLerran. “The colour glass condensate: An introduction”. In *QCD perspectives on hot and dense matter*, pages 73–145. Springer, (2002).
- [215] Larry McLerran. “The CGC and the Glasma: Two lectures at the Yukawa Institute”. *Progress of Theoretical Physics Supplement*, 187:17–30, (2011).

-
- [216] LN Lipatov. “Reggeization of the vector meson and the vacuum singularity in nonabelian gauge theories”. *Sov. J. Nucl. Phys*, 23:338, (1976).
- [217] Eh A Kuraev, LN Lipatov, and Victor S Fadin. “Pomeranchuk singularity in non-Abelian gauge theories”. *Zhurnal Eksperimental’noj i Teoreticheskoy Fiziki*, 72(2):377–389, (1977).
- [218] Ya Ya Balitskii and LN Lipatov. “Pomeranchuk singularity in quantum chromodynamics”. *Sov. J. Nucl. Phys.(Engl. Transl.);(United States)*, 28(6), (1978).
- [219] L.A. Harland-Lang, A.D. Martin, P. Motylinski, and R.S. Thorne. “Parton distributions in the LHC era: MMHT 2014 PDFs”. *Eur. Phys. J. C*, 75(5):204, (2015).
- [220] Leonid Vladimirovič Gribov, Eugene M Levin, and Michail G Ryskin. “Semihard processes in QCD”. *Physics Reports*, 100(1-2):1–150, (1983).
- [221] Alfred H Mueller and Jianwei Qiu. “Gluon recombination and shadowing at small values of x ”. *Nuclear Physics B*, 268(2):427–452, (1986).
- [222] Javier L Albacete and Cyrille Marquet. “Gluon saturation and initial conditions for relativistic heavy ion collisions”. *Progress in Particle and Nuclear Physics*, 76:1–42, (2014).
- [223] Larry McLerran and Raju Venugopalan. “Computing quark and gluon distribution functions for very large nuclei”. *Phys. Rev. D*, 49:2233–2241, (1994).
- [224] K.G. Klimenko. “Three-dimensional Gross-Neveu model at nonzero temperature and in an external magnetic field”. *Z. Phys. C*, 54:323–330, (1992).
- [225] V.P. Gusynin, V.A. Miransky, and I.A. Shovkovy. “Catalysis of dynamical flavor symmetry breaking by a magnetic field in (2+1)-dimensions”. *Phys. Rev. Lett.*, 73:3499–3502, (1994). [Erratum: *Phys.Rev.Lett.* 76, 1005 (1996)].
- [226] VP Gusynin, VA Miransky, and IA Shovkovy. “Dimensional reduction and catalysis of dynamical symmetry breaking by a magnetic field”. *Nuclear Physics B*, 462(2-3):249–290, (1996).
- [227] Florian Preis, Anton Rebhan, and Andreas Schmitt. “Inverse magnetic catalysis in dense holographic matter”. *JHEP*, 03:033, (2011).
- [228] V.P. Gusynin, V.A. Miransky, and I.A. Shovkovy. “Dynamical chiral symmetry breaking by a magnetic field in QED”. *Phys. Rev. D*, 52:4747–4751, (1995).
- [229] Kenji Fukushima, Dmitri E. Kharzeev, and Harmen J. Warringa. “Chiral magnetic effect”. *Phys. Rev. D*, 78:074033, (2008).
- [230] N.O. Agasian and S.M. Fedorov. “Quark-hadron phase transition in a magnetic field”. *Phys. Lett. B*, 663:445–449, (2008).
- [231] Eduardo S. Fraga and Ana Julia Mizher. “Chiral transition in a strong magnetic background”. *Phys. Rev. D*, 78:025016, (2008).

-
- [232] Alejandro Ayala, Angel Sánchez, Gabriella Piccinelli, and Sarira Sahu. “Effective potential at finite temperature in a constant magnetic field: Ring diagrams in a scalar theory”. *Phys. Rev. D*, 71:023004, (2005).
- [233] Alejandro Ayala, C.A. Dominguez, L.A. Hernandez, M. Loewe, and R. Zamora. “Magnetized effective QCD phase diagram”. *Phys. Rev. D*, 92(9):096011, (2015). [Addendum: *Phys.Rev.D* 92, 119905 (2015)].
- [234] D.T. Son and Ariel R. Zhitnitsky. “Quantum anomalies in dense matter”. *Phys. Rev. D*, 70:074018, (2004).
- [235] Max A. Metlitski and Ariel R. Zhitnitsky. “Anomalous axion interactions and topological currents in dense matter”. *Phys. Rev. D*, 72:045011, (2005).
- [236] D.T. Son and M.A. Stephanov. “Axial anomaly and magnetism of nuclear and quark matter”. *Phys. Rev. D*, 77:014021, (2008).
- [237] Mark G. Alford, Juergen Berges, and Krishna Rajagopal. “Magnetic fields within color superconducting neutron star cores”. *Nucl. Phys. B*, 571:269–284, (2000).
- [238] Efrain J. Ferrer, Vivian de la Incera, and Cristina Manuel. “Magnetic color flavor locking phase in high density QCD”. *Phys. Rev. Lett.*, 95:152002, (2005).
- [239] V.A. Okorokov. “Magnetic field in nuclear collisions at ultra high energies”. *MDPI Physics*, 1(2):183–193, (2019).
- [240] Yang Zhong, Chun-Bin Yang, Xu Cai, and Sheng-Qin Feng. “A systematic study of magnetic field in relativistic heavy-ion collisions in the RHIC and LHC energy regions”. *Advances in High Energy Physics*, 2014, (2014).
- [241] Vladimir Skokov. “Photon azimuthal anisotropy and magnetic field in heavy-ion collisions”. *J. Phys. Conf. Ser.*, 432:012021, (2013).
- [242] D.N. Voskresensky and N.Yu. Anisimov. Properties of a pion condensate in a magnetic field. *Sov. Phys. JETP*, 51:13–22, (1980).
- [243] Neda Sadooghi. “Chiral MHD description of a perfect magnetized QGP using the effective NJL model in a strong magnetic field”. *arXiv preprint arXiv:0905.2097*, 5 (2009).
- [244] W. Ehehalt and W. Cassing. “Relativistic transport approach for nucleus nucleus collisions from SIS to SPS energies”. *Nucl. Phys. A*, 602:449–486, (1996).
- [245] W. Cassing and E.L. Bratkovskaya. “Hadronic and electromagnetic probes of hot and dense nuclear matter”. *Phys. Rept.*, 308:65–233, (1999).
- [246] S.S. Adler and PHENIX collaboration. “Systematic studies of the centrality and $\sqrt{s_{NN}}$ dependence of the $dE(T)/d\eta$ and $dN_{ch}/d\eta$ in heavy ion collisions at mid-rapidity”. *Phys. Rev. C*, 71:034908, (2005). [Erratum: *Phys.Rev.C* 71, 049901 (2005)].

-
- [247] Y. Burnier, D.E. Kharzeev, J. Liao, and H.-U. Yee. “From the chiral magnetic wave to the charge dependence of elliptic flow”. *arXiv preprint arXiv:1208.2537*, 8 (2012).
- [248] Gokce Basar, Dmitri Kharzeev, Dmitri Kharzeev, and Vladimir Skokov. “Conformal anomaly as a source of soft photons in heavy ion collisions”. *Phys. Rev. Lett.*, 109:202303, (2012).
- [249] Julian Schwinger. “On Gauge Invariance and Vacuum Polarization”. *Phys. Rev.*, 82:664–679, (1951).
- [250] Kaushik Bhattacharya. “Gauge invariance of elementary particle processes taking place in presence of a background magnetic field”. *Int. J. Mod. Phys. A*, 21:3151–3170, (2006).
- [251] Alexander Kuznetsov and Nickolay Mikheev. “*Electroweak processes in external electromagnetic fields*”, volume 197. Springer Science & Business Media, (2003).
- [252] Alejandro Ayala, J. J. Cobos-Martínez, M. Loewe, María Elena Tejeda-Yeomans, and R. Zamora. “Finite temperature quark-gluon vertex with a magnetic field in the hard thermal loop approximation”. *Phys. Rev. D*, 91:016007, (2015).
- [253] Vladimir A Miransky and Igor A Shovkovy. “Quantum field theory in a magnetic field: From quantum chromodynamics to graphene and Dirac semimetals”. *Physics Reports*, 576:1–209, (2015).
- [254] Larry McLerran and Bjoern Schenke. “The glasma, photons and the implications of anisotropy”. *Nuclear Physics A*, 929:71–82, (2014).
- [255] Alex Krasnitz, Yasushi Nara, and Raju Venugopalan. “Coherent Gluon Production in Very-High-Energy Heavy-Ion Collisions”. *Phys. Rev. Lett.*, 87:192302, (2001).
- [256] Chandrodoy Chattopadhyay, Rajeev S. Bhalerao, Jean-Yves Ollitrault, and Subrata Pal. “Effects of initial-state dynamics on collective flow within a coupled transport and viscous hydrodynamic approach”. *Phys. Rev. C*, 97:034915, (2018).
- [257] Longgang Pang, Qun Wang, and Xin-Nian Wang. “Effects of initial flow velocity fluctuation in event-by-event (3+1)D hydrodynamics”. *Phys. Rev. C*, 86:024911, (2012).
- [258] Alekski Kurkela, Aleksas Mazeliauskas, Jean-François Paquet, Sören Schlichting, and Derek Teaney. “Matching the Nonequilibrium Initial Stage of Heavy Ion Collisions to Hydrodynamics with QCD Kinetic Theory”. *Phys. Rev. Lett.*, 122:122302, (2019).
- [259] Steffen A Bass et al. “Microscopic models for ultrarelativistic heavy ion collisions”. *Progress in Particle and Nuclear Physics*, 41:255–369, (1998).
- [260] Marcus Bleicher et al. “Relativistic hadron-hadron collisions in the ultra-relativistic quantum molecular dynamics model”. *Journal of Physics G: Nuclear and Particle Physics*, 25(9):1859, (1999).
- [261] R. M. Barnett and Particle Data Group. “Review of Particle Physics”. *Phys. Rev. D*, 54:1–708, Jul 1996.

-
- [262] Lev Davidovich Landau and Evgenii Mikhailovich Lifshitz. “*The classical theory of fields*”. Pergamon, (1971).
- [263] Bartke Jerzy. “*Introduction to relativistic heavy ion physics*”. World Scientific, (2008).
- [264] R Vogt. “Relation of hard and total cross sections to centrality”. *arXiv preprint nucl-th/9903051*, (1999).
- [265] A. Adare and PHENIX collaboration. “Low-momentum direct photon measurement in Cu+Cu collisions at $\sqrt{s_{NN}} = 200$ GeV”. *Phys. Rev. C*, 98(5):054902, (2018).
- [266] Aritra Bandyopadhyay, Chowdhury Aminul Islam, and Munshi G. Mustafa. “Electromagnetic spectral properties and Debye screening of a strongly magnetized hot medium”. *Phys. Rev. D*, 94:114034, (2016).
- [267] Koichi Hattori and Kazunori Itakura. “Vacuum birefringence in strong magnetic fields: (I) Photon polarization tensor with all the Landau levels”. *Ann. Phys.*, 330:23–54, (2013).
- [268] Ken-Ichi Ishikawa, Daiji Kimura, Kenta Shigaki, and Asako Tsuji. “A numerical evaluation of vacuum polarization tensor in constant external magnetic fields”. *Int. J. Mod. Phys. A*, 28:1350100, (2013).
- [269] E. J. Ferrer and A. Sanchez. “Magnetic field effect in the fine-structure constant and electron dynamical mass”. *Phys. Rev. D*, 100:096006, (2019).
- [270] J. Alexandre. “Vacuum polarization in thermal QED with an external magnetic field”. *Phys. Rev. D*, 63:073010, (2001).
- [271] W Dittrich and M Reuter. *Effective lagrangians in quantum electrodynamics springer lect. Notes Phys*, 220, (1985).
- [272] James D. Bjorken and Sidney D. Drell. “*Relativistic quantum mechanics*”. McGraw-Hill, (1965).
- [273] Andreas Ringwald. “Pair production from vacuum at the focus of an X-ray free electron laser”. *Phys. Lett. B*, 510(1-4):107–116, (2001).
- [274] Vladimir Stepanovich Popov. “Schwinger mechanism of electron-positron pair production by the field of optical and X-ray lasers in vacuum”. *Jetp Lett.*, 74(3):133–138, (2001).
- [275] E. Brezin and C. Itzykson. “Pair Production in Vacuum by an Alternating Field”. *Phys. Rev. D*, 2:1191–1199, (1970).
- [276] Eemeli Annala, Tyler Gorda, Alekski Kurkela, Joonas Nättilä, and Alekski Vuorinen. “Evidence for quark-matter cores in massive neutron stars”. *Nature Physics*, pages 1–4, (2020).
- [277] William R. Tavares, Ricardo L. S. Farias, and Sidney S. Avancini. “Deconfinement and chiral phase transitions in quark matter with a strong electric field”. *Phys. Rev. D*, 101:016017, (2020).

-
- [278] Han Gao, Zonglin Mo, and Shu Lin. “Photon Self-energy in Magnetized Chiral Plasma from Kinetic Theory”. *arXiv preprint arXiv:2002.07959*, (2020).
- [279] A Rebhan. “Hard thermal loops and QCD thermodynamics”. *arXiv preprint hep-ph/0111341*, (2001).
- [280] Mujeeb Hasan and Binoy Krishna Patra. “Dissociation of heavy quarkonia in a weak magnetic field”. *Phys. Rev. D*, 102:036020, (2020).
- [281] Tzuu-Kang Chyi, Chien-Wen Hwang, W. F. Kao, Guey-Lin Lin, Kin-Wang Ng, and Jie-Jun Tseng. “Weak-field expansion for processes in a homogeneous background magnetic field”. *Phys. Rev. D*, 62:105014, (2000).
- [282] Louise Dolan and Roman Jackiw. “Symmetry behavior at finite temperature”. *Physical Review D*, 9(12):3320, (1974).
- [283] Joseph I Kapusta and Charles Gale. *Finite-temperature field theory: Principles and applications*. Cambridge University Press, (2006).